Predicting Abnormal Combustion Phenomena In Highly Booted Spark Ignition Engines

Giles, Karl

Award date:
2018

Awarding institution:
University of Bath

Predicting Abnormal Combustion Phenomena in Highly Boosted Spark Ignition Engines

Karl Giles

A thesis submitted for the degree of Doctor of Philosophy

University of Bath

Department of Mechanical Engineering

February 2018

Abstract

As powertrains and IC engines continue to grow in complexity, many vehicle manufacturers (OEMs) are turning to simulation in an effort to reduce design validation and calibration costs. Ultimately, their aim is to complete this process entirely within the virtual domain, without the need for any physical testing. Practical simulation techniques for the prediction of knock in spark ignition (SI) engines rely on empirical ignition delay correlations (IDCs). These IDCs are used to approximate the complex ignition delay characteristics of real and surrogate fuel compositions with respect to temperature, pressure and mixture composition. Over the last 40 years, a large number of IDCs have been put forward in the literature, spanning a broad range of fuels, operating conditions and calibration methods. However, the applicability of these tools has yet to be verified at the high brake mean effective pressure (BMEP) operating conditions relevant to highly boosted, downsized engines.

Here, the applicability of 16 gasoline-relevant IDCs for predicting knock onset at high loads (BMEP > 30bar) has been investigated by comparing the knock predictions from each IDC against experimentally measured knock onset times. Firstly, a detailed investigation into cylinder pressure data processing techniques was performed to determine which knock detection and angle of knock onset (aKO) measurement methods were most appropriate at high loads. A method based on the maximum amplitude pressure oscillation (MAPO) during knock-free operation best estimated cycle classifications, whilst Shahlari's Signal Energy Ratio technique [1] most accurately predicted knock onset. To the author's knowledge, this is the first time that such a comprehensive study on the accuracy of these techniques at such high loads has been conducted. Importantly, these findings represent a valuable framework to inform other researchers in the field of knocking combustion on which techniques are needed to extract accurate and relevant information from measured cylinder pressure records.

Secondly, the data processing techniques derived were applied to experimental data collected across a wide range of high BMEP operating conditions (up to a maximum of 32 bar) using a 1.6 litre, 4-cylinder SI engine. Trapped charge composition and temperature

were predicted using a calibrated 1D model of the engine, whilst the temperature of a hypothetical hotspot in the unburned zone was estimated separately by assuming adiabatic compression from a point after intake valve closing and by mapping γ (the ratio of specific heat capacities) as a function of temperature. This revealed that none of the IDCs tested performed well at conditions relevant to modern, downsized engines. The IDC that achieved the best overall balance between aKO accuracy and cycle-classification agreement was the "cool-flame" correlation for iso-octane proposed by Ma [2]. However, this had an unacceptably high average aKO error of ±3.5° compared to the ±2°CA limit observed within the literature, and its average cycle-classification accuracy was below 60%. The main reason for this relatively modest accuracy was a large number of false-positive cycle classifications, which mainly occurred in slow or late burning cycles. Further work should therefore focus on methods to reduce the number of false positive classifications obtained with this correlation, which could be achieved using empirical correlations to describe the latest point in the cycle for which knock would be permitted to occur in terms other measureable combustion parameters.

Overall, this research has generated a unique insight into combustion at very high loads, as well as an extensive dataset that can be used for future research to improve the accuracy of empirical knock modelling techniques. Furthermore, this work has demonstrated that for the purposes of virtual spark timing calibration and the avoidance of knock, the current crop of practical simulation tools is not accurate enough at the conditions relevant to modern SI engines and has provided a better understanding of their limitations. These findings represent a major contribution to the field from both a research perspective and for industrial applications.

Acknowledgements

I would like to express my sincerest thanks and appreciation to my supervisors, Professor Chris Brace and Professor Sam Akehurst for their guidance, supervision and continued support over what has been a long and challenging period.

I would also like to thank Dr Andrew Lewis for his support, both as a colleague working on the Ultraboost project and as a friend, offering support and advice whenever it was asked.

I must also thank all the PVRC technician team (James Burge, Bob Gusthart, James Cansell and Tom Holley) for their efforts maintaining and modifying the test facility, for fixing my mistakes, putting up with stupid questions and for undoing the things I couldn't!

I would like to thank collaborators at the various institutions involved in the Ultraboost programme along the way, in particular Dr Rishin Patel, Professor Jamie Turner, Mr Andrew Popplewell, Mr Nick Luard, Mr John Geddes and Mr Niall Turner from Jaguar Land Rover, and Dr Roger Cracknell, Dr Sarah Remmert, Dr Jan-Hendrik Redmann and Dr Arjun Prakash from Shell Global Solutions. The financial support of the Technology Strategy Board, JLR and Shell Global Solutions is gratefully acknowledged.

I would also like to thank all of my colleagues at the PVRC (past and present). In particular, Dr Deepak Hari, Dr Huayin Tan, Dr Qingning Zhang, Dom Parsons, Dr Edward Chappell, Dr Simon Pickering, Dr Tomasz Duda, Davide Di Blasio and Darren Millwood.

Finally, I would like to thank all of my close friends and family for the incredible support they have lent me over the last six years. In particular, I would like to thank my parents, Sue and Paul Giles, for all of the opportunities they have given me in life and for supporting me in all of my ventures. My deepest thanks also go to my incredibly talented girlfriend, Dr Charlotte Barthen, for reading every word of this thesis front to back and for putting up with me being "nearly there" for so long. I couldn't have done it without you.

Thank you all.

Table of Contents

Abstract I

Acknowledgements III

List of Figures VIII

List of Tables XV

Abbreviations XVII

Chapter 1 – Introduction 1

1.1 Background and motivation 1

1.2 Aims and objectives 3

Chapter 2 – Literature Review 4

Chapter Summary 4

2.1 Forms of Abnormal and Knocking Combustion 5

2.2 Knock Mitigation Strategies 11

2.2.1 Spark Retard 12

2.2.2 Compression Ratio Reduction 13

2.2.3 Turbulence Enhancement 14

2.2.4 Cooling Strategies 18

2.3 Fuel Effects 24

2.4 Knock Simulation Approaches 28

2.4.1 Single-Step IDCs (with fixed parameter values) 29

2.4.2 3-Arrhenius IDCs 33

2.4.3 Cool-Flame/Stage L+W Integral IDCs 35

2.4.4 Advanced Single Step IDCs (with variable parameter values) 39

2.5 Summary/Conclusions 43

Chapter 3 – Test Facilities and Experimental Methods 45

Chapter Summary 45

3.1 Test Cell Facilities 46
3.1.1 Engine Dynamometer 46
3.1.2 Forced Induction Simulator 46
3.1.3 EGR Pump 48
3.1.4 Temperature Control 48
3.2 Engine Specification 49
3.3 Instrumentation and Data Acquisition 51
3.4 Experimental Test Conditions 53
3.5 Experimental Results 56
3.5.1 Effects of Load on Knock 56
3.5.2 Effects of EGR on Knock 60
3.6 Conclusions 64
Chapter 4 – Knocking Cycle Detection and Angle of Knock Onset Estimation 65
Chapter Summary 65
4.1 Introduction 66
4.2 Knocking Cycle Detection Methods 66
4.2.1 Signal Types Used 66
4.2.2 Cylinder Pressure Based Knock Intensity Metrics 73
4.2.3 Automated Knocking Cycle Detection Methods 87
4.3 Angle of Knock Onset Estimation 98
4.4 Manual Cycle Classification and Angle of Knock Onset Estimation 102
4.4.1 Experimental Data 102
4.4.2 Experimental Data Processing and Calculations 102
4.4.3 Manual Knocking Cycle Detection and aKO Estimation 106
4.5 Results and Discussion 111
4.5.1 Knock Intensity Metric Assessment 111
4.5.2 Knocking Cycle Detection Method Assessment 117

4.5.3 Angle of Knock Onset Estimation Method Assessment 123
4.6 Conclusions 128
Chapter 5 – Assessment of Existing Empirical Ignition Delay Correlations using a 1D Engine Model 130
Chapter Summary 130
5.1 Introduction 131
5.2 Engine Modelling Theory 133
5.2.1 1D Engine Modelling Theory 133
5.2.2 SI Combustion and Knock Modelling in GT-Power 135
5.3 Engine Model Development 139
5.4 Engine Model Calibration 142
5.4.1 Input Data Quality Checks 142
5.4.2 Calibration Objectives 144
5.4.3 Blowby and Fuel Evaporation Sub-Models 146
5.4.4 Calibration of key engine parameters 150
5.4.5 1D Model Calibration Results 153
5.5 Knock Modelling Methodology 160
5.5.1 Operating Conditions Investigated 160
5.5.2 Hotspot Temperature Modelling 163
5.5.3 Ignition Delay Correlations 168
5.6 Knock Modelling Results 176
5.6.1 Assessment of IDCs using L+W Integral Error 176
5.6.2 Assessment of IDCs using aKO RMSE 179
5.6.3 Assessment of IDCs using Cycle Classifications 183
5.6.4 Summary of IDC Assessments 186
5.6.5 Improving the classification accuracy of the Ma correlation 191
5.6.6 Detailed analysis of the Yates 3-Arrhenius IDC at low speed/high load 193

5.7 Conclusions 199

Chapter 6 – Conclusions and Further Work 205

Chapter Summary 205

6.1 Conclusions 205

6.2 Further Work 209

Bibliography 211

List of Figures

Figure 2.1 – Types of abnormal combustion phenomena in SI engines 6
Figure 2.2 - Illustration of tumble (left) and swirl (right). Taken from [23], cited in [8]. 15
Figure 2.3 – Traditional turbulence-enhancing devices. On the left are different types of swirl inducing port geometries: a) deflector wall, b) directed, c) shallow-ramp helical, d) steep-ramp helical. On the right are different types of swirl inducing inlet valves. Taken from [6]. 17
Figure 2.4 – Simulated ignition delay times for a range of pure fuels at 30 bar [45]. Note the strong NTC behaviour in the intermediate temperature range (highlighted) for paraffinic fuels such as iso-octane, n-heptane and butane, whilst fuels such as toluene (an aromatic) and ethanol (an oxygenate) exhibit no NTC behaviour at all [45] 26
Figure 2.5 – Simulated temperature profiles for the autoignition of stoichiometric n-heptane mixtures at various initial temperatures in a constant volume reactor at 20 bar [46] 27
Figure 2.6 – Weisser's simplified approach for describing overall ignition delay of NTC exhibiting fuels, drawing an analogy between ignition delays and electrical resistors. 34
Figure 2.7 – Example of 3-Arrhenius IDC formulation in practice, showing how the NTC behaviour of a fuel could be recreated. Results obtained using Weisser's 3-Arrhenius IDC [65] for n-heptane at 10 bar. 34
Figure 2.8 – Ignition delay predictions for PRF91 and TRF91 at initial pressures of 12 bar and 40 bar [71] 38
Figure 3.1 – Test cell configuration, showing the twin dynamometer arrangement used ... 46
Figure 3.2 – Forced Induction Simulator (FIS) used to simulate boosted operation for the experimental engine 47
Figure 3.3 – Cable-operated butterfly valve used by the FIS to control exhaust manifold pressure 47
Figure 3.4 – EGR pump schematic 48
Figure 3.5 – Ultraboost cylinder head, showing location of cylinder pressure transducer installation. 51
Figure 3.6 – Rose plots of the two cam-timing combinations investigated in this work. 55
Figure 3.7 – Measured IMEP against angle of 50% mass fraction burned (CA50) for the 3500rpm, supercharger biased engine configuration 56

Figure 3.8 – Measured knock intensity (defined using the MAPO metric) against angle of 50% mass fraction burned (CA50) for the 3500rpm, supercharger biased engine configuration 57
Figure 3.9 – Spark advance, combustion phasing (CA50), IMEP, combustion duration (CA10-90), exhaust manifold pressure (PEXH) and exhaust gas temperature (EGT) at the KLSA, all plotted against intake manifold pressure for the four engine configurations tested. 59
Figure 3.10 – Effect of EGR on knock intensity as ignition timing was varied at the 1500rpm, supercharger-biased engine configuration 60
Figure 3.11 – Spark advance, combustion phasing (CA50), IMEP, combustion duration (CA10-90), exhaust gas temperature (EGT), maximum cylinder pressure (PMAX), IMEP CoV and brake thermal efficiency (BTE) at the KLSA, all plotted against EGR rate for the 1500rpm, supercharger biased engine configuration. 62
Figure 4.1 – Typical spark timing history for an active knock control system under overly advanced initial conditions (green) and overly retarded initial conditions (red) [83] 67
Figure 4.2 – Cross section view of an uncooled piezo-electric pressure transducer on the left [87], and a typical water-cooled pressure transducer with an M8 thread on the right [88] 69
Figure 4.3 – Comparison of in-cylinder pressure and ion current traces for three different levels of knock (top = no knock, middle = light knock, bottom = heavy knock). Recorded on a 6.0 litre V12. [93] 70
Figure 4.4 – Comparison of light intensity and cylinder pressure measurements recorded over a single knocking cycle in an Opel C20XE 4 cylinder SI engine. Light intensity was measured using a fibre optic spark plug sensor. [95] 71
Figure 4.5 – Optical fibre spark plug sensors with 8 (left) and 40 (right) optical fibres installed around the head of a conventional spark plug [96] 72
Figure 4.6 – MAPO plotted against AMPO and AEPO using experimental data from the experimental engine running under heavy knock at 1500rpm/17bar BMEP. Similar trends were observed across a range of speeds and loads up to 3500rpm/28bar BMEP. 76
Figure 4.7 – MAPO plotted against Checkel (left) and Ferraro (right) KI metrics using experimental data from the experimental engine running under heavy knock at 1500rpm/17bar BMEP. Similar trends were observed across a range of speeds and loads up to 3500rpm/28bar BMEP. 77
Figure 4.8 – $PPRR_{LPF}$ vs MAPO (5-45 kHz band pass filtered) for 300 consecutive cycles recorded from one cylinder of the experimental engine at a range of heavy knock operating conditions 79

Figure 4.9 – Difference between angle of MAPO (approximated here as the angle of AI onset for SI engines) and angle of $PPRR_{LPF}$. Data collected from the experimental engine operating under heavy knock (i.e. where most cycles were knocking) across a range of EOCs. 79
Figure 4.10 – Left: Brecq's dimensionless knock indicator (DKI) plotted using experimental data collected across a range of engine speeds and loads. Right: Mean MAPO values for comparison, from which approximate KLSA values can be derived. 81
Figure 4.11 – Unburned mass fraction of fuel at the approximate aKO plotted against MAPO. Data from the experimental engine, collected at 1500rpm, 17bar BMEP. 83
Figure 4.12 – AEPO (calculated over the entire band-pass filtered pressure trace) vs AEFD for heavy and light knock (collected from the experimental engine at 1500rpm, 17bar BMEP). 85
Figure 4.13 – MAPO plotted against AEFD (left) and MAFD (right) using experimental data from the experimental engine running under heavy knock at 1500rpm/17bar BMEP. Similar trends were observed across a range of speeds and loads up to 3500rpm/28bar BMEP. ... 86
Figure 4.14 – $MAPO$ versus relative spark advance (the spark advance relative to KLSA) for a range of EOCs. Data presented in the lower plot windows have been normalised by the values recorded at the most retarded spark setting. Data collected from the experimental engine. 88
Figure 4.15 – Plot showing how Maximum Non-knocking Value (MNV) method of KI threshold calibration used in practice. For clarity, $\log_{10}$ is used for pressure-based data on the left axes of each plot window. Experimental data collected from the experimental engine at 1500rpm, 17bar BMEP..... 90
Figure 4.16 – 95^{th} percentile MAPO plotted against spark timing, with piecewise linear regression used to fit two linear lines of best fit. Data collected from the experimental engine at 1500rpm, 17bar BMEP. 91
Figure 4.17 – Frequency distributions for MAPO as spark timing advanced from no-knock to heavy knock. KI thresholds calculated using Ferraro method shown in red. Data recorded on the experimental engine at 1500rpm, 17bar BMEP. 94
Figure 4.18 – Plots showing how $MAPO$, Ferraro KI thresholds and the knock frequency (derived using the Ferraro threshold method) evolve between cylinders as spark timing swept. Data recorded on the experimental engine at 1500rpm, 17bar BMEP. 95
Figure 4.19 – Top: Knock frequency predictions obtained using the method proposed by Lee [86] that suggests using a normalised KI threshold of 3 for all KI metrics. Bottom: Knock

frequency predictions obtained using Lee's method but with the normalised KI threshold values tailored for each KI metric to achieve the best match with the manually estimated knock frequency. Data derived from measurements taken from the experimental engine at 1500rpm, 17bar BMEP. 96
Figure 4.20 – Example of TVE method of aKO estimation resulting in a late aKO prediction. Data recorded on the experimental engine at 1500rpm, 17 bar BMEP. 99
Figure 4.21 – Example of Shahlari and Checkel aKO estimation methods. 100
Figure 4.22 – Comparison of cumulative SEPO traces for knocking and non-knocking cycles. Shaded areas correspond to the 10°CA segment over which the reference linear LOBF is fitted. 101
Figure 4.23 – Example figure window presented to the operator to enable the manual classification of cycles. The vertical red line in each subplot is a mouse-operated cursor added to facilitate aKO estimation. 107
Figure 4.24 – Decision tree for manual knocking cycle classification exercise. 109
Figure 4.25 – The effect of Lee and Siano normalisation approaches on mean values of MAPO and AEPO, calculated from experimental data collected on the experimental engine across a range of EOCs. 115
Figure 4.26 – The effect of Lee normalisation approach on mean values of Checkel and MAFD KI metrics, calculated from experimental data collected on the experimental engine across a range of EOCs. 116
Figure 4.27 – Knock frequency predictions and resulting accuracy statistics for all nine metric/method pairs evaluated for cylinder 4 at 1500rpm, 17bar BMEP. Note that manual knocking cycle classification was only performed at three spark settings, each corresponding to varying degrees of knock intensity. 119
Figure 4.28 – Examples of the linear regression plots (left) and Bland-Altman plots (right) that were used to compare Xiaofeng aKO estimates with manual aKO estimates. The red lines in both plots are linear regression lines. The data displayed is for cycles that were manually identified as knocking from a sample of 600 cycles collected at 3500rpm, 19bar BMEP. .. 125
Figure 5.1 – Schematic of discretised flow path, showing vector quantities evaluated at volume boundaries and scalar quantities evaluated at volume centroids [111]. 135
Figure 5.2 – Schematic of the single-cylinder GT-Power model used throughout this investigation. 140

Figure 5.3 – Variability of indirect mass air flow (MAF) measurements used to calibrate the air path of the GT-Power TPA model. Data recorded on the experimental engine at 3500rpm, with 30°CA intake cam advance and 20°CA exhaust cam retard.....144
Figure 5.4 – Effect of fuel vaporisation constant $CA50_{fuel}$ on predicted liquid fuel mass fraction at 3500rpm, 280kPa intake manifold pressure.....148
Figure 5.5 – Effect of fuel vaporisation constant $CA50_{fuel}$ on predicted fresh charge temperatures at IVC for a range of engine operating conditions.....149
Figure 5.6 – Influence of the charge cooling effects of fuel evaporation on predicted hotspot temperature evolution and knock onset. Condition modelled is 3500rpm, intake manifold pressure of 280kPa. "100% Evap" refers to the case where $CA50_{fuel}$ = 25°CA and all fuel evaporates before the start of combustion.....150
Figure 5.7 – 1D model mass air flow (MAF) predictions, compared with ±5% measured MAF limits.....154
Figure 5.8 – Left: Lower Heating Value (LHV) multiplier values applied by GT to balance the energy in-flows and out-flows for the 1D model. Right: Imposed fuel mass fraction burned values (calculated from measured unburned hydrocarbon concentrations).....155
Figure 5.9 – 1D model cylinder pressure predictions at 2.0bar intake manifold pressure for all four EOCs considered during the model calibration process.....156
Figure 5.10 – 1D model cylinder pressure predictions plotted on a Log(Pressure)-Log(Volume) axis. Data presented for the 2.0bar intake manifold pressure condition at all four of the EOCs considered during the model calibration process. 157
Figure 5.11 – The effect of decreasing Woschni convective heat transfer multiplier from 2.0 to 1.4 on cylinder pressure during the expansion stroke. 158
Figure 5.12 – 1D model predictions of trapped lambda and residual gas fraction (RGF) for all four EOCs considered during the model calibration process. 159
Figure 5.13 – Graphical representation of EOCs in the engine speed – Intake manifold pressure – cam timing/exhaust manifold pressure model domain.....162
Figure 5.14 – Summary of overall method employed for assessment of IDC performance. 163
Figure 5.15 – Effect of different modelling approaches on predicted hotspot temperature profile.....166
Figure 5.16 – The effect of temperature on the γ of the various species that make up air/fuel/residual gas mixtures.....167

Figure 5.17 – The effect of residual gas fraction (left) and lambda (right) on the γ of air/fuel/residual gas mixtures. 167
Figure 5.18 – The effect of assuming fixed vs temperature-varying γ on the predicted temperature evolution of a hypothetical hotspot. The non-adiabatic unburned-zone temperature profile predicted by GT-Power (black line) has been added for reference. Data presented for EOC #1 (1500rpm, 14bar BMEP) 168
Figure 5.19 – Predicted ignition delay times for each of the IDCs investigated in this study at pressure = 60bar, λ = 1.0, RGF = 0%. 169
Figure 5.20 – Steurs L+W accuracy metric L+W integral error plotted for all IDCs. "Score" refers to the mean of the L+W integral error metric calculated over all 12 EOCs for each IDC. 177
Figure 5.21 – Steurs L+W accuracy metric L+W integral error for six highest-ranking IDCs (based on their respective mean L+W integral error values calculated over the relevant speed EOCs). 178
Figure 5.22 – Example of staged L+W integral traces using the Yates cool flame IDC. 179
Figure 5.23 – RMSE of aKO predictions for all IDCs. 180
Figure 5.24 – RMSE of aKO predictions for six highest-ranking IDCs (based on their respective mean aKO RMSE values calculated over the relevant speed EOCs). 181
Figure 5.25 – Mean L+W integral at measured aKO for EOC #1 (1500rpm, 14bar BMEP) .. 181
Figure 5.26 – Mean of knock classification agreement statistics 183
Figure 5.27 – Mean of knock classification agreement statistics for the six highest-ranking IDCs (based on their respective mean values calculated over the 12 EOCs). 184
Figure 5.28 – Prevalence of knocking cycles at each EOC considered in this investigation. 185
Figure 5.29 – Predicted and measured knock frequency vs. spark advance at EOC #11 (3500rpm, 23bar BMEP) 185
Figure 5.30 – Ignition delay times predicted by the Ma, Yates cool-flame, Yates 3-Arrhenius and Kalghatgi correlations as a function of temperature at P = 20bar and P = 60bar (λ = 1, RGF = 0%). The fuel modelled is iso-octane for the Ma and Yates cool-flame IDCs, and 95 RON gasoline for the Kalghatgi and Yates 3-Arrhenius IDCs. 187
Figure 5.31 – Maximum L+W integral values and L+W integral values at measured aKO plotted against MAPO (normalised by the knock detection threshold) for the Ma, Kalghatgi and both Yates correlations. 189

Figure 5.32 – Angle of knock onset plotted against fuel mass fraction burned at angle of knock onset. Data for knocking cycles (measured and simulated using the Ma correlation) has been pooled across all 12 EOCs. 191
Figure 5.33 – Angle of knock onset plotted against fuel mass fraction burned at angle of knock onset. Data for knocking cycles (measured and simulated using the Kalghatgi and Yates 3-Arrhenius correlations) has been pooled across all 12 EOCs..... 192
Figure 5.34 – Knock classification agreement statistics for all 900 cycles recorded at EOC #4. Yates 3-Arrhenius IDC on the left, Wayne 1-Arrhenius IDC on the right. 193
Figure 5.35 – Maximum L+W integral versus MAPO for all 900 cycles modelled at EOC #4 (1500rpm, 31 bar BMEP) using the Yates 3-Arrhenius IDC. 195
Figure 5.36 – Measured cylinder pressure data (both raw and band-pass filtered), predicted hotspot temperatures and the resulting L+W integrals plotted against crank angle for the four cycles identified in this analysis. 197

List of Tables

Table 2.1 – Operating conditions for the research and motor octane rating methods 25
Table 2.2 – Optimised constants for use with Equation 2.14 and Equation 2.15 in determining A, n and B for single-step IDCs of the form described by Equation 2.2 [76] 41
Table 3.1 – Experimental engine specification 50
Table 3.2 – Summary of experimental test conditions 54
Table 4.1 – Engine operating conditions considered for the knocking cycle detection and aKO estimation method assessment. 102
Table 4.2 – Variable numbers for the KI metrics considered for knocking cycle detection. 111
Table 4.3 – Correlation coefficients for the nine KI metrics listed above in Table 4.2, determined from experimental data collected on the experimental engine at 1500rpm, 17bar BMEP and a range of spark settings corresponding to both knock-free and heavy knock conditions. 112
Table 4.4 – Correlation coefficient matrices for MAPO, AEPO, Checkel and MAFD (variables 1 – 4 respectively) calculated from experimental data collected on the experimental engine across a range of EOCs. 113
Table 4.5 – Summary of KI threshold calibration methods and KI metrics used as part of the investigation into knocking cycle detection methods. 117
Table 4.6 – Example contingency matrix, used to present and evaluate the output of each automated knocking cycle detection method. 120
Table 4.7 – Contingency matrix for the MNV/MAPO knock detection method pairing, using cycle classification data that was pooled across all 16 cylinder/EOC combinations considered in this chapter. 122
Table 4.8 – Overall agreement results for each of the twelve metric/method pairs that were tested for their knock detection capabilities. 122
Table 4.9 – Mean fit statistics for each aKO estimation method when compared with manual aKO estimates across four EOCs. 125
Table 4.10 – Overall fit statistic ranks for each aKO estimation method. 126
Table 4.11 – Overall ranks for each aKO estimation method at each EOC considered. 127
Table 5.1 – Parameter values for GT-Power 3-Arrhenius IDC [63] 138
Table 5.2 – Engine operating conditions used for calibration and subsequent validation of 1D single cylinder model. 145

Table 5.3 – Parameter values for the calibrated 1D engine model used in this work. 152
Table 5.4 – Engine operating conditions considered as part of the IDC assessment 161
Table 5.5 – Summary of IDCs investigated as part of this work. 171
Table 5.6 – Six best ranking IDCs across all 12 EOCs according to the three evaluation techniques considered in this study 186
Table 5.7 – Features of the four cycles highlighted in Figure 5.35 195

Abbreviations

AI	Autoignition
AFR	Air-Fuel ratio
aBDC	after Bottom Dead Centre
ACT	Air Charge Temperature
AEPO	Average Energy of Pressure Oscillations
aTDC	after Top Dead Centre
bBDC	before Bottom Dead Centre
BMEP	Brake Mean Effective Pressure (bar)
BSFC	Brake Specific fuel Consuption (g/kWh)
bTDC	before Top Dead Centre
CA	Crank Angle
CA50	Crank Angle of 50% Mass Fraction Burned of Fuel
CAC	Charge Air Cooler
CAD	Crank Angle Degrees
CFD	Computational Fluid Dynamics
CKM	Chemical Kinetic Modelling
CO	Carbon Monoxide
CO_2	Carbon Dioxide
CoV	Coefficient of Variation
CR	Compression Ratio
CV	Cyclic Variability
DI	Direct Injection
DOHC	Double Over Head Cams
ECP	Exhaust Cam Phasing
ECU	Engine Control Unit
EGR	Exhaust Gas Recirculation
EOC	Engine Operating Condition
EVC	Exhaust Valve Closing
EVO	Exhaust Valve Opening
FIS	Forced Induction Simulator
GDI	Gasoline Direct Injection

HCCI	Homogenous Charge Compression Ignition
ICE	Internal Combustion Engine
IDC	Ignition Delay Correlation
ICP	Intake Cam Phasing
IMEP	Indicated Mean Effective Pressure
IVC	Intake Valve Closing
IVO	Intake Valve Opening
JLR	Jaguar Land Rover
KI	Knock Intensity
KLCR	Knock Limited Compression Ratio
KLSA	Knock Limited Spark Advance
MAPO	Maximum Amplitude Pressure Oscillation
LSPI	Low Speed Pre-ignition
MBT	Maximum Brake Torque
MFB	Mass Fraction Burned
MON	Motor Octane Number
NA	Naturally Aspirated
NEDC	New European Drive Cycle
NOx	Oxides of Nitrogen
NTC	Negative Temperature Coefficient
PFI	Port Fuel Injected
PI	Pre-ignition
PRF	Primary Reference Fuel
PVRC	Powertrain and Vehicle Research Centre
R^2	Coefficient of Determination
RMSE	Root Mean Square Error
RON	Research Octane Number
RPM	Revolutions per Minute
SA°	Spark Advance (CAD)
SI	Spark Ignition
TDC	Top Dead Centre
TRF	Toluene Reference Fuel
UHCs	Unburned Hydrocarbons

VVT	Variable Valve Timing
θ	Crank Angle
λ	Lambda
ϕ	Equivalence Ratio
γ	Ratio of specific heat capacities
Cp	Specific heat capacity at constant pressure
X_{O2}	Mole fraction of Oxygen

Chapter 1 – Introduction

1.1 Background and motivation

In recent years, downsizing has become a major trend within the automotive industry as a means to reduce the tailpipe CO_2 of gasoline engines. The primary advantages offered by downsizing are avoidance of regions of high pumping losses at part load and reduced frictional losses (assuming the route taken also involves cylinder reduction). Extreme downsizing, as seen in several demonstrator projects in recent years [3-5] requires operation at high brake mean effective pressures (BMEPs) in order to maintain vehicle performance levels. Unfortunately, efficient operation at high BMEPs is limited by knock, the sound associated with damaging forms of abnormal combustion.

The ability to simulate knock is critical to our understanding of the factors that influence it, and therefore how to design engines that successfully avoid it. Predictive techniques are also useful in the early stages of product design and development. Indeed, the long-term aim of many OEMs is to be able to design and calibrate powertrain solutions entirely within the virtual domain, without the support of any experimental work. It is therefore vital that accurate yet practical simulation tools exist for the simulation of knock. Numerous knock simulation approaches exist within the literature, however most are yet to be evaluated at the BMEPs expected of heavily downsized engines.

Knock is the general term used to describe the sound associated with high frequency pressure oscillations produced by autoignition inside gasoline engines. These pressure oscillations are undesirable for two reasons – the first is that they are a nuisance to the occupants of the vehicle; the second (and arguably more significant) is that when severe, they have the potential to cause significant engine damage.

Autoignition describes the ignition of gaseous air/fuel mixtures that is not initiated by an external ignition source. It is sensitive to mixture composition, fuel properties, pressure and temperature (the latter in particular). In spark ignition engines, the stimulus for autoignition is provided by compression of the air/fuel mixture by both the movement of the piston and by the heat released during combustion. Heat transfer from hot combustion chamber surfaces and mixing with hot residual gases also play significant roles, leading to the

prevailing theory that autoignition originates from hotspots – localised regions of comparatively high temperature gas ahead of the flame front.

Practical autoignition simulation tools rely on empirical correlations to predict the ignition delay times for air/fuel mixtures under specific conditions. These correlations approximate the complex ignition-delay characteristics of real and surrogate fuel blends with respect to temperature, pressure and mixture composition. Broadly speaking, these correlations fall into two categories – those that are based on measured data from real engines, and those that are based on fundamental ignition delay time measurements acquired using specialist apparatus (rapid compression machines and shock tubes). The second of these categories can be further divided into simple ignition delay correlations that are similar in form to those developed using engine data, and also much more detailed models that attempt to describe the chemistry of autoignition. Correlations of the first type are often limited in that they are only valid for specific fuels, are based on data collected at relatively low BMEPs, and are inherently tuned to match the specific knocking characteristics of the engine used. Correlations of the second type meanwhile are limited by the practical limitations of the apparatus used to collect the ignition delay data. Typically, this constrains the valid pressure range of these correlations to less than 60 bar. Cylinder pressures in modern SI engines can often exceed twice this limit. Consequently, there is a need for tools that can be applied with confidence to the simulation of autoignition in highly boosted, SI engines.

1.2 Aims and objectives

The primary aim of this investigation was to further the understanding of knock in high BMEP engines and to assess the state of the art in terms of practical simulation tools used for modelling knock at high BMEPs. The specific objectives required to achieve this aim are listed below in the order that they have been carried out in this thesis:

1) To conduct a detailed literature review on the factors that affect autoignition and knock in SI engines, and to achieve a thorough understanding of the limitations posed by the various empirical autoignition modelling approaches available.
2) To design and execute an experimental campaign capable of delivering combustion data across a broad range of knock-limited operating conditions relevant to downsized engines. The product of this objective is a rich data set that can be used to support further research in this field.
3) To develop data processing techniques that can accurately extract knock-relevant metrics from cylinder pressure data collected at high loads.
4) To build a one-dimensional model of the experimental engine, and to calibrate it to the necessary degree of accuracy using measured data.
5) To critically evaluate the performance of a variety of ignition delay correlations under conditions relevant to highly boosted, downsized engines by comparing knock onset predictions with experimentally measured knock onset times, to identify which correlations perform the best overall and propose areas in which they could be improved.
6) To review the major findings from this thesis and make recommendations for further work.

Chapter 2 – Literature Review

Chapter Summary

In this chapter, knocking combustion and its various guises are introduced, followed by a review of established knock mitigation strategies. The effects of fuel properties on knock behaviour are then discussed, followed by a detailed account of the various knock modelling approaches used within in the literature.

The objectives of this chapter are to provide the reader with:

- A clear understanding of knocking combustion and the various forms that it can take.
- An awareness of the most widely used knock mitigation strategies, as well as their respective pros and cons with respect to their cost and their impacts on efficiency, performance and emissions.
- An understanding of the fuel octane rating system, how fuel properties and composition affect anti-knock performance and how the ignition delay characteristics of fuels have influenced knock modelling techniques.
- An awareness of the various knock modelling approaches and their respective pros and cons with regards to their adaptability, computational efficiency, and their ability to describe the underlying physics of the autoignition process.

2.1 Forms of Abnormal and Knocking Combustion

In the context of SI engine operation, abnormal combustion is defined as the process by which some or all of the air/fuel mixture is ignited by any source except the intended ignition provided by the spark plug [6]. The various forms of abnormal combustion considered in this review are highlighted in Figure 2.1. The primary distinction between these modes is their respective initiation sources, be that end-gas autoignition or surface ignition. Autoignition is the terms used to describe ignition of the mixture that is not initiated by the spark or by the normally advancing flame front [7], thus it encompasses all forms of abnormal combustion initiation in SI engines. End-gas autoignition refers specifically to spontaneous, inflammation of some or all of the unburned mixture (end-gas) ahead of the normally advancing flame front. It occurs when the characteristic ignition delay time of the mixture (i.e. the time taken for a particular mixture at a given temperature and pressure to spontaneously ignite without further input from the surroundings) is less than that taken for the flame front to reach the end-gas. End-gas autoignition usually results in the well-known acoustic phenomenon of knock, which when severe has the potential to cause significant engine damage and driveability issues due to high in-cylinder pressures, oscillatory loading of mechanical components and objectionable noise for the vehicle occupants [6].

Surface ignition on the other hand refers to autoignition that arises through contact with hot surfaces inside the combustion chamber (such as overheated exhaust valves, spark plugs or incandescent carbon deposits). It can be further divided into the classifications of pre-ignition and post-ignition depending on whether autoignition is initiated before or after the spark. Following surface ignition, an additional flame front to that produced at the spark plug propagates outwards from the surface ignition origin and across the combustion chamber, increasing the effective burn rate. As indicated by Figure 2.1, surface ignition and end-gas autoignition can occur in isolation or together in the same cycle. In cases where both occur (such as pre-ignition), the two modes occur sequentially, with surface ignition giving rise to end-gas autoignition later in the cycle.

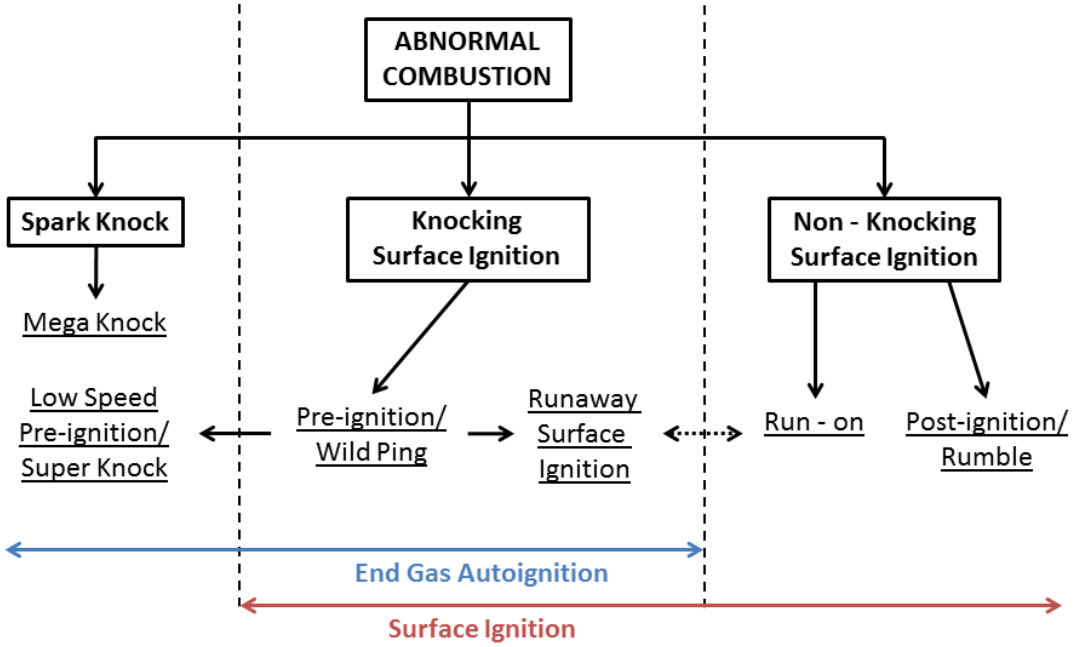

Figure 2.1 – Types of abnormal combustion phenomena in SI engines

Knock is defined as the "sharp metallic sound associated with vibrating pressure waves created by the burning of some part of the mixture in advance of the normal flame front" [7]. It is characterised by extremely rapid heat release towards the end of the combustion process followed by high frequency pressure fluctuations within the cylinder. The rapid heat release is a product of virtually instantaneous inflammation of some or all of the end-gas by autoignition – a mode of combustion whereby air/fuel mixtures spontaneously ignite after a characteristic period of time known as the ignition delay. The rate of heat release is so high within the autoignition centre that it elevates the pressure locally within the combustion chamber. This creates a pressure wave that propagates throughout the combustion chamber at the local speed of sound. Reflections of this pressure wave form a series of standing pressure oscillations that cause the combustion chamber to resonate at frequencies dependent on its geometry and the temperature of the gas within it. These oscillations lead to structural block vibrations that can be heard by the vehicle occupants.

Prolonged exposure to severe knock can be highly damaging to SI engines, particularly to the top land and ring grooves of pistons, causing erosion of the piston crown and eventually piston crown failure [8]. Knocking pressure waves break down the otherwise stable thermal boundary layer in the combustion chamber, resulting in overheated chamber surfaces and loss of strength [9]. This also increases the probability of knock in subsequent cycles because of increased heat transfer to the end-gas. Overheating damage can cause piston and ring

seizures and fusion of spark plug electrodes and pistons. Cylinder head pitting and erosion is also common because of the extremely high local pressures and temperatures at the autoignition centre. In some engines, this tends to occur on the cooler, intake side of the combustion chamber because of the slower flame propagation rates in this direction. The subsequent delay in consumption of the end-gas on the intake side of the combustion chamber by the normal flame front allows more time for autoignition to initiate, increasing the probability of knock. This can be mitigated by careful consideration of spark plug orientation and location such that the end-gas is evenly distributed between the intake and exhaust valve sides of the combustion chamber, and also by the use of cooler running sodium-filled exhaust valves to level the flame progression rates in either direction from the spark plug [10].

Starting from the left hand side of Figure 2.1, spark knock is defined as when end-gas autoignition followed by knock occurs repeatedly between groups of otherwise normal combustion cycles [6]. It is the result of ignition timing that is too advanced, creating in-cylinder pressures and temperatures high enough to cause spontaneous inflammation of the end-gas prior to the arrival of the normally advancing flame front. The spark timing at which the transition to knocking combustion occurs, known as the knock limited spark advance (KLSA), is a function of the air fuel ratio (AFR), the fuel's ignition delay properties and the cumulative temperature/pressure history of the end-gas. This last factor is engine specific and itself a function of many variables including engine operating point, combustion chamber and cooling system design, coolant temperature, etc. Accurate prediction of the KLSA for a particular engine and fuel combination is a very difficult undertaking, relying largely on complicated three dimensional CFD simulations of in-cylinder heat transfer and empirically derived relationships for the ignition delay characteristics of the fuel concerned. Spark knock is controllable by spark advance, with more advanced ignition timing resulting in more severe knock and vice versa. Retarding ignition timing has the effect of delaying heat addition, resulting in lower in-cylinder pressures and temperatures and therefore a reduced the probability of knock.

Megaknock is a term recently coined to describe extremely severe spark knock events, capable of producing pressure oscillations in excess of 60 bar in amplitude and peak cylinder pressures greater than 200 bar [10, 11]. The amplitude of pressure oscillations (defined as the zero to peak pressure of the high pass filtered in-cylinder pressure trace) is one of the

most commonly used metrics for evaluating the severity of knock. This is because of its relevance to the method by which knock inflicts damage on engines and because several studies have shown that its amplitude is proportional to the quantity of end-gas that autoignites [6]. The process of filtering the pressure signal removes its low frequency (sub 1 kHz) components, leaving only the high frequency vibrations produced by knock. Knock events of this severity are linked to high engine speeds [11] and high boost pressures [10], therefore they are becoming an increasingly common observation as the limits of engine downsizing are explored. To put the magnitude of megaknock into perspective, OEMs often define a maximum tolerable knock peak pressure no greater than 1 bar per 1000rpm engine speed. At low speeds, these limits are primarily for driver comfort, whereas at high speeds they are intended to minimise the risk of engine damage. A typical gasoline engine has a maximum speed of around 6000rpm, therefore the maximum allowable continuous knock amplitude is around 6 bar – some ten times less than that of the average megaknock event. Megaknock therefore has significant potential for engine damage since the localised loads on pistons and connected driveline components during megaknock events can far exceed the design limits of an engine.

Sidestepping super knock and low speed pre-ignition for the moment, knocking surface ignition is widely regarded as the result of early ignition of the mixture by incandescent carbon deposits [6]. Surface ignition often results in severe knock because of the higher pressures and temperatures produced by burning that occurs at multiple flame fronts. Although not always followed by knock, post-ignition is undesirable because of the low pitched thudding noise it produces (called rumble) and a perceived increase in engine "roughness" by the driver [6]. Pre-ignition on the other hand has a high probability of resulting in severe knock because it effectively advances the start of combustion. If combustion is initiated in advance of TDC, the expanding gases place considerable strain on the piston, connecting rod, bearings and crankshaft as the piston tries to compress the mixture. Of the two surface ignition modes, pre-ignition is therefore the more likely to result in damage due to the higher cylinder pressure and increased severity of knock. It is analogous to spark knock in that the earlier the pre-ignition (PI), the more severe the resulting knock.

Wild ping is the name given to describe a short sequence of consecutive knocking PI events [6]. It is characterised by a number of short, sharp cracking sounds and again, has traditionally been thought to be caused by glowing combustion chamber deposits that have

become dislodged from the chamber surfaces. Once these deposits are completely burned or have been evacuated from the cylinder, the PI events cease.

Runaway surface ignition has the highest potential for causing major engine damage. It refers to the case of uncontrollable, consecutive PI events caused by surface ignition (although it may begin as either deposit or hot surface induced post-ignition). The higher surface temperatures associated with high speed/high load operation increase its probability of occurring at these conditions. Following the first surface ignition event, the temperature of the offending surface is likely to increase, allowing it to continue acting as a source of ignition for subsequent cycles. As its temperature increases further, surface ignition occurs earlier and earlier in the cycle, transitioning into knocking PI in just a few cycles if it didn't start off as such. Through this mechanism, surface induced PI can be self-amplifying, allowing it to quickly reach a stage whereby persistent, heavy knock occurs every cycle. Several consecutive cycles of very heavy knock can be enough to cause severe engine damage in the form of localised melting of the piston crown and spark plug electrodes as the thermal boundary layer is stripped from the combustion chamber surfaces and their temperatures increase above their designed limits.

Non-knocking surface ignition phenomena are typically associated with very late post-ignition by glowing deposits. As previously mentioned, rumble is the low-pitched (600 – 1200 Hz) thudding noise that results from rapid heat release at the end of the combustion process because of the presence of multiple flame fronts. Very high pressure rise-rates are possible under rumbling conditions because of this rapid heat release, causing an increase in the perceived "harshness" of the engine. The flame fronts attributable to surface ignition are formed sufficiently late in the cycle such that their contribution to the overall heat release is small and has little effect on the autoignition pre-reactions taking place in the end-gas. It is however possible for knock and rumble to occur together [6]. Run-on meanwhile describe the case where the engine continues to fire after the ignition system has been switched off. This is only an issue for older, carburetted of port-fuel injected (PFI) engines where large pools of liquid fuel can build up inside the inlet manifold after prolonged periods of high load operation. In these cases, fuel vapour will continue to enter the combustion chamber after fuelling has ceased. In Figure 2.1, the link to run-away surface ignition is illustrated to emphasise the similarity in the fact that control of combustion is removed from the ECU for an appreciable number of consecutive cycles, although in reality this is the only similarity

shared by the two phenomena. Run-on is non-knocking and can be the result of either deposit induced surface ignition or compression ignition of the mixture, therefore the categorisation as a purely surface ignited combustion phenomenon is not strictly true.

Fortunately, all forms of abnormal surface ignition phenomena are avoidable through careful design of the combustion chamber and appropriate specification of charge cooling equipment, fuel, lubricant and combustion chamber components such as spark plugs and exhaust valves. For example, run-away surface ignition can be all but eliminated within the operating limits of modern SI engines by combining appropriate combustion chamber cooling strategies with the use of high heat rating spark plugs, sodium filled exhaust valves and carefully designed pistons. As with any design decision however, there are important trade-offs to be considered. Besides the increased cost and complexity of such technologies, in the case of cooler running spark plugs there is an added compromise to be considered between improved surface ignition limits at high speed/high load and worse low speed/low load ignition performance. This decreased performance is the result of greater heat transfer away from the flame kernel during its early development (thus decreasing burn rate throughout the combustion process and increasing cycle-to-cycle variability) and fouling of the insulator cone surface. In the case of piston geometry optimisation, the trade-off is between improved heat transfer and additional tooling/component costs, whereas with liner and head cooling, the challenge is maintaining efficiency and low tailpipe hydrocarbon emissions by only dissipating the minimum required amount of heat. The correct solution is therefore a complex marriage of these technologies and many others, such that the final design is able to meet the requirements of the user in terms of driveability and reliability without exceeding any legislative limits concerning emissions and fuel economy.

Coming back to the left hand side of Figure 2.1, low speed pre-ignition (LSPI) is a term recently coined to describe a form of knocking PI only seen in modern engines employing a combination of direct injection and boosting. Although still not fully understood, it is thought to be the result of autoignition of oil/fuel droplets that enter the combustion chamber from the top land crevice volume [9, 12-14]. LSPI occurs in the low speed, high load regime and like surface ignited PI, it can result in very severe levels of knock – hence the associated term “super-knock”. LSPI events can occur as one or two consecutive PI cycles, or as sequences of up to several dozen alternating PI and normal combustion events. Fortunately, LSPI sequences are self-curing (provided they do not lead to run-away surface ignition). Following

this observation, Amman [15] suggested that LSPI is the result of a hydrocarbon-based accumulation inside the combustion chamber and that LSPI events are triggered by the discharge of this accumulation. Combined with the previously stated theory of oil droplet autoignition, Amman conclude that the accumulation occurs as a result of fuel dilution of the oil film by wall wetting and that it is stored in the top land piston crevice volume. The results of Dahnz [12] seem to corroborate this theory as they showed that by reducing wall wetting and oil film dilution rates with hotter cylinder liner temperatures, the frequency and duration of LSPI events could be reduced.

Although no clear explanation for the cyclic PI/normal combustion behaviour of LSPI has been found in the literature, some similarity between the alternating strong and weak combustion events previously seen at the part load combustion stability limits of other engines can be observed. In these cases, the alternating pattern is the result of partial misfires or incomplete combustion. The fuel-rich residual gas results in a richer overall mixture for the following cycle and therefore a stronger combustion event. One could therefore imagine a similar dependency between consecutive cycles during LSPI sequences. Amann [16] build on this theory by suggesting that due to the very high peak pressures and fast heat release rates which occur during PI events, it is possible that exhaust dynamics and gas exchange dynamics are altered such that in the following cycle, the in-cylinder conditions (pressures, temperatures and residuals content for example) are unfavourable for PI. This causes the following cycle to progress normally, despite the source of LSPI still being active, and so the pattern of alternating PI/normal cycles will continue until this source has been fully discharged.

It is believed that further downsizing and fuel economy gains are being constrained by the low speed/high load limits imposed by super-knock and LSPI [15]. Methods of eliminating their occurrence are therefore valuable research areas. The current focus is on the effects of piston design, crevice volume and injection strategies on LSPI [17].

2.2 Knock Mitigation Strategies

Knock is one of the primary barriers to increased thermal efficiency of SI engines. Knock mitigation is therefore a critical step in the development of more efficient engine operation,

particularly at high loads [18]. The following paragraphs outline some of the commonly employed knock mitigation strategies in today's SI engines.

The tendency of an engine to knock depends on its design and on any operating variables that influence the end-gas temperature, pressure, and the time spent at high values of these two properties [6]. In order to avoid knock it is essential to control in-cylinder conditions and burn rates such that the end-gas is always consumed by the normal flame front instead of by autoignition [10]. Ignition timing and compression ratio have significant influence over in-cylinder pressure and temperature for example, whilst turbulence has been shown to have a dominating effect on burn rate. It is not surprising therefore that these three parameters have formed the basis of most traditional knock mitigation strategies. Other strategies generally seek to lower the temperature of the end-gas (thus increasing the ignition delay and reducing the probability of knock) or to improve the antiknock characteristics of the mixture by enhancing the fuels chemical resistance to autoignition.

2.2.1 Spark Retard

Optimal combustion phasing (that is to say the spark timing that achieves maximum brake torque, MBT) is a compromise between two opposing mechanisms. Combustion that is too advanced results in high cylinder pressures and an increase in the compression work done by the piston, reducing overall torque output and efficiency. On the other hand, combustion that is too retarded results in lower and later peak cylinder pressures, thus decreasing the work done by the gas during the expansion stroke and therefore also decreasing efficiency. The spark timing which corresponds to MBT is somewhere between these two extremes, with factors such as flame propagation rate, mixture properties, operating condition and overall engine design affecting its absolute location. Empirical rules of thumb suggest that the best compromise occurs in SI engines when:

- The maximum pressure occurs at approximately 16° aTDC
- The angle of 50% mass fraction burned (MFB) occurs at approximately 10° aTDC

At high loads however, knock often prevents the spark timing from being advanced to the point of MBT as the higher pressures and temperatures increase the probability of end-gas autoignition. The spark timing at these conditions must therefore be retarded in order to reduce the in-cylinder temperatures and pressures. Unfortunately, this strategy has the

negative effects of decreasing thermodynamic efficiency, increasing exhaust gas temperatures and increasing the thermal stresses on combustion chamber and exhaust components. To counter the increased risk of thermal damage, cooling of the mixture with excess fuel is often required, particularly at higher engine speeds where heat losses are lower and exhaust gas temperatures are higher. This strategy further penalises high load fuel consumption, as well as emissions of carbon monoxide (CO) and unburned hydrocarbons (UHCs). Spark timing at high loads is therefore a compromise between preventing unacceptable levels of knock and trying to minimise the negative effects of retarded combustion. The result is that spark timing is calibrated to produce the maximum allowable level of knock, as defined by the NVH and durability limits specified by OEMs.

Traditional knock mitigation strategies employing spark retard rely on block mounted accelerometers to measure the amplitude of the structural vibrations induced by knock. The open loop spark timing is retarded a few degrees whenever the high frequency (3kHz – 30kHz) component of engine block acceleration exceeds a predefined threshold. The magnitude of this threshold is often determined experimentally by correlating cylinder pressure measures of knock intensity with the amplitude of block vibrations. After a knock event, the spark timing is gradually returned to the open loop value by algorithms in the ECU, unless a system of continuously updating the spark timing maps for each cylinder is available, as in some modern engines.

2.2.2 Compression Ratio Reduction

Compression ratio (CR) has a strong impact on an engine's knock characteristics and thermal efficiency, with lower CR favouring the former and higher CR favouring the latter. In the absence of viable alternatives, CR reduction has traditionally been used to mitigate knock. To this day, CR reduction of at least 1.5 is common when comparing boosted engines to their naturally aspirated (NA) counterparts [19]. Unfortunately, this strategy severely penalises fuel consumption at part and low load operating conditions where the majority of vehicles operate most of the time and where knock is not a concern. What is more, low CRs lead to increased exhaust gas temperatures at high loads, requiring exhaust cooling strategies such as fuel enrichment and further penalising high load fuel economy and emissions.

A mechanism by which an engine could vary its CR depending on engine load would therefore offer significant thermal efficiency and knock mitigation gains. Broadly speaking, there are two ways that this could be achieved:

- Using complicated piston-crank assemblies (requiring widespread changes to the design, manufacture and assembly of engines)
- Using fixed CR engines equipped with variable valve timing (VVT) systems, allowing the timing of inlet valve closure (IVC) to be controlled and thus varying the effective compression ratio.

Although the latter solution is favourable in terms of its simplicity, there is a trade-off to be considered between achieving the desired effective compression ratio and incurring greater volumetric losses because of early/late IVC [20]. However, Wirth [21] suggest that combined with the improved combustion phasing afforded by lower CRs, boosting of an engine at high loads can easily overcome any additional volumetric losses incurred. Furthermore, by maintaining the full expansion ratio of an engine, the thermodynamic efficiency penalty can be minimised [9] and the exhaust gas temperatures can be reduced, reducing the requirement for fuel enrichment. The use of late IVC is often referred to as the Atkinson cycle. The Miller cycle is identical except for the fact that the loss in power density (due to the decrease in the trapped mass of air inside the cylinder) is recovered by boosting.

2.2.3 Turbulence Enhancement

The occurrence of knock represents the outcome of a race between the normally advancing flame front and the pre-flame chemical reactions occurring in the end-gas [6]. Any strategy that is able to increase the speed of the normally advancing flame front will therefore decrease the chance of autoignition occurring in the end-gas, provided that it does not also lead to significant reductions in the characteristic ignition delay time of the mixture. Since turbulence has a positive influence on flame speed, increasing the level of turbulence inside the cylinder at the time of combustion decreases the probability of knock at a given spark timing (or for a given probability of knock, will permit more advanced spark timing). Furthermore, faster combustion retards the position of MBT spark timing [7]. The result is much improved combustion phasing at the KLSA, thereby increasing torque and thermal efficiency.

Turbulent motion of the combustion chamber contents is primarily a product of the unsteady, turbulent jet that enters the cylinder during the intake stroke. Overall turbulence has been shown to peak sharply during the period of the induction stroke when the inlet jet is active, however as soon as this jet is cut off by the intake valve closing, the turbulence level rapidly decays due to the viscous properties of the fluid [22]. During the compression stroke, what turbulence that remains is amplified due to the increasing charge density and the breakup of larger turbulent length scales. From a combustion point of view, it is the turbulence at and around TDC that is of primary interest, since it is this that facilitates rapid flame front propagation[1]. Organised flow motions called tumble and swirl are the primary contributors in this regard.

Swirl is the term used to describe organised rotational motion of the fluid about the cylinder axis whilst tumble describes rotational motion about the orthogonal axis (see Figure 2.2). Their respective formation rates are highly sensitive to the intake system design. Swirl formation is favoured by asymmetric intake port layouts, particularly single-port engines or twin-port engines capable of selective port deactivation at light loads (such as the Honda VTEC-E engine). Tumble formation on the other hand is favoured by twin-port, pent-roof combustion chamber designs. Both forms of flow motion help to preserve the kinetic energy of the inlet air jet and therefore slow the rate at which the turbulence decays.

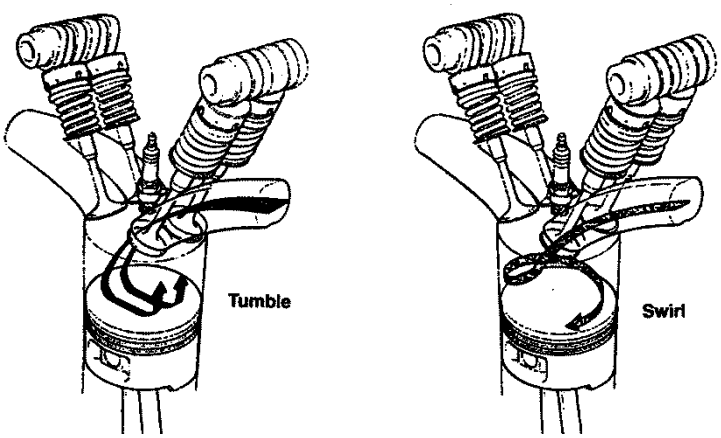

Figure 2.2 - Illustration of tumble (left) and swirl (right). Taken from [23], cited in [8].

[1] The turbulence levels during the compression stroke are also of interest however, particularly for homogenous charge direct injection engines as it is the turbulence present during this stage that is responsible for the preparation of the air, fuel and residual gas mixture. Inconsistent stoichiometry of the mixture surrounding the spark plug at the time of ignition will result in highly variable initial flame front propagation rates, ultimately leading to irregular torque delivery and poor driveability of the engine.

Tumble has been shown to contribute more towards the turbulence levels at TDC because of the manner in which it breaks down into smaller, less organised flow motions near TDC. In the absence of complex chamber geometries and squish zones (areas of the combustion chamber where the piston crown and chamber roof come very close to one another), swirl has been shown to survive the compression process. By not breaking up into smaller, less organised length scales, swirl does not contribute significantly to the small-scale turbulent motion required for fast flame front propagation in the radial direction [22][2]. Squish zones however can be highly beneficial in bringing about the breakdown of swirl close to TDC. Firstly, the fluid squeezed out of the squish zones creates organised motion inside the combustion chamber that interacts with the other flows, causing it to break up into turbulence. More importantly however, the sudden change in cylinder radial cross section has a dynamic effect on swirl motion, forcing it to accelerate in an effort to conserve angular momentum. This acceleration has the potential to break up the previously organised motion of swirl due to the higher shear stresses within the fluid, dramatically increasing turbulence at TDC and promoting faster flame front propagation [8]. Unfortunately, large squish zones are difficult to implement in today's four-valve pent-roof engines due to spatial restrictions in the head. Their use is largely confined to bowl-in-piston combustion chamber geometries used in diesel applications.

Today, 3D CFD simulation and CAD modelling is used to quickly and cost-effectively determine the turbulence generating capabilities of a given intake system design. In the early 1900s however, no such technologies existed. Consequently, much of the early breakthroughs in the field of turbulence and its effect on burn rate and knock were discovered in a purely empirical manner, with the features of successful engines simply upheld in subsequent designs rather than being truly understood. One such example of this is the DOHC pent-head engine design, originally developed for racing in the early 1910s and subsequently used widely in aviation. The original aim of the design was to maximise valve area and thereby improve volumetric efficiency, however it was not widely known at the time was that this arrangement of the inlet ports and valves produces high levels of tumble. The breakdown of tumble near TDC increased the turbulence throughout the combustion process, resulting in faster burn rates and most importantly, improved resistance to knock. Improved mixture preparation and homogeneity of the fresh charge lead to decreased cyclic

[2] This high "survival rate" does however make swirl particularly useful in the application of stratified charge and lean burn engines as it helps to limit mixing of the air/fuel mixture prior to ignition.

variability at high load, which allowed for spark timing calibration to be less pessimistic as the frequency of "rogue" fast cycles capable of producing heavy knock was dramatically reduced. This development paved the way for more powerful, higher CR engines that had the additional advantages of being more efficient and being compatible with the same fuel as any other engine of that time.

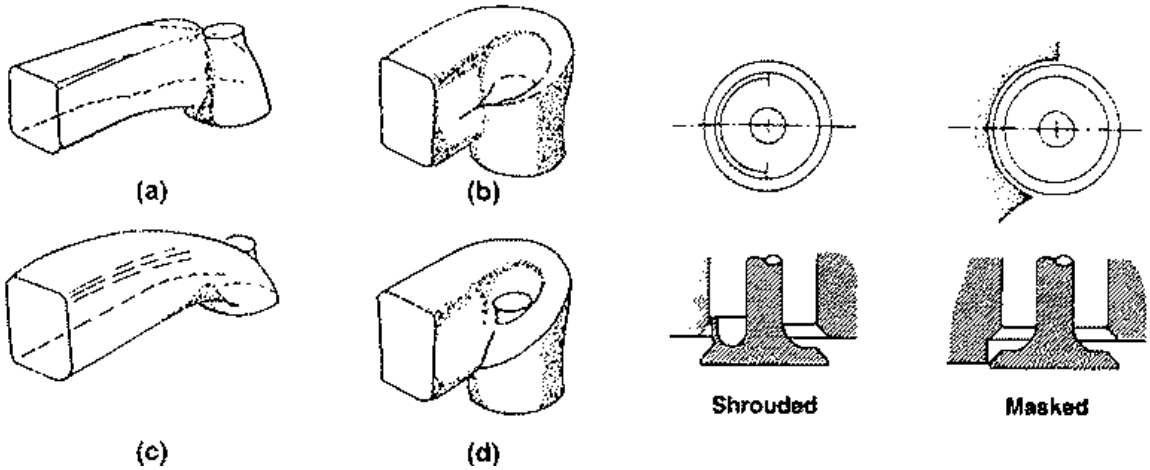

Figure 2.3 – Traditional turbulence-enhancing devices. On the left are different types of swirl inducing port geometries: a) deflector wall, b) directed, c) shallow-ramp helical, d) steep-ramp helical. On the right are different types of swirl inducing inlet valves. Taken from [6].

Once the effects of turbulence were realised, several approaches were developed to maximise its production. This was primarily achieved using swirl generating devices such as shrouded intake valves and helical or directed intake ports (see Figure 2.3). Unfortunately, such technologies restrict the flow passage through the intake valves, penalising their discharge coefficients and decreasing the engine's volumetric efficiency at high loads. A strategy that largely overcame this limitation was that developed by Honda for use on their VTEC-E engines, although the primary aim of this system was not to improve high-speed knock performance but to improve low speed turbulence generation for more stable combustion under lean conditions [8]. More recently, high-tumble intake port designs that have minimal impact on volumetric efficiency losses have been implemented in engines capable of BMEPs in excess of 30 bar [3].

Finally, an additional benefit of high turbulence levels is increased heat transfer away from the end-gas throughout the combustion process [7]. As shall be discussed in the following section, cooler end-gas temperatures decrease the probability of autoignition occurring.

2.2.4 Cooling Strategies

Engine cooling mechanisms serve three primary purposes. The first is to improve engine output by limiting heat transfer to the fresh charge from hot engine surfaces, thereby promoting high volumetric efficiency and charge density. The second is to prevent operation from exceeding the metallurgical limits of engine components, thus preventing mechanical failure due to thermal fatigue. The third reason for cooling systems is to prevent abnormal combustion from taking place [9, 24]. This section highlights the various ways in which knock suppression is achieved using novel cooling strategies.

As previously discussed, knock is the product of autoignition of some or all of the end-gas ahead of the normally advancing flame front. Strategies that cool the end-gas will slow the rates of the pre-flame chemical reactions occurring in this region and therefore reduce the probability of autoignition. Over the years, many cooling strategies have been developed in an effort to mitigate knock. These strategies can be separated into two categories; those that directly cool the fresh charge before combustion is initiated and those that indirectly cool the end-gas throughout the cycle by decreasing the temperature of chamber surfaces and components.

Direct charge cooling strategies

Direct charge cooling is by no means a new concept. For turbocharged and supercharged engines, the use of air-to-air and air-to liquid charge air coolers (CACs) is synonymous. The primary function of CACs is to increase the density of the incoming charge by cooling it post-compression. This increases the trapped mass of air, allowing more fuel to be burned and increasing an engine's absolute power output. However, another significant benefit of this process is the much improved knock performance afforded by cooler in-cylinder gas temperatures throughout the cycle prior to ignition. For a given load or boost pressure, these cooler temperatures allow both the KLSA and the KLCR to be extended, resulting in improved combustion phasing, torque output and thermal efficiency across an engine's operating map.

Over-fuelling or fuel enrichment is another strategy that has long been used to decrease the knocking tendency of an engine under high power conditions. Gasoline has a high enthalpy of evaporation (approximately 350 kJ/kg), therefore the more liquid fuel that evaporates in a given mass of air, the cooler that mixture will become and the less likely it will be to

autoignite. Unfortunately, over fuelling in this manner severely penalises full load fuel consumption, as well as emissions of CO and UHCs. In anticipation of forthcoming higher load emissions legislation, alternative charge cooling strategies to fuel enrichment are currently being sought.

Charge dilution (either by the use of excess air or exhaust gas recirculation) is one such alternative. Although charge dilution does not cool the fresh charge directly, it achieves knock suppression through reducing the peak temperatures and pressures of the end-gas during combustion. The primary mechanism here is an increase in trapped mass and thermal capacity of the chamber contents at a given load, resulting in a smaller temperature rise during combustion. A secondary effect of dilution is a reduction in the laminar flame speed. This slows the overall burn rate and results in lower peak pressures and temperatures for a given angle of 50% mass fraction burned [25]. Importantly, modest dilution rates can eliminate the need for fuel enrichment at high loads without unnecessarily compromising combustion stability and driveability [25, 26]. Combustion stability issues are a concern at higher dilution rates, however Cairns [26] showed that the enhanced spark advance benefit of EGR over excess air dilution was sufficient to maintain acceptable IMEP CoV (<3%) with EGR at dilution rates of up to 15%.

Of the available diluents, cooled EGR has therefore emerged as the most likely alternative to fuel enrichment at high loads [26-30]. Although greater thermal efficiencies are possible through dilution with excess air (owing to the higher γ of air compared to exhaust gas), the excess oxygen in the exhaust hampers NOx conversion in conventional three-way catalysts, resulting in unacceptably high NOx emissions [25].

Gasoline direct injection (GDI) is another strategy that serves to improve knock performance through charge cooling effects. Compared to PFI, GDI is able to achieve greater charge cooling because the energy required to evaporate the injected fuel comes almost exclusively from the inducted charge, rather than from the hot intake port and valve surfaces. This charge cooling effect increases an engine's volumetric efficiency by up to 5% compared to PFI equipped engines [9]. At fixed load, GDI reduces charge temperatures across the entire cycle, allowing spark timing to be advanced and/or CR to be increased. GDI additionally offers synergies with lean burn and stratified charge combustion modes thanks to the greater level of control it permits over the fuel metering process.

Building on the cooling benefits of GDI, the use of alcohol-based fuels has the potential to further enhance the knock benefit of direct injection (DI). Pure ethanol (E100) for example has roughly twice the heat of vaporisation of gasoline, and therefore offers much greater charge cooling capabilities. This is reflected its high octane rating of 107RON [9]. Indeed, in the time since lead alkyl anti-knock additives were phased out, ethanol's use as an anti-knock agent in gasoline (typically 5-15% by volume) has become widespread. Recent research has focussed on the synergies offered between downsizing, direct injection and the use of high ethanol content gasoline blends such as E85 (85% ethanol, 15% gasoline by volume) [31-34]. As with cooled EGR, the additional charge cooling effect can also eliminate the requirement for over fuelling, improving high load BSFC and emissions. The issues concerning ethanol's use as a mainstream alternative to gasoline include its lower specific energy content, minor infrastructural challenges and ethical issues regarding its production from biomass. Alternative alcohol production methods have been proposed, such as the synthesis of methanol from water and atmospheric carbon dioxide [35]. Unfortunately, these methods seem unlikely to be able to deliver fuel production on the scales required to have an impact on global CO_2 levels anytime soon.

Finally, several researchers have proposed novel boosting configurations whereby additional charge cooling (above that provided by the CAC) is achieved through expansion of the cooled high pressure charge across either a standalone turbine [36], a turbo-expander [37], or a supercharger [38]. In each of these systems, the intake air is over compressed before being passed through a standard intercooler and then expanded across a second device to the desired boost pressure. Referred to as turbo-expansion, systems of this type can theoretically deliver intake air at temperatures below ambient at full load since the expander is situated post-CAC. The knock mitigation benefit of cooler air charge temperatures would permit higher CR for boosted or downsized engines and improve combustion phasing, bringing the usual benefits in terms of increased thermal efficiency and decreased exhaust gas temperatures. Unfortunately, the success of such systems depends heavily on the isentropic efficiency of the expander. Engine tests performed in [36] using an Opcon twin-screw expander and simulation results in [38] using an Eaton R410 supercharger both suggest that currently, the technology available is unable to deliver the efficiencies required for turbo-expansion to provide an overall BSFC benefit.

Combustion chamber surface cooling strategies

Indirect cooling methods are those that achieve lower end-gas temperatures through lower combustion chamber surface temperatures. One such example is the use of sodium filled exhaust valves. These hollow valves run cooler than their solid counterparts thanks to improved heat transfer between the valve head and the valve stem (facilitated by the sloshing movement of the liquid sodium inside the valve stem as it is actuated) [9]. Besides reducing the probability of surface ignition, cooler running exhaust valves also promote a more even temperature distribution within the combustion chamber, reducing the discrepancy between the flame propagation speeds on either side of the cylinder, thereby decreasing the overall likelihood of knock on the intake side of the cylinder [10].

In a similar vein, the use of high heat rating spark plugs also reduces surface temperatures within the combustion chamber without the need for additional liquid cooling. Principally, these spark plugs have lower running temperatures because of shorter heat flow paths between the plug casing and the exposed electrodes. Although their effects on spark knock mitigation are not well documented, in high specific power engines (such as those that are downsized), high heat rating spark plugs are often essential for avoiding surface-induced pre-ignition at high loads.

In modern engines, cooling of the remaining combustion chamber surfaces is largely taken care of by pressurised liquid cooling systems. These systems typically use a mechanically driven pump to flow an aqueous mixture of ethylene glycol and water through passages within the cylinder head and block. The heat conducted to the coolant is then rejected to atmosphere using a fan blow heat exchanger. Electrically driven pumps offer greater control of pump flow rate, allowing for improved mechanical efficiency by preventing overcooling of components at low speeds and loads [39]. Their high cost however has so far prevented them from becoming commonplace in passenger cars. Due to their limited heat transfer capabilities, air-cooled systems are limited to applications of low power output and cost, such as on small two-stroke engines.

Due to their high specific power outputs, downsized SI engines tend to have increased head and block cooling requirements compared to their larger, NA counterparts. Indeed many researchers and commercial enterprises investigating extreme downsizing have even found it necessary to install water-cooled exhaust manifolds to limit exhaust gas temperatures at high loads and prevent the requirement for over fuelling [40]. Unfortunately, increased

engine-cooling results in greater heat loss and reduced thermal efficiency. Coupled with the pressures of increasingly stringent emissions legislation, cooling system optimisation has drawn considerable attention from researchers. Of primary interest is the trade-off between improved volumetric efficiency and knock performance versus the increased mechanical losses that arise due to poorer lubricant performance at low block temperatures [41]. This balance has contributed to the development of split flow or dual circuit cooling systems that separate the coolant circuits flowing through the head and the block, thus allowing the cooling requirements of each area to be met individually and with less compromise. The greater control over temperature distribution afforded by such arrangements has the potential to significantly benefit high load BSFC, particularly in the low to mid speed range when engines are typically over-cooled. Cooler head temperatures improve volumetric efficiency and high load knock performance whilst hotter liner temperatures decrease wall wetting and the thickness of quenched flame boundaries. The result is more complete combustion of the injected fuel and reduced UHC emissions. Furthermore, hotter block temperatures reduce frictional losses in the crank train, improving mechanical efficiency [9]. Finally, the improved knock performance at high load/low engine speed allows for the CR of an engine to be increased, increasing thermal efficiency across the engine map.

In applications of high specific power output however, dual circuit systems are still likely to overcool combustion chamber components at low to medium loads. Precision cooling systems aim to address this issue by only providing cooling where it is needed and at a rate proportional to the local heat flux [9]. This is achieved by way of narrow cooling channels near critical components (such as the exhaust valve area, the valve bridge, injector nozzles, etc.) whilst the rest of the head is left largely uncooled. The claimed benefits of such systems are a more even temperature distribution within the head and the possible elimination of surface “hot spots”. However, prediction of the coolant boiling behaviour inside the narrow passages is difficult, leading to complications in the design of precision cooling systems. This factor is important because although nucleate boiling of the coolant fluid can lead to a ten-fold increase heat transfer coefficient, excessive boiling can result in large bubble formation and “dry-out” of the narrow cooling passages as the bubbles pass through them. This can lead to very high surface temperatures and an increased threat of surface ignition and thermal failure.

Takahashi [42] identify cooling of the cylinder liners (particularly the higher sections near the exhaust valves) as the best compromise between improving an engine's knock performance and minimising the overall heat loss. In an earlier study, Nishino [41] tested such a strategy by milling thin, shallow slots in the block material between adjacent cylinders, thus connecting the cooling jackets either side of the cylinders and allowing coolant to flow through this upper region. Their results indicated that a significant drop in wall temperature between cylinders could be achieved depending on the width and depth of the machined slots. Correspondingly, the presence of these slots also reduced the average gas temperatures inside the combustion chamber, extending the KLSA.

Pistons constitute one of the largest and hottest surfaces inside the combustion chamber [41]. Unlike the cylinder walls (which are also exposed to the hot combustion gasses), pistons traditionally receive no additional cooling and therefore any thermal energy they accrue has to be conducted radially outwards to the liner via the piston rings. This conduction path is long and inefficient as the contact area between piston and cylinder wall is very small. What is more, the presence of a lubricating oil film between the piston rings and liner means that there is actually very little metal-to-metal contact, further impeding heat transfer away from the piston [8]. Improved piston cooling can be achieved by targeting oil sprays at the underside of the piston. Broadly speaking, this can be achieved in two ways. The first (and least affective) method is by using oil drillings in either the big or small end of the connecting rod. As the cranks shaft rotates, a limited amount of oil is squirted intermittently across the piston underside, increasing heat transfer away from the piston and reducing crown temperatures. However, a more effective and reliable method of achieving piston underside cooling is to use continuously fed oil jets aimed directly at the piston underside. Cooling systems of this type can be further enhanced by the use of multiple jets and cooling galleries within the pistons (additional ring shaped voids between the piston underside and crown). Oil is introduced into the piston gallery by targeting the oil jets at an entry hole on the underside of the piston. This practice significantly increases heat transfer from the piston by increasing the oil wetted surface area and shortening heat transfer paths from temperature critical areas of the piston geometry [43].

Additional design considerations affecting piston operating temperatures include material selection and piston ring design. Material choice dictates the piston's thermal conductivity and coefficient of expansion, whilst the design and number of piston rings used affects the

piston's ability to control oil intrusion and conduct heat to the cylinder walls. From a knock perspective, these are important considerations as their combined effects determine the surface temperatures of the piston that ultimately affects the temperatures of the end-gas throughout the cycle (and therefore its propensity to knock). Meanwhile excessive oil intrusion by blow-by has been associated with high knock frequencies since lubricating oil is believed to have lower ignition delay times than conventional air/fuel mixtures [12].

Despite its relatively high coefficient of thermal expansion and lower melting point, aluminium alloy is normally used for piston manufacture in preference to cast iron or steel because of its low density (reduces reciprocating mass). Its superior thermal conductivity also helps reduce the severity of thermal temperature gradients, lowering both the risks of surface ignition due to hotspot formation and of thermal fatigue failure due to high levels of thermal strain [9].

2.3 Fuel Effects

As previous sections have described, autoignition is highly sensitive to factors that influence the physical properties of the end gas – i.e. its temperature, pressure, and the time spent at high values of these parameters before the arrival of the spark-induced flame front. However, autoignition is a chemical process and as such, it is also highly sensitive to the chemical composition of the fuel in question. Practical fuel blends are complex mixtures of a wide range of hydrocarbon types: alkanes (paraffins), alkenes (olefins), cyclanes (napthenes), aromatics and alcohols (oxygenates). Ignition delay characteristics vary enormously between hydrocarbon types, and even between hydrocarbon species of the same type. It is therefore very difficult to predict the autoignition resistance of practical fuel blends.

Fortunately, practical methods have been devised to benchmark the autoignition resistance of real fuels. The property that defines this resistance is called "octane number" (ON). The higher a fuels ON, the higher its resistance to autoignition. The scale by which ON is judged uses two reference fuels – iso-octane (assumed to have ON = 100) and n-heptane (assumed to have ON = 0). These fuels are referred to as Primary Reference fuels (PRFs). The ON of a practical fuel is defined as the volume fraction of iso-octane in the PRF blend that achieves the equivalent autoignition tolerance as the practical fuel. A PRF blend of 50% iso-octane by

volume therefore has an ON of 50. The two most widely used test methods for measuring a fuels octane number relative to these reference fuels are the ASTM[3] Research method and the Motor method. These two methods use a standardised single-cylinder engine developed by the Cooperative Fuel Research (CFR) Committee. The conditions at which the two tests are run are given in Table 2.1.

	Research Method	**Motor Method**
Inlet Temperature	52°C	149°C
Inlet Pressure	Atmospheric	
Humidity	0.0036 – 0.0072 kg water per kg dry air	
Coolant Temperature	100°C	
Engine Speed	600rpm	900rpm
Spark Advance	13°CA bTDC (fixed)	19 – 26°CA bTDC (depends on CR)
Air/Fuel Ratio	Adjusted for maximum knock	

Table 2.1 – Operating conditions for the research and motor octane rating methods

The principles of the Research (RON) and Motor (MON) tests are as follows:

- At each test condition, the engine is first run with the fuel being tested. The AFR is varied to produce maximum knock intensity (measured using a magneto-restrictive pressure transducer installed within a proprietary ASTM "Knock Detector").
- The CR of the engine is then adjusted to produce knock of a standardised intensity.
- The test is repeated using two different PRF blends not more than two ON apart, with one required to achieve a higher CR at the standard knock intensity compared to the test fuel and the other required to achieve a lower CR.
- The RON or MON of the test fuel is then calculated by interpolating the ON of the two PRF blends that bracket the observed knock performance of the test fuel.

From Table 2.1, one can see that the MON test is the harsher of the two, with conditions much less favourable to knock avoidance. For practical fuels, MON is therefore usually lower than RON, with the difference between these numbers defined as *sensitivity*:

[3] ASTM = American Society for Testing Materials

$$Sensitivity = RON - MON$$ Equation 2.1

By definition, the sensitivity of PRFs is zero (i.e. RON = MON). Since practical fuels tend to have non-zero sensitivity (i.e. RON > MON), PRFs can be said to exhibit stronger resistance to autoignition under MON-like conditions that practical fuels. This increased resistance is due to the characteristic ignition delay behaviour of paraffins – the class of hydrocarbon in which iso-octane and n-heptane are members. Paraffins display a particular characteristic called negative temperature coefficient (NTC) behaviour, whereby in the intermediate temperature regime, their resistance to autoignition actually increases as temperature increases [44]. This behaviour is shown below in Figure 2.4, where predicted ignition delay times at constant pressure and temperature are plotted for a variety of single-component fuels.

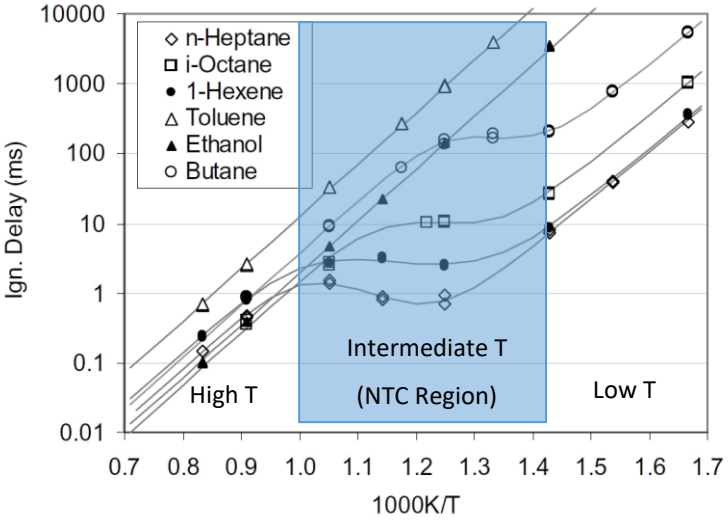

Figure 2.4 – Simulated ignition delay times for a range of pure fuels at 30 bar [45]. Note the strong NTC behaviour in the intermediate temperature range (highlighted) for paraffinic fuels such as iso-octane, n-heptane and butane, whilst fuels such as toluene (an aromatic) and ethanol (an oxygenate) exhibit no NTC behaviour at all [45]

It is generally true that aromatics, oxygenates and olefins exhibit no NTC behaviour [45]. These fuel types therefore display high sensitivity in comparison to paraffinic fuels. Since practical gasolines are blends of hydrocarbons from all four categories, one would expect them to exhibit a degree of NTC behaviour, but less than that displayed by purely paraffinic fuel blends.

For many hydrocarbon fuels, autoignition at low temperatures proceeds in a two-stage manner. Yates [46] provides a useful graphic to help explain this process (see Figure 2.5).

Considering the case of 700K initial temperature, the mixture initially displays a period of very low chemical reactivity (implied by the very gradual increase in temperature between 0 and 7.5ms). This is followed by an abrupt increase in temperature caused by the passing of what is known as the "cool-flame" – a low temperature combustion phenomenon where only a fraction of the reactants react before the reaction is quenched, and which is accompanied by a faint blue light [6]. This is followed by a second period of relative inactivity (albeit very short in this case) before finally, the second "hot" stage of ignition occurs and the bulk of the fuels energy is released. From Figure 2.5, one can see that as the initial temperature is increased, the cool flame ignition delay becomes shorter and the cool-flame temperature rise becomes smaller. When the initial temperature enters the high temperature regime (T>1000K), ignition occurs by a single-stage process without a cool flame.

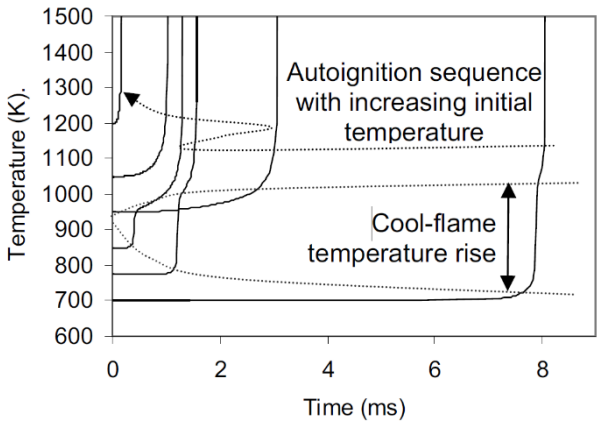

Figure 2.5 – Simulated temperature profiles for the autoignition of stoichiometric n-heptane mixtures at various initial temperatures in a constant volume reactor at 20 bar [46]

Many researchers have drawn a link between the cool flame phenomenon and the NTC behaviour of fuel. Fuels that exhibit strong NTC behaviour have been shown to display pronounced cool-flames, whilst fuels such as methanol that exhibit no NTC behaviour have been shown to display no cool-flames and autoignition proceeds exclusively in a single-stage manner. In [46], Yates argues that the transition in ignition delay behaviour in the NTC regime is a result of the decreasing amplitude of the cool-flame temperature rise at higher initial temperatures.

In general, the conditions inside boosted DISI engines fall into the low temperature/high pressure category. Experimental investigations by Kalghatgi and co-workers using HCCI engines showed that the low temperature heat release by the cool flame was significant

under these types of conditions, whilst it was negligible for the same fuels at higher inlet temperatures and lower inlet pressures [47]. Meanwhile, Goldsborough [48] and Tao [49] both concluded from their simulation-based studies that under conditions of low temperature/high pressure, the low-temperature chemistry (i.e. the reactions that include the cool-flame), could be significantly enhanced, leading to greater levels of heat released by the cool flame and therefore shorter overall ignition delays. Due to the practical limitations of the apparatus currently used to measure ignition delay, there is unfortunately a lack of experimental ignition delay data at such conditions. The role of cool flames and the NTC characteristics of practical fuels and their surrogates are therefore areas rich for further investigation. The consensus is also that their consideration is critical if we are to be able to predict knock onset accurately in highly boosted, DISI engines.

2.4 Knock Simulation Approaches

The ability to simulate autoignition (AI), and therefore knock, in SI engines poses many advantages. It is particularly useful in the early stages of engine design and performance optimisation, where an awareness of knock limits can have a significant impact on the specification of boosting hardware or charge cooling equipment for example. At a later stage, accurate knock modelling tools can be used to supplement the costly experimental calibration process, potentially reducing development costs.

AI simulation tools fall into two distinct categories – simple ignition delay correlations (IDCs) and complex chemical kinetic mechanisms (CKMs). CKMs model AI by considering the individual chemical reactions that take place between intermediate species. To do so for real fuels (with their complex formulations) is beyond the realms of current understanding. Fortunately, techniques have been devised to approximate the ignition delay behaviour of real fuels at low pressures with surrogate fuel blends [50], and considerable effort has been spent developing CKMs for blends of these compounds [51]. Unfortunately, CKMs are too detailed for most applications, resulting in excessively long simulation run times. The most detailed CKMs for example consist of approximately 6000 reactions and 1500 intermediate species [52]. Reduced CKMs have been devised by eliminating reactions that have little impact on overall reaction rate predictions, but these are still vastly more computationally expensive than alternative AI modelling techniques [53].

IDCs represent a computationally efficient alternative to CKMs. Instead of predicting the detailed chemical processes involved in AI, these phenomenological models simply predict the overall ignition delay time as a function of key mixture properties. The simplest IDCs achieve this by employing a single-step Arrhenius function in the form of Equation 2.2, effectively describing the entire AI process as a single chemical reaction. They therefore represent a significant computational advantage over CKMs, but at the cost of reduced insight into the underlying physics of the AI process. As with CKMs, IDCs are calibrated empirically using fundamental ignition delay data from rapid compression machines (RCMs) and/or shock tubes. They can however be calibrated using real engine data or with predicted ignition delay times from CKMs. Given that IDCs contain far fewer calibrateable terms than CKMs (there are only three coefficients in Equation 2.2 for example), they are also much easier to modify for a given engine or fuel for example.

Given the practical advantages discussed above, this work will concern itself with the applicability of IDCs rather than CKMs for modelling AI and knock in highly boosted SI engines.

2.4.1 Single-Step IDCs (with fixed parameter values)

Many IDCs adopt the conservation of ignition delay principle proposed by Livengood and Wu [54]. Published in 1955, this method was the first to correlate ignition delay measurements from RCMs (where pressure and temperature are nominally constant) with AI onset times observed in real engines (where temperature and pressure are continuously changing). At the heart of this approach is the assumption that under fixed pressure and temperature, the ignition delay of a mixture can be approximated by a single-step Arrhenius function of the form described by Equation 2.2. Here, τ is the ignition delay, T and P are the mixture temperature and pressure, and A, n and B are empirical constants. These constants are determined by matching ignition delay predictions with RCM measurements.

$$\tau = A \cdot P^{-n} \cdot e^{b/T} \qquad \textit{Equation 2.2}$$

The conservation of ignition delay principle (or L+W Integral) stipulates that the overall ignition delay of an air/fuel mixture under variable pressure and temperature conditions can be determined by integrating the reciprocal of the instantaneous ignition delay trace with respect to time. The point in time at which this cumulative integral reaches unity is defined

as the onset of AI. Mathematically, the L+W integral is expressed by Equation 2.3, where t_0 is the time at the start of compression (normally assumed to be intake valve closure, t_{IVC}), t_c is the time at the point of AI onset, and τ(t) is the instantaneous ignition delay at time t.

$$\int_{t\,=\,t_0}^{t\,=\,t_c} \frac{dt}{\tau(t)} \;=\; 1 \qquad \textit{Equation 2.3}$$

Thanks to its relative simplicity, the conservation of ignition delay principle has been widely adopted for AI prediction in SI and HCCI engines. In the time since its conception, several modifications have been proposed to account for shortcomings in the way the original L+W formulation represents certain fuel behaviours, whilst many expressions for τ have been developed to account for different fuels and changes in engine operating strategies (lean operation, or EGR for example).

One such development pertinent to SI engines and their fuels is that proposed by Douaud and Eyzat (D+E) [55]. Using experimental data collected from a Cooperative Fuels Research (CFR) engine, D+E adapted the single-step Arrhenius expression for τ used by L+W to create an empirical correlation for the ignition delay of primary reference fuel (PRF) blends in the range 80-100 ON (Octane Number). Calibration of the coefficients A, n and B was achieved via a simple mathematical routine whereby the sum of the squared errors of the L+W integral at measured AI onset angles was minimised over a large sample of experimental cylinder pressure traces. Mathematically, the D+E correlation is written as:

$$\tau \;=\; 17.68\left(\frac{ON}{100}\right)^{3.402} \; P^{-1.7} \; e^{3800/T} \qquad \textit{Equation 2.4}$$

Where τ is measured in milliseconds, pressure in atmospheres (absolute) and temperature in Kelvin. ON is the octane number of the PRF in question. From comparison with Equation 2.2, it is apparent that consideration of PRF octane number is factored into the A term, whilst n = 1.7 and B = 3800.

As mentioned, the D+E correlation was developed using cylinder pressure data obtained from a single-cylinder CFR engine, fuelled with blends of PRFs (iso-octane and n-heptane). This choice of hardware and fuels has important implications for the applicability of the D+E IDC. Firstly, the CFR engine is not typical of most modern SI engines [56]. Unchanged since 1929, the CFR engine is naturally aspirated and carburetted. Compared to most modern SI engines, which are generally boosted and equipped with direct injection, in-cylinder

temperatures are generally hotter and pressures generally lower inside the CFR engine. In addition, the combustion chamber of the CFR engine has a flat roof with a side-mounted spark plug. In contrast, most modern engines have pent-roof combustion chambers with the spark plug mounted centrally. This location minimises the distance that the flame must travel in order to consume all of the fresh charge, thereby increasing overall burn rate. Given these differences, and the impact that in-cylinder conditions have on knock behaviour, one could argue that the data upon which the D+E correlation is based is not particularly representative of modern SI engines[4].

Secondly, practical fuels are mixtures of hundreds of different compounds spanning various classes of hydrocarbon. They therefore have very different AI properties compared to two-component blends of iso-octane and n-heptane, both of which belong to the "paraffin" (alkanes) class of hydrocarbon. To illustrate this point, one only needs to consider the fact that for PRF blends RON = MON (by definition), whereas for practical gasolines RON tends to be roughly 10 ON higher than MON. This observation also raises the question of how to define "ON" when using the D+E correlation to simulate practical fuels. Consensus in the literature suggests that ON should be set equal to the RON of the fuel in question [34, 59-62], whilst the GT-Suite User Manual [63] suggests using the average of RON and MON (also known as the Anti-Knock Index, or AKI). Implementation of the D+E correlation within GT-Suite does however include an overall induction delay multiplier, which could be used to compensate for the fact that AKI is lower than RON for most practical fuels.

Thirdly, and unrelated to the choice of engine and fuel used in its formulation, the D+E IDC also makes no consideration towards the knock-suppressing effects of dilution (either with EGR or excess air).

Despite the above criticisms, the D+E correlation is a remarkably flexible and efficient knock modelling tool. To this day, it is still one of the most widely used IDCs for predicting knock in SI engines with several researchers observing that reasonably accurate knock onset predictions can be obtained for practical fuels with only minor modification to model constants [34, 59, 62, 64]. Over the years, many researchers have proposed minor modifications to Equation 2.4 to enable it to consider the effects of dilution, equivalence ratio and fuel properties. However, there appears to be a distinct lack of correlations that

[4] Indeed many researchers have questioned the relevance of the RON and MON tests for assessing the anti-knock properties of practical fuels in modern SI engines [47][56-58].

have been generated using engine data recorded at high BMEPs. The highest BMEP IDC found in the course of this investigation is that presented by Chen [61], where cylinder pressure data collected at 18bar BMEP was used to calibrate the model parameters.

One flaw of the D+E correlation, which has been omitted from the above discussion, stems from the use of a single-step Arrhenius function to describe ignition delay. Many fuels (particularly paraffins such as iso-octane and n-heptane) exhibit an ignition delay characteristic in the intermediate temperature regime known as Negative Temperature Coefficient (NTC) behaviour. As previously explained, ignition delay is observed to plateau or even increase as temperature is increased within this temperature regime, contrary to the monotonically decreasing trends observed in both the high and low temperature regions. This is displayed graphically in Figure 2.4, where CKM predictions of log(τ) are plotted against temperature for a variety of pure fuels. In modern SI engines, temperatures of the end-gas during combustion rarely stray into the high temperature regime. From a knock modelling point of view, it is therefore critically important that ignition delay characteristics in the low and intermediate temperature regions are accurately described by the modelling approach used. Taking logs of Equation 2.2 and plotting the resulting data on top of Figure 2.4 would clearly result in a straight line with gradient B and y-intercept log(A) – nlog(P). Whilst this approach would be appropriate for modelling the ignition delay of fuels that display no NTC behaviour (such as ethanol and toluene), it could introduce large errors when applied to fuels that *do* display NTC behaviour. Ironically, the paraffinic fuels iso-octane and n-heptane upon which the D+E IDC is based exhibit some of the strongest NTC behaviour of the six fuels plotted in Figure 2.4.

The suitability of the single-step Arrhenius expression for predicting AI therefore depends on the following factors:

a) The temperature region of interest. As has been pointed out by other researchers [45], if only the low or high temperature regions are of relevance to a particular combustion process, then it would be perfectly admissible to use a single-step Arrhenius function to model ignition delay. Some recalibration of the original D+E coefficients would likely be necessary depending on the properties of the fuel considered, and ideally separate correlations should be used for the high and low temperature regimes. It is worth pointing out however that apart from at very low

loads, the in-cylinder conditions inside practical SI engines will generally involve the NTC region to some degree.

b) The NTC characteristics of the fuel considered. If a fuel exhibits no NTC behaviour, then a single-step Arrhenius function would adequately describe the ignition delay characteristics of said fuel. If a fuel exhibits significant NTC behaviour, a single step Arrhenius expression (in theory) should not yield accurate results.

2.4.2 3-Arrhenius IDCs

Most practical fuels exhibit moderate levels of NTC behaviour due to their high paraffin content. As mentioned, the PRFs iso-octane and n-heptane (both paraffins), also exhibit significant NTC behaviour. PRFs are an integral component of the octane rating system, which means that they also receive a lot of attention as gasoline surrogates in simulation environments. Coupled with the need for computationally efficient yet physically accurate ignition delay models from within the CFD community, there has been significant impetus to develop IDC formulations that *can* model the NTC behaviour of fuel surrogates.

The first major development in this respect was Weisser's "3-Arrhenius" model in 2001 [65]. As the name suggests, this model consists of three separate Arrhenius functions. Each function models the characteristic ignition delay timescales within one of the three temperature regimes. Its formulation accounts for the fact that the low and intermediate temperature reactions occur sequentially (giving rise to two-stage ignition) whilst the high temperature reactions represent a competing, single-stage ignition process that occurs in parallel. Drawing an analogy between ignition delays and electrical resistors, Weisser proposed that the overall ignition delay of a mixture could be described using Equation 2.5, where τ is the overall ignition delay and $\tau_{1\text{-}3}$ are the individual timescales representative of the low, medium/NTC and high temperature ignition regimes respectively. Each timescale is described by a single Arrhenius function of the form presented in Equation 2.2. This simplified configuration is depicted graphically in Figure 2.6 and Figure 2.7 below.

$$\frac{1}{\tau} = \frac{1}{\tau_1 + \tau_2} + \frac{1}{\tau_3} \qquad \textit{Equation 2.5}$$

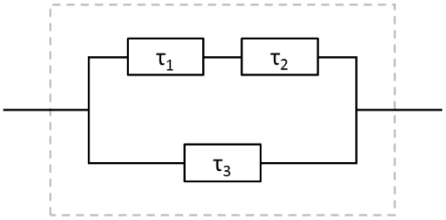

Figure 2.6 – Weisser's simplified approach for describing overall ignition delay of NTC exhibiting fuels, drawing an analogy between ignition delays and electrical resistors.

Yates extended Weisser's 3-Arrhenius model for use with gasoline relevant surrogates such as iso-octane, ethanol and toluene in 2005 [45]. Interest in the influence of ethanol and toluene on ignition delays stems from their increasing use as anti-knock additives in practical gasolines over the years. Indeed toluene is the most abundant aromatic hydrocarbon in modern gasolines, occupying up to 10% by volume [66], and it is not uncommon to see similar volume fractions for ethanol in EN228 compliant market gasolines. In Yates' work, ignition delay predictions derived from simulations using detailed CKMs were used to develop parameter sets for $\tau_{1\text{-}3}$ for each pure fuel. A mixing-rule based on the volume-fraction of each fuel component was proposed and validated for estimating the ignition delay of blends of PRFs. Finally, a parameter set was also determined for a 5-component gasoline surrogate with an estimated RON of 95 and the following composition: 10% n-heptane, 25% iso-octane, 20% toluene, 10% ethanol and 10% butane. The presence of compounds such as toluene and ethanol (which do not display NTC behaviour) suggests that the MON of this surrogate blend would be lower than the RON; a characteristic that is typical of practical gasolines.

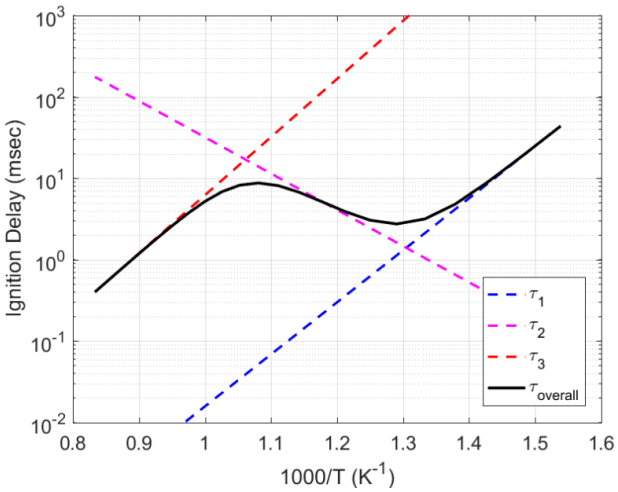

Figure 2.7 – Example of 3-Arrhenius IDC formulation in practice, showing how the NTC behaviour of a fuel could be recreated. Results obtained using Weisser's 3-Arrhenius IDC [65] for n-heptane at 10 bar.

Following on from Yates, Vandersickel subsequently extended the 3-Arrhenius IDC to account for the effects of EGR on ignition delay (see Equation 2.6) [67][5]. Calibration of the model parameters was achieved using experimental shock tube ignition delay data for several HCCI-relevant fuels and a combination of linear regression and sensitivity analysis. EGR was simulated in the shock tube experiments by varying the volume fraction of nitrogen in the mixture. The concentration ratio $[N_2]/[O_2]$ in Equation 2.6 is representative of the EGR rate. Although not validated, it is assumed that the same functional form would be valid for engine-derived EGR containing additional CO_2 and H_2O (one would just have to substitute $[N_2]$ for the relevant species concentrations). The last term in Equation 2.6 was introduced to account for the change in temperature dependence under varying dilution rates, but was only necessary within the NTC region (i.e. $e_1 = e_3 = 0$).

$$\tau_i = A_i P^{-n_i} \phi^{m_i} T^{c_i} exp\left(\frac{B_i}{T}\right) \left(\frac{[N_2]}{[O_2]}\right)^{d_i} exp\left(\frac{[N_2]\, e_i}{[O_2]\, T}\right), \quad for\ i = 1-3 \qquad \textit{Equation 2.6}$$

Further developments to the 3-Arrhenius model have generally pertained to recalibration of the model terms for use with alternative fuels or to further refinement of its capabilities with respect to PRFs. For example, Steurs developed separate 3-Arrhenius IDCs for iso-octane and ethanol using ignition delay predictions from detailed CKMs [68]. Meanwhile, AlAbbad recently produced a 3-Arrhenius correlation for PRFs in the range 70-95 ON using experimental ignition delay data from shock tubes [69]. Neither of these correlations consider the effects of residual gas fraction however.

2.4.3 Cool-Flame/Stage L+W Integral IDCs

An alternative "NTC-equipped" IDC formulation was proposed by Yates in 2008 [46]. Derived from ignition delay predictions using detailed CKMs, this empirical model attempts to predict the two-stage ignition process that occurs in the NTC regime for blends of PRFs and methanol (a single-stage or "non-NTC" fuel). It does this by tracking the development of the low and

[5] It is worth pointing out that the simple power-law relationships between ignition delay, equivalence ratio and temperature were indeed part of Weisser's original 3-Arrhenius expression. It is unclear from the literature at which point these relationships became widely accepted, however Yates reported the validity of a power law to explain the influence of equivalence ratio in 2005 [45]. Vandersickel reports that sensitivity analysis showed that the temperature exponent c_i of Equation 2.6 was only required within the NTC region (i.e. $c_1 = c_3 = 0$).

high temperature AI chemistries in parallel and using separate Arrhenius functions for each regime. The Arrhenius expression for describing ignition delay in the low temperature regime (τ_c) is used solely for predicting the onset of the cool-flame. For a system with dynamically changing pressure and temperature, the onset of the cool flame is estimated using the conventional L+W integral. Alongside this integral, a separate L+W integral using a different Arrhenius function (τ_h) is evaluated for the high temperature chemistry. Due to the changes in temperature and pressure incurred at the passing of the cool flame, this high temperature integral has to be performed over two stages – the pre-cool flame stage (t_0 to $t_{CF)}$ and the post cool flame stage (t_{CF} to t_{ign}). As a result, this type of IDC is often referred to as a "staged" or "cool-flame" model.

The Yates cool-flame IDC predicts AI to occur when Equation 2.7 is satisfied, with $\tau_{h,i}$ and $\tau_{h,CF}$ corresponding to the high temperature Arrhenius expressions pre and post cool flame respectively. The onset of the cool flame, t_{CF} is estimated using Equation 2.8, whilst the temperature rise associated with the cool flame is estimated from an empirical relationship based on initial conditions and equivalence ratio (Equation 2.13). A termination function (Equation 2.12) is introduced to prevent the cool flame temperature rise from assuming negative values at high temperatures since this is not physically possible. The three Arrhenius functions used to describe τ_c, $\tau_{h,i}$ and $\tau_{h,CF}$ are expressed by Equations 5.8 – 5.10, where ϕ is the equivalence ratio, P_i and T_i are the initial pressure and temperature and P_{CF} is the post cool-flame pressure (calculated using the ideal gas law and the cool-flame temperature rise, ΔT_{CF}). In total, there are 13 coefficients associated with the Yates cool-flame model, many of which are expressed as functions of PRF number. These coefficients were calibrated against a database of approximately 1500 ignition delay predictions spanning a broad range of temperatures, pressures, equivalence ratios and fuel blends. The calibration was carried out using non-linear least squares curve fits.

$$\int_{t_0}^{t_{CF}} \frac{dt}{\tau_{h,i}} + \int_{t_{CF}}^{t_{ign}} \frac{dt}{\tau_{h,CF}} = 1 \qquad \textit{Equation 2.7}$$

$$\int_{t_0}^{t_{CF}} \frac{dt}{\tau_c} = 1 \qquad \textit{Equation 2.8}$$

$$\tau_c = A_c P_i^{-n_c} \phi^{m_c} e^{B_c/T_i} \qquad \textit{Equation 2.9}$$

$$\tau_{h,i} = A_h P_i^{-n_h} \phi^{m_h} e^{B_h/T_i} \qquad \textit{Equation 2.10}$$

$$\tau_{h,CF} = A_h P_{CF}^{-n_h} \phi^{m_h} e^{B_h/(T_i + X\Delta T_{CF})} \quad \text{Equation 2.11}$$

$$\Delta T_{CF} = 0.5\left(\Delta T + \sqrt{\Delta T^2 + 4750}\right) \quad \text{Equation 2.12}$$

$$\Delta T = \omega\left(T_i - T_{EQ} P^{\kappa} \phi^{\mu} \left(\frac{100}{99 + \phi}\right)^{\sigma}\right) \quad \text{Equation 2.13}$$

In 2010, Yates extended the original cool-flame model to include blends of PRF80 and ethanol, and to offer some model refinements with respect to the formulation of certain coefficients [70]. Iqbal subsequently recalibrated Yates' cool-flame model for use with a single toluene/PRF blend (often called toluene reference fuels or TRFs) and introduced an additional term for the consideration of EGR rate [71]. TRFs are often regarded as better gasoline surrogates than PRFs because like practical gasolines, their RON is greater than their MON. The difference between RON and MON is known as sensitivity. This characteristic is significant because it indicates the degree with which the AI tendency of the fuel is affected by temperature (relative to PRFs). Toluene does not exhibit NTC behaviour and has a high resistance to autoignition. For a given pressure, its anti-knock properties are therefore proportionally much better than PRF blends at low temperatures than they are at high temperatures (see Figure 2.4).

Iqbal used the detailed TRF mechanism produced by Andrae [72] to simulate ignition delay times for a TRF blend over a broad range of initial temperatures, pressures, equivalence ratios and EGR rates. EGR was simulated by introducing the complete products of stoichiometric combustion (i.e. CO_2, H_2O and N_2). The TRF blend had a RON of 93 and MON of 89, resulting in a sensitivity of four and an anti-knock index of 91, hence it was referred to as TRF91. Figure 2.8 shows how the ignition delay characteristics of TRF91 compare with an equivalent AKI PRF, highlighting how the presence of toluene slightly mutes the NTC behaviour of TRFs compared to PRFs and results in shorter ignition delay times in the low and medium temperature regimes. From these observations, Iqbal suggests that using PRFs instead of TRFs as gasoline surrogates could over predict ignition delay times for most operating conditions. Figure 2.8 also shows how the NTC behaviour of paraffinic fuels becomes less obvious at higher pressures, whilst the effects of pressure on ignition delay are most significant in the NTC region. Unfortunately, Iqbal provides no parameter values for their TRF IDC so it has not been possible to verify its performance.

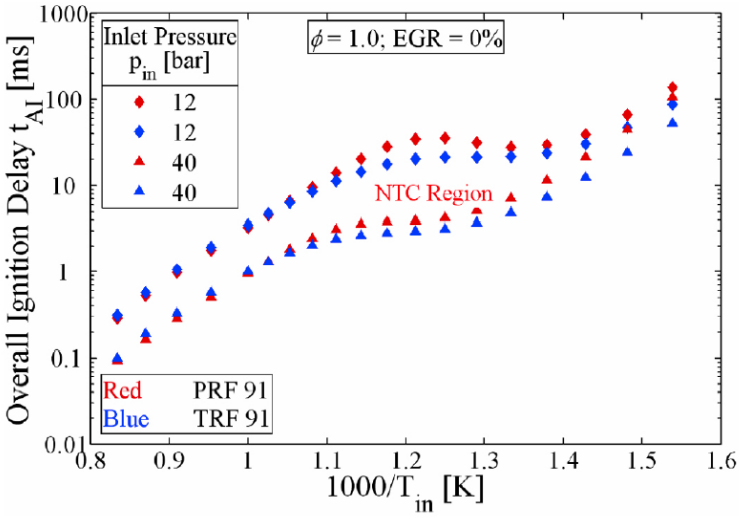

Figure 2.8 – Ignition delay predictions for PRF91 and TRF91 at initial pressures of 12 bar and 40 bar [71]

Finally, in 2016 Ma unified the previous developments by Yates and Iqbal to create a 3-Arrhneius IDC capable of modelling ignition delays for blends of iso-octane, n-heptane, ethanol and toluene [2]. Separate cool-flame IDCs were built for each of the pure fuels using experimental shock tube data from the literature. A mixing rule based on the mole-fractions of each component was proposed to estimate the overall ignition delay for any mixture of the four constituents, whilst a rule based on specific heat capacities was proposed to estimate the overall cool flame temperature rise. The performance of these rules were validated by comparison with experimental shock tube data for a range of blends, achieving satisfactory results.

It is worth pointing out that several alternative 3-Arrhenius formulations can be found in the literature. For example, Hernandez [73] proposed a formulation which uses a single-step Arrhenius expression to model ignition delay but with three different parameter sets for A, n and B (one for each of the three temperature regimes). The boundaries between temperature regimes were defined using separate functions expressed in terms of pressure and equivalence ratio. Coupled with a single L+W integral of the form described by Equation 2.3, this method provides a simple means of considering NTC behaviour. Unfortunately, it does not attempt to resolve the effects of the cool-flame on low temperature chemistry and as a result, struggles to predict two stage ignition delays with an acceptable level of accuracy [49]. Meanwhile, Pan proposed an approach whereby the L+W integral for the second stage of ignition is only initiated once the integral for the first stage (i.e. the cool flame) reaches unity [74]. In addition, two parameter sets are provided to model the second stage of

ignition, one for mixtures in the intermediate temperature region and one for those in the high temperature region. Tao [49] also recently adopted this approach. Unfortunately, all of these formulations have been calibrated for use with low octane, HCCI-relevant fuels, making them unsuitable in this case without recalibrating for use with SI-relevant fuels.

2.4.4 Advanced Single Step IDCs (with variable parameter values)

Like the original D+E IDC, this last category of IDC utilises a single-step Arrhenius expression and the original L+W integral described by Equation 2.2 and Equation 2.3. *Unlike* the original D+E IDC, the values of A, n and B in the expression for ignition delay are expressed as (sometimes complex) functions of pressure, temperature and/or fuel properties such as RON and MON. As a result, these correlations are able to capture complex fuel behaviours for a variety of fuels.

Goldsborough proposed the first IDC of this type in 2009 [48]. Assuming a traditional Arrhenius expression of the form $\tau = A\phi^{\alpha}P^{\beta}\chi_{O2}^{\gamma}e^{\lambda}$, changes in functionality with respect to each of the three temperature regimes were incorporated by expressing the parameters α/β/γ/λ as third order polynomial functions of temperature (ϕ = equivalence ratio, P = pressure and χ_{O2} = oxygen mole fraction). The resulting correlation, not shown here for the sake of brevity, contains 7 equations and 37 constants. These constants were calibrated for iso-octane using 661 experimental RCM and shock tube data points gleaned from the literature. A broad range of initial conditions was considered: ϕ = 0.2 – 2.0, P = 1 – 60 bar, χ_{O2} = 0.125 – 21% and T = 650 – 2000K. The correlation appears to recreate the experimental data with acceptable accuracy, and the experimentally optimised expressions for α/β/γ/λ compare very well with equivalent expressions optimised using ignition delay times predicted by detailed iso-octane CKM.

In 2016, DelVescovo extended Goldsborough's correlation to include consideration of PRF blends in the range PRF0 (100% n-heptane) to PRF100 (100% iso-octane) [75]. Like the original correlation, DelVescovo used third order polynomial functions of temperature to vary α/β/γ/λ and capture the NTC behaviour of the fuel. Exponential roll-off functions were used to force these parameters to converge on certain values at low temperatures. The location and rate of these roll-off functions were defined using linear functions of PRF #, thus incorporating the effects of blend composition into the overall correlation. In total,

DelVescovo's correlation contains 41 constants. These constants were calibrated using ignition delay predictions from 6480 constant volume reactor simulations coupled with a reduced CKM for gasoline surrogates. The calibrated correlation is claimed to predict ignition delay with and average error of ±24% compared to the reduced CKM over a range of conditions relevant to engine operation.

Finally, Kalghatgi developed a single-step IDC of the form described by Equation 2.2 whereby the three coefficients A, n and B are expressed as polynomial functions of RON and MON [76]. These functions were determined by fitting single-step Arrhenius expressions to predicted ignition delay data for 20 different TRFs [50]. Only ignition delay predictions under 15msec were considered as part of this fitting process, the justification being that even at engine speeds as low as 1500rpm, ignition delays greater than 15msec contribute very little towards the overall L+W integral and therefore do not significantly influence the predicted AI onset. Ignition delay predictions were obtained for a range of initial conditions using the detailed TRF CKM developed by Andrae [77]. The 20 TRFs represented a broad spectrum of compositions and RON/MON values[6]. Finally, the 20 sets of optimised AnB coefficients were collated and plotted against linear combinations of RON and MON, thus enabling the relationships between "AnB" and RON/MON to be established. These relationships are summarised below by Equation 2.14, Equation 2.15 and Table 2.2.

$$Z = \alpha X^2 + \beta X + \gamma \qquad \textit{Equation 2.14}$$

$$X = RON + \delta(RON - MON) \qquad \textit{Equation 2.15}$$

[6] Numerous studies have shown that two fuels with identical RON/MON but different compositions will still auto-ignite at the same instant if subjected to the same pressures and temperatures [47][78]. This observation suggests that the exact composition of fuels is not as critical for accurate ignition delay predictions as previously believed, and that TRFs could represent appropriate surrogates for practical gasolines.

Z	α	β	γ	δ
A (msec)	0	-1.74e-3	0.1957	0.6464
n (n/a)	0	-1.66e-3	1.4056	8
B (K)	3.4615	-5.68e2	30068	0.3125

Table 2.2 – Optimised constants for use with Equation 2.14 and Equation 2.15 in determining A, n and B for single-step IDCs of the form described by Equation 2.2 [76]

Kalghatgi's approach raises some interesting questions. By opting to use a single-step Arrhenius function, Kalghatgi readily admits that this method does not consider the effects of NTC behaviour on ignition delay. He argues however that at conditions where ignition delays are relevant to SI engine time scales (i.e. where $\tau < 15$msec), the NTC behaviour of TRFs can be ignored without significant loss of model accuracy. Figure 2.8 shows that the NTC behaviour of TRFs becomes less pronounced at higher pressures. However, it also shows that the entire NTC regime (and much of the low temperature regime) can be expected to illicit ignition delays less than 15msec when the pressure is approximately 40 bar. It is impossible that Kalghatgi's engine experiments were conducted solely in the high temperature regime where a single-step reaction is a good approximation of the ignition process, yet this appears to be the region that has been focussed on for calibration of the IDC. It is therefore surprising that such good agreement between experimental and simulated knock onset times was achieved (mean error was reportedly less than ±1°CA).

One aspect of Kalghatgi's correlation that has not been discussed is the arbitrary specification of a temperature difference between the main charge and a hypothetical hotspot. It is widely recognised that AI initiates from within regions of elevated temperature called hotspots. To model this phenomenon, Kalghatgi imposes a temperature delta (ΔT) of +10K between the hotspot and main charge when the cylinder pressure reaches 15bar. The adiabatic temperature evolution of the hotspot is then used in the L+W integral to calculate the onset of AI. To match experimental knock onset times at an intake manifold pressure (PMAN) of 1.0bar (abs), a ΔT of +10K was required. In contrast, when the PMAN was raised to 1.65 bar, a ΔT of 30K was required. Increasing the hotspot temperature in this way suggests that by ignoring the influence of the NTC region, Kalghatgi's correlation could have a tendency to over-predict ignition delay at high cylinder pressures. However, it is worth pointing out that for the same intake manifold temperature (TMAN), one would obviously

expect the bulk gas temperature at a cylinder pressure of 15 bar to be considerably lower when PMAN = 1.65bar than when PMAN = 1.0bar. Imposing a slightly larger difference between hotspot and bulk gas temperatures at higher PMAN therefore makes some sense.

It is worth mentioning that several other researchers have attempted to develop correlations of this type (variable parameter models), but for fuels that are of little interest to this investigation. For example, Vancoillie developed a variable parameter correlation for pure methanol whereby three of the exponents in the ignition delay expression were described by polynomial functions of equivalence ratio, residual gas fraction (RGF) and temperature [79]. Unfortunately, pure methanol is not an appropriate surrogate for practical gasoline given its very high RON (~109) and non-existent NTC behaviour. All of the experimental data in the current study was collected using a single, EN228 compliant 95RON pump gasoline, hence why only correlations based on gasoline or gasoline surrogates have been discussed.

2.5 Summary/Conclusions

Knock is one of the primary barriers to increasing the high load efficiency of SI engines. Knocking combustion occurs in SI engines in many different forms. In all cases however, it originates from autoignition – the spontaneous ignition of some or all of the end gas by any source other than that provided intentionally by the spark plug. Autoignition of air/fuel mixtures is a complex chemical process that is sensitive to temperature, pressure, mixture composition and the reactivity of the fuel (i.e. its resistance to autoignition).

Over the years, many strategies have been devised to mitigate knock. Traditional knock mitigation techniques (such as spark retard and compression ratio reduction) penalise efficiency. More recently devised strategies have tended to focus on ways to cool the fresh charge, be that directly using direct injection or turbo-expansion, or indirectly using EGR or advancing engine cooling systems. EGR has emerged as one of the more promising knock mitigation techniques, offering advantages of improved combustion stability and NOx emissions when compared with dilution with excess air. There are however, practical concerns with EGR, such the ability to deliver sufficient flow under certain conditions and the impact that water/soot ingress has on compressor life.

A fuel's resistance to autoignition is defined using the RON and MON tests. These tests are carried out in a single-cylinder engine, under conditions that some argue bear little relevance to modern, boosted DISI engines. The fuels used to define the octane rating scale are iso-octane and n-heptane, both of which belong to the paraffin class of hydrocarbon. Paraffinic fuels are known to exhibit a high degree of Negative Temperature Coefficient (NTC) behaviour – where ignition delay times in the temperature range 700-1000K are observed to increase as temperature is increased at fixed pressure. Real gasolines on the other hand are complex blends of multiple classes of hydrocarbon, some of which display no NTC behaviour at all. As a result, real fuels would be expected to exhibit lower levels of NTC behaviour than PRFs. This difference in NTC behaviour causes real fuels to exhibit lower resistance to autoignition at temperatures in the intermediate and high temperature regimes, which is reflected in the lower MON values that RON values.

In the low and intermediate temperature regimes, autoignition has been observed to proceed in a two-stage manner for fuels that exhibit NTC behaviour, where the first stage is the low temperature heat release caused by the passing of the cool-flame, and the second

stage encompasses the high temperature reactions that release the bulk of the fuel's energy. Several researchers have concluded that at the conditions relevant to modern, highly boosted SI engines (i.e. high pressure/low temperature), the magnitude of the low temperature heat release can be significantly enhanced, leading to shorter ignition delays and earlier knock onset. Unfortunately, there is a lack of experimental data from which to verify these claims due to the practical limitations of the apparatus conventionally used to measure ignition delay.

Autoignition simulation methods fall into two categories – phenomenological ignition delay correlations (IDCs) that approximate the real process of autoignition with simple Arrhenius-based expressions, and complex chemical kinetic mechanisms (CKMs) that attempt to predict the detailed chemical reactions that take place during autoignition. IDCs represent a computationally efficient alternative to CKMs. Single-step IDCs can adequately describe the ignition delay characteristics of non-NTC fuels, or for any fuel used in engines that operate outside of the NTC regime. They cannot however model the behaviour of NTC fuels across the low/intermediate/high temperature regimes due to the simplicity of their construction. Due to their high fraction of paraffins, practical fuels exhibit a moderate degree of NTC behaviour. More advanced IDC formulations have been devised that are able to describe the NTC behaviour of practical fuels. These correlations have a larger number of parameters, and as such can only be calibrated using constant pressure ignition delay measurements or predictions obtained from CKMs. In both cases, the valid operating range of the resulting IDC is limited by the aforementioned availability of experimental ignition delay data, which can only be collected at pressures less than 60 bar.

With their fewer coefficients, single step IDCs can be calibrated using experimental data from real engines under knocking conditions, and therefore are not necessarily constrained by the same pressure limitations as the more complex IDCs derived from ignition delay measurements or CKM predictions. This observation represents an interesting opportunity for engines that operate exclusively in the low temperature regime, a category that may include highly boosted, DISI engines due to the high pressure/low temperature in-cylinder conditions with which they operate. At the very least, there appears to be a need for correlations based on high BMEP engine data as the highest load IDC observed within the literature only used data up to 18bar BMEP for its calibration [61].

Chapter 3 – Test Facilities and Experimental Methods

Chapter Summary

This chapter provides information concerning the setup of the engine test-bench and the experimental campaign that was carried out. The configuration of the experimental engine is provided, along with details of the instrumentation installed. Also included, is a summary of the experimental data, with some brief analysis to highlight the key behaviours observed. The data collected at this stage of the investigation was critical to the over-arching aim of this investigation – to evaluate the performance of ignition delay correlations available in the literature at operating conditions relevant to downsized SI engines.

3.1 Test Cell Facilities

3.1.1 Engine Dynamometer

The experimental engine was coupled to a twin dynamometer arrangement consisting of a 200 kW AVL AC unit and an equivalent power Froude eddy current brake, thus providing a total power absorption capacity of 400kW. The AC machine allowed the engine to be motored when required, such as when debugging controllers or measuring engine friction. The dynamometer was operated exclusively in speed control mode, with engine load controlled by pedal position demand or by the intake manifold pressure delivered by the forced induction simulator (discussed below). Brake torque was measured using a 1kN HBM T10F torque flange.

Figure 3.1 – Test cell configuration, showing the twin dynamometer arrangement used

3.1.2 Forced Induction Simulator

A forced induction simulator (FIS) developed at the University of Bath was used to simulate boosted operation for the experimental engine. An industrial compressor system supplied the FIS with dry air at a pressure of 7 bar. The compressed air was first filtered to remove any particulates and contaminants, and then passed through a mechanical regulator to reduce the pressure to 5 bar. The total mass air flow into the FIS was measured at this point by measuring the pressure drop across an orifice plate. A 15kW electrical heater allowed the air charge temperature to be varied between ambient conditions (approximately 15°C) and 85°C. Intake manifold pressure was controlled by a butterfly valve within the FIS, which itself

was controlled by a close-loop PID controller. Any excess air flow not inhaled by the engine was dumped to the test cell via an ABB Sensyflow FMT700-P air mass flow meter, accurate to within ±1%. The mass air flow delivered to the engine was thus calculated from the difference between the total flow into the FIS and the dumped flow. Figure 3.2 shows the FIS unit disconnected from the engine and the dry air supply.

The exhaust manifold pressure was controlled by a 50mm diameter, cable-operated butterfly valve (shown in Figure 3.3), which was close-coupled to the exhaust manifold outlet to simulate the presence of a turbine.

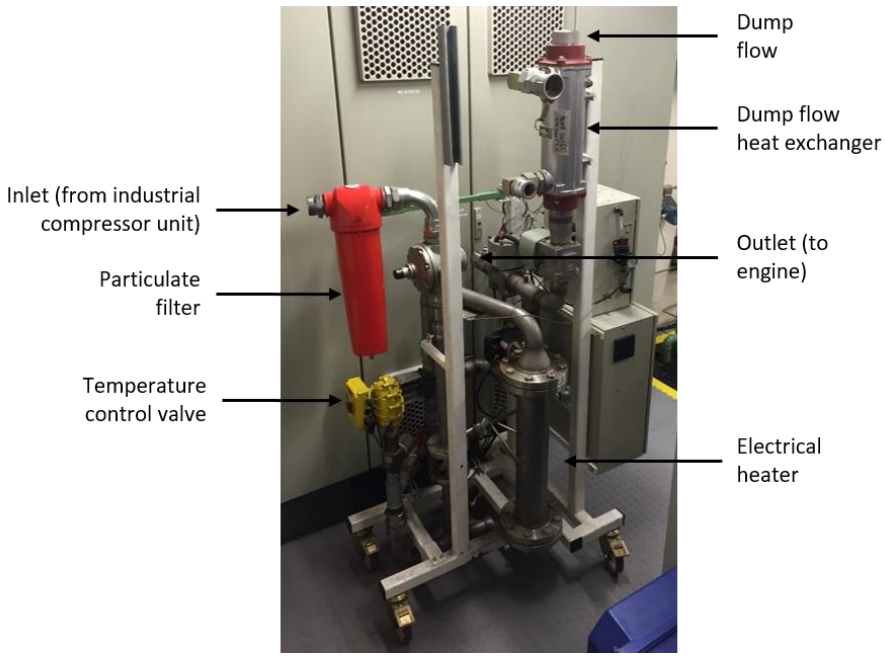

Figure 3.2 – Forced Induction Simulator (FIS) used to simulate boosted operation for the experimental engine

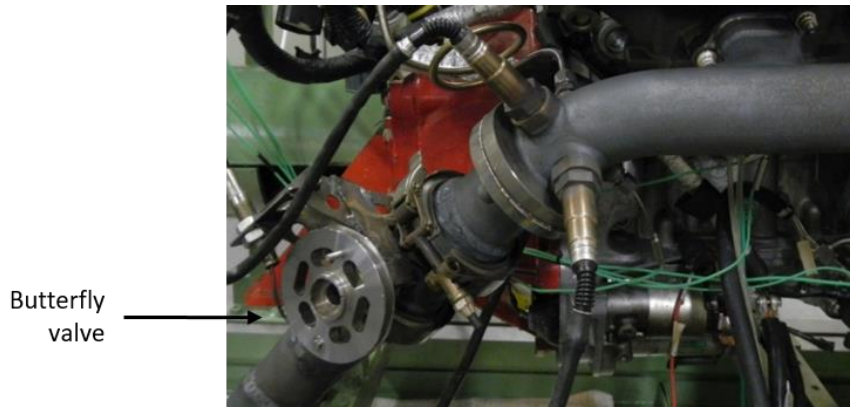

Figure 3.3 – Cable-operated butterfly valve used by the FIS to control exhaust manifold pressure

3.1.3 EGR Pump

With no low-pressure EGR introduction points in the intake system, exhaust gas had to be pumped manually to enable operation of the engine with EGR. This was achieved using an in-house developed EGR pump, a schematic of which is shown in Figure 3.4.

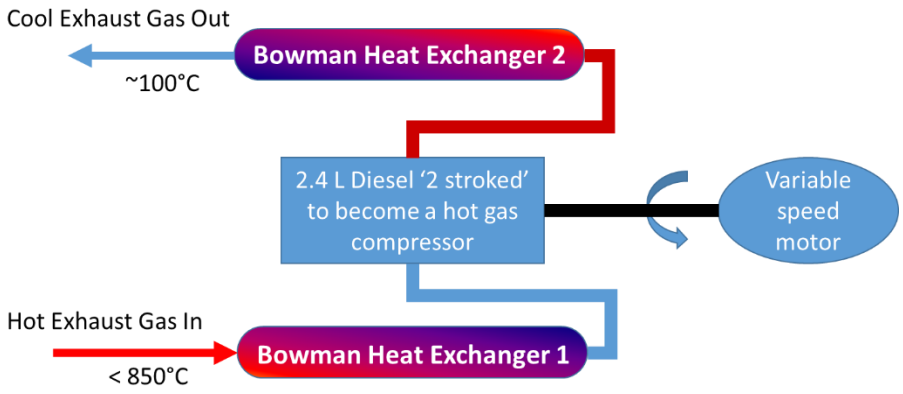

Figure 3.4 – EGR pump schematic

Exhaust gas was first drawn into the pump from a location downstream of the FIS backpressure valve via a Bowman heat exchanger. The cooled exhaust gas was then compressed using a 2.4 litre diesel engine converted to two-stroke operation for enhanced flow capability. The compressed gas was cooled via another Bowman heat exchanger before being reintroduced just downstream of the FIS outlet, allowing ample time for the exhaust gas and air to mix fully before reaching the engine. The pump was driven by a variable speed electric motor, allowing EGR rate to be varied between 0 and 20% via the host control system. The EGR pump was operated with an independent coolant circuit controlled to a temperature of 90°C to prevent condensate dropout within the pump. The EGR pump therefore had no impact on the experimental engine other than for the intended purpose of supplying cooled exhaust gas to the intake manifold.

3.1.4 Temperature Control

The ambient air temperature within the test cell was not actively controlled, however the high throughput of the cell ventilation system limited the variation in ambient temperature to less than 10°C. Air temperature within the test cell was monitored by the host system, with an alarm set at 35°C to alert the operator to potential failures of the ventilation system.

Cooling water for the EC dyno, FIS and engine coolant heat exchangers was supplied from a large capacity reservoir exposed to the outside ambient temperature. Although seasonal weather changes would have influenced the temperature of this reservoir, excess cooling capacity was designed into all of the water-cooled test bed facilities, minimising any impact on engine operation.

3.2 Engine Specification

The experimental engine used throughout this investigation was a 1.6 litre, 10.7:1 CR, in-line 4 cylinder gasoline engine. This engine is a modified version of the 2.0 litre, 9:1 CR engine used throughout the original Ultraboost programme – a collaborative venture between JLR, the University of Bath and a number of additional technical partners from both industry and academia [3]. Piston top deck height and crankshaft throw were modified to enable the changes in displacement and CR. The locations of the ring grooves were unchanged from the original 9:1 compression ratio design, resulting in a large top-land volume. Engine geometry and other details regarding ancillary systems are provided in Table 3.1.

Engine control was achieved using an open source ECU made by EFI Technology. A proprietary ECU calibration software produced by Lotus Engineering was used to communicate with the ECU and modify calibration tables from a standalone PC. Selected ECU variables were sent across to the host-system PC for logging using the ASAP3 communication protocol.

Engine Type	In-line 4 cylinder, 4 valves per cylinder.
Capacity (cc)	1623
Bore (mm)	83
Stroke (mm)	75
Compression Ratio	10.68 : 1
Firing Order	1 – 3 – 4 – 2
Construction	All aluminium. AJ133 (JLR 5.0 litre, V8 engine) cylinder block converted to single-bank operation.
Combustion System	Pent-roof combustion chamber with asymmetric central DI (solenoid operated) and spark plug. Heat level 9 spark plugs and high-energy ignition coils (100mJ). High tumble intake ports.
Valve Train	Chain driven double overhead camshafts (DOHC) - Intake cam duration = 250°CA, MOP = 150°CA aTDC - Exhaust cam duration = 250°CA, MOP = 126°CA bTDC Dual continuously variable camshaft phasors (DCVCP) - Intake cam advance = 62 ± 2°CA - Exhaust cam retard = 50 ± 2°CA
Engine Control Unit	Lotus E8 (made by EFI Technology)
Maximum BMEP	~ 32 bar @ 3500 rpm
Other	External cooled EGR. Water cooled exhaust manifold (WCEM). 145 bar in-cylinder pressure limit.

Table 3.1 – Experimental engine specification

3.3 Instrumentation and Data Acquisition

All engine control and data acquisition functions were performed using a Sierra-CP Cadet V14 host control system. The FIS and EGR pump were also both controlled from this host system. As part of the modelling work intended to be carried out after the experimental phase of this investigation, it was necessary to measure crank-angle resolved cylinder, intake and exhaust port pressures. A 16-channel AVL Indiset was used for this purpose, providing sufficient channel capacity for direct measurement of up to four ECU signals using current clamps. Crank angle position was measured using a 3600 pulse/rev crank-shaft encoder.

Figure 3.5 – Ultraboost cylinder head, showing location of cylinder pressure transducer installation.

Cylinder pressure was measured in all four cylinders at 0.1°CA resolution using Kistler 6041B water-cooled piezo-electric pressure transducers. These sensors are capable of measuring pressures up to 250bar within an accuracy of ±1 bar, and were chosen primarily for their high resistance to thermal shock and relatively small size (M8). Their natural frequency of >70kHz is well above the range of acoustic resonant frequencies expected within the experimental engine under knocking conditions. Transducer excitation was therefore not expected to interfere with the measurement of knocking pressure oscillations. Furthermore, each transducer was flush-mounted to prevent any issues arising through channel resonance of the connecting bore. The transducers were mounted off-centre in the cylinder head, along the longitudinal axis of engine as shown in Figure 3.5. Although this off-centre location was ideal for capturing the acoustic response of the circumferential resonant modes, its position along one of the primary radial resonant frequency node lines was not ideal for measuring the true response of the radial resonant frequencies. In theory, a mounting location between

the two intake valves would have been preferable, but tighter clearances would have required a different pressure transducer design at considerable cost to the project. Cylinder pressure zero-level correction (pegging) was achieved by setting the cylinder pressure at -180°CA (BDC induction) equal to the average of the intake port pressure calculated over the range -187.5 to -182.5°CA from cylinder 1.

Intake and exhaust port pressures were measured for all four cylinders at 1°CA resolution using Kistler type 4007 and 4049 piezo-resistive sensors respectively. Both transducer types have an operating range of 0-5 bar absolute and the 4049 transducers were water-cooled to permit steady operation within gas flows up to 1100°C. The protective screens supplied with these sensors were regularly removed and cleaned using an ultrasonic bath to prevent the build-up of soot that would otherwise dampen the sensors transient response. A standalone Kistler Type 2621F temperature control unit run on a 50:50 blend of ethylene glycol and distilled water provided the necessary cooling capacity for the cylinder and exhaust-port pressure transducers. A Kistler Signal Conditioning Platform (SCP) unit was used to amplify and condition the raw fast pressure signals before they were measured by the Indiset.

Finally, an array of K-type thermocouples, PRTs, general-purpose pressure sensors and flow meters was used to monitor vital engine parameters, and ensure safe operation of the test cell. Exhaust species concentrations were measured using a Horiba MEXA-7000 series analyser equipped with the ability to measure intake CO_2 levels and thus infer EGR rate. Closed-loop control of exhaust lambda was performed by the ECU, however independent lambda (and EGR) measurements were obtained using a LabCell ECM 5230 EGR analyser equipped with a Bosch LSU 4.2 Type-P wideband oxygen sensor (accurate to $\lambda \pm 0.008$). Fuel flow rate was measured using an ELITE Series Coriolis flow meter, accurate to ±0.1%.

3.4 Experimental Test Conditions

Experimental data was collected at four primary engine configurations. These configurations (listed in Table 3.2) were devised to represent the types of conditions experienced inside highly boosted, downsized gasoline engines. Two engine speeds were considered, and at each engine speed, two exhaust manifold pressure models were applied. The lower of the two exhaust manifold pressure models corresponded to a supercharger-biased two-stage boosted configuration and the higher of the two corresponded to a turbocharger-biased two-stage boosted configuration. Exhaust manifold pressure targets for each configuration were based on experimental data collected from two different engines, both equipped with a low pressure turbocharger stage and a high pressure supercharger stage. The supercharger (SC) biased model was based on data from the original 2.0 litre/9:1 CR Ultraboost engine fitted with a Garrett GT30 turbocharger an Eaton R410 supercharger. The turbocharger (TC) biased model on the other hand was based on data from a 1.0 litre, three-cylinder engine fitted with a fixed-geometry turbocharger and a CVT driven centrifugal compressor.

At each of the four primary engine configurations, intake manifold pressure was ramped in 0.2 bar increments from a starting point of 1.6 bar absolute pressure. The maximum pressure reached varied between configurations. At each intake manifold pressure setting, a detailed spark sweep was performed from a starting point that corresponded to heavy knock. Spark timing was then retarded in 1°CA increments until either the IMEP CoV exceeded 3%, the exhaust manifold temperature reached 1000°C, or the length of the spark sweep reached 10°CA, whichever came first. Measurements consisted of a 300-cycle log from the indicating system and a 10-second average of all of the channels monitored through the host system. Cylinder pressure data was recorded at a resolution of 0.1°CA to accurately capture the high frequency content of knocking pressure oscillations, whilst intake and exhaust port pressures were measured at 1°CA resolution. Knock intensity was assessed online by monitoring real-time $\overline{MAPO}$ values for each cylinder over the previous 100 cycles. Previous experience in running this engine had showed that heavy knock could be guaranteed by targeting $\overline{MAPO}$ values of 1bar/1000rpm. Independent spark timing was not employed between cylinders, therefore spark timing was only advanced as far as necessary for one cylinder to reach a state of heavy knock. Occasionally, this practice resulted in only one of the cylinders exhibiting heavy knock, but was considered a necessary precaution to prevent engine damage.

Finally, EGR sweeps were performed at several intake manifold pressure settings for the two supercharger-biased engine configurations. EGR rate was ramped from 0% to 15% in 5% increments, with detailed spark sweeps carried out at each EGR rate using the methods described above. EGR rate was quantified using the CO_2 ratio method defined in Equation 3.1, where $[CO_2]$ is the measured dry CO_2 concentration. The operating conditions where EGR was varied are listed in Table 3.2.

Primary Configuration #	**1**	**2**	**3**	**4**
Boost Pressure Ramps:				
Engine Speed (rpm)	1500	1500	3500	3500
Exhaust Manifold Pressure Model	SC biased	TC biased	SC biased	TC biased
Intake Manifold Pressure (bar A)	1.6 – 2.8	1.6 – 3.0	1.6 – 3.0	1.6 – 2.6
Exhaust Manifold Pressure (bar A)	1.2 – 1.7	1.4 – 2.4	1.5 – 2.5	1.65 – 2.8
ICP / ECP (°CA)	60/30	30/20	60/30	30/20
BMEP (bar)	17.5 – 31	14 – 25	19 - 34	15 – 23
EGR Sweeps:				
Intake Manifold Pressure (bar A)	1.6 – 2.2	n/a	1.6 – 2.2	n/a
EGR Rate (%)	0 – 15%	n/a	0 – 15%	n/a
BMEP (bar)	17.5 – 23.5	n/a	19 – 25	n/a
Standard Conditions:				
Intake Man. Temp. (°C)	40 ± 1°C			
Coolant Temp. (°C)	90 ± 1°C			
Lamba (#)	1.0 ± 0.02			

Table 3.2 – Summary of experimental test conditions

$$EGR = \frac{[CO_2]_{Intake} - [CO_2]_{Background}}{[CO_2]_{Exhaust} - [CO_2]_{Background}}$$

Equation 3.1

The experimental engine was equipped with dual continuously variable cam phasors (DCVCP), allowing the intake camshaft to be advanced 60°CA and the exhaust cam phase to be retarded 48°CA from their respective parked positions. All of the supercharger-biased operating conditions listed in Table 3.2 were run at an intake cam phase (ICP) of 60°CA and an exhaust cam phase (ECP) of 30°, generating approximately 64°CA of valve overlap (the period where both intake and exhaust valves are open at the same time). For the two-stage boosted engine developed in the original Ultraboost programme, this cam combination resulted in the best compromise between torque output and preventing rich misfire. Air mass flow was greatest at this condition for the original two-stage boosted engine (identical to the experimental engine used in this study in all but displacement and CR) for two reasons. The first is that the location of IVC was as close to BDC as possible, maximising trapped mass. The second is that the high level of valve overlap allowed ample time for some of the fresh charge to short-circuit the cylinder and flow straight into the exhaust port, which increased the overall mass flow and helped the turbocharger to generate more boost.

All of the turbocharger-biased operating conditions meanwhile were run at ICP/ECP = 30/20. Exhaust oxygen levels at the 60/30 cam combination were observed to be beyond the practical limits for steady state operation of a three-way catalyst. A decision was therefore made to limit the concentration of oxygen in the exhaust to less than 3%. This was achieved by reducing the valve overlap period by the minimum amount necessary, thus minimising the loss of performance that resulted from the reduced air mass flow at a given boost pressure. Figure 3.6 below shows the differences between the two cam timing combinations graphically using “rose” plots, highlighting the difference in valve overlap period.

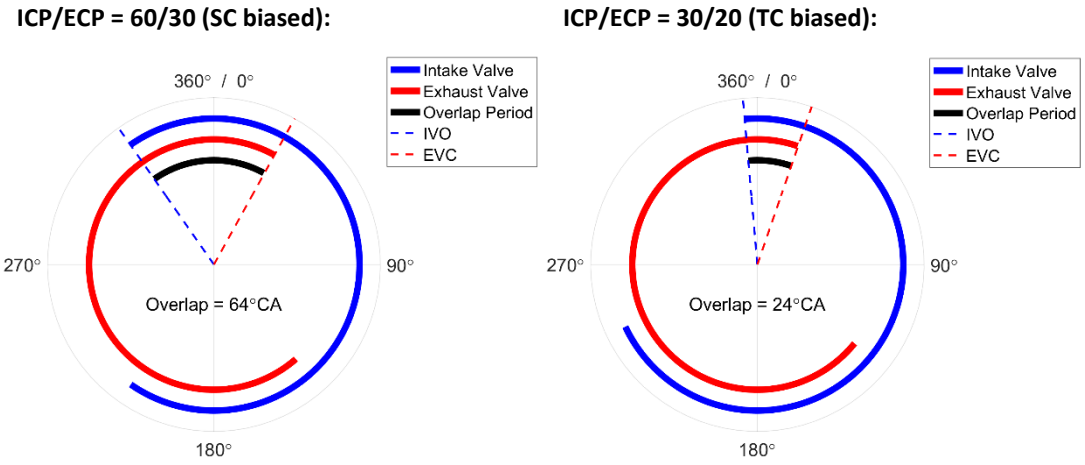

Figure 3.6 – Rose plots of the two cam-timing combinations investigated in this work.

3.5 Experimental Results

3.5.1 Effects of Load on Knock

In Figure 3.7 below, IMEP is plotted against the angle of 50% mass fraction burned (referred to henceforth as CA50 or combustion phasing) for the boost ramp data collected at the 3500rpm, supercharger-biased engine configuration. Immediately apparent is that as intake manifold pressure was increased, the duration of the spark sweeps became shorter. This behaviour occurred because the increased propensity to knock at higher pressures limited the amount of spark advance that could be applied, and the hotter exhaust gas temperatures (EGTs) at higher loads limited the amount of spark retard that could be applied. Safe engine operation at IMEPs greater than 35 bar would not have been possible at this engine configuration since any further increases in boost pressure would have caused the knock limit and EGT limit to coincide with one another. This configuration has been used as an example, however similar observations could be drawn from the other three configurations, with the exception that at the 1500rpm configurations, spark retard was limited by IMEP CoV rather than EGT.

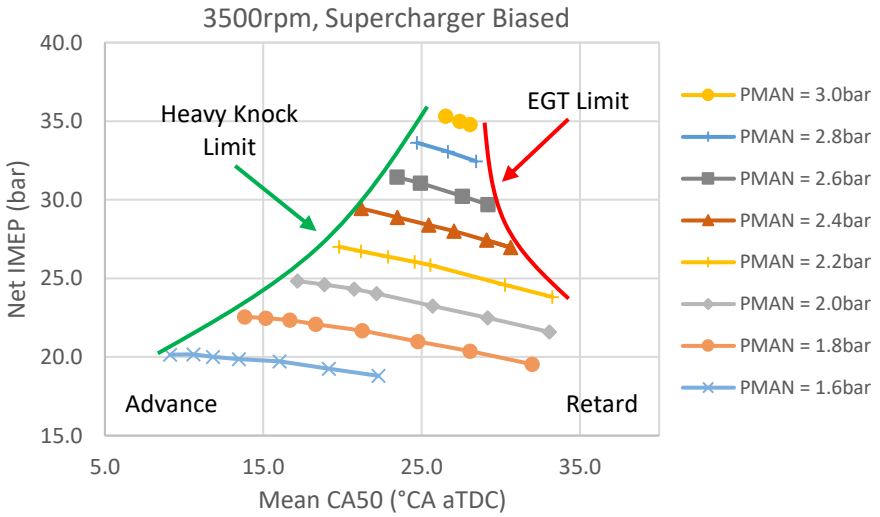

Figure 3.7 – Measured IMEP against angle of 50% mass fraction burned (CA50) for the 3500rpm, supercharger biased engine configuration

Figure 3.8 meanwhile plots the corresponding mean knock intensity data gathered from the same 3500rpm, supercharger-biased engine configuration. Knock intensity has been defined in this case as the maximum amplitude pressure oscillation (MAPO)[7]. One can see from this

[7] The various knock intensity metrics are discussed in detail in Chapter 4.

figure that as the spark timing (and combustion phasing) was advanced from a retarded position, the mean knock intensity increased in a linear, gradual manner. At a certain combustion phasing, the rate of change in knock intensity with respect to combustion phasing increased rapidly. This point typically coincides with the audible knock limit as the intensity of the heaviest knock events becomes sufficiently loud for the human ear to detect. The inflection point in this relationship was therefore defined as the knock limited spark advance (KLSA), or in this case, the knock limited combustion phasing.

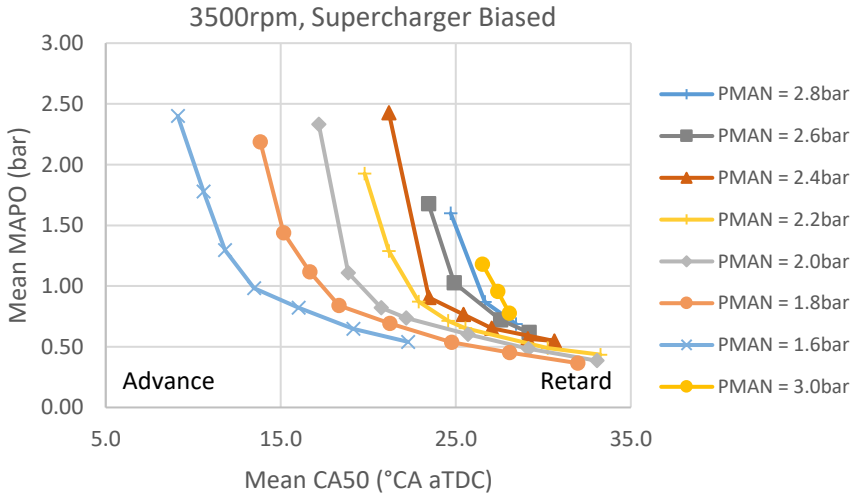

Figure 3.8 – Measured knock intensity (defined using the MAPO metric) against angle of 50% mass fraction burned (CA50) for the 3500rpm, supercharger biased engine configuration

The boost ramp data collected at the KLSA for each of the four engine configurations is summarised in Figure 3.9. Across all configurations, the KLSA became more retarded as intake manifold pressure was increased (see panel "a"). This behaviour was due to the increased propensity of air/fuel mixtures to autoignite at higher pressures, and was compounded by the hotter end gas temperatures during combustion at higher loads. All four configurations saw the KLSA retard by nominally the same rate (~0.75°CA per 0.1 bar PMAN) over the intake manifold pressure range plotted, however the KLSA values themselves were different between configurations. Interestingly, only engine speed was observed to have an impact of the achievable knock limited combustion phasing at a given intake manifold pressure, suggesting that the combustion duration at the turbocharger-biased configuration must have been longer than that observed at the supercharger-biased configuration. This hypothesis is confirmed within panel "d" of Figure 3.9 where combustion duration (defined here as the crank angle period between 10% and 90% mass fraction burned) at the KLSA is

plotted. The longer combustion durations under turbocharger-biased conditions were likely caused by the substantially increased residual gas fraction relative to the supercharger-biased configuration. This was a product of less favourable conditions for scavenging of residual gases due to a shorter valve overlap period and a smaller pressure difference between intake and exhaust manifold pressures. The difference in exhaust manifold pressure models is illustrated in panel “e”, where the influence of exhaust manifold pressure on combustion duration can be seen, with very similar trends observed for both parameters.

Panel “c” plots the IMEP achieved at the KLSA for each engine configuration. It is interesting to note the difference in performance between the supercharger-biased configuration and the turbocharger-biased configuration, with the latter producing much lower IMEPs for a given intake manifold pressure. This observation is primarily due to the difference in IVC between the two configuration, with the IVC applied to the turbocharger-biased configuration being 30°CA later, resulting in lower trapped mass of air per cycle. It is possible to infer from this figure that at nominally constant IMEP, the reduced effective compression ratio and higher internal EGR rates combine to provide a slight KLSA benefit. However, this benefit does not extend to combustion phasing, with the turbocharger-biased configuration resulting in considerably later CA50 at nominally constant IMEP. This could be attributable to the effect of hot exhaust gas residuals effectively reducing flame speed but at the same time, increasing the engines propensity to knock.

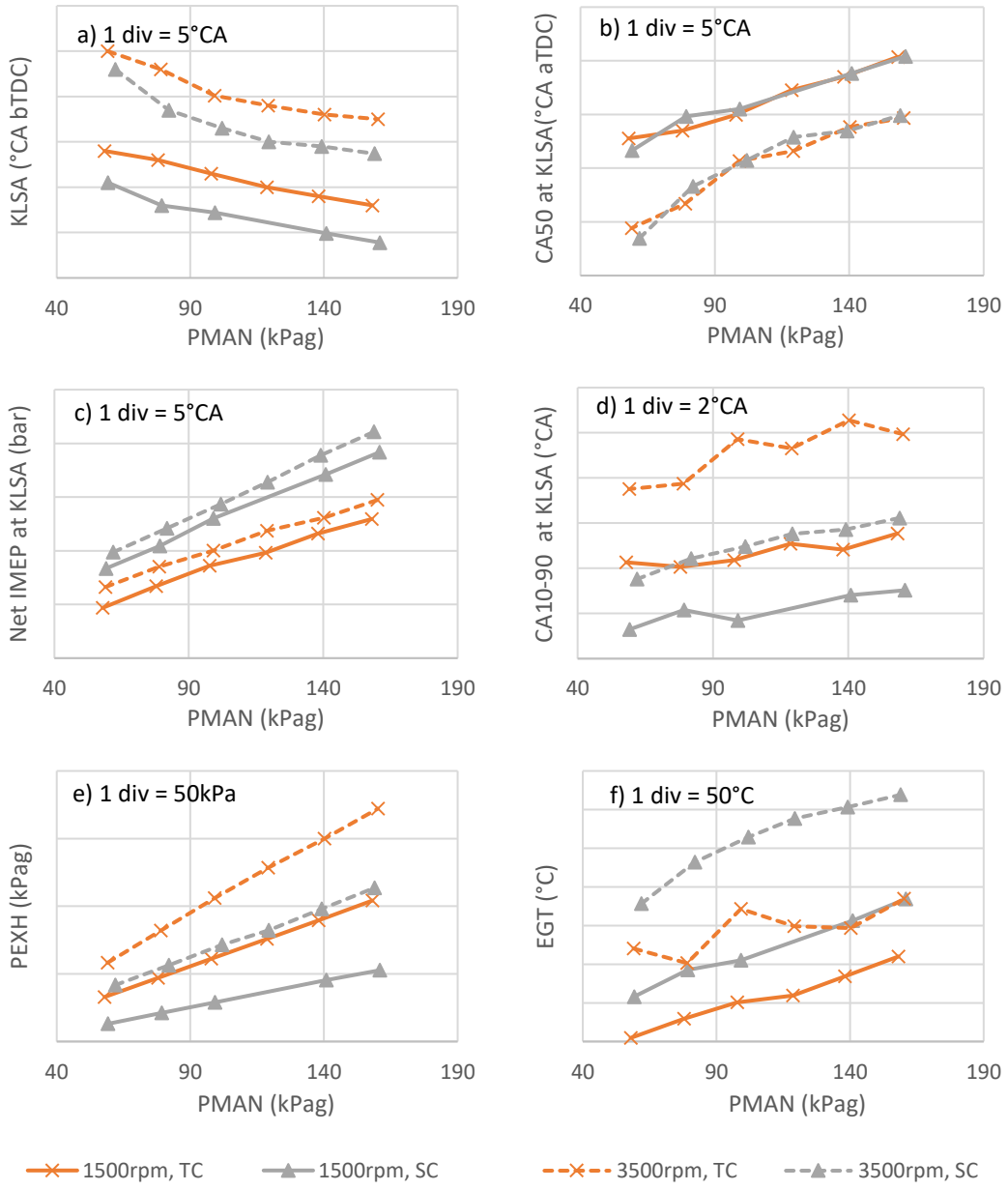

Figure 3.9 – Spark advance, combustion phasing (CA50), IMEP, combustion duration (CA10-90), exhaust manifold pressure (PEXH) and exhaust gas temperature (EGT) at the KLSA, all plotted against intake manifold pressure for the four engine configurations tested.

Finally, panel "f" plots exhaust gas temperatures measured at the exhaust manifold exit. The hottest temperatures at a given intake manifold pressure were measured under the supercharger-biased configuration at 3500rpm. It is possible that that this observation is a result of the highest power being observed at this condition, however the differences in IMEP and combustion phasing between this configuration and the turbocharger-biased

configuration at the same speed are not that significant. It therefore seems unusual that such a large temperature difference was observed between the two 3500rpm configurations.

3.5.2 Effects of EGR on Knock

Figure 3.10 shows that at higher EGR rates, the knock limited combustion phasing was more advanced. Admittedly, some of this advance is attributable to the decrease in load observed as EGR rate was increased since no reboosting was performed here to account for the loss in airflow at higher EGR rates.

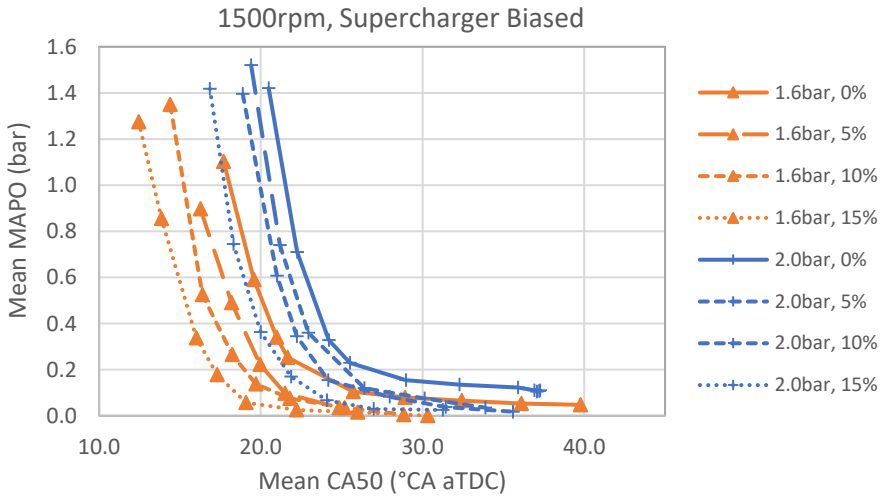

Figure 3.10 – Effect of EGR on knock intensity as ignition timing was varied at the 1500rpm, supercharger-biased engine configuration

Numerous investigations have observed similar behaviour to that presented above, reporting that the benefits of EGR with respect to extending knock limits are primarily two-fold. Firstly, the additional mass at constant load acts as a heat sink, lowering peak temperatures during combustion and therefore slowing the chemical reactions that take place in the end-gas prior to autoignition. Secondly, the higher Cp of EGR + air/fuel mixtures also acts as a heat sink, achieving the same benefits described above [26, 60, 80]. Although secondary to the thermal effects highlighted above, the presence of NO within recirculated exhaust gas can also impart a chemical effect on the autoignition process. Roberts observed that for fuels that exhibit a strong level of NTC behaviour, the presence of NO in the recirculated exhaust gas serves to suppress autoignition, whilst for fuels that exhibit no NTC behaviour, the opposite is true [81].

Figure 3.11 summarises the EGR sweep data collected at the KLSA for the 1500rpm, supercharger-biased engine configuration. Plot “a” shows that at higher EGR rates, it was possible to advance the spark timing further before reaching the KLSA. As discussed above, some of this added advance will have been due to the reduction in load at higher EGR rates caused by running these tests at constant intake manifold pressure rather than constant load. Plot “c” highlights this point, showing that at each manifold pressure setting, the net IMEP reduced by 2-3 bar. The rate at which IMEP reduced with respect to EGR rate was surprisingly non-linear. The largest reduction in IMEP occurred between 0% and 5% EGR, with similar reductions observed between 10% and 15% at intake manifold pressures of 1.8 and 2.0 bar. Intake and exhaust manifold pressures were held firmly constant throughout each EGR sweep, therefore the reasons for this non-linearity are unclear.

Figure 3.11, Plot “b” suggests that on balance, the knock limited combustion phasing advanced as EGR rate was increased at fixed manifold pressure. It is unclear why the opposite was observed at 1.6 bar intake manifold pressure between 0% and 5% EGR. One possible explanation is that the recirculated exhaust gas failed to mix adequately with the air delivered by the FIS before the mixture reached the cylinders. At conditions of relatively low air mass flow (such as in this case), the required EGR pump speeds were relatively low. If adequate mixing was not achieved, it is possible that EGR was delivered to the engine in “slugs” at these conditions. Evidence to support this theory is provided in Plot “g” where there was a sharp increase in IMEP CoV when transitioning from 0% to 5% EGR. Thereafter, the IMEP CoV actually decreased as EGR rate was increased – a result that would seem to contradict many of the published articles concerning the effects of EGR on combustion stability. Following this experiment, recommendations were made to mitigate the possible pulsing effect of the EGR pump by bypassing most of the cooled EGR flow straight to the exhaust extraction system in the test cell. This way, the pump could be operated at a constant high speed and the EGR flow to the engine controlled using the bypass valve. This is not expected to have impacted subsequent modelling work carried out in this investigation since EGR was only simulated at higher loads and EGR rates.

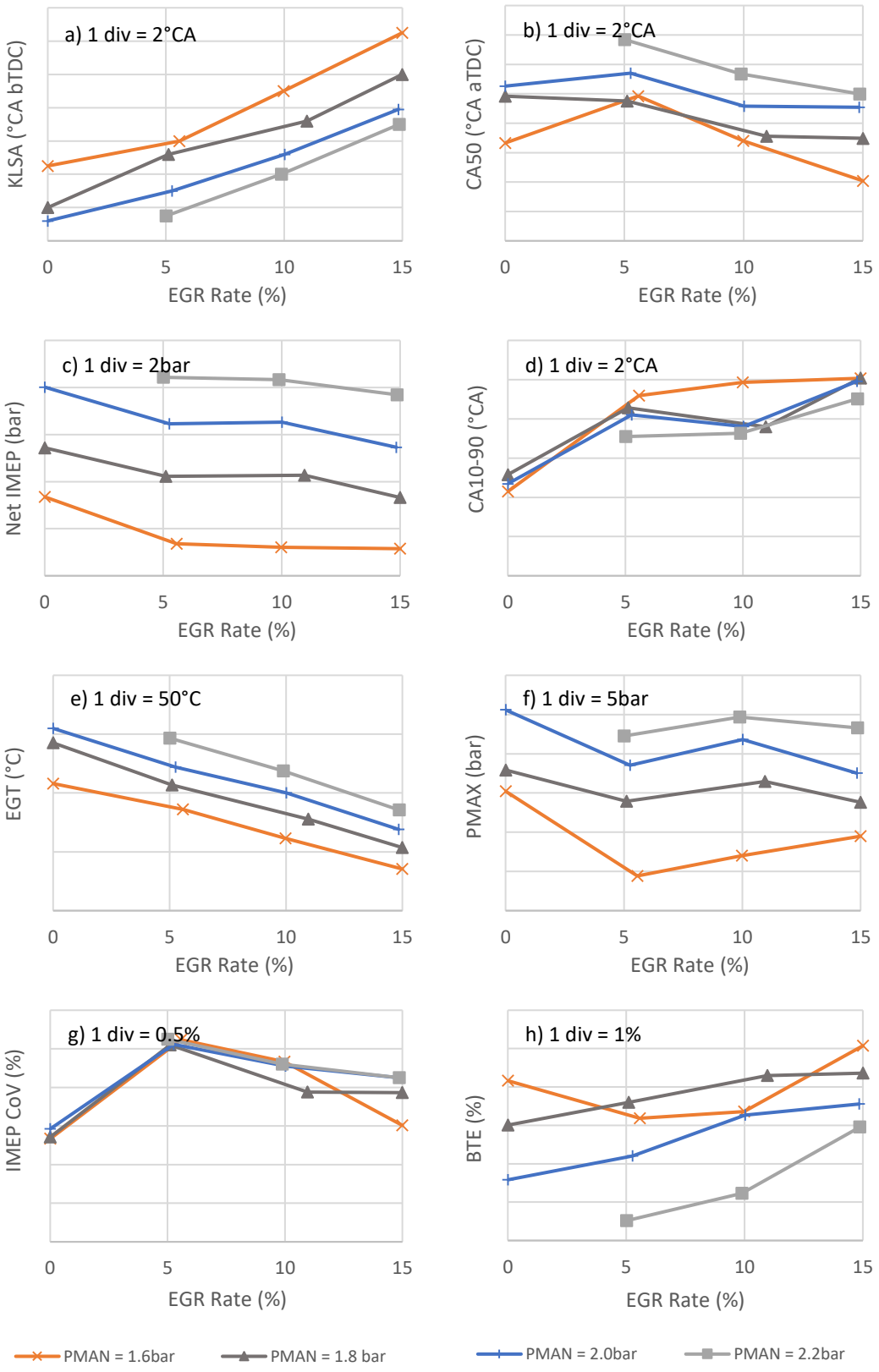

Figure 3.11 – Spark advance, combustion phasing (CA50), IMEP, combustion duration (CA10-90), exhaust gas temperature (EGT), maximum cylinder pressure (PMAX), IMEP CoV and brake thermal efficiency (BTE) at the KLSA, all plotted against EGR rate for the 1500rpm, supercharger biased engine configuration.

Figure 3.11, Plot “b” shows that as expected, increasing EGR rate led to an increase in combustion duration. The 10% and 90% mass fraction burned angles were derived directly from measured cylinder pressure data using the first law thermodynamic approach within Indicom (the proprietary AVL software used to configure and control the Indiset data acquisition system). This approach assumed a fixed value for the ratio of specific heats, γ = 1.30 over the whole four-stroke cycle.

Figure 3.11, Plot “e” shows that exhaust gas temperatures decreased as EGR rate increased at a given intake manifold pressure. Again, this result is not a surprise given the aforementioned heat sink effects of EGR, as well as the fact that constant load was not maintained as EGR rate was varied. Figure 3.11, Plot “f” meanwhile shows that on balance, maximum cylinder pressure decreased as EGR rate increased at a given intake manifold pressure. Since load effectively decreased as EGR rate increased, this result was expected, however the observed trends are somewhat inconsistent. Previous investigations at constant load have shown that maximum cylinder pressure at the knock limit can in fact increase as EGR rate is increased due to the improved overall combustion phasing [26].

Finally, Figure 3.11, Plot “h” shows that brake thermal efficiency increased as EGR rate increased at a given intake manifold pressure. Some of this improvement would be attributable to reduced heat losses from lower gas temperatures. In addition, the higher γ at higher EGR rates would have had a beneficial thermodynamic effect on efficiency.

3.6 Conclusions

Overall, these results show that the four engine configurations investigated in this chapter provided a sound base from which the knocking combustion behaviours of the experimental engine could be investigated. The experimental engine also proved to be a capable platform for investigating knock at very high BMEPs, achieving a maximum net IMEP of approximately 35bar at 3500rpm, 3.0bar intake manifold pressure. The experimental data was found to be of sufficient quality, agreeing with the expected trends and with data published in the literature. The only inconsistent results appear to stem from the pulsed nature with which the EGR pump delivered cooled exhaust gas to the engine. At lower speeds and loads (i.e. where air mass flow was relatively low), it is possible that the slow rotational speed of the pump at low EGR rates may have resulted in poor mixing of the cooled exhaust gas and fresh air before the mixture reached the engine. From this observation, recommendations have been made to improve the EGR pump design. The operating conditions that could have been most affected by this phenomenon have also been eliminated from consideration in the simulation work carried out in the following chapters.

Chapter 4 – Knocking Cycle Detection and Angle of Knock Onset Estimation

Chapter Summary

This chapter details the work carried out to determine the most appropriate methods of knocking cycle detection and angle of knock onset estimation from measured cylinder pressure data at high engine loads. These tasks are important prerequisites to assessing the predictive capabilities of ignition delay correlations as they provide the reference with which to compare model predictions. After introducing a wide variety of knock intensity metrics, a shortlist of four metrics is formulated. These metrics are combined with three knock intensity threshold calibration methods, resulting in twelve knock intensity metric/threshold calibration method combinations to test. The knock detection capabilities of these twelve metric/calibration method pairs are evaluated by comparing their output against manual classifications made by the author across a range of engine operating conditions. Finally, ten unique angle of knock onset estimation methods are introduced and their performance evaluated (again using manually derived angle of knock onset estimates from a range of engine operating conditions). The best performing knocking cycle detection and angle of knock onset estimation methods are identified.

4.1 Introduction

One of the principle aims of this investigation is to assess the accuracy of current ignition delay correlations (IDCs) at high engine loads. The performance of IDCs is typically evaluated using two key attributes – the accuracy with which they are able to separate knocking and non-knocking cycles, and the accuracy with which they are able to predict the angle of knock onset (aKO) for knocking cycles. These two attributes are assessed by comparing model predictions with experimental data. To enable this comparison, it is necessary to be able to extract the relevant data from experimental measurements with a high degree of accuracy. To this end, several knock detection and knock onset estimation methods have been investigated with the aim of identifying the best approaches to each problem. The results from each method have been compared against samples of experimental data for which the author a) manually classified cycles as either knocking or non-knocking and b) manually estimated aKO for those cycles classed as knocking.

4.2 Knocking Cycle Detection Methods

4.2.1 Signal Types Used

Traditionally, knock detection and KLSA determination is carried out by human operators who are attuned to the sound of knock being transmitted through an engine's structure. Although simple and inexpensive, this method of knock detection is highly subjective and open to bias. For a start, every operator is different. They will each have their own impression of what constitutes an acceptable level of knock, and hearing capabilities will vary from one individual to the next. Secondly, perception of sound level by the human ear can be influenced by a large number of factors. Higher levels of background noise at higher engine speeds for example mean that lighter knock events can be perceived as more intense at lower engine speeds. The sensitivity of human hearing with respect to pitch is also non-linear, peaking at around 3kHz and decreasing at different rates either side of this. As a result, noises of equal sound level but of different frequency are perceived to be at different intensities. In addition, the sensitivity of the human ear with respect to sound level is logarithmic, which negatively affects our ability to gauge sound level with a high degree of repeatability [82]. Finally, sound transmission to the operator can be affected by the

presence of any noise dampening material, their position relative to the engine, the engine design and the material that it is made from. These factors highlight the need for a more consistent, quantitative approach to knock detection.

In modern SI engines, online knock detection forms an important component of the engine management system. Its primary aim is to maintain an acceptably low level of knock without overly penalising engine efficiency. Fundamentally, this is achieved using a closed loop system which monitors knock intensity in real time and takes corrective action (typically spark retard) whenever the knock intensity limit is exceeded. To minimise any penalties to fuel economy and performance, the spark timing is then gradually advanced until the knock intensity limit is again exceeded. This cyclic process results in the saw-tooth spark timing pattern shown in Figure 4.1 below. Automatically managing the spark timing in this way allows the ECU to adapt the spark timing calibration to suit any change in the engine's propensity to knock (such as when a fuel with a markedly different AKI is used). This ensures near-best spark timing and engine thermal efficiency given the current external conditions (fuel quality, air temperature, etc.), without causing the engine to exhibit excessive knock.

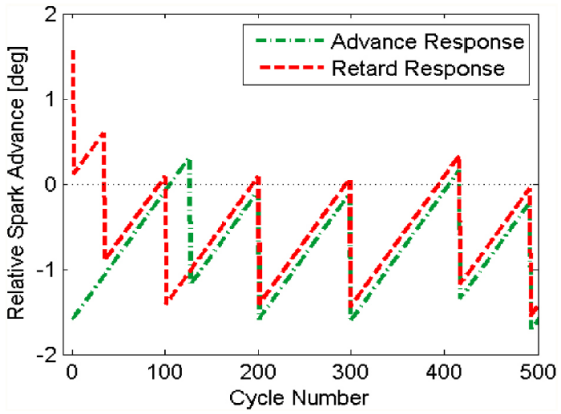

Figure 4.1 – Typical spark timing history for an active knock control system under overly advanced initial conditions (green) and overly retarded initial conditions (red) [83]

Closed loop knock detection relies on feedback to inform the ECU of the current knock level. A variety of signal types can be used to provide this feedback. In production engines, block mounted accelerometers measuring engine vibration are typically used due to their low cost and ease of installation. The measured vibration signals are processed by the ECU (in either the time or frequency domains) in an effort to isolate the vibrations transmitted into the engine structure from knocking pressure oscillations. This task is often complicated by

interference from a large number of additional mechanical vibration sources on an engine (particularly at high engine speeds), and also by the fact that an accelerometers response to these sources is highly dependent on its location on the block. Reliable knock detection across all cylinders and at all operating conditions usually requires several accelerometers, each mounted at carefully chosen locations around the block. To maximise the knock detection potential of accelerometer signals, consideration of the crank angle windows and frequency bands which correspond to knock in each cylinder is also important [84, 85].

Given that knock is an audible phenomenon, it is possible to detect knock using microphone signals. Although still affected by background noise and microphone position relative to the engine, the human factors which can cloud the assessment of knocking conditions can be replaced with quantitative analysis of the measured sound level. Several laboratory-based studies have shown that metrics designed to characterise the intensity of knock events derived from sound measurements taken close to the engine structure correlate well with those derived from other signal types (block vibrations and cylinder pressure for example) [82, 86]. With appropriate time alignment and data processing techniques, sound signals can be used to distinguish between knock in different cylinders on multi-cylinder engines and to estimate the crank angle of knock onset, all at relatively low cost.

Cylinder pressure measurement offers the most direct approach for knock detection since knocking combustion produces high frequency pressure oscillations inside the combustion chamber. Due to the high cost of piezo-electric pressure transducers and their associated electronics, cylinder pressure measurement is however exclusively limited to research and laboratory environments. These high costs are compounded by the fact that each sensor can only be used to measure the pressure in one cylinder, meaning that as many transducers as cylinders are usually required when testing multi-cylinder engines. Installation of pressure transducers is also a challenge since modifications to the cylinder head (which is already usually quite crowded) are required. Finally, heavy knock events (such as those resulting from PI) can irreversibly damage the piezo-electric crystal inside the sensor, rendering it useless.

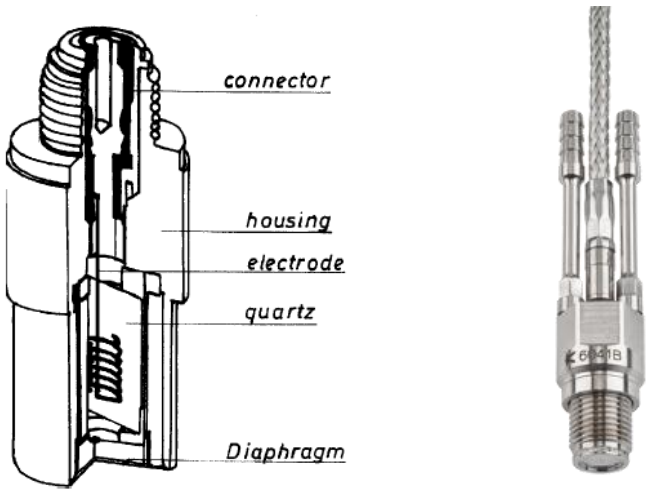

Figure 4.2 – Cross section view of an uncooled piezo-electric pressure transducer on the left [87], and a typical water-cooled pressure transducer with an M8 thread on the right [88]

Like block mounted accelerometers, careful consideration needs to be given to the location of pressure transducers within the combustion chamber. Installation along an acoustic node line for example will reduce the sensitivity of the transducer to any acoustic modes which share that node line [89, 90]. Centrally mounted transducers are therefore not recommended due to their inevitable proximity to all radial acoustic node lines [84]. Finally, consideration should also be given to the length of the connecting bore between the combustion chamber and the transducer diaphragm. Ideally, this length should be zero (i.e. the transducer should be flush mounted) to avoid the risk of interference between knocking pressure oscillations and those that result from acoustic resonance of the connecting bore itself [91]. Flush mounting does however increase the threat posed by thermal shock (where measurement errors arise due to mechanical deflection of the sensor diaphragm when exposed to high levels of heat flux from the flame front [92]). Water-cooled sensors with reduced susceptibility to thermal shock are available, however they are more expensive than uncooled transducers and often considerably larger which makes packaging within the cylinder head more difficult.

Ion current sensing offers a cheap alternative to cylinder pressure measurement whilst maintaining the ability to measure knock intensity directly on a cylinder by cylinder basis and with a good signal to noise ratio. It operates on the principle that combustion behaviour can be monitored by measuring changes in the electrical conductivity of the gases inside the combustion chamber. These changes are measured by applying a current bias to the

electrodes of the spark plug in each cylinder after the spark, effectively turning each spark plug into an in-cylinder combustion monitor. After the initial spark and flame front development, the ion current signal mirrors the characteristics of the cylinder pressure trace. The ion current signal can therefore be used to identify knocking combustion since the pressure oscillations generated by knock are mirrored by oscillations in the measured ion current (demonstrated in Figure 4.3 below). This characteristic has been utilised to develop production-level knock detection systems, several of which have seen use in high performance, low volume applications by mainstream vehicle manufacturers such as BMW, Mercedes and Ferrari. The additional cost of such a system versus a conventional accelerometer-based knock detection system is easily justified in such high cost, high performance applications where accurate knock detection is even more critical.

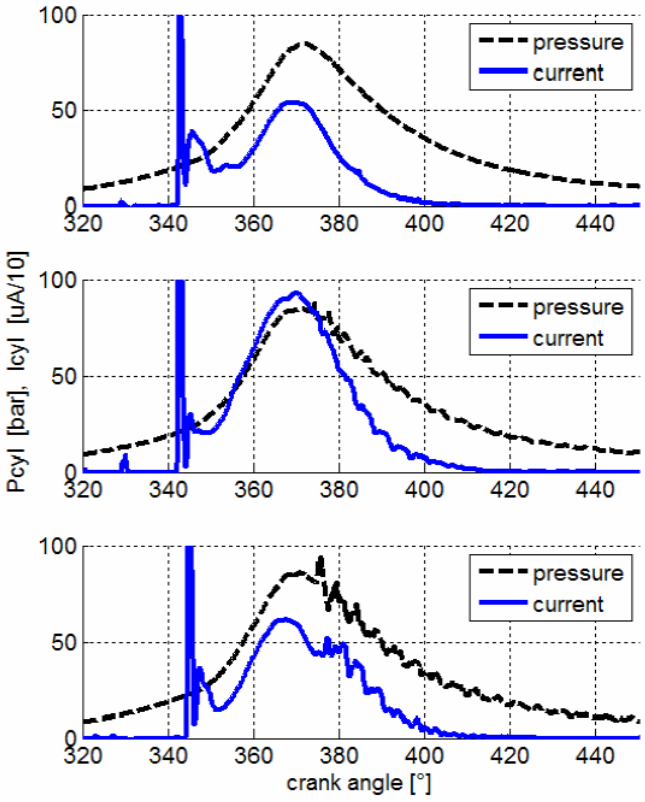

Figure 4.3 – Comparison of in-cylinder pressure and ion current traces for three different levels of knock (top = no knock, middle = light knock, bottom = heavy knock). Recorded on a 6.0 litre V12. [93]

The above paragraphs describe the most common methods used for online knock detection in both production and laboratory settings. One important approach omitted from discussion here is the use of optical-access engines and photographic equipment to capture visual information regarding flame front progression and the occurrence of knock. Typically used

for more fundamental combustion research than for the detection of knocking cycles, optical techniques can be credited with many of the most significant discoveries concerning the origins of knock in SI engines. A detailed review of the many optical combustion analysis techniques is beyond the scope of this investigation, however in the context of knock detection it is worth mentioning fibre optic probes. For knock detection, these sensors operate on the principle that the pressure oscillations associated with knock result in phase-aligned oscillations of the local light intensity measured through an optical fibre directed at the combustion chamber. The magnitude of the light intensity oscillations (representative of the magnitude of the density oscillations of the burned gas as the pressure waves pass though it) can therefore be used to identify knocking cycles in much the same way that the magnitude of pressure oscillations can [94, 95].

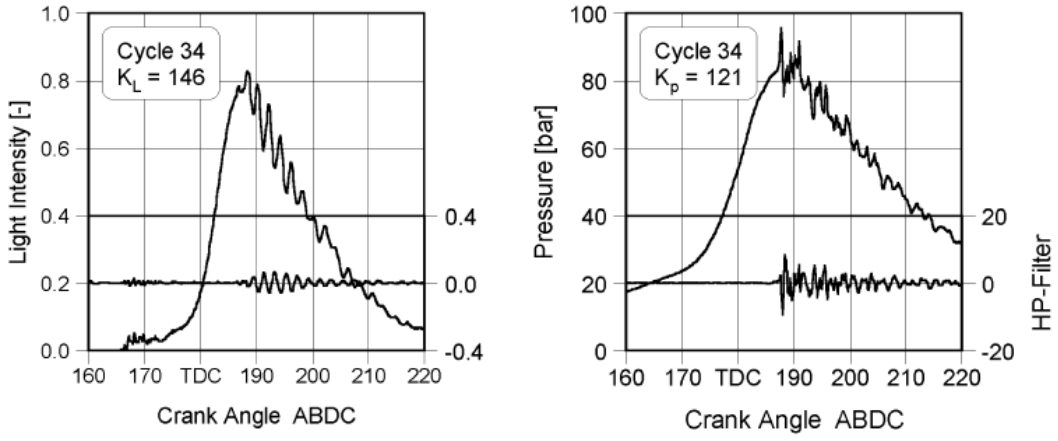

Figure 4.4 – Comparison of light intensity and cylinder pressure measurements recorded over a single knocking cycle in an Opel C20XE 4 cylinder SI engine. Light intensity was measured using a fibre optic spark plug sensor. [95]

An additional benefit of most optical fibre sensors is their ability to pinpoint the approximate location of the knock origin within the combustion chamber. This can be a particularly useful tool during the early stages of engine development as it can help to identify mixture preparation issues or hotspots within the combustion chamber, and it can help to evaluate the influence of charge motion on knock distribution [94, 96]. Thanks to their small size, up 80 optical fibres can be installed in a single sensor, providing a high degree of angular resolution for light intensity measurements. Specially modified spark plugs are usually used as the carrier for the optical fibres (see Figure 4.5 below), although stand-alone optical fibre sensors are available. Quantifying the phase differences between the light intensity

oscillations measured by each optical fibre makes it possible to map the trajectory of the initial pressure wave and identify which angular segment of the combustion chamber knock was likely to have originated from. The primary barriers to the widespread use of optical fibre spark plugs is their cost, contamination/dirtying of the optical fibres and the development of defects within the fibres themselves. In both latter cases, light transmission (and therefore sensor effectiveness) is reduced over time.

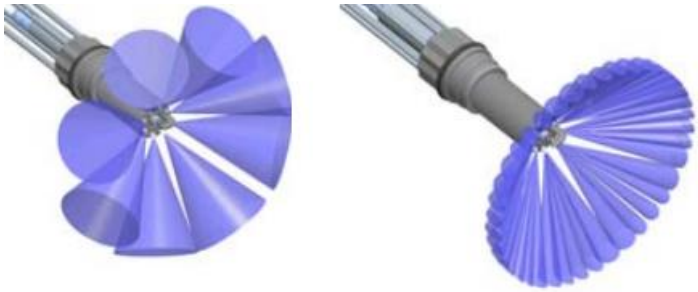

Figure 4.5 – Optical fibre spark plug sensors with 8 (left) and 40 (right) optical fibres installed around the head of a conventional spark plug [96]

Finally, several knock detection methods based on temperature measurement also exist. For example, exhaust gas temperature is known to drop during knocking combustion due to the relatively advanced combustion phasing exhibited by knocking cycles. A comparatively low mean exhaust port temperature for a given cycle would therefore indicate that that cylinder is knocking [97]. Similarly, the pressure oscillations which accompany knock have been shown to increase the heat flux into the surfaces of the combustion chamber. A comparatively high mean wall temperature measurement inside the combustion chamber would therefore also suggest a high level of knock [98]. These methods are not widely used however due to the challenges they pose with respect to identifying knock during transient engine operation. They are also unable to accurately identify the timing of onset of knock, and the instrumentation required (thin film/high response rate thermocouples) are both expensive and fragile.

4.2.2 Cylinder Pressure Based Knock Intensity Metrics

The quantification of knock intensity (KI) is a topic that receives regular review by researchers investigating the subject of knock. As a result, many methods exist for calculating the KI of a cycle and for separating knocking from non-knocking cycles. Unfortunately, no clear consensus has yet emerged as to which method is the most appropriate.

In general, KI metrics based on cylinder pressure fall into any of the following categories:

1) Frequency OR time domain
2) Pressure OR heat release based
3) Single value OR integral/mean value

The majority of time domain metrics are derived from the band-pass filtered cylinder pressure trace. The aim of filtering the data is to a) remove the low frequency component of the pressure trace and b) remove any interference from high frequency noise sources (such as that caused by mechanical resonance of the pressure transducer). The energy content of knocking pressure oscillations is predominantly contained within the lower order acoustic modes. For this reason, common band-pass filter limits are 4-5 kHz at the lower end and 30-40 kHz at the upper. Several time-domain metrics based on the low pass (sub 4 kHz) filtered pressure trace have been proposed, however support for their use within the literature is relatively limited.

Frequency domain metrics on the other hand are derived exclusively from the power spectral density (PSD) estimate of the pressure trace (either filtered or unfiltered). The PSD estimate is a type of Fourier transform and it describes how the power of the filtered pressure trace is distributed across the frequency spectrum.

The second category differentiates knock intensity metrics derived from cylinder pressure and those derived from rate of heat release (which is itself derived from cylinder pressure). Finally, the third category of KI metrics distinguishes between those that are based on single values, such as cycle maxima or minima, and those that are averaged or integrated over a predefined window (be that in the time or frequency domain).

Time Domain KI metrics (Pressure Based)

Considering pressure-based metrics first, knock intensity can be quantified using signals in either the time domain or the frequency domain. The most widely used time-domain metric is the maximum amplitude of the high/band-pass filtered pressure trace, known as MAPO (Maximum Amplitude Pressure Oscillation) or MATD (Maximum Amplitude Time Domain). This single value metric is intuitive and easy to calculate, but is susceptible to influence from signal noise and constructive interference between waves from the various acoustic modes of the combustion chamber [1]. It is calculated using Equation 4.1, where P_{BPF} is the band pass filtered cylinder pressure trace.

$$MAPO = \max\{P_{BPF}\} \qquad \textit{Equation 4.1}$$

Another commonly used time domain metric is the integral of the modulus of the band-pass filtered pressure trace, IMPO (Integral of the Modulus of Pressure Oscillations). IMPO is calculated by integrating the absolute values of the high/band-pass filtered cylinder pressure trace over the crank angle window Δθ from a starting crank angle of θ_0. It has the advantage of considering both the amplitude and time duration of the knocking pressure oscillations. Δθ can take values of 5-20°CA, whilst θ_0 typically corresponds to the approximate angle of knock onset. To limit the dependence of IMPO on Δθ, one can divide IMPO by Δθ, resulting in a metric called AMPO (Average Modulus of Pressure Oscillations). Similarly, to limit any bias that might be introduced as a result of the aKO estimation process, one can calculate IMPO across a broad range of θ_0 values and simply use the maximum value to describe the KI of a given cycle [1]. This approach does however add considerable computational expense to the determination of IMPO/AMPO.

The signal energy of pressure oscillations (SEPO) can be calculated using the same approach as that described for IMPO, only the square of the filtered pressure trace is used rather than to the modulus. Once again, dividing by Δθ limits the influence of the integration window length, and results in a metric called AEPO (Average Energy of the Pressure Oscillations).

$$IMPO = \int_{\theta_0}^{\theta_0 + \Delta\theta} abs\,(P_{BPF})\; d\theta \qquad \textit{Equation 4.2}$$

$$AMPO = \frac{IMPO}{\Delta\theta} \quad \text{Equation 4.3}$$

$$SEPO = \int_{\theta_0}^{\theta_0 + \Delta\theta} (P_{BPF})^2 \, d\theta \quad \text{Equation 4.4}$$

$$AEPO = \frac{SEPO}{\Delta\theta} \quad \text{Equation 4.5}$$

Component failures attributed to knock often occur as a result of fatigue caused by the cyclic nature of the strains exerted by knocking pressure oscillations. By integrating the amplitude of the pressure oscillations over time, IMPO and SEPO capture an element of the fatigue-inducing characteristics of a knock event. Furthermore, because they are calculated over a broad crank angle window, IMPO and SEPO should be relatively insensitive to the odd noise spike or constructive interference event.

Figure 4.6 plots MAPO against AMPO and AEPO using experimental data collected from the experimental engine under heavy knock at 1500rpm, 17bar BMEP. Good correlations have been achieved in both cases by assuming linear and quadratic correlations for AMPO and AEPO respectively. Similarly good correlations have been observed at higher loads and higher engine speeds. Given the strong linear relationship between MAPO and AMPO, it is unlikely that one of these metrics would offer much advantage over the other with respect to knock detection. The quadratic relationship between MAPO and AEPO meanwhile indicates that AEPO might offer improved differentiation between knocking and non-knocking cycles.

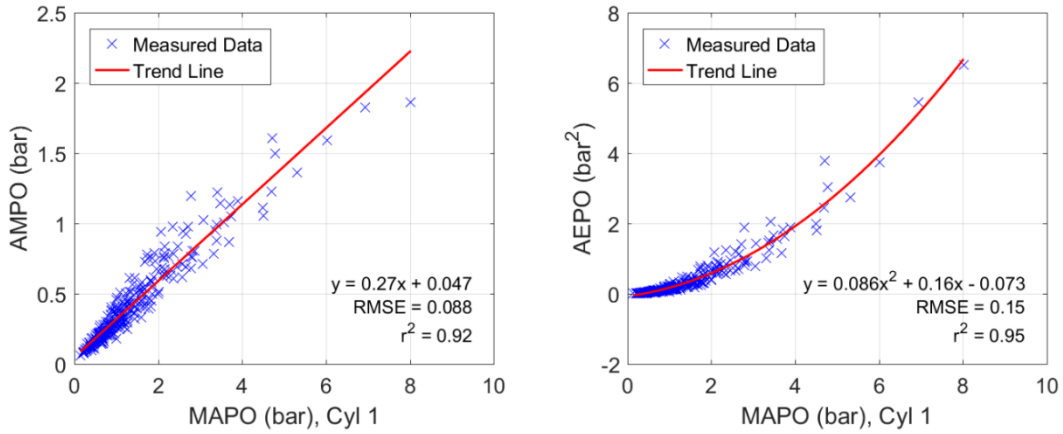

Figure 4.6 – MAPO plotted against AMPO and AEPO using experimental data from the experimental engine running under heavy knock at 1500rpm/17bar BMEP. Similar trends were observed across a range of speeds and loads up to 3500rpm/28bar BMEP.

Time-domain KI metrics have also been devised using derivatives of the cylinder pressure trace. Checkel [99] for example proposed a metric based on the minimum value of the third derivative of the low pass filtered pressure trace (P_{LPF}). Although less intuitive as an indicator of knock intensity, the magnitude of this metric was reported to correlate well with MAPO in a subsequent study [100], and the location of its minimum value provides an estimate of the aKO for any given cycle. Ferraro [101] meanwhile proposed a metric similar to IMPO except that the integration is performed over the first derivative of the band-pass filtered pressure trace.

$$KI_{Checkel} = \min\left(\frac{d^3 P_{LPF}}{d\theta^3}\right) \qquad \textit{Equation 4.6}$$

$$KI_{Ferraro} = \int_{\theta_0}^{\theta_0 + \Delta\theta} abs\left(\frac{dP_{BPF}}{d\theta}\right) d\theta \qquad \textit{Equation 4.7}$$

Checkel and Ferraro KI metrics are plotted against MAPO in Figure 4.7 using the same experimental data as that presented in Figure 4.6. $KI_{Checkel}$ exhibits a relatively poor correlation with MAPO, achieving an r^2 value of just 0.5. $KI_{Ferraro}$ meanwhile exhibits a strong linear correlation with MAPO, despite their very different formulations.

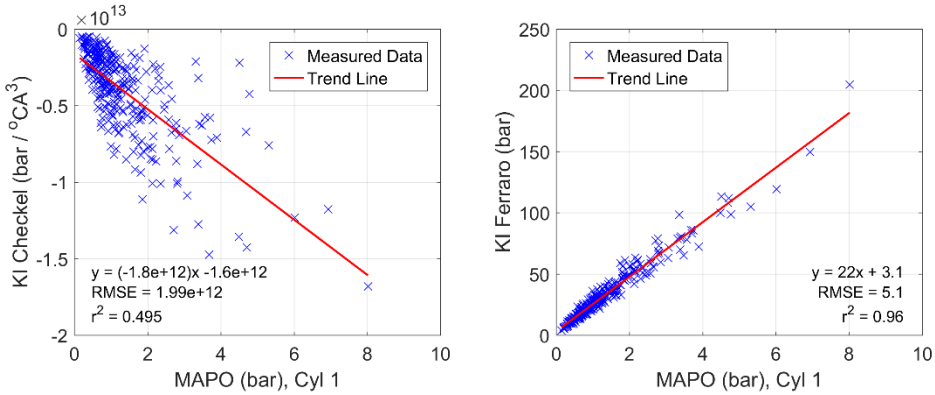

Figure 4.7 – MAPO plotted against Checkel (left) and Ferraro (right) KI metrics using experimental data from the experimental engine running under heavy knock at 1500rpm/17bar BMEP. Similar trends were observed across a range of speeds and loads up to 3500rpm/28bar BMEP.

In the field of HCCI knock, a time domain metric called ringing intensity (RI) is often used to quantify knock intensity. RI is defined by an empirical correlation proposed by Eng [102], which relates the amplitude of knocking pressure oscillations in HCCI engines to the maximum value of the first derivative of the low-pass filtered pressure trace. The correlation is based on Equation 4.8, which defines the power of a single-frequency harmonic wave per unit area (the acoustic intensity, I) at pressure P, temperature T and ratio of specific heats γ. ΔP is the amplitude of the harmonic wave. For a signal that is composed of multiple harmonic waves, as is the case with knocking pressure oscillations, the overall intensity is equal to the sum of the individual intensities of each harmonic present (see Equation 4.9).

$$I = \frac{1}{2\gamma} \cdot \frac{(\Delta P)^2}{P} \cdot \sqrt{\gamma R T} \qquad \textit{Equation 4.8}$$

$$I_{Total} = \sum_{i=1}^{n} I_i \qquad \textit{Equation 4.9}$$

From experimental data collected on a single cylinder research engine, Eng observed that the MAPO of HCCI knock was linearly proportional to the low pass filtered peak pressure rise rate ($PPRR_{LPF}$) with a coefficient of proportionality β = 0.05. Since HCCI knock occurs near TDC, movement of the piston could be ignored at the time of knock and gas temperature and pressure could be approximated using the cycle maxima. From these assumptions, Eng adapted Equation 4.8 to produce the overall expression for RI as defined by Equation 4.10. The primary advantage of this metric is that it allows the severity of knock to be predicted by simple zero-dimensional combustion models. These models lack the ability to resolve

pressure wave behaviour inside the combustion chamber, so in order to predict KI they rely on empirical sub-models. RI values between 2 – 6 MW/m^2 have been used within the literature to define the knock limit for HCCI engines [103].

$$RI \approx \frac{1}{2\gamma} \cdot \frac{\left(\beta \frac{dP}{dt}_{max}\right)^2}{P_{max}} \cdot \sqrt{\gamma R T_{max}} \qquad \textit{Equation 4.10}$$

Equation 4.10 specifically relates the pressure rise rate due to AI to the amplitude of the ensuing pressure oscillations in HCCI engines. For this approach to be applicable to SI engines, the $PPRR_{LPF}$ of a knocking cycle should be attributable to AI and not to normal flame front propagation (since the latter is not directly responsible for producing knocking pressure oscillations). Provisional analysis of measured cylinder pressure data recorded under knocking conditions on the experimental engine suggests that $PPRR_{LPF}$ exhibits no correlation with MAPO (see Figure 4.8). From Figure 4.9 it is also apparent that for the majority of cycles, the angle of $PPRR_{LPF}$ typically occurs over 5°CA before the angle of MAPO. If the appearance of knock were directly attributable to $PPRR_{LPF}$, one would expect this difference in crank angles to be much smaller (in the order of 0 – 2°CA). It has been assumed at this point that aMAPO is a good approximation for the angle of auto-ignition onset since pressure oscillations decay relatively quickly after aKO. This data suggests that for SI engines, the $PPRR_{LPF}$ is predominantly a result of the main flame front propagation and not of AI events late in the cycle. It is therefore not recommended that RI be used as a knock intensity metric for SI engines.

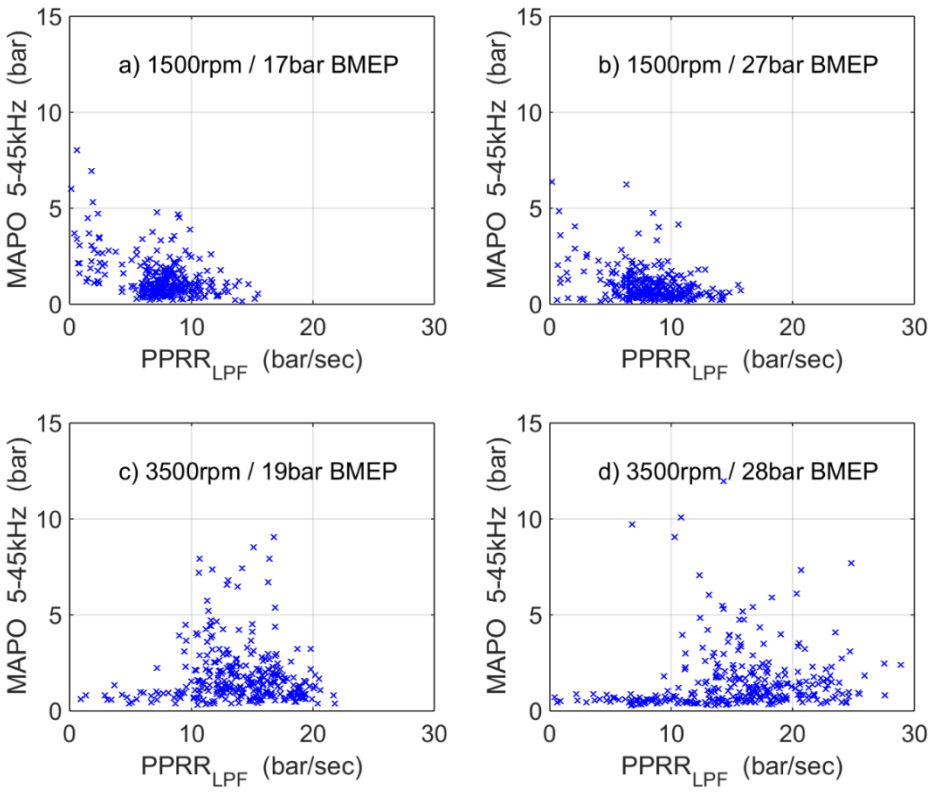

Figure 4.8 – PPRR$_{LPF}$ vs MAPO (5-45 kHz band pass filtered) for 300 consecutive cycles recorded from one cylinder of the experimental engine at a range of heavy knock operating conditions.

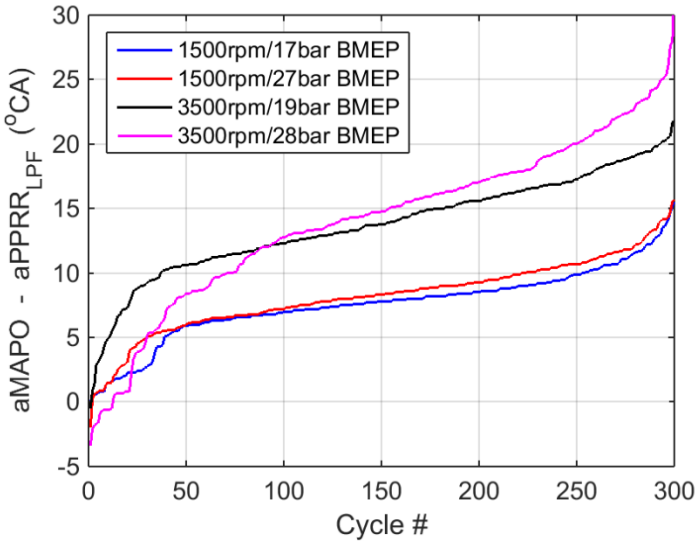

Figure 4.9 – Difference between angle of MAPO (approximated here as the angle of AI onset for SI engines) and angle of PPRR$_{LPF}$. Data collected from the experimental engine operating under heavy knock (i.e. where most cycles were knocking) across a range of EOCs.

Several studies have investigated using combinations of the time-domain metrics described above in an effort to obtain an overall metric that is both dimensionless and insensitive to factors such as engine operating condition (EOC), signal type and measurement location. Typically, this is achieved by normalising KI values by the background noise level, or by a reference KI value as described by Equation 4.11. Lee [86] proposed that the mean of the lightest 5% of KI values observed at a particular EOC be used to estimate the background noise level at that EOC. A normalised KI value of three was claimed to be an effective threshold for knocking cycle detection across a range of operating conditions and KI metrics. The performance of this dimensionless knock threshold was also reported to be unaffected by sensor type and pressure transducer mounting location, although only block mounted accelerometers and in-cylinder pressure transducers were investigated, and only two pressure transducer mounting locations were evaluated. The effects of speed and load were also not investigated.

Siano [104] on the other hand suggested an approach whereby background noise was evaluated on a cycle-by-cycle basis. This method involved calculating a reference KI value over the 20°CA window at the end of the compression stroke, and normalising the actual KI value as described by Equation 4.11. Siano applied this approach to normalise MAPO. A fixed $MAPO_{norm}$ threshold of 27 was proposed for knocking cycle detection irrespective of engine speed and load, however no evidence was provided to support the accuracy or validity of this approach.

$$KI_{\ norm} = \frac{KI}{KI_{ref}} \qquad \textit{Equation 4.11}$$

Finally, Brecq [105] proposed the dimensionless knock indicator (DKI) given by Equation 4.12, where $\overline{IMPO}$ and $\overline{MAPO}$ are the log-averaged values of IMPO and MAPO respectively and Δθ is an arbitrary crank angle window length[8]. The value of this metric was found to be constant at non-knocking spark settings across a range of engine operating conditions, showing that it was insensitive to operating condition and background noise level. As spark was advanced into knock at each operating condition, the value of this metric decreased linearly. A simple threshold value equal to the noise level of this metric (minus a small delta

[8] It is unclear from [105] whether Δθ in Equation 4.12 is the same as that used to calculate IMPO. If that is the case however, Equation 4.12 would simplify to DKI = AMPO/MAPO.

to prevent false detection) was proposed as an effective method for determining the KLSA, however the effect of engine speed on this threshold was not investigated. No method of individual knocking cycle detection was proposed, however a threshold based on the background noise level would be easy to implement.

$$DKI = \frac{\overline{IMPO}}{\overline{MAPO} \times \Delta\theta} \qquad \text{Equation 4.12}$$

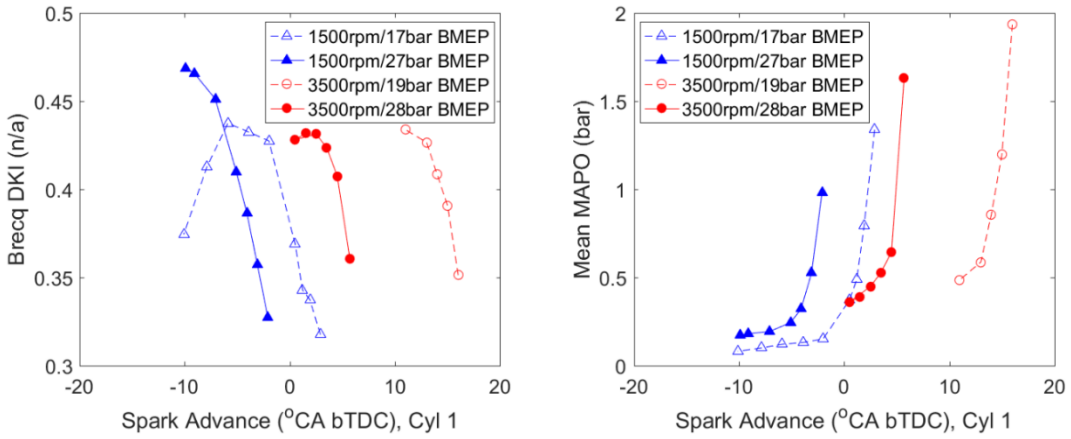

Figure 4.10 – Left: Brecq's dimensionless knock indicator (DKI) plotted using experimental data collected across a range of engine speeds and loads. Right: Mean MAPO values for comparison, from which approximate KLSA values can be derived.

Figure 4.10 shows DKI values calculated using experimental data from a range of engine speeds and loads. In contrast with Brecq's findings, DKI was not found to converge on a constant value under non-knocking conditions. Admittedly, the 3500rpm data shown in Figure 4.10 is not particularly appropriate for this evaluation because these spark sweeps were not retarded far enough into the non-knocking regime. As a result, it is unclear whether the DKI converges on a constant value under non-knocking conditions at higher speeds. The 1500rpm spark sweeps clearly were retarded into the non-knocking regime however, as indicated by the very flat progression of $\overline{MAPO}$ at retarded spark settings. At 1500rpm/17bar BMEP, the DKI does indeed level off as spark is retarded from the approximate KLSA of -2°CA. Retarding beyond -6°CA results in a sharp decrease in DKI values. From the limited data available at 3500rpm/28 bar BMEP, it would appear that a similar trend might have developed had the spark timing been retarded further. Interestingly, the peak DKI values observed for these two EOCs were very similar. Any hypothesis that there could be a ceiling on DKI values is swiftly rejected however by the data collected at 1500rpm/27bar BMEP.

Here, the DKI continues to rise steeply even as spark is retarded beyond the approximate KLSA of -6°CA, achieving values considerably higher than those observed at the other EOCs.

Time Domain KI Metrics (Heat Release Based)

Heat release based metrics are the final category of time-domain KI metrics discussed in this section. Neglecting the effects of heat transfer, heat release rate can be calculated using Equation 4.13 below (where γ is the ratio of specific heats, P and V are the cylinder pressure and volume respectively and θ refers to crank angle) [6]. It is clear from Equation 4.13 that heat release rate is dependent on cylinder pressure, therefore knock intensity metrics derived directly from heat release rate are unlikely to provide additional insight to those derived directly from cylinder pressure [1]. Having said that, the cumulative heat release trace can provide useful information regarding the fraction of the fresh charge burned (Mass Fraction Burned, MFB) by the time knock is initiated. Chun and Xiaofeng independently observed strong links between mean levels knock intensity and MFB at knock onset across a range of EOCs [106, 107]. An increase in mean knock intensity was linked to a decrease in the mass fraction burned at knock onset. Unfortunately, these correlations broke down when viewed on a cycle-by-cycle basis. They argue that this was primarily because the location of AI onset within the combustion chamber varies considerably cycle to cycle. This high degree of variability has a strong effect on the acoustic response of the cylinder, which in turn affects both the calculated KI and the estimated aKO. Clearly, this method also requires a reliable approach to estimating aKO (i.e. one that is consistent and independent of sensor type and installation).

$$\frac{dQ}{d\theta} = \frac{\gamma}{\gamma - 1} . P . \frac{dV}{d\theta} + \frac{1}{\gamma - 1} . V . \frac{dP}{d\theta} \qquad \textit{Equation 4.13}$$

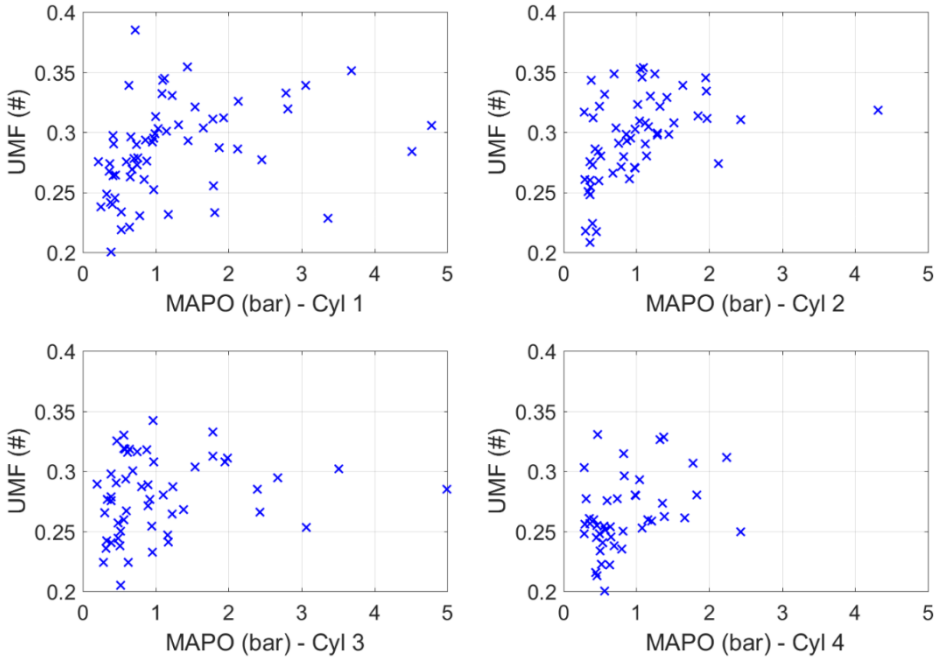

Figure 4.11 – Unburned mass fraction of fuel at the approximate aKO plotted against MAPO. Data from the experimental engine, collected at 1500rpm, 17bar BMEP.

Figure 4.11 tells a similar story to that reported by Chun and Xiaofeng. Unburned mass fraction (UMF = 1 – MFB) of fuel has been plotted against MAPO for manually identified knocking cycles obtained under heavy knock conditions. Unburned mass fraction of fuel at aKO was estimated by integrating the output of Equation 4.13 and normalising the resulting trace by the maximum value observed. aKO was estimated for each cycle manually using the process described in Section 3.4.3. It is clear from this figure that on an individual cycle basis, MFB at aKO does not correlate well with conventional KI metrics such as MAPO. This observation is in line with recently published results whereby the MFB at knock onset was found to depend on operating condition [108]. Interestingly, not a single cycle identified as knocking exhibited a UMF value at aKO less than 0.2, suggesting that for the EOC considered in Figure 4.11, knock only occurred if auto-ignition was triggered before 80% of the fuel was burned. This figure of 80% should be taken with a large pinch of salt however since the UMF at aKO is very sensitive to assumptions regarding the ratio of specific heats (γ) and how the end of combustion is defined. Elmqvist observed that knock did not occur later than 93% fuel mass fraction burned for a 2.0 litre 4-cylinder turbocharged SI engine across a range of AFRs at 3000rpm [59].

Frequency Domain KI Metrics

Moving on to frequency domain KI metrics, converting from the time domain to the frequency domain is achieved by determining the Power Spectral Density (PSD) estimate of a signal. The PSD estimate is a type of Fourier transform. It describes how the power of a signal with finite length is distributed across the frequency spectrum. To reduce spectral leakage in the Fourier transform output, the signal is windowed prior to estimating its PSD. Windowing affects the amplitude of the signal across all but its central portion. When applied to the study of knock, it is important to minimise the degree of attenuation applied by the window to the knocking pressure oscillations. This is achieved by centring the window on the angle of knock onset (the angle of maximum cylinder pressure is normally used as a good approximation). Finally, the signal is also typically band pass filtered over the frequency range of interest prior to estimating the PSD. This is done to remove the low frequency component of the pressure trace as well as any high frequency aliasing/pressure transducer resonance that may be present in the original signal. With regards to knock in conventional SI engines, this frequency range is approximately 5 kHz to 40 kHz [109].

$$AEFD = \int_{f1}^{f2} \wp(f)\, df \qquad \text{Equation 4.14}$$

$$MAFD = \max(\wp(f)) \qquad \text{Equation 4.15}$$

The two most commonly used frequency domain metrics derived from the PSD are AEFD (Average Energy of the Frequency Domain) and MAFD (Maximum Amplitude of the Frequency Domain). These metrics are defined by Equation 4.14 and Equation 4.15 respectively, where $\wp$ is the PSD of the band-pass filtered cylinder pressure trace. PSD output is expressed in units of energy per unit frequency (i.e. signal magnitude squared per Hz) which as previously highlighted, is linearly additive across any frequency range (see Equation 4.9). The average energy of a signal in the range $f_1 < f < f_2$ can therefore be expressed as the integral of the power spectrum, $\wp(f)$ over this frequency range. Parseval's theorem states that the energy content of a signal in the time domain should be equal to that derived from the frequency domain, assuming that both are calculated over the same frequency range. If the integration limits of AEPO are extended to cover the entire length of the signal for which the PSD estimate was derived, then the values of AEPO and AEFD derived for the same cycle should be nominally equal. This theory has been tested in Figure 4.12 below using a sample of data collected from the experimental engine at 1500rpm, 17bar BMEP. The excellent

correlation between AEPO and AEFD indicates that the appropriate precautions have been taken in the processing of both the time and frequency domain data. More detail on the specific methods used to derive AEPO and AEFD are provided in Section 4.4.2 of this chapter.

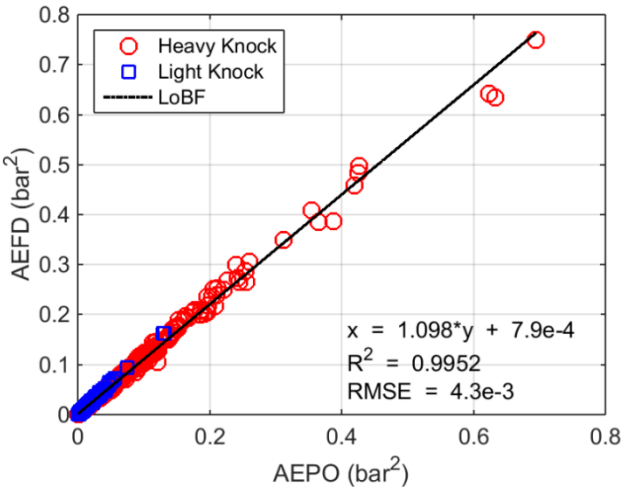

Figure 4.12 – AEPO (calculated over the entire band-pass filtered pressure trace) vs AEFD for heavy and light knock (collected from the experimental engine at 1500rpm, 17bar BMEP).

The right panel of Figure 4.13 shows that MAPO and MAFD display a modest positive linear correlation (evaluated using experimental data again collected at 1500rpm, 17bar BMEP using the experimental engine). A large spread of MAFD values occurs at any given MAPO value, suggesting that these two KI metrics would likely perform very differently when used for knocking cycle detection. The left panel of Figure 4.13 shows a strong quadratic correlation exists between AEFD and MAPO. Given the strong linear dependence between AEPO and AEFD, this result was expected since a similar quadratic correlation was achieved between MAPO and AEPO in Figure 4.6. It is worth pointing out that different length integration windows ($\Delta\theta$) were used to calculate the AEPO data presented in Figure 4.6 and Figure 4.12, hence why the AEPO data in Figure 4.6 is not equal to the AEFD data in Figure 4.13.

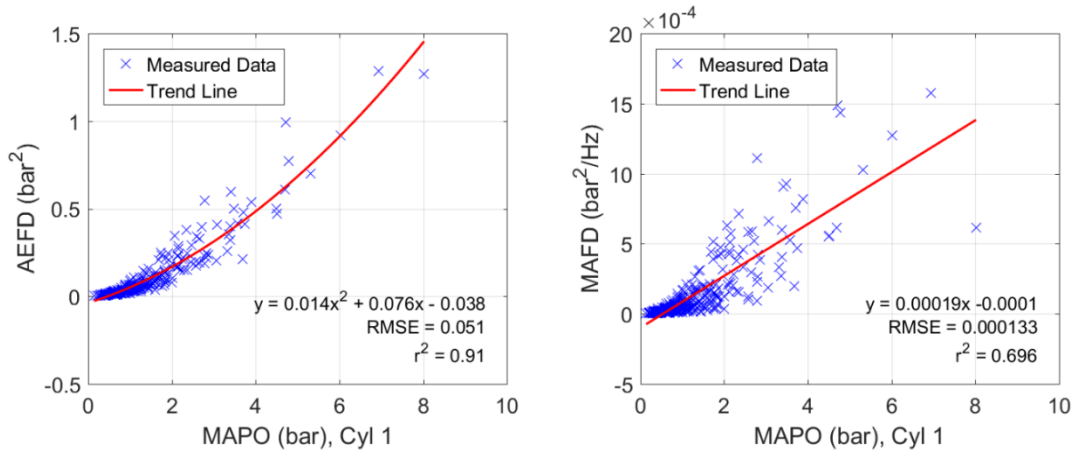

Figure 4.13 – MAPO plotted against AEFD (left) and MAFD (right) using experimental data from the experimental engine running under heavy knock at 1500rpm/17bar BMEP. Similar trends were observed across a range of speeds and loads up to 3500rpm/28bar BMEP.

Summary of KI Metrics Discussion

From the above discussion concerning pressure-based KI metrics, a number of conclusions can be drawn:

1) Using integral/mean value metrics rather than single value metrics is generally recommended by the literature since the former are reportedly less susceptible to noise and constructive interference. Integral/mean value metrics should therefore be more reliable as indicators of knock, particularly at light knocking conditions where spurious pressure oscillations would be more easily mistaken for genuine knock.
2) KI metric normalisation has been investigated by several authors with a view to obtaining KI estimates that are insensitive to measurement location, transducer type, EOC and data processing methods. In this respect, metric normalisation using the methods proposed by Lee and Siano would be worth investigating.
3) Preliminary analysis using experimental data collected from the experimental engine suggests that Brecq's dimensionless knock indicator (DKI) does not in this case converge on a single value at non-knocking conditions, as was found in [105]. In fact, Brecq's DKI metric exhibits an unusually large amount of variability as spark timing is varied, even under non-knocking conditions where one would expect a KI metric to remain relatively stable. In this work, DKI does not appear well suited to the

process of KI threshold calibration and therefore will not be considered for individual knocking cycle detection.

4) Ringing intensity, a metric commonly employed to quantify knock intensity in HCCI engines, has been found to correlate poorly with conventional SI KI metrics. The reason for this poor correlation is that the PPRR in SI engines is principally a result of normal flame front progression and not AI.
5) KI metrics based on rate of heat release (ROHR) provide little additional insight into knocking behaviour compared to pressure based metrics because ROHR is calculated from cylinder pressure. This includes the unburned fuel mass fraction at knock onset, which has been shown in this work to exhibit no obvious correlation with conventional KI metrics such as MAPO.
6) Several metrics display strong linear correlations with one another, suggesting that not all of the metrics discussed above need to be considered as part of the investigation into knock detection methods.

4.2.3 Automated Knocking Cycle Detection Methods

In this section, a range of knocking cycle detection methods (to be used in conjunction with the KI metrics highlighted previously) is introduced. Knock detection is most easily implemented by comparing the KI of individual cycles with a predefined threshold value. Cycles with a KI greater that this threshold are classified as knocking and vice versa. This threshold must be high enough to prevent false positives (the misclassification of non-knocking cycles as knocking) but low enough to minimise false negatives (the misclassification of knocking cycles as non-knocking). To minimise false positives, the threshold should be greater than the background noise level for the KI metric in use. The challenge in this regard is that the background noise level varies between engines, between sensor and signal types, and between engine operating conditions. In addition, the effects of cyclic variability will result in a spread of knock intensity values for each operating condition, the magnitude of which will likely depend on the KI metric used. For these reasons knock intensity thresholds should be determined for each EOC individually, factoring in the background noise level and the specific statistical properties of the KI metric being used.

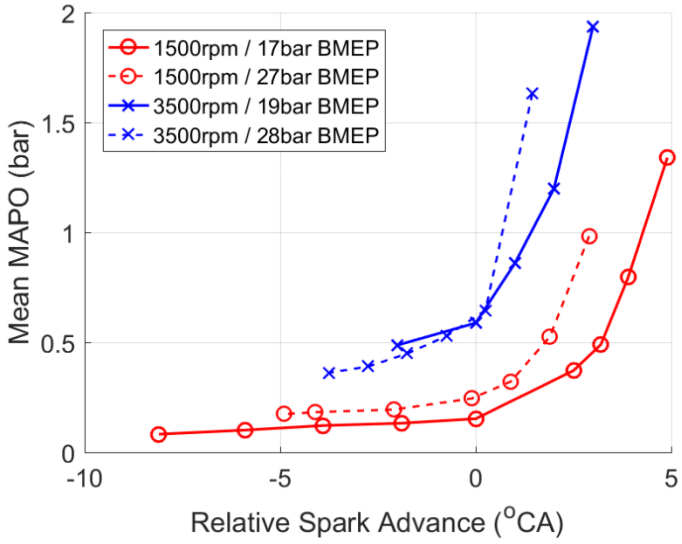

Figure 4.14 – $\overline{MAPO}$ versus relative spark advance (the spark advance relative to KLSA) for a range of EOCs. Data presented in the lower plot windows have been normalised by the values recorded at the most retarded spark setting. Data collected from the experimental engine.

Figure 4.14 illustrates the variability of background noise in pressure trace records, plotting $\overline{MAPO}$ against spark advance relative to the KLSA at several EOCs. The background noise level at a particular EOC can be inferred from the KI value at the most retarded spark setting (assumed to be knock free). Comparing the mean KI values at 3500rpm and 1500rpm, it would be safe to assume that higher engine speeds result in higher levels of background noise. This assumption is in line with observations made throughout the literature. The effect of engine load on background noise level is less consistent, with the 1500rpm and 3500rpm data potentially showing opposing trends. However, background noise level does clearly vary with engine load.

Traditionally, knock intensity thresholds have been based on operator experience or from empirically derived rules of thumb. One such rule for example is to assume a knock frequency of 5% at the audible knock limit. The 95th percentile KI value at the audible knock limit is therefore often used as a threshold for knocking cycle detection. As previously discussed, pinpointing the audible knock limit is however a highly subjective process that can be easily influenced by external factors. The methods presented in this section attempt to do away with the subjective characteristics of traditional knock detection methods, and rely instead on the quantitative properties of experimental data to determine appropriate KI thresholds.

Maximum Non-knocking Value (MNV) Knocking Cycle Detection Method

The fundamental aim of KI threshold calibration is to determine the minimum KI value necessary to avoid false knock detection. When spark sweep data is available, a good estimate of this value can be obtained by setting the KI threshold equal to the maximum KI value recorded at the most retarded spark setting (assumed to be non-knocking). Evidently, this method requires data to be collected at spark timings sufficiently retarded to be considered completely knock free. It also requires a large number of cycles to be collected, otherwise it is difficult to declare a KI threshold with any degree of confidence.

Figure 4.15 demonstrates how the MNV method of KI threshold calibration is implemented in practice. One can see that in this case, there is a high degree of variability in the knock behaviour between cylinders at the same operating condition. Cylinder 4 presents a case where the MNV method appears to be well suited. At non-knocking spark settings (where SA° ≤ -2°CA bTDC), the maximum individual cycle KI value was nominally constant. This characteristic enables the MNV method to correctly predict approximately 0% knock frequency at these points. MAPO data from the other three cylinders however shows that the maximum individual cycle KI value was rarely constant as spark timing was varied under non-knocking conditions. For cylinder 2, the maximum individual cycle MAPO decreased as spark timing was advanced from -10°CA to -6°CA bTDC, at which point it remained stable until the KLSA was reached. Cylinders 1 and 3 meanwhile showed the opposite trend with the maximum individual cycle MAPO increasing as spark was advanced up to -6°CA bTDC. As a result, the KI thresholds determined for cylinders 1 and 3 using the MNV method are too low to avoid false knock detection. This observation is supported by the improbably high knock frequency predictions obtained for these two cylinders at advanced spark timings.

The advantages of the MNV method are its simplicity and the absence of any “calibrateables” that could influence the KI threshold computed. It is however vulnerable to changes in background noise level as spark is varied under knock free operation. To limit this risk, KI data from a large number of cycles (>10,000) should be collected when carrying out KI threshold calibration.

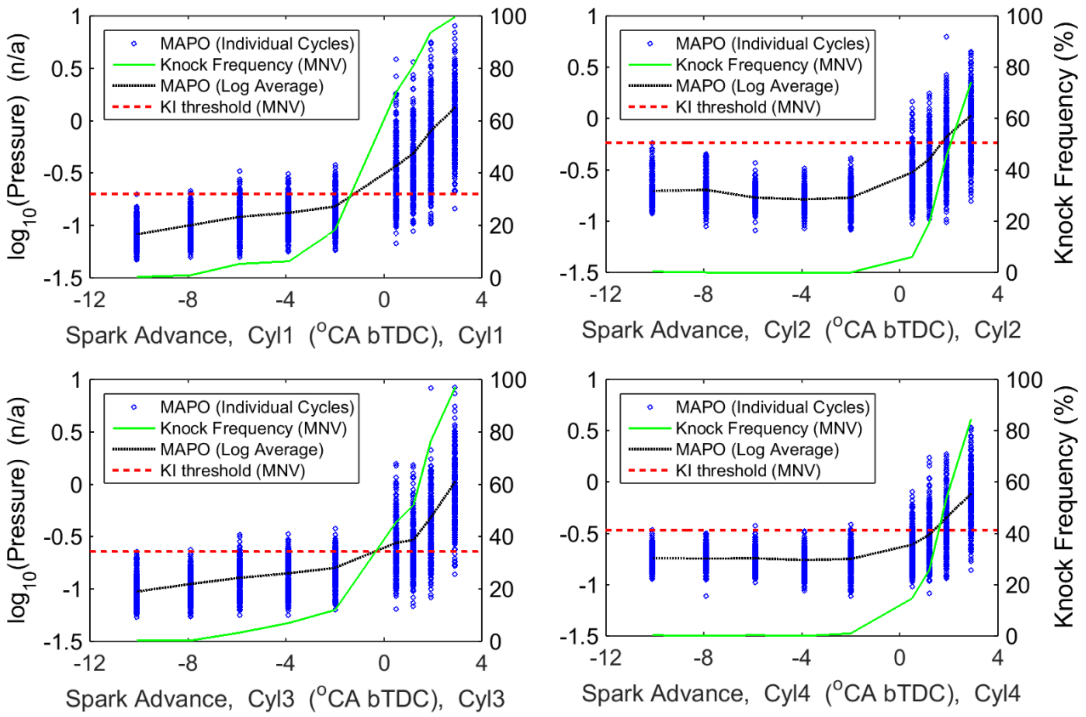

Figure 4.15 – Plot showing how Maximum Non-knocking Value (MNV) method of KI threshold calibration used in practice. For clarity, log_{10} is used for pressure-based data on the left axes of each plot window. Experimental data collected from the experimental engine at 1500rpm, 17bar BMEP.

Piecewise Linear Regression (PLR) Knocking Cycle Detection Method

The results presented for the MNV method highlight how the KI threshold calibration process might benefit from knowledge of where the KLSA is along a spark sweep. For example, cycles collected at spark settings less advanced than the KLSA could be pooled and used collectively for KI threshold calibration. This approach would allow any changes in background noise level as spark is advanced under knock-free conditions, to be factored in to the KI threshold calibration process.

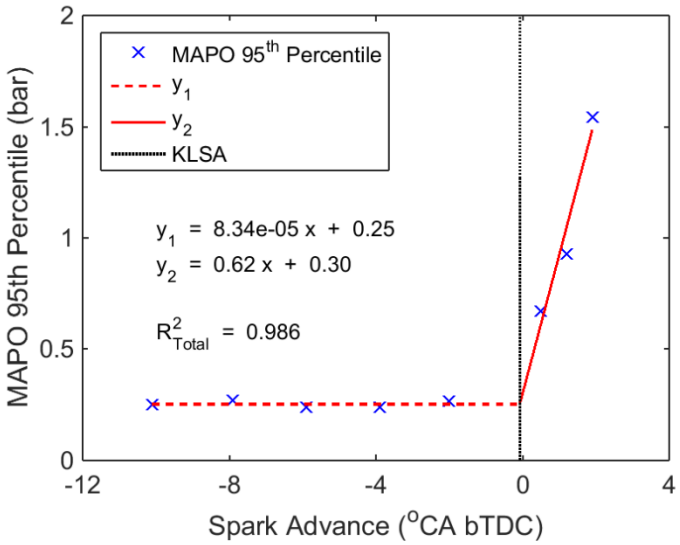

Figure 4.16 – 95th percentile MAPO plotted against spark timing, with piecewise linear regression used to fit two linear lines of best fit. Data collected from the experimental engine at 1500rpm, 17bar BMEP.

Figure 4.16 shows the typical relationship between KI (expressed using the 95th percentile MAPO value in this case) and spark timing. This relationship can be divided into two linear regimes; one at retarded spark settings that exhibits a very slight increase in KI as spark timing is advanced, and a second at advanced spark settings that exhibits a much steeper increase in KI as spark is advanced. Piecewise linear regression (PLR) was used to generate this figure. PLR is a technique where the independent variable of a bivariate data set is split into segments. Linear regression lines are fitted to the data within each segment using the least squares principle. The regression lines are additionally constrained such that they must intersect those in adjacent segments at their common boundary. In this instance, the intersection of the two trend lines serves two purposes. Firstly, it offers a convenient estimate of the KLSA. In practice, this estimate would be rounded down to the spark timing at the next most advanced measurement location. Secondly, it provides an impartial means by which the KI threshold can be calibrated. There are several approaches that can be used in this regard:

1) Set the KI threshold equal to the y ordinate at the intersection of the two trend lines.
2) Pool the data collected at spark settings less advanced than the PLR KLSA estimate and set the KI threshold equal to the maximum individual KI value observed within this subset.

3) As above, but assume that a small fraction of cycles collected at spark settings less advanced than the PLR KLSA estimate will be knocking. Instead of using the maximum KI value observed within this subset of data, one could use the 95th percentile for example.

In this instance, the 95th percentile KI values are used to estimate the KLSA, and the third approach listed above is used for KI threshold calibration since a small fraction of cycles would still be expected to knock at spark settings marginally less advanced than the KLSA. The exact percentile used to calibrate the KI threshold at each EOC is adjusted upwards from a starting value of 95 until 0% knock frequency is achieved at the most retarded spark setting.

One of the advantages of the PLR method is that it only uses the shape of the data provided, thus it requires no external input or prior knowledge of what constitutes a sensible KI threshold. On the other hand, the location of the KLSA estimate (and hence the KI threshold) is very sensitive to the number of data points provided. Removing the most advanced data point for example can have a significant impact on the predicted KLSA since the rate of increase in KI_{95} is sometimes exponential beyond the KLSA. Rounding the KLSA prediction down to the next most advanced measurement location has proven to be effective at limiting this impact. Another disadvantage of the PLR method is that a complete spark sweep of data is required, with measurements taken well into the knocking regime. In contrast, none of the alternative KI threshold calibration methods discussed in this section require data to be collected beyond the KLSA. Doing so puts the engine at risk and increases the amount of time and cost associated with gathering the necessary data.

Ferraro Knocking Cycle Detection Method

Ferraro [101] proposed a method of knocking cycle detection based on the change in shape of knock intensity distributions as spark timing is varied. Ferraro observed that under knock-free conditions, the maximum knock intensity measured for a single cycle was 2 – 4.5 times the mean knock intensity depending on the KI metric used. This ratio between peak and mean values under knock free conditions was termed “K Factor”. As spark timing was advanced, Ferraro observed that the spread of KI values increased until eventually, a small portion of cycles (1-2% of the total) displayed knock intensities greater than K Factor multiplied by the mean KI of the current operating point. This spark timing coincided with

the audible knock limit across a range of operating conditions for the engine used in their experiments. Ferraro thus proposed that the KLSA for a given EOC was equal to the spark timing at which 1-2% of the recorded cycles exhibited KI values greater than the KI threshold given by Equation 4.16 and Equation 4.17 (where $\overline{KI}_{KLSA}$ is the mean knock intensity at Ferraro's definition of the KLSA).

$$K\ Factor\ =\ \left[\frac{KI_{max}}{\overline{KI}}\right]_{Non-Knocking} \qquad \textit{Equation 4.16}$$

$$KI_{Ferraro}\ =\ K\ Factor\ \times\ \overline{KI}_{KLSA} \qquad \textit{Equation 4.17}$$

Ferraro's method effectively scales the threshold defined using the MNV method by the percentage increase in the log-average KI at each spark setting relative to that observed at the most retarded condition. Figure 4.17 and Figure 4.18 demonstrate this approach in practice. Plot window A of Figure 4.17 shows the MAPO frequency distribution under non-knocking spark timing. This condition is used to define K-Factor, which results in a KI threshold equal to the maximum observed KI value and a knock frequency of 0%. Plot windows B and C of Figure 4.17 show how the MAPO frequency distribution varies as spark timing is advanced into incipient knock (i.e. the KLSA) and into heavy knock respectively. It is clear from these plot windows that as the average KI increases, the KI frequency distributions become increasingly positively skewed. This characteristic is precisely what Ferraro's knock detection method is based upon as this increasing skewness is the reason why a growing number of cycles end up exhibiting KI values greater than K-Factor x $\overline{KI}$. Figure 4.18 meanwhile shows how the knock threshold is modified as spark timing is advanced. In practice, the KI threshold is initially defined using K-Factor and the $\overline{KI}$ at each point. The KLSA is then determined as the most retarded spark setting exhibiting a knock frequency greater than or equal to 2%. The KI threshold at the KLSA ($KI_{Ferraro}$ or KI_{final} in Figure 4.18) is then applied to all logs that are advanced of the KLSA.

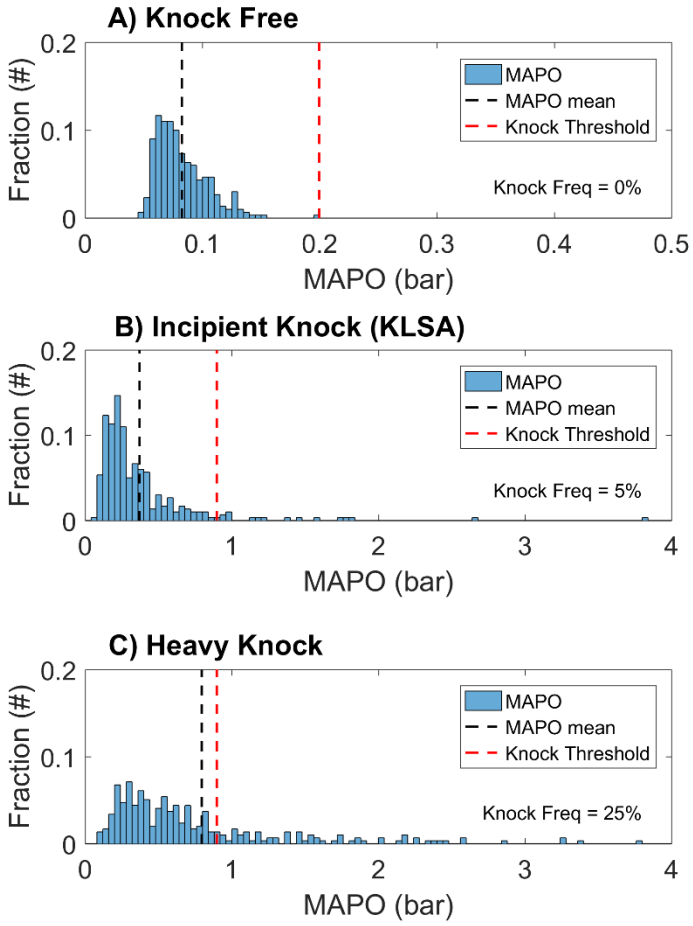

Figure 4.17 – Frequency distributions for MAPO as spark timing advanced from no-knock to heavy knock. KI thresholds calculated using Ferraro method shown in red. Data recorded on the experimental engine at 1500rpm, 17bar BMEP.

Figure 4.18 also demonstrates the high degree of variability in knock behaviour between cylinders. Cylinder 1 for example displays considerably higher mean MAPO values than the other three cylinders at advanced spark timings. Any number of factors could be responsible for this difference, ranging from differences in scavenging dynamics and trapped hot residual gases, to the direction of coolant travel through the head and block resulting in wall temperature differences between cylinders. From the shape and amplitude of the mean MAPO traces, it is possible that in reality the KLSA for cylinder 1 was probably 1-2 degrees less advanced than the KLSA for the other three cylinders at this operating condition. By overestimating the KLSA for cylinder 1 in this case, Ferraro's knock detection method has probably settled on a KI threshold that is marginally too high. Consequently, the knock frequency for cylinder 1 is likely to be underestimated. This conclusion is supported by comparing the mean knock intensities and calculated knock frequencies for cylinders 1 and

4 at advanced spark timings. Cylinder 4 displays much lower mean KI values than cylinder 1 (despite exhibiting a higher background noise level), yet the knock frequency calculated at a given spark timing for cylinder 4 is greater than that calculated for cylinder 1.

It is apparent from Figure 4.18 that Ferraro's knock detection method warrants further investigation. For the example operating condition presented, sensible KLSA and knock frequency results were obtained for all cylinders, although there is scope to improve its accuracy. A useful characteristic result of this method is that it should always return a knock frequency of 0% for the log displaying the lowest level of knock along a given spark sweep. For this result to be accurate however, it is important that the experimental data being analysed is recorded at spark settings sufficiently retarded that the assumption of 0% knock frequency is valid. A further benefit of Ferraro's method is that unlike the MNV method, it adapts the KI threshold to account for any variation in the background noise level as spark timing is advanced under knock-knock free conditions. This dynamic threshold setting approach is beneficial as it would help reduce the likelihood of false positive classifications.

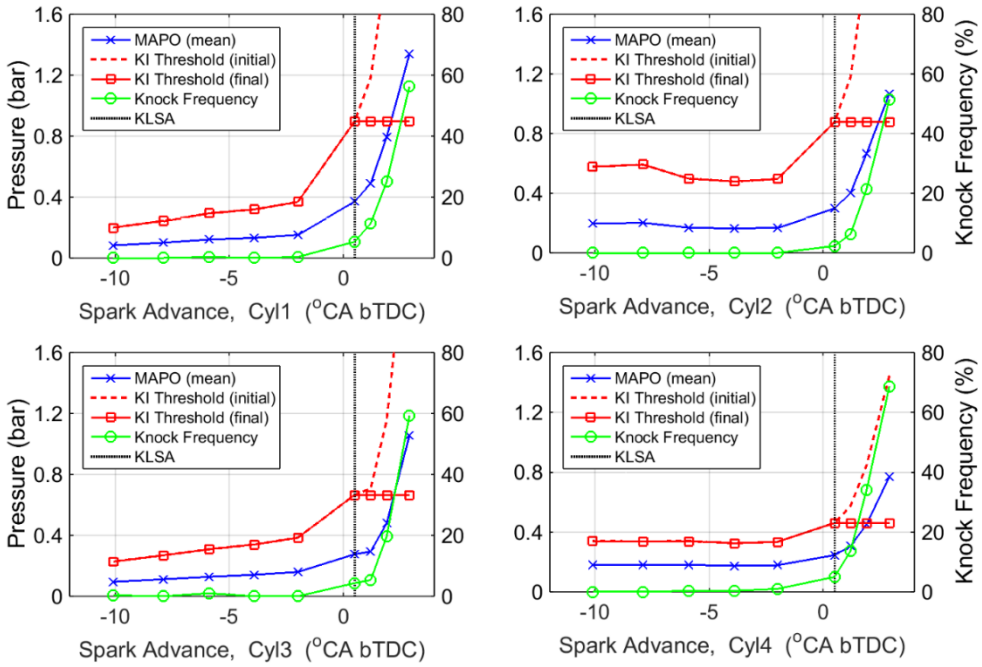

Figure 4.18 – Plots showing how $\overline{MAPO}$, Ferraro KI thresholds and the knock frequency (derived using the Ferraro threshold method) evolve between cylinders as spark timing swept. Data recorded on the experimental engine at 1500rpm, 17bar BMEP.

Lee Knocking Cycle Detection Method

Lee [86] devised a simple KI threshold calibration process based on observations made regarding the ratio of the mean KI calculated from the strongest and weakest 5% of cycles at each spark setting. This method relies on normalising the KI of every cycle at each spark setting by the log average of the weakest 5% of cycles. Lee observed that a normalised KI value of three served as an effective threshold for knocking cycle detection, irrespective of sensor type and KI metric. In this work, only KI metrics based on cylinder pressure have been investigated. In contrast with Lee's findings however, preliminary analysis suggests that a KI threshold value of three is not appropriate for all metrics.

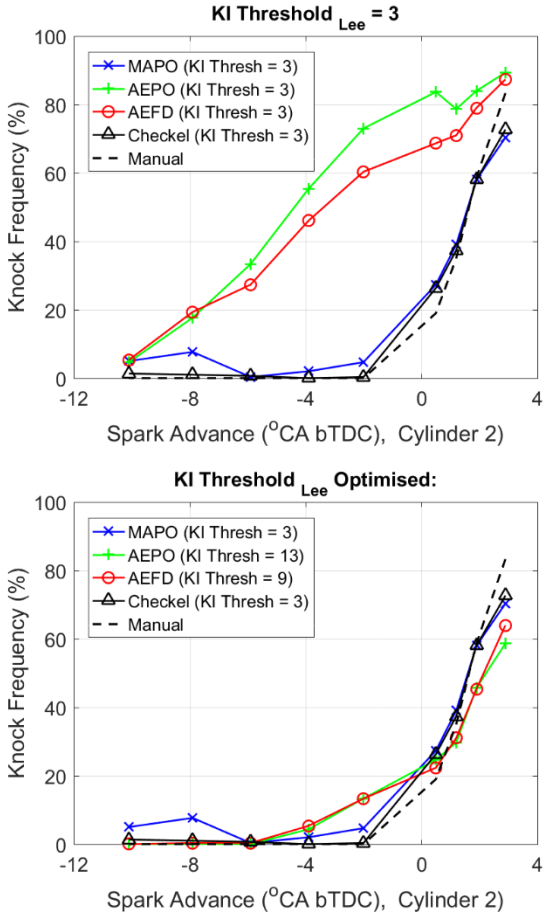

Figure 4.19 – Top: Knock frequency predictions obtained using the method proposed by Lee [86] that suggests using a normalised KI threshold of 3 for all KI metrics. Bottom: Knock frequency predictions obtained using Lee's method but with the normalised KI threshold values tailored for each KI metric to achieve the best match with the manually estimated knock frequency. Data derived from measurements taken from the experimental engine at 1500rpm, 17bar BMEP.

Figure 4.19 compares knock frequency predictions obtained using Lee's approach (combined with a variety of metrics) versus predictions derived manually by the author[9]. It is clear from the top panel of this figure that for the KI metrics AEPO and AEFD, a normalised KI threshold of three results in considerable false knock detection. For MAPO and Checkel KI metrics however, a threshold value of three seems entirely appropriate. The bottom panel shows the knock frequency predictions obtained after optimising the normalised KI threshold for each metric. This optimisation was performed by selecting the KI threshold value that minimised the mean difference between predicted and manually derived knock frequency results across the entire spark sweep. Values of three did indeed turn out to be effective for MAPO and Checkel KI metrics, but considerably higher values were required for AEPO and AEFD. This observation contradicts Lee's findings suggesting that the optimum KI threshold for knocking cycle detection is insensitive to KI metric choice.

Unfortunately, optimisation of the KI threshold to suit individual KI metrics contradicts the spirit of this investigation. The intention here is to pursue methods that utilise the specific statistical properties of the measured data for KI threshold calibration, rather than those that require calibration by comparison with subjective knock detection methods. For this reason, the knock detection method proposed by Lee has not been investigated further. The method of metric normalisation using the mean KI of the weakest 5% of cycles at each log has however been investigated further, and combined with the other three knock threshold calibration methods described in this section.

[9] Additional details on the method adopted for manual knock frequency estimation is provided in the following section.

4.3 Angle of Knock Onset Estimation

In-cylinder signal types (such as cylinder pressure, ion-current or light intensity) are typically used for aKO estimation because of their high signal to noise ratios and fast response rates. These characteristics make it is possible to estimate aKO with a good degree of accuracy. Only cylinder pressure based techniques are discussed in this work, although the principles of aKO estimation using other signal types are fundamentally the same.

Cylinder pressure based aKO estimation methods all start by band-pass filtering the cylinder pressure trace to remove both the low frequency component and any high frequency noise that might be present. Typical cut-off frequencies are the same as those used to determine knock intensity (i.e. roughly 5 kHz at the lower limit and 30-40 kHz at the upper limit). The simplest aKO estimation technique is known as the Threshold Value Exceeded (TVE) technique. In its most basic form, this approach uses a constant threshold value (TV) of between 0.5-1.0 bar, and aKO is taken to be the earliest crank angle at which the band-pass filtered cylinder pressure trace exceeds this threshold. Much like threshold definition for knocking cycle detection, the threshold for TVE must be high enough to avoid false triggers such as noise spikes or the occasional constructive interference event, yet low enough to obtain a realistic estimate of aKO. If the threshold is too high, there is a risk that the resulting aKO estimates will be late when compare with the actual aKO. An example of this scenario is shown below in Figure 4.20 where the initial pressure oscillations immediately after aKO are below the threshold defined for this case, resulting in an inaccurate aKO estimate[10].

Knocking signal characteristics are highly variable and as Figure 4.20 highlights, the first pressure oscillation observed after knock onset does not necessarily exhibit the largest amplitude. Defining a constant threshold that can accurately and reliably estimate aKO across a range of EOCs is therefore something of a challenge. Many authors have proposed slight modifications to the basic TVE method to make it less susceptible to the high degree of variability seen in knock event characteristics. For example, Elmqvist [59] proposed that the aKO threshold be defined on an individual cycle basis as a threshold factor multiplied by MAPO, as described by Equation 4.18. A threshold factor of 0.7 was found to be a good compromise between avoiding false aKO detection and achieving accurate results. Worret

[10] The aKO estimation threshold for this particular EOC was defined as the maximum MAPO observed at the most retarded spark setting for which cylinder pressure data was recorded.

[90] on the other hand proposed an initial threshold factor of 0.65, which would then be halved if the signal energy after the initial aKO estimate was above a certain threshold. Halving the threshold factor in this way was only allowed once per cycle but it improved the accuracy of aKO estimates for heavy knock cycles where the threshold value would otherwise have been too high to accurately capture the true aKO. Worret additionally introduced the concept of locating the last sign change in the BPF cylinder pressure trace ahead of the initial aKO estimate and using this point as the aKO estimate.

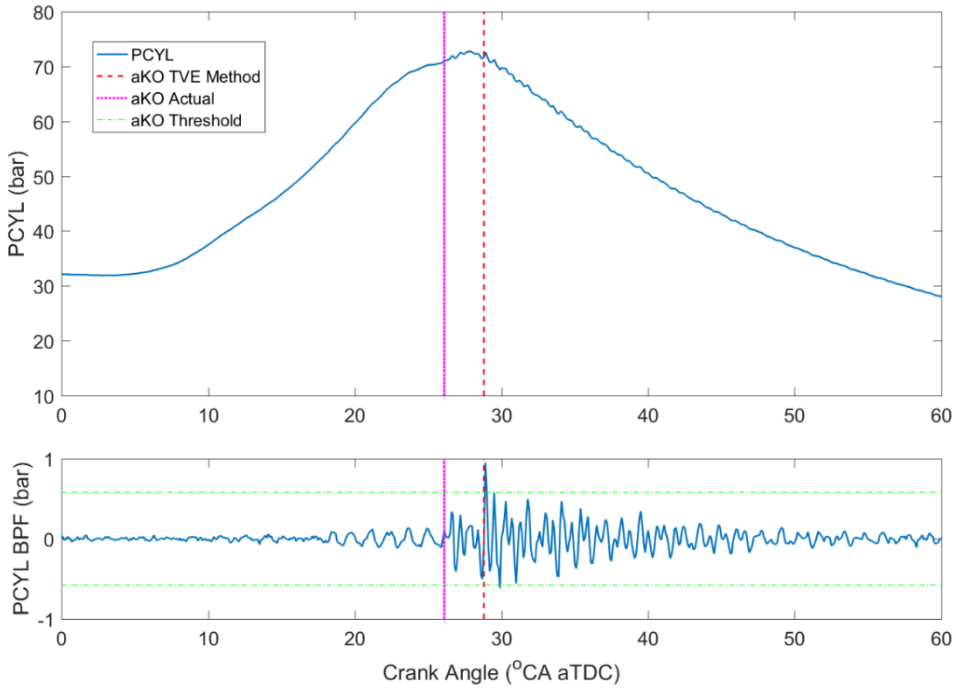

Figure 4.20 – Example of TVE method of aKO estimation resulting in a late aKO prediction. Data recorded on the experimental engine at 1500rpm, 17 bar BMEP.

$$aKO\ Threshold\ Value_{\ i} \ = \ Threshold\ Factor \ \times \ MAPO_{\ i} \qquad \textit{Equation 4.18}$$

Despite their relative simplicity, TVE methods have the obvious disadvantages of requiring some degree of calibration if they are to provide accurate aKO estimates. Several authors have devised aKO estimation methods that instead utilise the locations of maximum/minimum values for key properties of the pressure trace, thus eliminating the need for threshold calibration. For example, Checkel suggested that the aKO could be estimated using the location of the minimum value of the third derivative of the low-pass filtered cylinder pressure trace [99]. Shahlari on the other hand stated that aKO could be estimated from the location of the maximum value of the signal energy ratio defined in

Equation 4.19 [1]. SEPO is calculated using Equation 4.4, with $SEPO_{fwd}$ calculated over the next Δθ (5°CA in this case), and $SEPO_{bwd}$ calculated over the previous Δθ. Both of these aKO estimation methods benefit from the fact that they do not depend on any threshold values.

$$SER = \frac{(SEPO_{fwd})^2}{(SEPO_{bwd})^{0.5}} \qquad \textit{Equation 4.19}$$

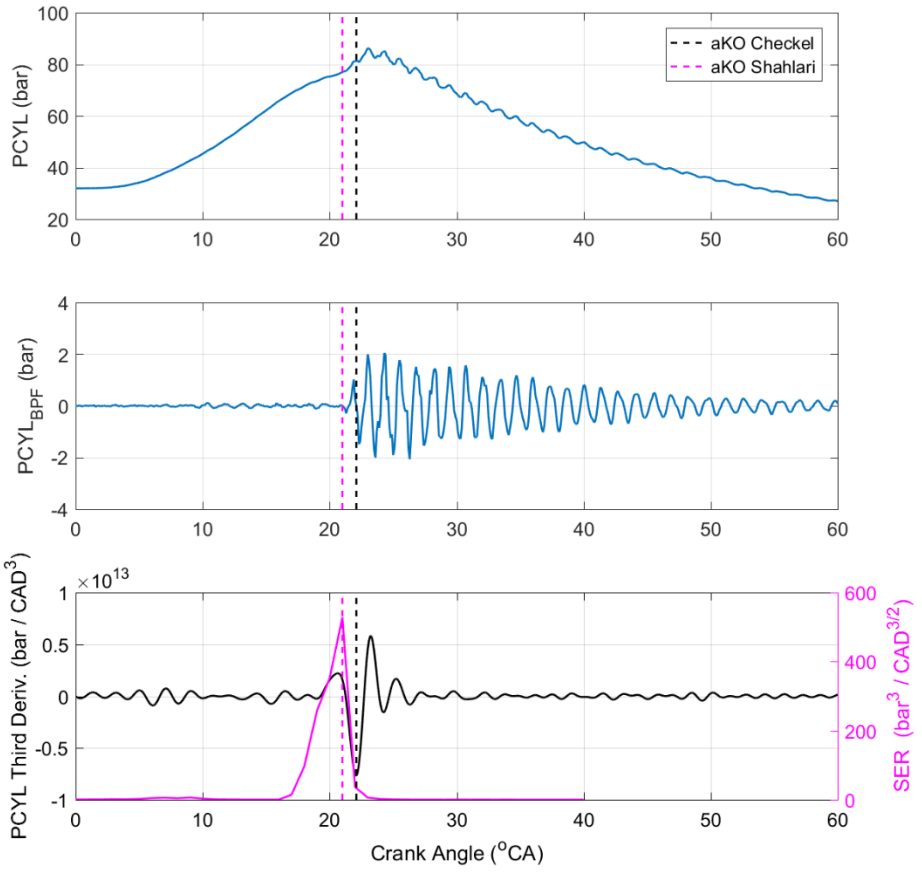

Figure 4.21 – Example of Shahlari and Checkel aKO estimation methods.

Finally, Xiaofeng proposed a method of aKO estimation based on the cumulative signal energy of the BPF cylinder pressure trace [107]. Figure 4.22 below provides examples of both knocking and non-knocking cumulative signal energy profiles and their corresponding cylinder pressure traces. Xiaofeng suggested that aKO could be inferred from the difference in gradients between the cumulative signal energy trace and a reference linear line of best fit (LOBF) plotted through the 10°CA segment prior to aPMAX – 5°CA. The aKO is taken to be the earliest point at which the gradient of the cumulative signal energy trace exceeds 1.3 times that of the linear LOBF. For the non-knocking case in Figure 4.22, the gradient

threshold was never exceeded (as expected for a non-knocking cycle) so aPMAX has been used in place of an aKO estimate.

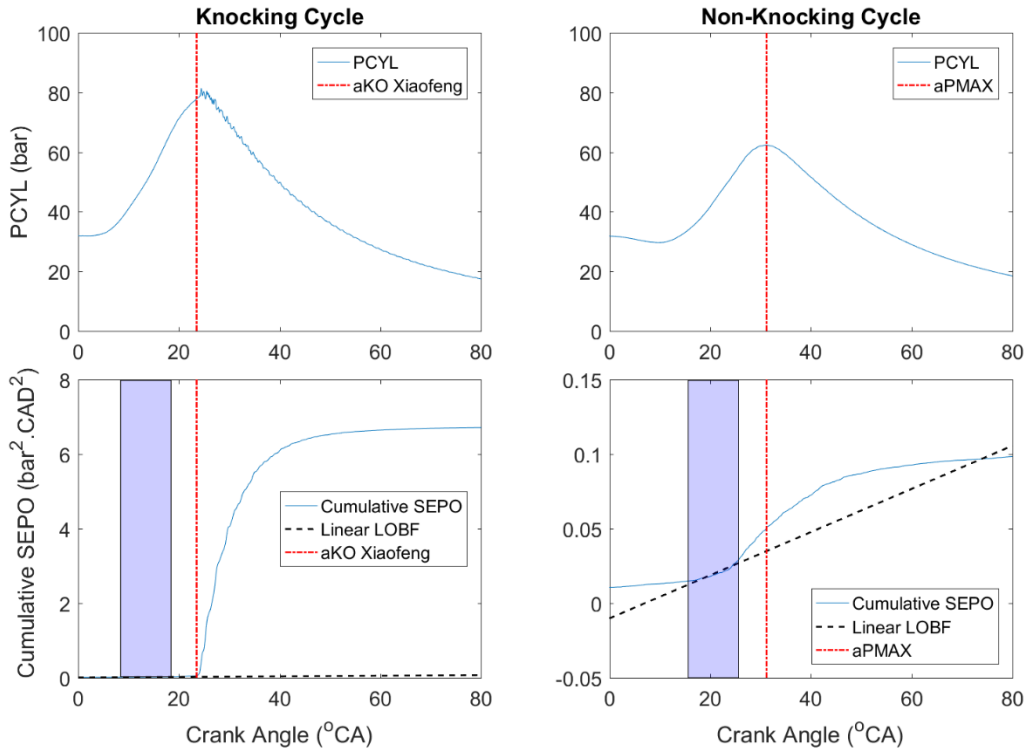

Figure 4.22 – Comparison of cumulative SEPO traces for knocking and non-knocking cycles. Shaded areas correspond to the 10°CA segment over which the reference linear LOBF is fitted.

4.4 Manual Cycle Classification and Angle of Knock Onset Estimation

4.4.1 Experimental Data

Experimental data was collected at the four EOCs listed in Table 4.1. These EOCs were chosen to provide a broad range of in-cylinder conditions and knocking behaviour, thus enabling a thorough assessment of the various knocking cycle detection and aKO estimation methods at high load conditions to be carried out. Details regarding the data collection techniques and apparatus used are provided in Chapter 3.

	EOC 1	EOC 2	EOC 3	EOC 4
Engine Speed (rpm)	1500	1500	3500	3500
Intake Manifold Pressure (bar A)	1.60	2.40	1.60	2.40
Exhaust Manifold Pressure (bar A)	1.20	1.55	1.45	2.05
BMEP (bar)	18 - 14	27 - 24	19 - 15	28 - 26
Intake Manifold Temp. (°C)	40 ± 1°C			
Coolant Temp. (°C)	90 ± 1°C			
Lamba (#)	1.0 ± 0.02			

Table 4.1 – Engine operating conditions considered for the knocking cycle detection and aKO estimation method assessment.

4.4.2 Experimental Data Processing and Calculations

Knocking Cycle Detection

Once all the experimental data had been gathered, the raw cylinder pressure traces were exported from AVL Concerto into Matlab for post-processing and analysis. With the exception of $KI_{Checkel}$, all of the KI metrics investigated in this work required the raw cylinder pressure trace to be band-pass filtered prior to their calculation to remove the low frequency component of the signal. Since it was only necessary to view the high pressure portion of the cylinder pressure trace for knock characterisation, cylinder pressure data outside of the range 30°CA bTDC to 90°CA aTDC was discarded prior to filtering. Using this crank angle range guaranteed that the knocking portion of the pressure trace was contained within the signals analysed, and significantly reduced the memory requirement of the desktop PC that was

used for data processing. The centre point of this crank angle range was also well aligned with the point in the cycle at which knock would typically occur (20-40°CA aTDC). As already discussed, centring the signal on the region of strongest knock minimised the amount of attenuation inflicted on the knocking pressure oscillations when the signals were windowed as part of the PSD estimation process.

When quoting figures derived from filtered data, it is important to provide details of the filtering method used, as filter characteristics can have a large impact on the amplitude and phase of the output data. Throughout this study, band-pass filtering was performed using digital finite impulse response (FIR) filters and a fixed passband of 5kHz to 40kHz. Low pass filtering on the other hand was performed using infinite impulse response (IIR) Butterworth filters, with pass and cut-off frequency limits set to 1 and 4kHz respectively. Matlab's "filtfilt" command was used to achieve zero phase shift between the filtered and original signals (an important characteristic if accurate aKO estimates are to be achieved).

MAPO was calculated according to Equation 4.1, whilst AEPO was calculated using Equation 4.5 with a $\Delta\theta$ value of 10°CA. The calculation was performed in 1°CA increments from 10°CA bTDC to 50°CA aTDC and the maximum value over this range is what has been quoted throughout this work. This approach (proposed by Shahlari [1]) eliminates any bias that might arise through a poor definition of θ_0.

MAFD was calculated according to Equation 4.15. The PSD of each cycle was estimated using Matlab's "periodogram" function. Each cycle was shortened to 1024 consecutive data points as signal lengths equal to powers of two were considerably quicker to process. Care was taken to align the aMAPO of each cycle with the centre point of the signal. A Hamming window was used to reduce the amplitude of the signal at its start and end to zero, thus reducing spectral leakage in the periodogram output.

$KI_{Checkel}$ was calculated according to Equation 4.6. The shortened cylinder pressure traces were low-pass filtered using a digital 10^{th} order Butterworth IIR filter with a cut-off frequency of 5kHz. Differentiation was performed using a simple numerical routine in Matlab. Ideally, the third derivative would have been calculated using the equation described by Checkel in [100]. Unfortunately, it was not possible to obtain sensible results using this equation. For brevity, Checkel's equation has not been included here but in essence, it is a combination of the low pass filtering and differentiating functions, combined with a cubic spine fitting function to reduce noise in the final output.

The normalisation process described by Lee [86] was applied to all four of the aforementioned metrics (MAPO, AEPO, MAFD and $KI_{Checkel}$) for each 300 cycle log analysed, whilst the approach described by Siano [104] could only be applied to MAPO and AEPO. Reference values were calculated for Siano metrics over the crank angle range 30 – 10°CA bTDC.

Angle of Knock Onset Estimation

Angle of knock onset was estimated from cylinder pressure records for each cycle using the approaches highlighted in Section 3.3. The same shortened cylinder pressure traces and filtering methods that were used for knocking cycle detection were also used for aKO estimation. Matlab's "filtfilt" command was used to achieve zero phase shift during the filtering process, thus allowing accurate aKO estimates to be derived from the filtered cylinder pressure traces.

Angle of knock onset was first estimated using a variety of TVE-based methods. The simplest of these methods, dubbed the maximum most retarded value (MMRV) method, used the MAPO observed at the most retarded spark setting as the aKO threshold for each EOC. The threshold derived using this method was therefore fixed for all cycles at a given EOC. MAPO was calculated using Equation 4.1. The second TVE method investigated was that proposed by Elmqvist [59]. A range of threshold factors from 0.5 to 0.7 was applied, with MAPO for each cycle again calculated using Equation 4.1. The threshold for aKO estimation was calculated using Equation 4.18. For both of the methods discussed in this paragraph, aKO was defined as the location of the last sign change in the BPF cylinder pressure trace ahead of the first instance of the threshold value being exceeded.

The third TVE method investigated is an iteration on that proposed by Worret [90]. Worret's original method used the high-pass filtered ROHR trace, a threshold factor of 0.65 and an average signal energy threshold calculated over the 7°CA after the initial aKO estimate equal to 15×10^{-4} J^2. If this average signal energy threshold was exceeded, the threshold factor was halved and a new aKO was estimated. In this work, the band-pass filtered cylinder pressure trace was used instead of the high pass filtered ROHR trace (for reasons previously explained) and a different approach altogether was adopted to indicate when the threshold factor should be halved. Rather than compare the average signal energy *after* the initial aTVE with

an arbitrarily defined threshold value, the average signal energy *before* the initial aKO estimate was compared with the maximum AEPO value calculated at the most retarded spark setting at a given EOC. If the AEPO before the initial aKO estimate for a particular cycle was greater than twice this threshold, then the threshold factor was halved and the process is repeated. This method of halving the threshold factor was used in preference to that suggested by Worret because for an aKO estimate to be accurate, one would expect the signal energy before the aKO estimate to be similar to the background noise level during the high pressure portion of the cycle. AEPO was calculated using Equation 4.5 and a $\Delta\theta$ value of 10°CA. In keeping with Worret's approach, the threshold factor could only be halved once from an initial value of 0.65, and aKO was defined as the location of the last sign change in the BPF cylinder pressure trace, ahead of the first instance of the threshold value being exceeded.

Finally, the last TVE aKO estimation method considered in this work is an adaptation of that proposed by Xiaofeng [107]. The cumulative SEPO trace was calculated in 0.1°CA increments by applying a cumulative integral version of Equation 4.4 to the entire band-pass filtered cylinder pressure trace. For each cycle, a linear LOBF was fit through the cumulative SEPO trace over the range aPMAX – 15° to aPMAX – 5°CA. The gradient of this LOBF provided the reference gradient for each cycle. The entire cumulative SEPO trace was then smoothed using a moving average smoothing function in Matlab and a span of five data points. This action was carried out to remove the impact of any spurious noise spikes on the instantaneous gradient of the cumulative SEPO trace. The first derivative of the cumulative SEPO trace was then divided by the reference gradient to determine the gradient ratio at every 0.1°CA. If the maximum gradient of the cumulative SEPO trace was greater than 20 times that of the linear LOBF, a gradient ratio threshold of 20 was used to estimate the aKO (i.e. aKO was estimated to be the earliest instance of the ratio of LOBF and cumulative SEPO gradients exceeding a value of 20). If however the maximum gradient ratio value for a given cycle was less than 20, a gradient ratio threshold of five was used. Maximum gradient ratio values less than five were typically associated with non-knocking cycles, in which case the aPMAX was stored in lieu of a sensible aKO estimate. The gradient ratio threshold values used in this work are considerably higher than the value of 1.3 proposed by Xiaofeng.

Two additional aKO estimation methods were tested on top of the TVE methods described above. The first of these is that proposed by Shahlari [1]. For this method, the signal energy

ratio (SER) was calculated in 1°CA increments along the entire length of the shortened BPF cylinder pressure trace using Equation 4.19. SEPO was calculated using Equation 4.4 and a range of Δθ values spanning 5 – 10°CA. As described in section 3.3, aKO was estimated from the location of the maximum SER value. By nature of this calculation approach, aKO could only be estimated to the nearest 1°CA. The second threshold-less aKO estimation method investigated in this work is that proposed by Checkel [99]. The calculation method is exactly the same as that described in the previous section with regards to knock intensity metrics.

In summary, four TVE methods of varying complexity (MMRV, Elmqvist, Worret and Xiaofeng) and two threshold-free methods (Shahlari and Checkel) of aKO estimation have been investigated in the course of this study. For some methods, a range of parameter values have been applied to investigate their influence and ultimately determine which parameter values provide the best match with manually derived aKO estimates.

4.4.3 Manual Knocking Cycle Detection and aKO Estimation

To assess the performance of the various knocking cycle detection and aKO estimation methods under test, comparison datasets were manually generated. For each cylinder and EOC, samples of 50 cycles were randomly selected at three different spark settings along the spark sweep (resulting in 2400 cycles in total). The spark settings were chosen to represent knock-free, incipient knock and heavy knock conditions, thus providing a good balance between the number of knocking and non-knocking cycles selected from each EOC. Sample populations were required to have mean and standard deviation MAPO values that were within 1% of the corresponding values obtained from the 300-cycle parent log. This action ensured that the sample data-sets were an accurate reflection of the actual knock intensity behaviour exhibited at each spark setting.

Manual cycle classification was carried out in Matlab. Cycles were presented to the author one at a time using a plot window identical to that displayed below in Figure 4.23. This figure window contained subplots for the raw cylinder pressure trace, the band-pass filtered cylinder pressure trace and its PSD estimate, the low-pass filtered ROHR and the mass fraction of fuel burned trace. Alongside the figure window, a menu window with radio buttons for “knocking” and “non-knocking” categories was presented, which allowed the author to input which category the current cycle belonged to.

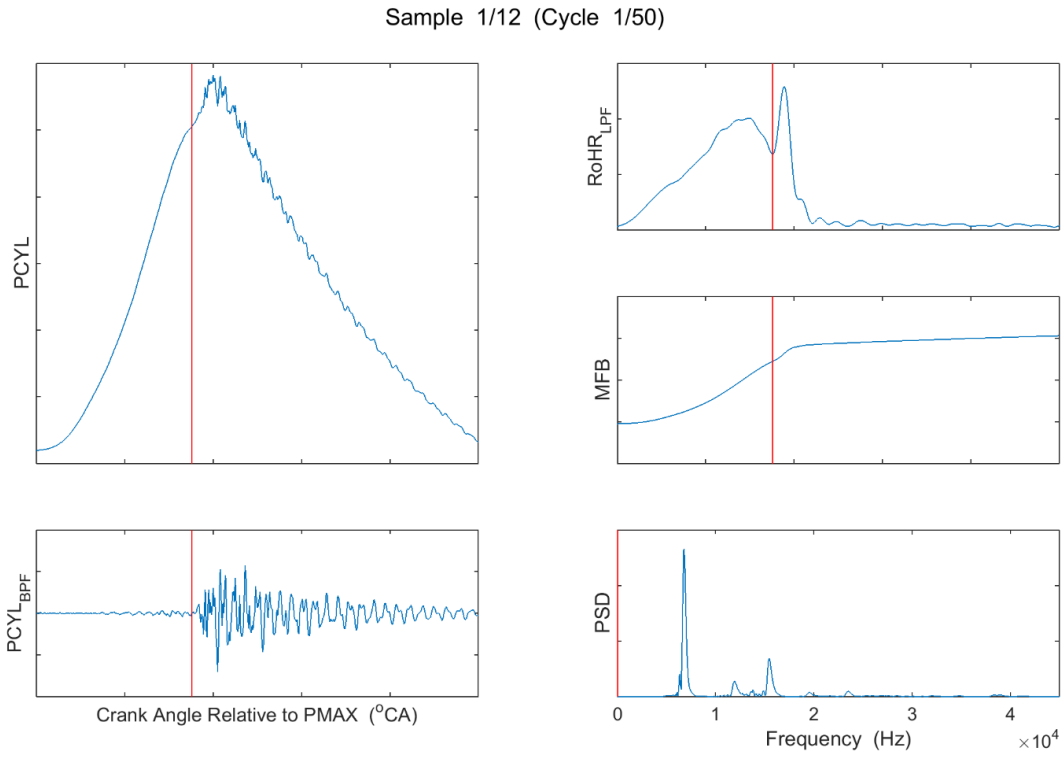

Figure 4.23 – Example figure window presented to the operator to enable the manual classification of cycles. The vertical red line in each subplot is a mouse-operated cursor added to facilitate aKO estimation.

Great care was taken to minimise the potential for operator-induced bias in the cycle categorisation process. The largest contribution towards achieving this aim came from anonymising the x and y-axes in the figure window presented. MAPO and MAFD would be easy to infer from the bottom row of subplots for example, were the y-axes present. This action prevented the operator from being able to formulate their own quantitative KI threshold (whether consciously or subconsciously). By anonymising the x-axis and by plotting crank angle resolved data over the narrow range of aPMAX – 20°CA to aPMAX + 30°CA, it was impossible for the author to determine which spark setting was being assessed. Thus, no preconceptions concerning the expected knock frequency for the current 50-cycle sample could be drawn. Additionally, each of the 12 x 50-cycle samples (3 spark settings x 4 cylinders) analysed at each EOC were anonymised and presented to the author in a random order. By removing these quantitative cues, the author was forced to rely on just the visible properties of the data that was presented, thus removing much of the scope for bias to affect their decision making.

To facilitate aKO estimation, a mouse-operated cursor was added to each subplot in the figure window presented to the operator (see the red lines in Figure 4.23). The cursors could

be moved along the x-axis by clicking the mouse button in any one of the subplots. Moving the cursor in one subplot moved the cursors in all of the other subplots to the same x-axis location. For cycles that were classified as knocking, the x-axis location of the cursors was taken as the aKO estimate. The band-pass filtered cylinder pressure and low-pass filtered RoHR traces were the primary guides in this process. The angle of knock onset was generally taken as the last zero crossing of the BPF cylinder pressure trace before any significant change in the pressure oscillations was observed. The LPF ROHR trace was also helpful in this regard as it could often be used to locate the approximate start of heat addition by an AI event. Again, the opportunity for operator-induced bias was minimised by incorporating the steps highlighted above, such as anonymising the x-axis for crank angle resolved data.

The purpose of this exercise was to build a large date set of knocking and non-knocking cycles that encompassed a range of EOCs. Since the intention was to use these cycles to validate empirical ignition delay correlations, the author was specifically looking for knock events that were likely to be the result of end-gas auto-ignition (AI). To qualify as a knocking cycle, certain characteristics had to be present in the data. Establishing an acceptable degree to which these characteristics needed to be visible however proved somewhat challenging. Light knock events for example were particularly difficult to categorise consistently because the amplitude of their pressure oscillations was similar to that of the background combustion noise near PMAX. To maximise consistency, a logical and methodical decision making process was employed in the categorisation of each cycle. This process is outlined in Figure 4.24.

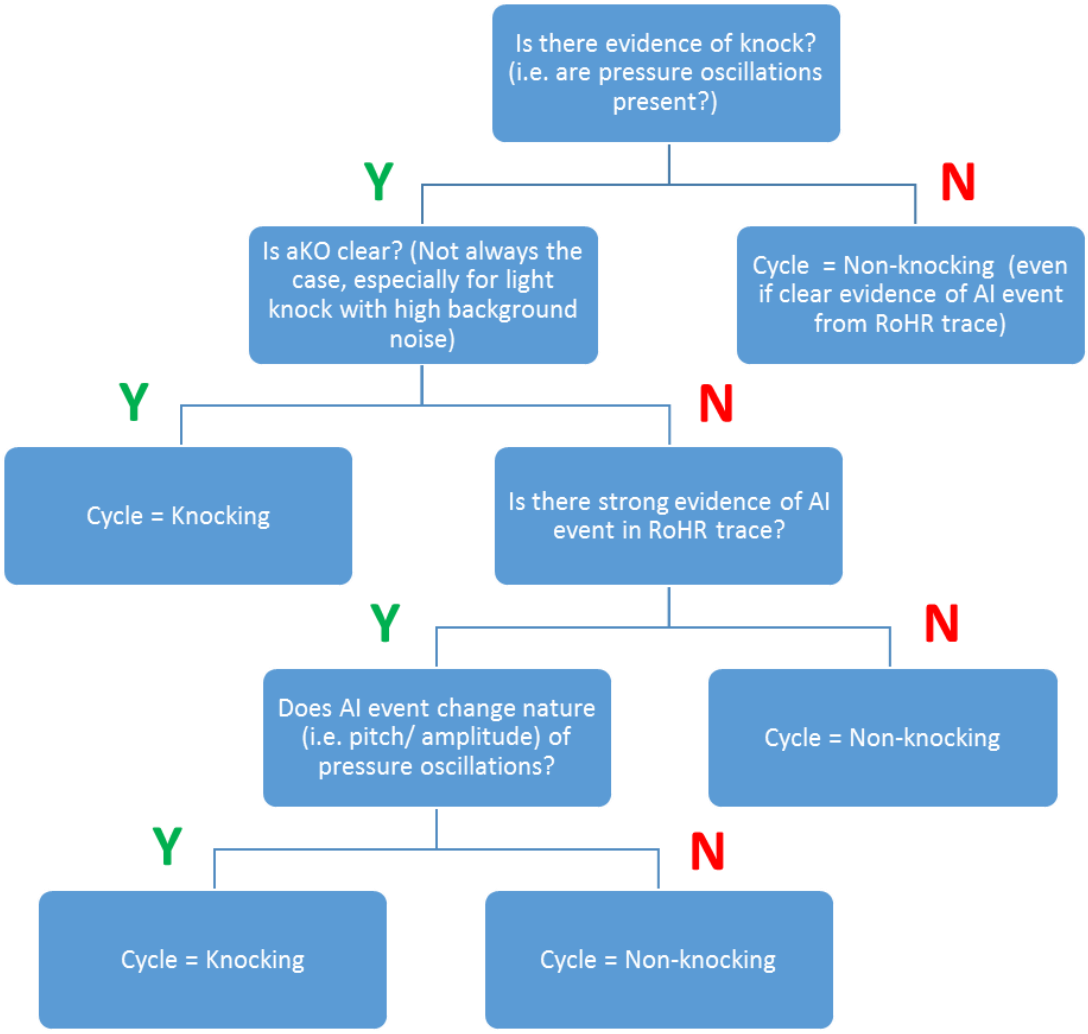

Figure 4.24 – Decision tree for manual knocking cycle classification exercise.

The most important criterion was whether any pressure oscillations were visible in the raw cylinder pressure trace, since without pressure oscillations there can be no knock. For cycles exhibiting pressure oscillations, the next question was whether the onset of these oscillations could be clearly identified. Lower amplitude pressure oscillations for example could be obscured by interference from background noise, or the amplitude of the oscillations could build very gradually, making it difficult to determine the angle of onset.

Cycles demonstrating a clear angle of knock onset could be confidently classed as knocking. For cycles with a less obvious aKO, it was necessary to look at their RoHR traces and ascertain whether any AI event(s) were likely to have occurred at or around the time of the observed pressure oscillations. AI events are easily detected from the RoHR trace as a secondary peak late in the combustion event. Figure 4.23 provides an example of a particularly strong AI

event which is clearly visible from the RoHR trace. In this example, the onset of AI is in phase with the onset of pressure oscillations, indicating that the source of the oscillations is end gas AI. For cycles without any obvious signs of end gas AI, it was assumed that the pressure oscillations observed were the result of some other abnormal combustion phenomena. Cycles for which it was necessary to scrutinise their respective RoHR trace often exhibited very light pressure oscillations. In the absence of evidence suggesting that end gas AI had taken place, these cycles were classified as non-knocking.

For cycles in which there was evidence of end gas AI, it was then necessary to determine whether the AI events actually contributed to the pressure oscillations observed (since end gas AI can occur without leading to knock). Cycles for which an AI event could be credited with a significant change in the pitch or amplitude of the pressure oscillations were duly classified as knocking. Naturally, there were still occasions where this final classification decision was not straight forward. A decision was still required regarding what constituted a "significant" change in the nature of the pressure oscillations. However, reducing the problem of cycle classification to a series of straightforward yes/no answers made for a consistent approach with minimal operator bias.

4.5 Results and Discussion

4.5.1 Knock Intensity Metric Assessment

As mentioned in earlier sections, there are a large number of cylinder pressure based knock intensity metrics. A simple method has been devised to reduce the number of metrics scheduled for consideration. The premise of this method is that metrics that correlate well with one another would be expected to produce very similar knock detection results. It is therefore only worth investigating one KI metric from any such group of well-correlated metrics.

The correlation coefficient describes the degree of linear dependence between two random variables. In this case, Matlab's "corrcoeff" function was used to return the Pearson correlation coefficient for each metric pair. Values of 1 indicate a perfect positive correlation, whilst values of 0 and -1 indicate no correlation and perfect negative correlation respectively. Matrix form is an efficient way to display correlation coefficient data for a large number of random variables. Each variable is numbered, thus the correlation coefficient for any variable pair can be found by reading the data contained in the relevant cell of the matrix. For example, given the variable numbers provided in Table 4.2, the data at location (3,4) in the coefficient matrix contained in Table 4.3 corresponds to the metric pair AMPO and SEPO. By definition, entries along the leading diagonal are equal to 1 because a perfect positive correlation is obtained whenever a data set is compared with itself. Coefficient matrices are also always symmetric since the correlation coefficient result does not depend on the order in which the comparison is made.

KI Metric	Variable #
MAPO	1
IMPO	2
AMPO	3
SEPO	4
AEPO	5
Checkel	6
Ferraro	7
AEFD	8
MAFD	9

Table 4.2 – Variable numbers for the KI metrics considered for knocking cycle detection.

Correlation Coefficients =

1	**0.98**	**0.98**	0.90	0.90	-0.83	**0.99**	0.91	0.84
	1	**1**	0.88	0.88	-0.83	0.96	0.91	0.89
		1	0.88	0.88	-0.83	0.96	0.91	0.89
			1	**1**	-0.67	0.88	**0.99**	0.89
				1	-0.67	0.88	**0.99**	0.89
					1	-0.86	-0.68	-0.62
						1	0.89	0.80
							1	0.94
								1

Table 4.3 – Correlation coefficients for the nine KI metrics listed above in Table 4.2, determined from experimental data collected on the experimental engine at 1500rpm, 17bar BMEP and a range of spark settings corresponding to both knock-free and heavy knock conditions.

The correlation coefficient matrix (Table 4.3) shows that several distinct groups of KI metrics correlate very well with one another. For clarity, matrix elements with coefficient values greater than 0.975 have been highlighted red. In the top left hand corner, one can see the high degree of agreement between MAPO and IMPO/AMPO in the top left hand corner of the coefficient matrix. This observation had already been established in the left hand panel of Figure 4.6. The perfect correlation between IMPO and AMPO was also expected since the only difference between these metrics is the scalar factor $\Delta\theta$. The same argument explains the perfect correlation between SEPO and AEPO. On this basis, both IMPO and AMPO can be eliminated from the pool of metrics carried forward for further analysis, as can one of SEPO/AEPO.

Moving on to the Checkel KI metric, a wide variety of correlation coefficients were obtained for this metric, justifying its selection going forward. Ferraro on the other hand exhibited a correlation coefficient of 0.99 with MAPO, suggesting that only one of these metrics is required. AEFD exhibited near perfect correlation with SEPO/AEPO as expected, whilst the correlation coefficient results obtained for MAFD suggest that its results were sufficiently unique to warrant further consideration.

On the basis of the above remarks, the following four KI metrics have been selected for investigation of their usefulness with respect to knock detection:

1. MAPO – selected to act as a reference single value metric, and because it is still one of the most widely used measures of KI.

2. AEPO – selected to act as a reference integral value metric.
3. Checkel – selected to act as a reference derivative-based metric.
4. MAFD – selected to act as a reference frequency-domain metric.

To confirm the validity of the above selection, their correlation coefficients were determined using experimental data collected across a range of knock limited EOCs. The results displayed in Table 4.4 show that none of the four KI metrics listed above exhibit overly strong linear correlations with one another (i.e. $r^2 > 0.975$), justifying their selection going forward and validating the earlier results displayed in Table 4.3. It is also apparent that quite a broad range of correlation results was obtained for these four metrics. MAPO/AEPO/MAFD correlate very well with each other across all four EOCs investigated, generally achieving $|r^2|$ values greater than 0.8. Correlation coefficients between $KI_{Checkel}$ and the other three KI metrics were somewhat less consistent however, particularly at higher engine speeds. $KI_{Checkel}$ may therefore not be as suitable for knock detection at higher engine speeds as the other three KI metrics.

1500rpm, 17bar BMEP (Cyl1):	**1500rpm, 27bar BMEP (Cyl2):**
$A = \begin{bmatrix} 1 & 0.90 & -0.83 & 0.84 \\ 0.90 & 1 & -0.67 & 0.89 \\ -0.83 & -0.67 & 1 & -0.62 \\ 0.84 & 0.89 & -0.62 & 1 \end{bmatrix}$	$B = \begin{bmatrix} 1 & 0.91 & -0.78 & 0.81 \\ 0.91 & 1 & -0.60 & 0.92 \\ -0.78 & -0.60 & 1 & -0.54 \\ 0.81 & 0.92 & -0.54 & 1 \end{bmatrix}$
3500rpm, 19bar BMEP (Cyl3):	**3500rpm, 28bar BMEP (Cyl4):**
$C = \begin{bmatrix} 1 & 0.89 & -0.44 & 0.92 \\ 0.89 & 1 & -0.22 & 0.97 \\ -0.44 & -0.22 & 1 & -0.29 \\ 0.92 & 0.97 & -0.29 & 1 \end{bmatrix}$	$D = \begin{bmatrix} 1 & 0.89 & -0.71 & 0.78 \\ 0.89 & 1 & -0.50 & 0.85 \\ -0.71 & -0.50 & 1 & -0.47 \\ 0.78 & 0.85 & -0.47 & 1 \end{bmatrix}$

Table 4.4 – Correlation coefficient matrices for MAPO, AEPO, Checkel and MAFD (variables 1 – 4 respectively) calculated from experimental data collected on the experimental engine across a range of EOCs.

Finally, the question regarding the worthiness of metric normalisation must be addressed. The approach proposed by Lee [86] has been applied to all four metrics, whilst the approach proposed by Siano [104] could only be applied to MAPO and AEPO (the reader is referred to

Section 4.4.2 for details regarding the calculation methods employed). Both approaches are intended to correct for background noise and permit the use of a single knock intensity threshold across a broad range of EOCs and KI metrics. Figure 4.25 and Figure 4.26 show the effects that the Lee and Siano normalisation approaches have on mean KI values for the four metrics in question. They plot mean KI against spark timing relative to the approximate KLSA.

With respect to MAPO and AEPO, it is clear that Siano's normalisation approach does little to level the effects of background noise across the EOCs considered here. Apart from increasing the magnitude of the KI values, Siano's approach appears to achieve very little, with the general shapes of both the MAPO and AEPO data sets appearing very similar before and after normalisation. Considerable differences in background noise level remain between data from different EOCs after applying Siano's approach.

Lee's normalisation approach has a stronger impact all four KI metrics. With the exception of MAFD, Lee's approach levels the background noise across all four EOCs considered relatively well. However, whilst the MAPO and Checkel KI metrics converge on values of 2 – 3 at retarded spark settings, AEPO converges on values approximately three orders of magnitude greater. This approach therefore is not insensitive to KI metric, as Lee suggests. MAFD values assume a similar order of magnitude as AEPO, however there is little evidence to suggest that they would converge on a single value under knock free conditions. Finally, several oddities appear within the data after applying Lee's approach. For example, in some cases the mean KI decreases as spark is advanced towards the most advanced measurement location. This observation is clearly unrealistic; it would be very unexpected for knock intensity to decrease as spark is advanced beyond the KLSA. This is likely to be a result of the mean KI of the lightest 5% of cycles increasing at a faster rate than the mean of the entire log when advancing spark into the heavy knock regime.

From the above discussion, there appears to be little benefit in adopting the metric normalisation approaches proposed by Lee and Siano. Siano's approach was found to have little effect on the variation in background noise between EOCs, whilst Lee's approach was inconsistent and sensitive to KI metric choice. These methods are therefore unlikely to offer any advantage compared to using un-normalised KI metrics. Only the four un-normalised metrics MAPO, AEPO, Checkel and MAFD were considered henceforth.

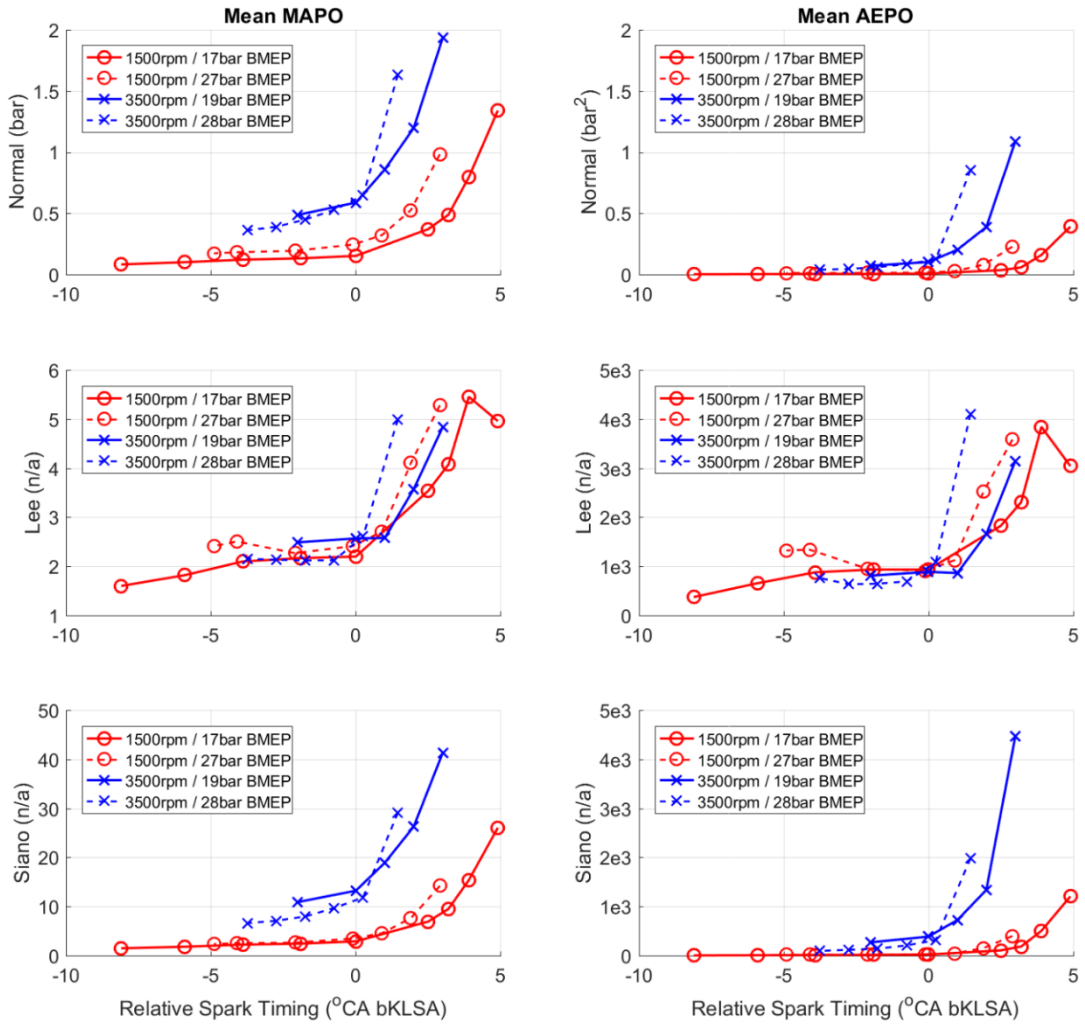

Figure 4.25 – The effect of Lee and Siano normalisation approaches on mean values of MAPO and AEPO, calculated from experimental data collected on the experimental engine across a range of EOCs.

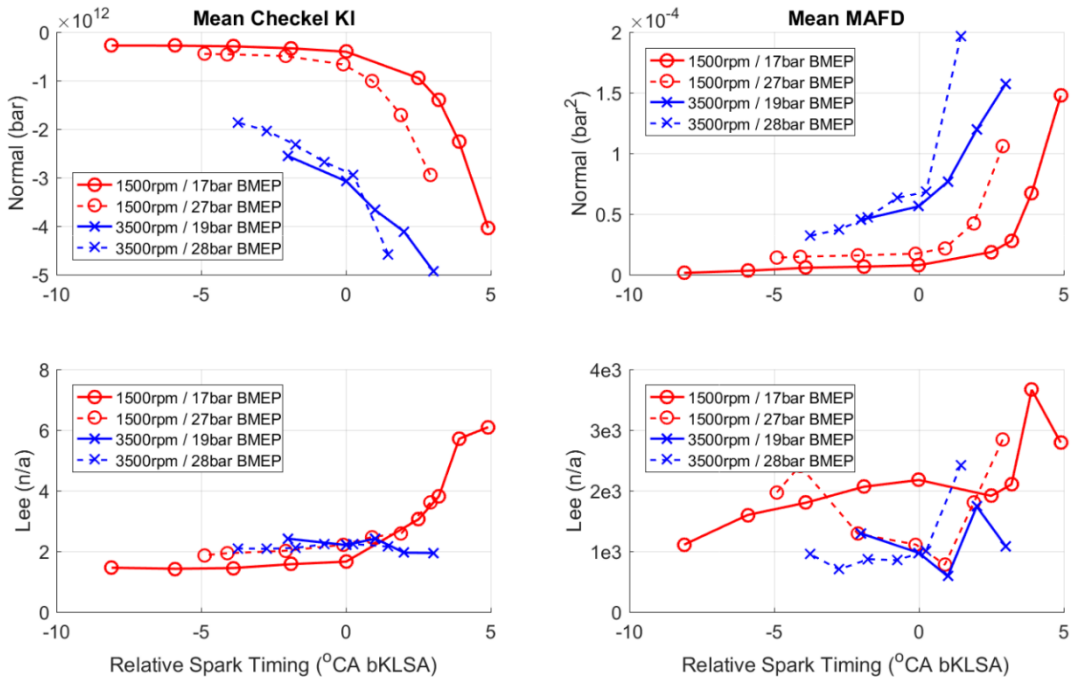

Figure 4.26 – The effect of Lee normalisation approach on mean values of Checkel and MAFD KI metrics, calculated from experimental data collected on the experimental engine across a range of EOCs.

4.5.2 Knocking Cycle Detection Method Assessment

Having devised a shortlist of three KI calibration methods and four KI metrics, the next step was to assess the knocking cycle detection capabilities of the twelve resulting method/metric combinations. Table 4.5 below summarises the metrics and methods that have been carried forward to this stage of the investigation.

KI Threshold Calibration Methods	Maximum Non-knocking Value (MNV)	KI threshold fixed at maximum individual cycle KI observed at most retarded spark timing
	Ferraro	KI threshold equal to MNV threshold scaled by ratio of current and most retarded mean KI values. Threshold fixed when knock freq. > 2%
	Piecewise Linear Regression (PLR)	KI threshold equal to KI value at intersection of two linear lines of best fit generated for 95th percentile KI vs spark timing plot
KI Metrics	MAPO	Maximum amplitude of the rectified, band-pass filtered cylinder pressure trace (see Equation 4.1)
	AEPO	Average signal energy of the band-pass filtered cylinder pressure trace over a 10°CA window (see Equation 4.5)
	Checkel	Minimum value of the third derivative of the low-pass filtered cylinder pressure trace (see Equation 4.6)
	MAFD	Maximum amplitude of the power spectral density estimate, frequency domain metric (see Equation 4.15)

Table 4.5 – Summary of KI threshold calibration methods and KI metrics used as part of the investigation into knocking cycle detection methods.

The knocking cycle predictions generated by each metric/method combination were compared against the manual predictions made by the author[11]. Manual cycle classifications

[11] It is worth reiterating that manual knocking cycle classification was only performed at three spark settings for each of the four main EOCs considered in this chapter. 50 cycles were manually classified at each spark setting for each cylinder. The spark settings were chosen to provide data at varying degrees of knock intensity, ranging from knock free to heavy knock.

were treated as the "gold standard". Correct classifications are therefore those where the automated knock detection method agrees with the manual classification. Figure 4.27 shows the predicted knock frequency (left hand column) and accuracy (right hand column) results obtained for all twelve metric/method pairs at one of the four EOCs considered in this chapter. Accuracy is defined as the number of correct classifications divided by the total number of cycles assessed.

Immediately apparent is the broad spread of accuracy results obtained for the four metrics when the Ferraro method was used. In the case of the Ferraro/MAFD pairing, very low knock frequency predictions were obtained at this particular EOC (even at advanced spark timing) because the predicted knock frequency never exceeded 2%. The KI threshold was therefore never fixed, allowing it to be scaled upwards according to the ratio of the mean KIs at the current and most retarded logs, all the way up to the heavy knocking condition. This trend was observed across a number of cylinders for the Ferraro/MAFD pair at this EOC.

Ignoring the Ferraro/MAFD pair, the majority of metric/method pairs were able to identify knocking cycles with a reasonable degree of accuracy. All metric/method pairs successfully predicted 0% knock frequency at spark settings that were known to be knock free (i.e. at very retarded spark settings). The MAPO and Checkel KI metrics tended to predict the highest knock frequencies at any spark setting, whilst the MAFD metric tended to predict the lowest knock frequencies, irrespective of the KI threshold calibration method used. In this case, AEPO was usually somewhere in between. These observations are consistent with those noted for all cylinders across the four EOCs considered.

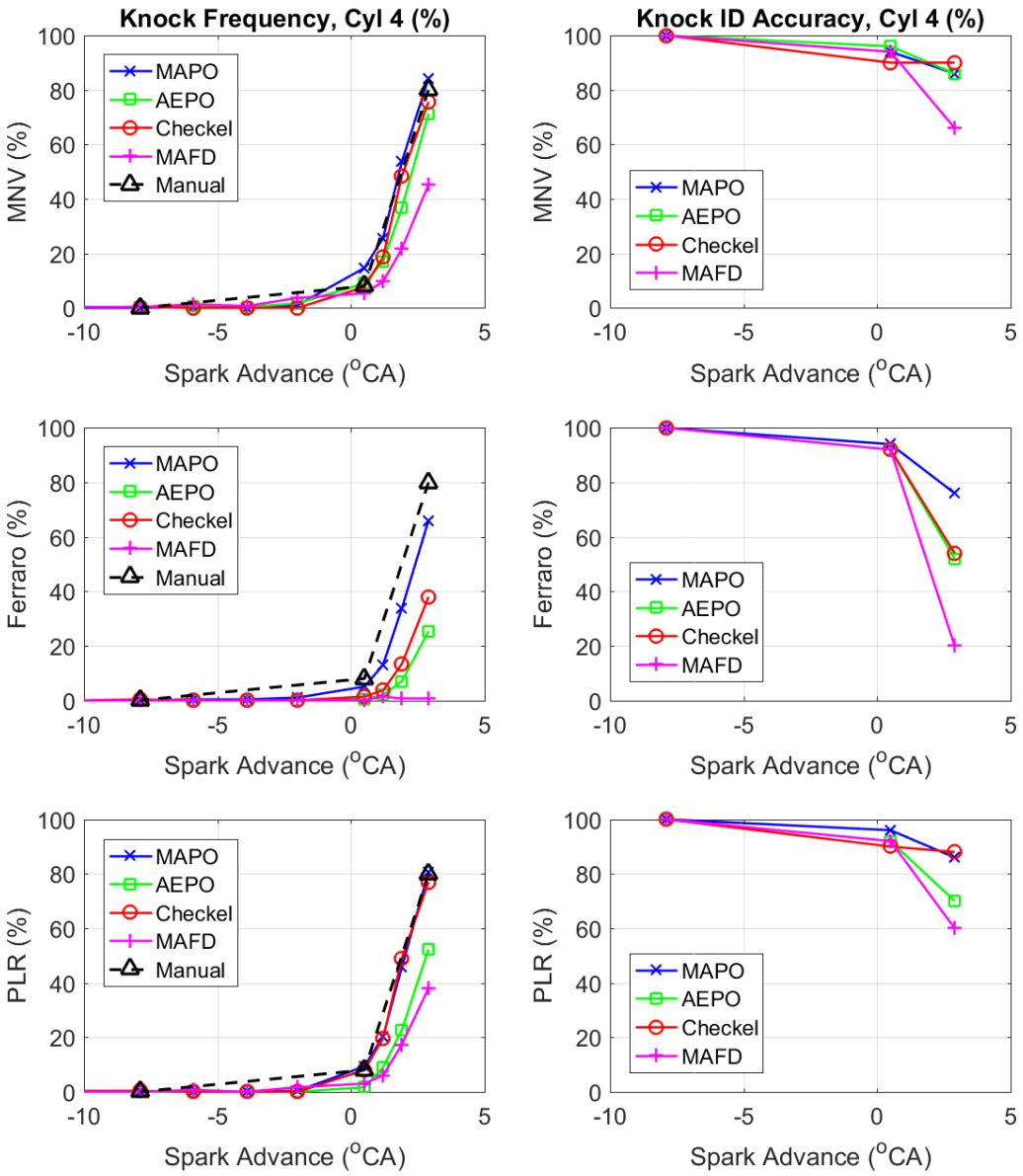

Figure 4.27 – Knock frequency predictions and resulting accuracy statistics for all nine metric/method pairs evaluated for cylinder 4 at 1500rpm, 17bar BMEP. Note that manual knocking cycle classification was only performed at three spark settings, each corresponding to varying degrees of knock intensity.

The plots in Figure 4.27 do not, however, fully reflect how well the various metric/method pairings differentiate between knocking and non-knocking cycles. Considering accuracy alone can be misleading, especially in cases where the prevalence of the category of interest is particularly low. For example, if a population of cycles to be sorted comprised predominantly of non-knocking cycles, then even an algorithm that failed to identify a single knocking cycle would achieve relatively decent accuracy results. To gain a more complete

picture of how well the automated knock classification predictions match those derived manually, additional measures of reproducibility have to be considered[12].

When presenting and evaluating data generated by classification algorithms, it is common practice to use contingency tables (also referred to as confusion matrices). Contingency tables are n x n square matrices, where n is the number of output categories. The sum of the elements in each column represents the number of times each class is KNOWN to have occurred, whilst the sum of the elements in each row represents the number of times each class is PREDICTED to have occurred. The sum of the leading diagonal is equal to the number of times the algorithm predicts the correct category, whilst the sum of all table elements is equal to the total number of observations. In this work, manually derived classifications are considered the "gold standard", against which the performance of each automated knocking cycle detection method is assessed. An example of the structure of a contingency table used in this work is presented in Table 4.6.

		ACTUAL ("Gold Standard" Results)	
		Knocking	Non-Knocking
PREDICTED (Alternative Results)	Knocking	A (true +ve)	B (false +ve)
	Non-Knocking	C (false –ve)	D (true –ve)

Table 4.6 – Example contingency matrix, used to present and evaluate the output of each automated knocking cycle detection method.

In this work, the data output by the various classification methods is in binary categorical form (i.e. there are two possible response categories for each cycle; "knocking" and "non-knocking"). In these circumstances, Cohen's Kappa (κ) is often used to evaluate the level of agreement between two data sets [110]. κ considers the possibility that agreement occurs by chance, making it a more robust measure of agreement than overall accuracy. Chance agreement between the two data sets can be evaluated for each category by multiplying the relevant row total of the contingency matrix by the corresponding column total and dividing by the overall number of observations, n. κ values of 1 indicate perfect agreement between data sets, whilst κ = 0 suggests that "the agreement is no better than that which would be obtained by chance alone" [110]. Values of κ > 0.8 indicate almost perfect fit.

[12] Reproducibility is the term used to describe the ability of two measurement methods to return the same result under identical conditions.

$$\kappa = \frac{Observed\ Agreement - Chance\ Agreement}{Maximum\ Agreement - Chance\ Agreement} = \frac{p_O - p_E}{1 - p_E}$$ Equation 4.20

$$p_O = \frac{(A + D)}{n}$$ Equation 4.21

$$p_E = \left(\frac{A + B}{n} \times \frac{A + C}{n}\right) + \left(\frac{C + D}{n} \times \frac{B + D}{n}\right)$$ Equation 4.22

In addition to accuracy and κ, a number of supplementary indices should be calculated to help assess the ability of each metric/method pairing to discriminate between knocking and non-knocking cycles. These indices are as follows:

- Sensitivity (also known as True Positive Rate) = Proportion of knocking cycles classified as knocking by the method under test = A/(A + C)
- Specificity (also known as True Negative Rate) = Proportion of non-knocking cycles classified as non-knocking by the method under test = D/(B + D)
- Positive Predictive Value (PPV) = Proportion of cycles classified as knocking by the method under test that are actually knocking = A/(A + B)
- Negative Predictive Value (NPV) = Proportion of cycles classified as non-knocking by the method under test that are actually non-knocking = D/(C + D)
- Prevalence = Proportion of cycles in the population that are actually knocking = (A + C)/n

Automated cycle classifications were previously made on an individual cylinder/EOC basis, providing 16 distinct samples of 150 cycles (4 EOCs x 4 cylinders). To help identify the overall best performing metric/method pair, the automated cycle classification data from these 16 sample was pooled, resulting in an overall sample population of 2400 cycles. The prevalence of knocking cycles in this overall sample (determined from the manual classification data) was 23%. It is necessary to determine the prevalence of a sample because it can influence both PPV and NPV values – PPV will tend to be high when prevalence is high whilst NPV will tend to be low (and vice-versa). When prevalence is relatively low (as in this case), high PPV scores are a strong indication that the test method performs well compared to the “gold standard” method.

Contingency tables were created for each of the twelve method/metric pairs under test using the appropriate data from the pooled cycle classifications. An example contingency table is provided in Table 4.7. For each metric/method pair, Cohen's kappa and the above listed indices were calculated. The resulting statistics can be found in Table 4.8.

		Manual Classification Data		
		Knocking	Non-Knocking	Total
MNV/MAPO Classification Data	Knocking	489	163	652
	Non-Knocking	63	1685	1748
	Total	552	1848	2400

Table 4.7 – Contingency matrix for the MNV/MAPO knock detection method pairing, using cycle classification data that was pooled across all 16 cylinder/EOC combinations considered in this chapter.

Metric/Method Pair	Cohen's Kappa, κ (%)	Accuracy (%)	Sensitivity (%)	Specificity (%)	PPV (%)	NPV (%)	Mean (%)
MNV/AEPO	0.72	0.90	0.76	0.95	0.81	0.93	0.85
MNV/MAPO	**0.75**	**0.91**	**0.89**	**0.91**	**0.75**	**0.96**	**0.86**
MNV/Checkel	0.68	0.88	0.81	0.90	0.71	0.94	0.82
MNV/MAFD	0.46	0.84	0.42	0.97	0.79	0.85	0.72
Ferraro/AEPO	0.21	0.80	0.16	1.00	0.91	0.80	0.65
Ferraro/MAPO	0.64	0.89	0.57	0.98	0.91	0.88	0.81
Ferraro/Checkel	0.63	0.89	0.56	0.98	0.92	0.88	0.81
Ferraro/MAFD	0.01	0.77	0.01	1.00	0.75	0.77	0.55
PLR/AEPO	0.65	0.89	0.64	0.96	0.83	0.90	0.81
PLR/MAPO	0.72	0.90	0.78	0.94	0.79	0.93	0.84
PLR/Checkel	0.65	0.88	0.68	0.94	0.78	0.91	0.81
PLR/MAFD	0.45	0.84	0.39	0.97	0.82	0.84	0.72

Table 4.8 – Overall agreement results for each of the twelve metric/method pairs that were tested for their knock detection capabilities.

Analysing the results in Table 4.8, the metric/method pair which achieved the highest average score across the six agreement statistics was MNV/MAPO, closely followed by MNV/AEPO and PLR/MAPO in second and third places respectively. Each of these three pairs achieved κ values > 0.7, indicating a substantial level of agreement (beyond that which could be obtained by chance alone) between their respective knock classifications and those generated manually by the author. The only metric by which MNV/MAPO did not perform particularly well is positive predictive value – the proportion of cycles that were predicted to be knocking that were also deemed knocking by the author. However, metric/method pairs that did score well in this regard (i.e. some of the Ferraro based methods) achieved very low sensitivity scores, indicating that they were poor at identifying knocking cycles in the first place.

Despite the shortfalls of the MNV threshold calibration method and the MAPO metric, their simplicity clearly benefits the consistency of their output. This pairing was therefore duly used for all subsequent knocking cycle detection purposes for the remainder of this work. It is worth pointing out that the results obtained here do not confirm which of the 12 metric/method pairs is the best outright identifier of knocking cycles but that which best agrees with the author's assessment of what constitutes a knocking cycle. Despite the author's best efforts, it is possible that an element of bias towards a certain MAPO threshold was developed subconsciously during the manual cycle classification process. In hindsight, it might therefore have been wiser not to display the raw cylinder pressure trace during manual classification as this could have provided the author with a reference by which to estimate MAPO. On reflection, the band-pass filtered cylinder pressure trace and the low-pass filtered ROHR trace (both on anonymous axes) would have been sufficient for knock classification and would have further minimised the opportunity for any subconscious bias to influence the categorisations made.

4.5.3 Angle of Knock Onset Estimation Method Assessment

Next, the output from various automated aKO estimation methods was compared with aKO estimates made manually by the author. The aim was to identify which automated aKO estimation method best agreed with the authors predictions across a broad range of EOCs.

There are many ways to quantify the degree of agreement between data sets. The correlation coefficient (r), as used earlier to quantify the linear dependence between different KI metrics, is one such method. Used in isolation, this metric can however be misleading, particularly when the returned r-values are in the range -0.5 to 0.5. For example, data sets with strong *non*-linear relationships (quadratic, cubic, etc.) will likely return quite low r-values. It is therefore important to plot and visually inspect the data before drawing any conclusions regarding the degree of correlation.

To this end, Bland-Altman plots (popular in the field of medical statistics) have been used to supplement the calculated r-values. Sometimes referred to as difference plots, Bland-Altman plots are a graphical means of evaluating the agreement between two data sets. Traditionally, they have been used to analyse the agreement between two measurement methods, thus their use is justified in this case. In Bland-Altman plots, the differences between observations from two data sets are plotted against the mean observed values or against the observations from one of the data sets alone. The latter approach is used in cases where one of the data sets is considered the "gold standard", or the reference by which other data sets should be judged. Horizontal lines are displayed to highlight the mean difference (i.e. the bias) and the limits of agreement (LoA), defined as the bias ± 1.96 times the standard deviation of the differences. Wide LoA are a strong indication of poor agreement, even in cases where the bias is near zero. Finally, a linear regression line is often plotted to highlight any proportional relationship between the differences and the magnitude of the observations. Ideally, the gradient and intercept of this regression line would both be equal to zero.

An example of a Bland-Altman plot is provided in the right hand panel of Figure 4.28. In this work, the manual aKO estimates were treated as the reference values, so the differences have been plotted against the manual aKO estimates. For each automated estimation method, plots like those in Figure 4.28 were generated and the various fit statistics gathered. These fit statistics have been collated for all four of the EOCs considered in this analysis, and their mean values tabulated (see Table 4.9).

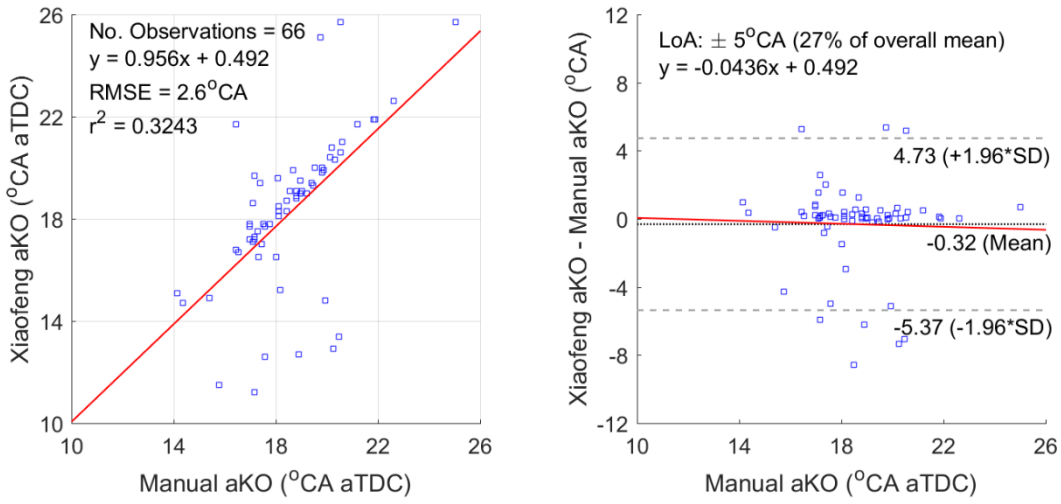

Figure 4.28 – Examples of the linear regression plots (left) and Bland-Altman plots (right) that were used to compare Xiaofeng aKO estimates with manual aKO estimates. The red lines in both plots are linear regression lines. The data displayed is for cycles that were manually identified as knocking from a sample of 600 cycles collected at 3500rpm, 19bar BMEP.

	Regression Plot			Bland-Altman Plot		
	r^2	RMSE (°CA)	Slope	Bias (°CA)	LoA (± °CA)	Slope
MMRV	0.70	2.01	1.16	0.64	4.09	0.16
Elmqvist (TV_{Factor} = 0.5)	0.28	3.28	0.75	0.84	6.66	0.25
Elmqvist (TV_{Factor} = 0.6)	0.60	1.96	0.85	0.44	3.99	0.15
Elmqvist (TV_{Factor} = 0.7)	0.61	1.91	0.86	0.65	3.89	0.14
Worret	0.65	1.83	0.89	0.52	3.69	0.13
Xiaofeng	0.61	1.85	0.92	0.36	3.80	0.14
Shahlari (Δθ = 5°CA)	0.75	1.37	0.94	0.60	2.76	0.08
Shahlari (Δθ = 7.5°CA)	0.74	1.59	0.95	0.86	3.18	0.07
Shahlari (Δθ = 10°CA)	0.48	2.49	0.87	1.89	5.01	0.16
Checkel	0.38	4.83	0.59	3.51	10.19	0.70

Table 4.9 – Mean fit statistics for each aKO estimation method when compared with manual aKO estimates across four EOCs.

To determine which of the ten aKO estimation methods best agreed with the manual aKO estimates, the mean fit statistic scores were ranked. Assuming equal weights for each fit statistic, the sum of the six ranks was then used to quantify the overall level of agreement for each aKO estimation method. This data has been tabulated in Table 4.10. The aKO estimation method that demonstrated the highest overall agreement with the manual aKO estimates across the four EOCs considered was the Shahlari method (used with a Δθ value of 5°CA). This result was confirmed by inspecting the overall ranks at each individual EOC (see Table 4.11).

Method	**Regression Plot**			**Bland-Altman Plot**			**Total Score**	**Rank**
	r^2	**RMSE (°CA)**	**Slope**	**Bias (°CA)**	**LoA (±CA)**	**Slope**		
MMRV	3	7	8	5	8	8	39	7
Elmqvist (TV_{Factor} = 0.5)	11	10	10	7	10	10	58	10
Elmqvist (TV_{Factor} = 0.6)	7	6	7	2	6	7	35	6
Elmqvist (TV_{Factor} = 0.7)	5	5	5	6	5	5	31	5
Worret	4	3	3	3	3	3	19	3
Xiaofeng	6	4	6	1	4	6	27	4
Shahlari (Δθ = 5°CA)	**1**	**1**	**2**	**4**	**1**	**2**	**11**	**1**
Shahlari (Δθ = 7.5°CA)	2	2	1	8	2	1	16	2
Shahlari (Δθ = 10°CA)	9	9	9	9	9	9	54	9
Checkel	10	11	13	11	12	13	70	11

Table 4.10 – Overall fit statistic ranks for each aKO estimation method.

Method	EOC (RPM/BMEP)				Summed Ranks	Overall Rank
	1500/ 17	1500/ 27	3500/ 19	3500/ 28		
MMRV	10	9	6	1	26	7
Elmqvist (TV_{Factor} = 0.5)	11	11	8	10	40	11
Elmqvist (TV_{Factor} = 0.6)	6	8	1	7	22	5
Elmqvist (TV_{Factor} = 0.7)	4	7	4	8	23	6
Worret	2	6	3	5	16	3
Xiaofeng	3	2	7	6	18	4
Shahlari (Δθ = 5°CA)	**1**	**1**	**5**	**3**	**10**	**1**
Shahlari (Δθ = 7.5°CA)	5	3	2	4	14	2
Shahlari (Δθ = 10°CA)	7	5	10	9	31	9
Checkel	9	4	12	13	38	10

Table 4.11 – Overall ranks for each aKO estimation method at each EOC considered.

With the exception of its bias score, the Shahlari method (Δθ = 5°CA) consistently scored in the top two for each fit statistic for all of the methods considered. The Xiaofeng aKO estimation method scored the lowest overall bias, however analysis of the regression and Bland-Altman plots suggests it was more prone to the occasional large error, hence the comparatively large LoA and RMSE scores. The adapted Worret method was the highest ranking TVE-based approach overall, achieving consistently high rankings and a mean bias of approximately 0.5°CA. Interestingly, at the two 3500rpm EOCs, the best performing methods were simple TVE approaches. Unfortunately, these methods lacked the consistency of some of the more advanced approaches, scoring poorly at other EOCs. These results do however suggest that with appropriate calibration, TVE methods can be used to good effect and the late aKO estimates with which they are associated can be overcome.

It is worth mentioning that the actual point of knock onset must have been some time before the cylinder pressure transducer detected any response. How far in advance would depend on the location of the AI centre relative to the pressure transducer. Unfortunately, with only one pressure transducer installed per cylinder, it was not possible to triangulate the location of the autoignition centre within the combustion chamber and thus estimate the true angle

of knock onset. Assuming that the nominal speed of sound inside the combustion chamber was approximately 950m/s, the maximum aKO error associated with the methods used in this work was less than 1°CA at 3500rpm.

4.6 Conclusions

Of the 12 knock intensity metrics discussed in section 3.2.2, only four were found to warrant further investigation with regards to their use for knocking cycle detection:

- Ringing Intensity was found to be of limited use with data obtained from SI engines.
- The dimensionless knock indicator proposed by Brecq did not achieve the claimed effect of levelling KI at all EOCs under non-knocking spark timing.
- In accordance with several past investigations, the unburned mass fraction of fuel at angle of knock onset was found to bear no correlation with conventional knock intensity metrics such as MAPO when viewed at a cycle-by-cycle level.
- Of the remaining nine KI metrics, only MAPO, AEPO, $KI_{CHECKEL}$ and MAFD exhibited linear correlation coefficients between one another that were less than 0.975, thus indicating that their outputs were sufficiently unique to warrant further investigation.

The KI metric normalisation methods investigated as part of this study seemed to offer little advantage with respect to KI threshold calibration compared to un-normalised KI metrics. Only the method proposed by Lee [86] appeared to show some benefit with regards to levelling the effects of background noise across multiple EOCs. However, this method also produced some unusual characteristics in the evolution of mean KI as spark was advanced. As a result, only un-normalised KI metrics were considered in the investigation into knocking cycle detection methods.

Of the twelve knocking cycle detection methods tested, the best overall match with cycle classifications made manually by the author was achieved using the MAPO/ Maximum Non-knocking Value pairing. This conclusion was drawn from data generated across four knock limited operating conditions, ranging from 1500rpm/17bar BMEP to 3500rpm/28bar BMEP. Irrespective of the KI metric used, the MNV KI threshold calibration method produced the most consistent results. The Ferraro method on the other hand was particularly inconsistent,

producing excellent results at some EOCs whilst failing to predict a single knocking cycle at others. This happened as a result of the KI threshold scaling process employed by the Ferraro method.

The novel piecewise linear regression approach to KLSA estimation and KI threshold calibration was found to perform admirably, but it offered no advantage over the MNV method at the EOCs tested in this work.

The maximum amplitude of the frequency domain (MAFD) KI metric tended to produce the worst match with manually generated knocking cycle classifications, irrespective of the knock intensity threshold calibration method that it was paired with. MAPO pairings on the other hand tended to perform very well. This observation might not be coincidental.

Of the ten aKO estimation methods tested, the best match with estimates made manually by the author across the same four knocking EOCs was achieved using the method proposed by Shahlari [1]. Simple “threshold value exceeded” techniques were also found to perform comparatively well at certain EOCs, suggesting that with proper calibration, TVE methods could provide a computationally effective way to estimate aKO.

The findings represent a valuable framework to inform other researchers in the field of knocking combustion on which techniques are needed to extract accurate and relevant information from measured cylinder pressure data recorded at high BMEPs.

Chapter 5 – Assessment of Existing Empirical Ignition Delay Correlations using a 1D Engine Model

Chapter Summary

In this chapter, the predictive capabilities of a wide range of ignition delay correlations (IDC) are evaluated by way of comparison with experimental data. First, the basics of 1D engine simulation are described and an outline of the 1D model calibration procedure used in this work presented. A detailed account of the methods employed to simulate knock in the experimental engine is then provided, including how temperature was modelled and how the tested correlations differ from one another. Finally, the results for each IDC are assessed by comparing measured and predicted knock onset times across a broad range of high load operating conditions. Finally, the best performing correlations are identified, with some recommendations given as to how they could be further improved.

5.1 Introduction

Knock is one of the primary barriers to improving the high load efficiency of SI engines. As the trend for downsizing continues, modern engines can expect to spend a much larger fraction of their lifetimes operating at high loads. In addition, legislative emissions tests have and will continue to become increasingly demanding, requiring strong emissions performance across the entire engine operating map. Emissions performance and efficiency at high load are therefore becoming increasingly important concerns for vehicle manufacturers, bringing the subject of knock into sharp focus.

It is widely accepted that knock is the acoustic by-product of auto ignition (AI) – the spontaneous ignition of some or all of the unburned charge ahead of the normally advancing flame front. AI depends on the temperature and pressure history of the end-gas, and on the anti-knock properties of the fuel [76]. The abrupt release of energy in the end gas produces pressure waves, which echo throughout the combustion chamber at the local speed of sound. These waves disrupt the thermal boundary layer, leading to increased heat transfer to the combustion chamber walls and an elevated risk of thermal failure for exposed surfaces such as the spark plug electrode and the exhaust valve bridge. Through this mechanism, it can also be self-reinforcing – the hot surfaces that promote knock become hotter, thus becoming more effective at promoting further knock events. In scenarios such as this, component failures can occur on very short time-scales. The cyclic loading that knocking pressure waves exert can also lead to fatigue failures in piston lands and rings.

Given its potential for damage, it is important for production engines to avoid knock. However, for best efficiency, this must be achieved whilst simultaneously operating as close to the knock limit as possible. To satisfy these contradictory objectives, advanced knock mitigation strategies that extend the knock limit beyond MBT must be sought, thus allowing efficient combustion phasing without the risks associated with knock.

The ability to simulate knock/AI in SI engines poses many advantages. It is particularly useful in the early stages of engine design and performance optimisation, where accurate simulation of knock limits can save considerable time when specifying boosting hardware or charge cooling equipment for example. As the cost and complexity of modern powertrains continues to grow, OEMs are repeatedly turning towards simulation as a means to reduce the cost of calibration and system validation. Indeed, several OEMs have ambitions to

develop entire vehicles in the virtual environment, complete with detailed powertrain component specifications, control strategies and calibrations that will be able to deliver the required vehicle attributes. For IC-engine and hybrid powered vehicles, accurate knock modelling tools could play an important part in achieving this aim.

In this chapter, the performance of a variety of IDCs has been assessed across a broad range of high load operating points. The primary engine parameters that have been investigated are engine speed, load and EGR rate. To achieve this objective, a 1D model of the experimental engine was built. This model was use to provide information concerning the composition and temperature of the fresh charge at intake valve closing (IVC). Matlab scripts were then used to model the temperature evolution of an adiabatic hotspot within the unburned zone, and to calculate knock onset using the methods described by each IDC under test. Cycle predictions are compared with measured data from the experimental engine, and the best performing correlations are identified.

5.2 Engine Modelling Theory

5.2.1 1D Engine Modelling Theory

The one-dimensional cycle simulation tool "GT-Power" was used throughout this study to simulate gas dynamics inside the experimental engine. Developed by *Gamma Technologies LLC.*, GT-Power is a market-leading tool in the simulation and optimisation of engine performance. With no prior experience of engine modelling, the decision to use GT-Power was based primarily on the advice of colleagues and collaborators. Alternative 1D-simulation tools such as Ricardo Wave or AVL Boost would no doubt have been equally capable from a technical point of view, however the claimed advantages of an efficient user interface, a responsive customer support network and a simple component management philosophy were enough to favour GT-Power's selection.

The primary task of the 1D flow model in GT-Power is to solve the Navier-Stokes equations, namely the conservation of continuity, momentum and energy (Equations 5.1 to 5.3 below). Resolution of these equations allows fluid properties to be estimated at any point along the flow path. These equations are solved in one dimension, therefore all the mixture properties are assumed to be uniformly distributed over any cross section perpendicular to the direction of flow. At each time step, the right hand sides of the conservation equations are determined using values from the previous time step. Integration of the results yields the quantities at the current time step. This process is repeated iteratively until convergence of the predicted fluid properties is reached.

Continuity:

$$\frac{dm}{dt} = \sum_{boundaries} \dot{m} \qquad \textit{Equation 5.1}$$

Energy:

$$\frac{d(me)}{dt} = -P\frac{dV}{dt} + \sum_{boundaries} (\dot{m}H) - hA_s\left(T_{fluid} - T_{wall}\right) \qquad \textit{Equation 5.2}$$

Momentum:

$$\frac{d\dot{m}}{dt} = \frac{dPA + \sum_{boundaries}(\dot{m}u) - 4C_f\frac{\rho u|u|}{2}\frac{dxA}{D} - K_p\left(\frac{\rho u|u|}{2}\right)A}{dx} \qquad \textit{Equation 5.3}$$

Where:

$\dot{m}$	Boundary mass flux into volume ($= \rho A u$)
m	Mass of the volume
V	Volume
P	Pressure
ρ	Density
A	Cross-sectional flow area
A_s	Heat transfer surface area
e	Total specific internal energy (internal energy plus kinetic energy per unit mass
H	Total enthalpy ($= e + P/\rho$)
h	Heat transfer coefficient
T_{fluid}	Fluid temperature
T_{wall}	Wall temperature
u	Velocity at the boundary
C_f	Fanning friction factor
K_p	Pressure loss coefficient
D	Equivalent diameter
dx	Length of mass element in the flow direction (discretisation length)
dP	Pressure differential acting across dx

To approximate the real flow path in an engine, GT-Power has a library of flow components and connections at its disposal. Pipe parts are used to represent volumes with two ports, whilst flow split parts are used to represent volumes with more than two ports. Orifice connections are used to connect flow parts. To improve model accuracy, pipes can be discretised into sequences of smaller volumes, but this increases the number of calculations to be performed and therefore increases simulation time. Flow splits can only be represented by a single volume. A simple example of this framework is provided in Figure 5.1, where the flow split volume is highlighted in red. The vector quantities of the Navier-Stokes equations are evaluated at the volume boundaries whilst the scalar quantities are assumed to be uniform over each volume and therefore are only evaluated at the volume centroids.

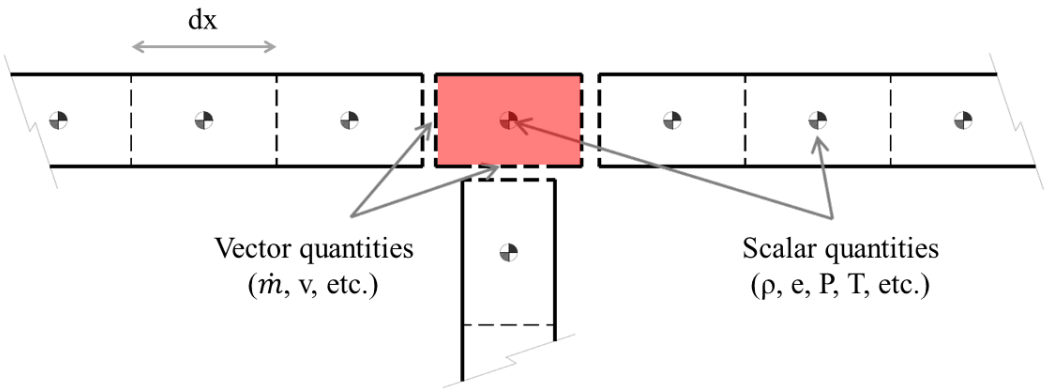

Figure 5.1 – Schematic of discretised flow path, showing vector quantities evaluated at volume boundaries and scalar quantities evaluated at volume centroids [111].

Simplified sub-models are used to represent aspects of the real flow path that cannot be approximate using pipes or flow splits (combustion chambers, turbochargers and injectors for example), thus allowing the entire engine to be modelled. Like most other 1D software packages, GT-Power also offers the ability to incorporate simple controllers within the engine model, or to couple the engine model with more advanced control logic defined externally within programs such as Matlab/Simulink.

5.2.2 SI Combustion and Knock Modelling in GT-Power

Combustion Modelling Approaches

SI combustion is modelled in GT-Power using zero-dimensional or quasi-dimensional phenomenological models, coupled with a two-zone description of the combustion chamber contents. The combustion models describe the rate of mass transfer from the unburned zone to the burned zone. GT-Power offers a variety of combustion models. The first is a non-predictive approach whereby the fuel burn rate is imposed on the model. Empirical burn rate data derived from a measured cylinder pressure trace can be used for this purpose, or alternatively an idealised cumulative burn rate profile described by a Wiebe function can be provided. A Wiebe function (see Equation 5.4) is a simple mathematical expression, which with appropriate calibration can provide a decent approximation of the cumulative burn rate profile for SI and CI engines. In GT-Power, calibration of a Wiebe function is achieved by inputting the desired 50% mass fraction burned angle (CA50), the desired combustion duration (Δθ, typically defined as CA90 - CA10) and an appropriate value for the Wiebe

exponent m (typically, m = 2-3). Start of combustion (θ_{SOC}) and the constant a are defined empirically using relationships based on the CA50 value provided and the mass fractions used to define combustion duration. Wiebe functions can be used to define semi-predictive combustion models whereby the model parameters m, CA50 and Δθ can be expressed as functions of key engine parameters such as speed and load.

$$Wiebe\ Mass\ Fraction\ Burned\ =\ 1 - exp\left[-a\left(\frac{\theta - \theta_{SOC}}{\Delta\theta}\right)^{m+1}\right] \qquad \textit{Equation 5.4}$$

As mentioned, burn rate can also be derived from measured cylinder pressure data. This practice is sometimes referred to as a "reverse run" because in contrast to conventional combustion modelling practices, cylinder pressure is the input and burn rate is the output [112]. The equations solved and assumptions made for a reverse run are the same as those made for a forward run simulation. The main difference is that in a reverse run simulation, the amount of fuel burned in each time step is iterated until the predicted cylinder pressure matches the measured cylinder pressure. GT-Power offers two approaches for calculating burn rate from measured cylinder pressure. The first uses cylinder pressure alone, and thus requires some assumptions to be made regarding difficult-to-measure parameters such as trapping ratio and residual gas fraction. Model predictions can of course be used for these parameters, however there could be a large element of uncertainty associated to their values. To minimise this uncertainty, GT offers a second approach whereby measured instantaneous intake and exhaust port pressure traces must also be provided. Imposing these dynamic pressure traces on the model ensures that air flow, trapping ratio and scavenging are predicted with the highest accuracy possible (assuming that the charge cooling effects of DI, heat transfer and the volumetric losses in the ports and across the valves are also well modelled). This second approach is called "three pressure analysis" (TPA). Thanks to the availability of measured intake and exhaust port pressure data, TPA has been used throughout this study, although primarily to ensure that accurate predictions for mixture composition and temperature at IVC could be obtained rather than for accurate burn rate predictions.

Alternatively, burn rate can be predicted using fully predictive phenomenological combustion models. For the majority of cases, this type of model is not applicable since they require extensive calibration to match measured combustion data and a detailed and quantified knowledge of the turbulence behaviour within the engine concerned. GT employs

one such model for SI combustion, capable of simulating burn rate and emissions for both homogenous and stratified air/fuel mixtures. This model includes provision for the presence of multiple spark plugs, is able to consider the effects of flame/wall interactions (if provided with CAD data of the combustion chamber) and includes a sub model for predicting laminar flame speed. A detailed description of this model is beyond the scope of this investigation and with over a dozen input parameters, calibration of this model requires considerable effort and extensive validation.

Knock Modelling Approaches

GT-Power offers a range of phenomenological knock models that can be used in conjunction with any of the previously described combustion modelling approaches. The first is the standard Douaud and Eyzat (D+E) model. This ignition delay correlation (as well as several others) is described in detail in Chapter 2. User inputs to this model are the fuel anti-knock index ($AKI = (RON + MON)/2$) plus values for two multipliers:

1) Knock induction time multiplier, M_1 (values less than 1 cause predicted knock onset timing to be advanced, i.e. knock becomes more likely)
2) Activation energy multiplier, M_2 (values less than 1 cause predicted knock onset timing to be retarded, i.e. knock becomes less likely)

The resulting Livengood and Wu (L+W) integral (converted for integration with respect to crank angle instead of time) is expressed as:

$$I\,(\theta) = \frac{1}{6(RPM)} \int_{\theta_{IVC}}^{\theta} \left[17.68\, M_1 \left(\frac{AKI}{100}\right)^{3.402} P^{-1.7} exp\left(\frac{3800}{M_2 T}\right) \right]^{-1} d\theta \qquad \textit{Equation 5.5}$$

Where pressure (P) is in atmospheres and temperature (T) is in degrees Kelvin. Knock is predicted to occur when $I = 1$.

GT-Power provides two alternative single-step correlations, the closely related Franzke and Worret correlations [90, 113]. Both of these correlations build upon the D+E correlation, using similar coefficient values and incorporating additional constraints to ensure that knocking cycle classifications are only accepted if knock is predicted to initiate before a critical crank angle. This critical crank angle is determined for any EOC using experimental

data collected from the engine in question at a single, reference knock-limited operating point. The implicit assumption is that the largest observed mass fraction burned (MFB) at aKO is nominally constant for all knock-limited operating conditions. Worret observed that actually, the largest MFB at measured knock onset angles varied somewhat between operating conditions. He developed several empirical relationships to describe how this upper MFB limit varied as a function of the 50% mass fraction burned angle and λ for the engine used in his experiments. Unfortunately, to the author's best knowledge, the evidence supporting these empirical relationships has only been published in German. Uptake of these correlations within the literature has been minimal, possibly due to the aforementioned language barrier, but also possibly due to their increased complexity and the need to provide experimental data from a reference knock-limited EOC. For these reasons, neither the Franzke nor Worret correlations have been considered in this investigation.

The fourth phenomenological knock model that GT-Power offers is a 3-Arrhenius formulation based on ignition delay predictions obtained using Ra's reduced CKM for multi-component gasoline surrogates [66]. No information is provided regarding the composition or expected RON/MON of the gasoline surrogate used in these simulations, or indeed the range of conditions considered in the calibration of this model. The overall form of this IDC is described by Equation 5.6 where parameters a_i – f_i are constants (see Table 5.1), M_1 and M_2 are the induction time and activation energy multipliers respectively, and square brackets are used to indicate concentrations (in mol/m^3). The diluent concentration is equal to the sum of the N_2, CO_2 and H_2O concentrations. Overall ignition delay is expressed in the same 3-Arrhenius form described by Equation 2.5 in Chapter 2.

$$\tau_i = M_1 a_i \left(\frac{AKI}{100}\right)^{b_i} [Fuel]^{c_i}[O_2]^{d_i}[Diluent]^{e_i} exp\left(\frac{f_i}{M_2 T}\right), \quad i = 1,2,3 \qquad \textit{Equation 5.6}$$

i	a	b	c	d	e	f
1	4.4e-7	3.613	-0.640	-0.564	0.398	1.3e4
2	1.2e4	3.613	-0.640	-1.4596	0.487	-1960
3	8.9e-7	0	-0.250	-0.547	0	1.7e4

Table 5.1 – Parameter values for GT-Power 3-Arrhenius IDC [63]

Finally, GT-Power also offers the capability for users to incorporate their own knock models using subroutines written in either the FORTRAN or C computing languages. An example FORTRAN script for the D+E correlation is provided to act as a starting point, however with no FORTRAN experience, this script was of little help to the author. To minimise the challenge of implementing IDCs not offered as standard within GT-Power, the decision was made to use Matlab to simulate knock. Matlab was used extensively to process and present experimental cylinder pressure data, therefore it made sense to also include the knock modelling functions of this investigation within its remit.

5.3 Engine Model Development

Collaborators at JLR kindly provided a partially validated, full-engine model of a slightly different version of the experimental engine (2.0 litre displacement, 9:1 CR). This model formed the basis of the engine models used throughout this investigation.

Given the availability of measured cylinder pressure and intake/exhaust port pressure data, the decision was made to use TPA to model the combustion process throughout this investigation. Since TPA simulations can only be run on single cylinder models, the first task was to reduce the full-engine model to a single cylinder. TPA models also only simulate gas behaviour between the locations of the intake and exhaust port pressure measurements, therefore all flow components upstream and downstream of these two locations had to be removed as well. Several additional modifications were also required to create the TPA model:

- The end environments (the green objects at either end of Figure 5.2) were changed to TPA-specific parts so that instantaneous port pressures could be imposed. TPA end environments contain special logic to vary the temperature about the measured average temperature in accordance with pressure fluctuations and reverse flow [112].
- The original semi-predictive Wiebe combustion model was removed and replaced with a TPA burn rate model based on the first law of thermodynamics, thus allowing the model to read in measured cylinder pressure data.

- Controllers for the pipe friction property of the intake and exhaust runner pipes were added to the model. The purpose of these controllers was to minimise the appearance of spurious pressure oscillations within the ports when the intake and exhaust valves are shut. This is achieved by artificially increasing the friction multiplier applied to these parts when the relevant valves are shut.
- In keeping with TPA best practice, the discretisation length for intake and exhaust pipe parts was decreased to 0.20 and 0.25 times the cylinder bore respectively. The simulation time step was also halved to 0.25°CA.
- The injector part was changed from an AFR-targeting component to one that injects a user-imposed quantity of fuel per cycle. For each simulation, the required injected mass of fuel was calculated from measured fuel flow rates.
- Minor changes to intake port lengths were required after independent measurements of the intake and exhaust port geometries revealed slight errors in the original model.

The resulting single cylinder model is shown below in Figure 5.2. The flow path has been represented using pipe and flow split components. Connections between the runners and the TPA end environments are defined using smooth orifice connections. The large “engine” component at the bottom of the model contains the options for specifying engine type, cylinder geometry and the friction sub-model. The “cylinder” component in the centre of the model contains the options for specifying burn rate, heat transfer, combustion chamber wall temperatures, blowby and fuel evaporation sub-models.

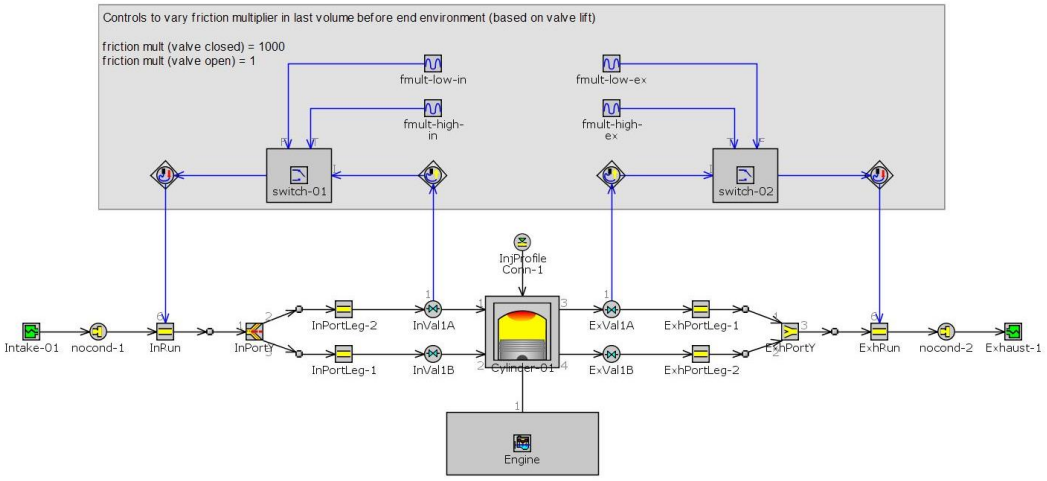

Figure 5.2 – Schematic of the single-cylinder GT-Power model used throughout this investigation.

In addition to the "three pressures", the following measurements were used to improve the boundary conditions description within the model:

- Intake port air temperature measurements were used to dictate the temperature of the inlet air at the inlet end environment.
- Measured hydrocarbon (HC) and carbon monoxide (CO) concentrations in the exhaust gas were used to impose fuel MFB and combustion efficiency limits on the simulations.
- Measured discharge coefficient data for both intake and exhaust valves was already present in the model received from JLR. This data was reportedly obtained from flow bench tests of the final experimental head assembly at Lotus Engineering. In keeping with GT-Power best practice, surface finish for the intake and exhaust ports was defined as perfectly smooth since the effects of friction in these parts was effectively included in the valve discharge coefficients. Elsewhere in the model, the default roughness value for steel was used (0.046mm). The correct valve lift profiles were used for both intake and exhaust cams.
- The injection profile and pressure were set to measured values. Rail pressure and SOI were measured by the host system via the ECU, whilst injection duration was determined from injector signal measurements obtained using current clamps and the high frequency data acquisition system.
- Finally, a custom fuel template was generated based on measured properties of the fuel used throughout this investigation. This template was used to list the following fuel properties – heat of vaporisation, density, carbon/hydrogen/oxygen content and lower heating value (LHV). Where measured data was not available, the properties listed in the "Indolene" fuel template were used. Indolene is a gasoline surrogate with similar LHV and C:H ratio as the experimental base fuel.

Where measured data was not available, estimates were used. For example, wall temperatures of 350K were assumed for the intake runner and ports. Accuracy was not that critical in this case since early simulation results showed that model predictions were relatively insensitive to this parameter (presumably because the pipe lengths associated with the intake runner and ports were so short – less than 80mm in total). Similarly, exhaust valve bridge temperature measurements were assumed a valid approximation for the mean cylinder head surface temperature (in the absence of any other temperature measurements

within the cylinder head). This assumption was justified on the basis that the valve bridge measurement itself was taken several millimetres away from the combustion chamber surface, resulting in temperature readings somewhat cooler than the actual cylinder head surface temperatures at this location. Furthermore, whilst it is true that the exhaust valve bridge is one of the hotter regions of the cylinder head, the exhaust valve faces (which occupy a considerable portion of the cylinder head area) are likely to have been considerably hotter than the measured valve bridge temperatures. On balance therefore, the measured valve bridge temperatures represented a sensible "mean" cylinder head surface temperature to use within GT-Power.

Exhaust valve bridge temperatures were observed to vary linearly with BMEP, therefore linear relationships with BMEP were also assumed to describe the mean surface temperatures for the piston crown and cylinder liner. Minimum and maximum temperature values for these surfaces were estimated based on information acquired from the literature and from collaborators. Finally, inlet air was assumed to be completely dry since that is how air was delivered to the FIS from the compressed air plant.

5.4 Engine Model Calibration

5.4.1 Input Data Quality Checks

Prior to calibrating the TPA model, a number of input data quality checks were performed. Firstly, the instantaneous intake and exhaust port pressure measurements were checked for sensor drift by comparing the mean of their output over one complete cycle with time-averaged gauge pressure measurements. The time-averaged and instantaneous pressure measurements were taken at approximately the same locations on the engine therefore significant differences between their mean values was not expected. Differences greater than 0.01 bar were adjusted for by applying offsets to the instantaneous pressure traces within GT-power. Any offset applied to the intake port pressure trace was also applied to the cylinder pressure trace in order to preserve proper referencing of the cylinder pressure signal.

Secondly, the target air mass flow was double-checked. Unfortunately, one of the disadvantages of the FIS used in this investigation is that airflow to the engine was not measured directly. Instead, it was inferred from two separate measurements – total airflow

into the FIS (measured using an orifice plate) and the airflow that was dumped to the cell (measured using an ABB airflow meter). Airflow to the engine was assumed equal to the difference between these two measurements. For each operating condition used in the calibration process, the MAF reported by the FIS was double-checked against alternative MAF estimates. These estimates were obtained from combinations of fuel mass flow rate (measured using a Coriolis flow meter accurate to within ±0.1%) and AFR or exhaust lambda. The emissions analysis equipment estimated AFR from measured exhaust gas composition using the Spindt correlation for gasoline. Lambda on the other hand was measured using a "standard" production-level wideband oxygen sensor via the ECU, and separately using a LabCell ECM 5230 EGR analyser. Both lambda measured were obtained at approximately the same location in the exhaust system, and both were accurate to within $\lambda \pm 0.008$ according to the product specification.

Figure 5.3 below shows the variability of the various MAF measurements for a boost ramp carried out at 3500rpm. The MAF estimate derived from the MEXA 7000 emissions analyser has been used as the reference measurement on the x-axis. The production and LabCell lambda meters both estimate slightly lower MAF values compared to the MEXA, but agree very well with each other. The FIS on the other hand appears to over-estimate MAF at high loads and under-estimate MAF at low loads (at least at this particular condition). Similar analysis performed across a range on conditions suggests that estimating MAF from the LabCell lambda meter readings is likely to be the most consistent and reliable approach. The "LabCell lambda MAF" was therefore used as the calibration target for the 1D model.

Thirdly, the measured cylinder pressure traces were visually inspected to check for TDC errors or any other unexpected characteristics that might indicate a malfunctioning pressure transducer. TDC errors of as little as 1°CA can result in IMEP errors of 0.5bar, and would have made it difficult for GT-Power to achieve a good qualitative match with the measured data.

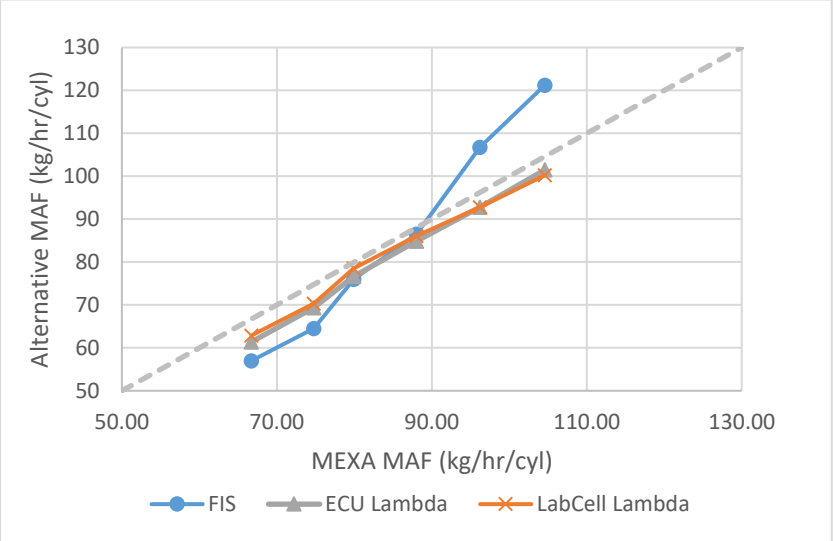

Figure 5.3 – Variability of indirect mass air flow (MAF) measurements used to calibrate the air path of the GT-Power TPA model. Data recorded on the experimental engine at 3500rpm, with 30°CA intake cam advance and 20°CA exhaust cam retard.

5.4.2 Calibration Objectives

Having verified the validity of the measured input data, the next step was to begin calibrating the GT model. This was achieved using experimental data from a range of operating conditions and the approach detailed in the GT-Power user manual. The primary aims of the calibration process were:

1. Match predicted and measured air mass flow rates to within ±5%
2. Achieve a good qualitative agreement between predicted and measured pressure traces
3. Achieve an overall energy balance error of less than ±5%.

Gamma Technologies (GT) recommends calibrating the air path at the operating condition corresponding to the highest expected air mass flow (i.e. where the pressure losses were expected to be greatest). In this work, experimental data was collected at two primary engine speeds – 1500rpm and 3500rpm. At each speed, detailed boost ramps were performed between manifold pressures of 1.6bar and 3.0bar absolute in 0.2bar increments. These data sets were used for model calibration because they were able to provide a broad range of air mass flow conditions with which to validate the model and confirm that all calibration targets were achieved. Table 5.2 summarises the experimental engine operating

conditions used for calibrating the 1D model. 300-cycle log-averages of the three pressures required for TPA were used for this stage of the investigation, all of which were taken from the nominal KLSA at each EOC.

Engine Speed (RPM)	Intake Cam Phase Advance (°CA)	Exh. Cam Phase Retard (°CA)	Intake Manifold Press. (bar abs)	Exh. Manifold Press. Model
1500	30	20	1.6 – 3.0	T/C Biased (high)
1500	60	30	1.2 – 2.8	S/C Biased (low)
3500	30	20	1.6 – 2.6	T/C Biased (high)
3500	60	30	1.2 – 2.8	S/C Biased (low)

Table 5.2 – Engine operating conditions used for calibration and subsequent validation of 1D single cylinder model.

The use of a FIS meant that exhaust manifold pressure was controlled manually depending on the assumed turbo-machinery configuration of the engine. The relationships used to guide this process were derived from experimental data. In this work, two turbo-machinery configurations were assessed – a turbocharger-biased configuration and a supercharger biased configuration. The turbocharger-biased model resulted in higher exhaust manifold pressures for a given boost pressure compared to the supercharger-biased model. The supercharger-biased exhaust manifold pressure model was based on data gathered from a 2.0 litre/9:1 CR version of the experimental engine fitted with a Garret GT30 turbocharger low pressure stage and an Eaton R410 supercharger high pressure stage. The turbocharger-biased model one the other hand was based on experimental data gathered from a 1.0 litre, three-cylinder engine equipped with a fixed geometry turbocharger as the low pressure stage and a CVT driven centrifugal compressor high pressure stage.

A good qualitative agreement between measured and predicted cylinder pressure traces was important for a number of reasons. Mismatches in cylinder pressure during the compression stroke for example can be indicative of a wide range of model errors such as incorrect intake manifold pressure, intake valve timing, heat transfer or compression ratio. Detailed inspection of cylinder pressure and intake port pressure traces during the pumping loop can

be useful to eliminate errors in this domain. Meanwhile, mismatches during the combustion event point to inaccurate prediction of burn and heat transfer rates.

Finally, GT-Power accounts for energy balance discrepancies by applying a multiplier to the lower heating value (LHV) of the fuel. Small LHV-multiplier values are a good indication that a model is well calibrated, but one must be careful to ensure that two modelling errors with opposing energy balance effects do not simply cancel one another out. Care and judgement must be exercised throughout the calibration process to ensure a sensible model calibration is achieved. The aim was to obtain a model calibration that maintained the LHV multiplier between 0.95 and 1.05 for all conditions listed in Table 5.2.

5.4.3 Blowby and Fuel Evaporation Sub-Models

The following paragraphs provide a summary of the calibration process. Firstly, an appropriate leak path diameter was determined to match predicted and measured blowby mass flow rates. Using the FIS meant that there were no low pressure points in the intake system to return the blowby gases. Blowby gases were therefore vented to the cell rather than returned to the intake of the engine. It was therefore important to simulate blowby since it represented a form of energy loss that would otherwise not have been considered by GT-Power[13]. In all cases, an equivalent diameter of 0.5mm was sufficient to match measured blowby rates.

Secondly, a cylinder evaporation sub-model was implemented to describe the rate of evaporation of the injected fuel. Without such a model in place, GT-Power assumes that evaporation only occurs at the flame boundary (i.e. after the start of combustion and at a rate determined by the burn rate). This approach would fail to capture the charge cooling effects of direct injection, and thus would likely lead to large errors in both the volumetric efficiency and the temperature at IVC. Since temperature and composition can significantly affect the likelihood of knock, accurate air flow and temperature predictions were critical to this work. GT-power models in-cylinder evaporation using Equation 5.7, where m_{liq} is the

[13] Subsequent investigation revealed that the blowby model within GT-Power actually only considers the transfer of air and burned gas species between the combustion chamber and the crank case, and not unburned fuel. Still, this would have a small effect on predicted trapped AFR, as well as the predicted cylinder pressure. It was therefore still worth considering, even if the primary reason for doing so transpired to be ignored by GT-Power.

mass of the liquid species, RPM_{ref} and T_{ref} are the reference speed and temperature (4000rpm and 600K respectively), $CA50_{fuel}$ is the crank angle duration for 50% of the fuel mass to evaporate at the reference condition, and a and b are the temperature and speed dependency exponents.

$$\frac{dm_{liq}}{dt} = -4.16\, m_{liq} \frac{RPM_{ref}}{CA50_{fuel}} \left(\frac{T}{T_{ref}}\right)^{a} \left(\frac{RPM}{RPM_{ref}}\right)^{b} \qquad \textit{Equation 5.7}$$

Unfortunately, evaporation rate data for the fuel used in this work was not available so several assumptions were made regarding its evaporation characteristics. The default values of 1.0 were assumed for both the temperature and engine speed dependency exponents, resulting in linear relationships between evaporation rate and temperature/engine speed. This only left the 50% evaporation duration to estimate. Very little evidence could be found to support estimates of this parameter for the evaporation of gasoline sprays in turbulent flow fields. Huang recently published gasoline spray images for a multi-hole injector operating at 60bar injection pressure into a constant volume chamber at atmospheric pressure [114]. For air temperatures of 400K, flash boiling of the injected gasoline occurred and complete evaporation was achieved within 6ms of the end of injection. The chamber was large enough to avoid wall wetting and the flow field could be considered static in comparison to that inside a reciprocating engine. One would therefore expect evaporation rates to be somewhat faster at the reference condition of GT's evaporation sub-model, where turbulent mixing would be significant and the temperature some 200K hotter.

Huang's observations have been used as a starting point for determining an appropriate $CA50_{fuel}$ value. At 4000rpm (the reference speed for $CA50_{fuel}$), 6ms equates to 144°CA. The maximum temperature of Huang's experiments (400K) is a good approximation for the average temperature during the intake and compression strokes. Based on these observations, it seems reasonable to assume that for the injection timings used in this work (at least 300°CA bTDC firing), all of the liquid fuel would be expected to evaporate before the start of combustion. A sweep of $CA50_{fuel}$ values was conducted within GT-Power for several EOCs. From Figure 5.4 one can see that at 3500rpm/280kPa intake manifold pressure, a value of $CA50_{fuel}$ = 25°CA resulted in virtually all of the injected fuel evaporating before TDC firing. Similar trends were observed at other speed/load operating points, with 25°CA being the largest value of $CA50_{fuel}$ that resulted in complete evaporation of the fuel before combustion in all cases.

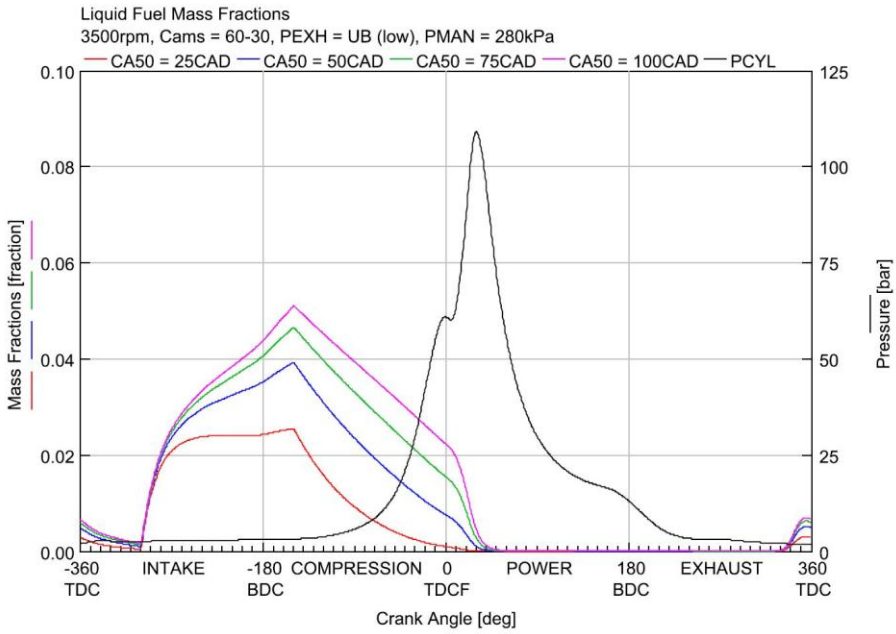

Figure 5.4 – Effect of fuel vaporisation constant $CA50_{fuel}$ on predicted liquid fuel mass fraction at 3500rpm, 280kPa intake manifold pressure.

The impact of $CA50_{fuel}$ on the predicted temperature at IVC is shown in Figure 5.5, with the effect of assuming no fuel evaporation added for reference (i.e. infinite $CA50_{fuel}$). As expected, fuel evaporation rate has a significant impact on predicted charge temperatures at IVC. Differences of approximately 15K were predicted between the two extreme cases of $CA50_{fuel}$ = 25°CA and "no evaporation". The impact of this temperature difference on the predicted temperature evolution of the end gas and on predicted knock onset is illustrated in Figure 5.6. Here the standard D+E correlation has been applied to simulate knock at 3500rpm/280kPa intake manifold pressure. Adiabatic compression from IVC and a constant ratio of specific heats equal to 1.3 have been assumed to simulate the temperature evolution of the end gas. In this case, the difference in knock onset times between the two limiting cases (labelled "No Evap" and "100% Evap" for brevity in Figure 5.6) is 2.9°CA. Across the four of the operating conditions plotted in Figure 5.5, the average difference in knock onset predictions between the two limiting cases was 3.5°CA. This difference would constitute a significant error and highlights the importance of considering the charge cooling effects of fuel evaporation when accurate charge temperature predictions are required (i.e. when simulating knock).

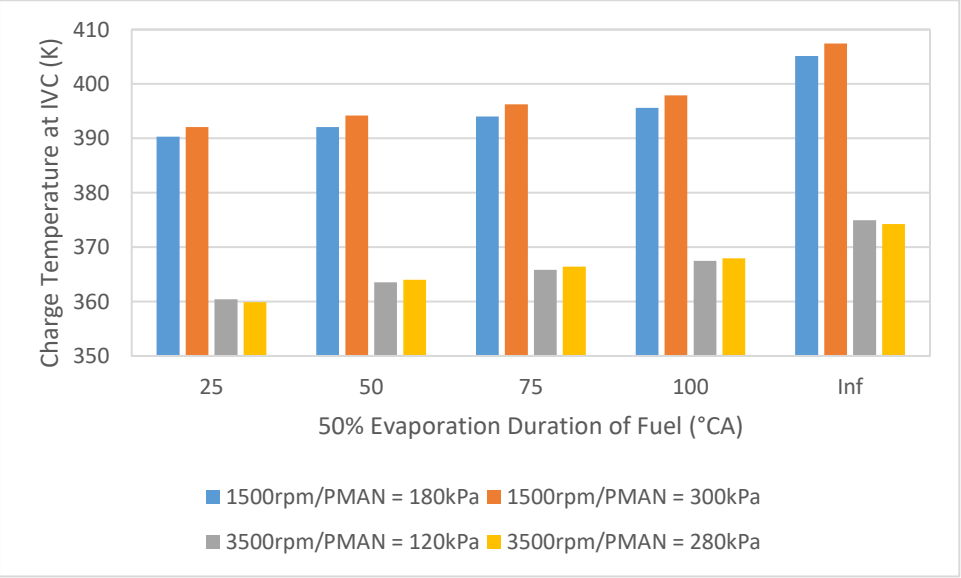

Figure 5.5 – Effect of fuel vaporisation constant $CA50_{fuel}$ on predicted fresh charge temperatures at IVC for a range of engine operating conditions.

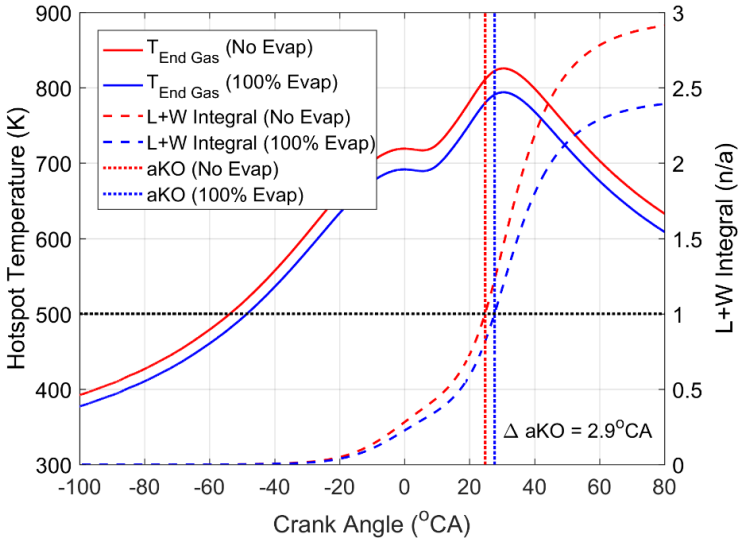

Figure 5.6 – Influence of the charge cooling effects of fuel evaporation on predicted hotspot temperature evolution and knock onset. Condition modelled is 3500rpm, intake manifold pressure of 280kPa. "100% Evap" refers to the case where $CA50_{fuel}$ = 25°CA and all fuel evaporates before the start of combustion.

Based on the above observations, a $CA50_{fuel}$ value of 25°CA was applied to the 1D model. Although this value may not be particularly accurate, the assumption of complete fuel evaporation before TDC firing is certainly more realistic than assuming no evaporation until ignition. To complete calibration of the evaporation sub-model, it was also assumed that 10% of the energy required to evaporate the fuel comes from the combustion chamber walls. This assumption was justified since a degree of wall wetting would be expected with any GDI system, particularly at high loads and 200bar injection pressures.

5.4.4 Calibration of key engine parameters

Following calibration of the blowby and fuel evaporation sub-models, an iterative process of fine-tuning key model parameters was undertaken to satisfy the calibration objectives listed at the start of this section. The parameters included in this process are listed below.

- **Intake and exhaust cam phase angles** (ICP and ECP respectively). Assembly tolerances of experimental engines and cam position feedback errors were assumed capable of producing cam-timing discrepancies of up to ±2°CA. Valve lash was fixed at 0.1mm for both intake and exhaust cams in the 1D model (common practice for engines equipped with hydraulic lash adjusters).

- **In-cylinder convective heat transfer multiplier**. Convective heat transfer inside the cylinders was estimated using the default "WoschniGT" model – a slightly modified version of the classic Woschni correlation without swirl. The modifications are designed to consider the increased levels of heat transfer that occur when the intake and exhaust valves are open and flow velocities are high. Despite these changes, it is still widely believed that the WoschniGT correlation underestimates convective heat transfer rates. As a result, it is normally necessary to apply a scalar multiplier in the range 1.1 – 1.4 to the Woschni heat transfer predictions [112].
- **Geometric compression ratio**. Assembly tolerances and measurement errors were assumed capable of producing a CR tolerance of ±0.25. This figure has been used internally within the PVRC on other gasoline-engine simulation exercises. Modifications to the cylinder head of the experimental engine to accommodate central and side-mounted cylinder pressure transducers were estimated to decrease CR by as much as 0.25. This reduction in CR corresponds to an increase in clearance volume of less than 5%, which is plausible given that the cylinder head was originally designed to accommodate a spark plug in the side mounting location and an uncooled M5 pressure transducer in the central mounting location. Throughout this investigation, M10 pressure transducers were installed in both locations. Being slightly recessed, switching to two M10 pressure transducers would have increased the clearance volume relative to the original spark plug + M5 pressure transducer configuration.

Starting with the measured CR and initial estimates for the other parameters, IVP and EVP were adjusted first in order to achieve a satisfactory match with measured air mass flow. CR was then adjusted to achieve a good match between measured and simulated cylinder pressure traces during the compression stroke. Finally, the Woschni convective heat transfer multiplier was adjusted to match measured cylinder pressure during the expansion stroke and to achieve an overall energy balance error or less than ±5%. This process was iterated until a single combination of model parameters capable of satisfying all of the calibration objectives across all of the operating conditions listed in Table 5.2 was obtained. Table 5.3 below lists the final combination of values for these parameters.

Parameter	Target/Book Value	Calibrated Value
Intake Valve Phase (IVP) Adjustment	±2°CA	- 2°CA
Exhaust Valve Phase (EVP) Adjustment	±2°CA	0°CA
Woschni Convective Heat Transfer Multiplier	1.1 – 1.4	2.0
Geometric Compression Ratio	10.68 +0.25/ -0.50	10.2

Table 5.3 – Parameter values for the calibrated 1D engine model used in this work.

From Table 5.3, one can see that it was necessary to retard the intake valve event by the maximum permissible amount in order to achieve an acceptable level of agreement between measured and predicted MAF. Predicted MAF was very sensitive to intake valve timing because of the effect of cylinder volume at IVC. The experimental engine employed a high degree of Miller-timing (late IVC). Retarding the intake valve event therefore reduced the cylinder volume at IVC and which in turn reduced the trapped mass of air per cycle. Exhaust valve timing had a significant impact on MAF predictions at operating conditions with high valve overlap (i.e. where ICP/ECP = 60/30°CA). The combination of a long overlap period and high positive pressure differential between the intake and exhaust manifolds as a result of the supercharger-biased exhaust pressure model used for 60/30 cam valve timings encouraged short circuiting of the fresh charge straight into the exhaust manifold. At the tests conditions utilising ICP/ECP = 30/20°CA, the combination of a shorter valve overlap period and higher, turbocharger-biased exhaust manifold pressures meant that the exhaust valve timing had a much less pronounced effect of MAF predictions. To obtain a single calibration across all four EOCs, it was necessary to fix the EVP adjustment at 0°CA and only use the intake cam to target measured MAF data.

Since IVP affected the dynamic compression ratio of the engine model, the geometric CR could only be calibrated once IVP had been finalised. In order to achieve a good agreement with measured cylinder pressure traces during the compression stroke it was necessary to reduce the geometric CR of the model by the maximum permissible amount.

Finally, a convective heat transfer multiplier of 2.0 was required to obtain acceptable overall energy balance errors across all four EOCs. This value is large compared to the upper limit

suggested by GT, however it is within the limits of those found in the literature (Vancoillie applied a multiplier of 4.5 during the expansion stroke when simulating combustion in a single cylinder CFR engine run on methanol [79]). A number of factors could explain this high value. Firstly, the experimental engine was subject to high boost pressures. This would have created high velocity inlet jets, which would have increased convective heat transfer between the combustion chamber walls and the incoming gasses. Secondly, the intake ports of the experimental engine were designed with the specific purpose of maximising tumble, a form of large-scale turbulence that helps to maintain the kinetic energy of the inlet jets during the compression stroke and increase overall turbulence levels during combustion. High levels of turbulence would be expected to increase convective heat transfer over the majority of the four-stroke cycle relative to a typical engine operating at lower manifold pressures and with less well-optimised intake ports. Furthermore, since the blowby model used in this work does not consider the transfer of fuel into the crankcase, this form of energy loss has been effectively lumped into the convective heat transfer multiplier. Measured blowby rates indicate that up to 1% of the combined air/fuel mass was vented to the test cell during the experiments utilised herein.

5.4.5 1D Model Calibration Results

Figure 5.7 presents the MAF predictions of the calibrated 1D model across all four EOCs considered. For the most part, the MAF predictions are within ±5% of the measured MAF (itself inferred from measured lambda and fuel flow rate). The predictions are generally towards the upper end of this range however. Potential reasons for this include low imposed inlet air temperatures, insufficient intake port and combustion chamber heat transfer to the fresh charge during the intake stroke, low imposed intake port and cylinder wall temperatures, excessive fuel evaporative cooling and/or high imposed intake port pressures.

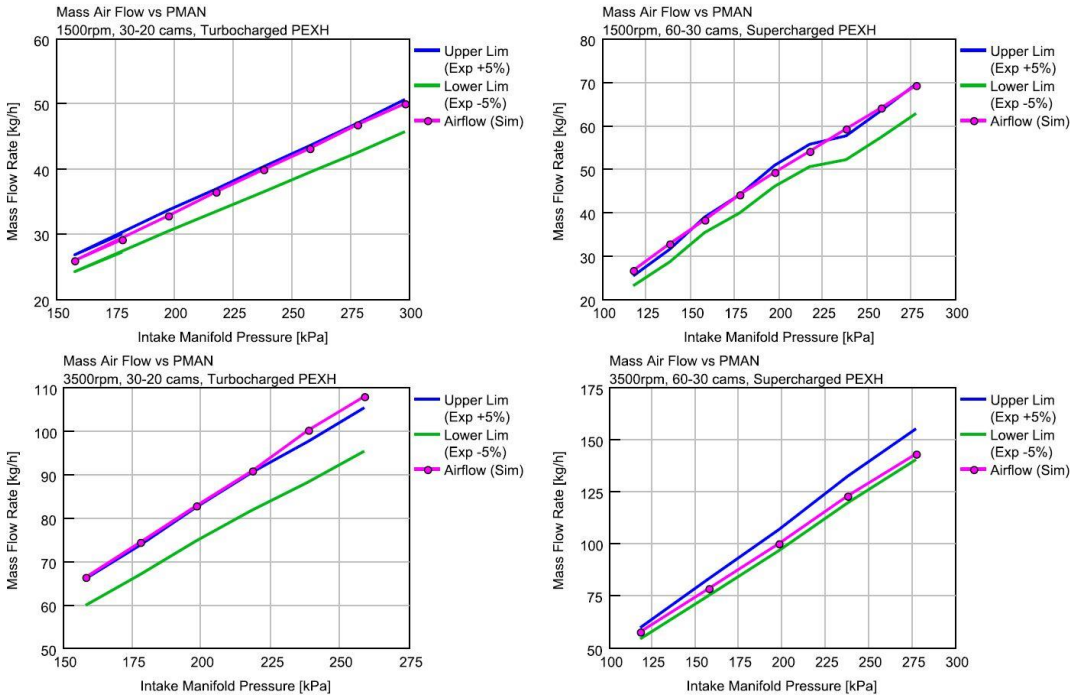

Figure 5.7 – 1D model mass air flow (MAF) predictions, compared with ±5% measured MAF limits.

As mentioned previously, the forward and reverse discharge coefficients for both the intake and exhaust valves were determined experimentally, and there was little doubt regarding their accuracy. Within reasonable limits, the influence of combustion chamber wall temperatures and intake port heat transfer were investigated, but both were found to have little effect on predicted MAF. In-cylinder convective heat transfer has already been discussed and with a high multiplier value already being utilised, the author was reluctant to increase this further just to lower the predicted MAF. The air charge temperatures imposed on the model were from measured data, all of which appeared consistent with other temperature measurements within the intake system. Fuel evaporation has already been discussed, and in the absence of any measurements to support re-calibration of the fuel evaporation sub-model, no changes were made. This only left high intake port pressures as a possible explanation for the high MAF predictions, which is a plausible given that the port pressure traces were generally adjusted upwards to match the measured intake manifold pressure. On balance however, the magnitude of these adjustments was typically less than 0.02bar, which would not be expected to have had a significant impact on predicted MAF.

Of course, it is possible that the measured MAF was lower than it should have been due to errors in the lambda or fuel flow-rate measurement. However, the lambda measurement used throughout this work correlates well with other independent lambda measurements

taken at the same location in the exhaust system, and the Coriolis flow meter has a measurement accuracy of ±0.1%. Overall MAF measurement errors are therefore not expected to be significant. As a result, the author has been unable to diagnose the source of the relatively high MAF predictions from the 1D model[14].

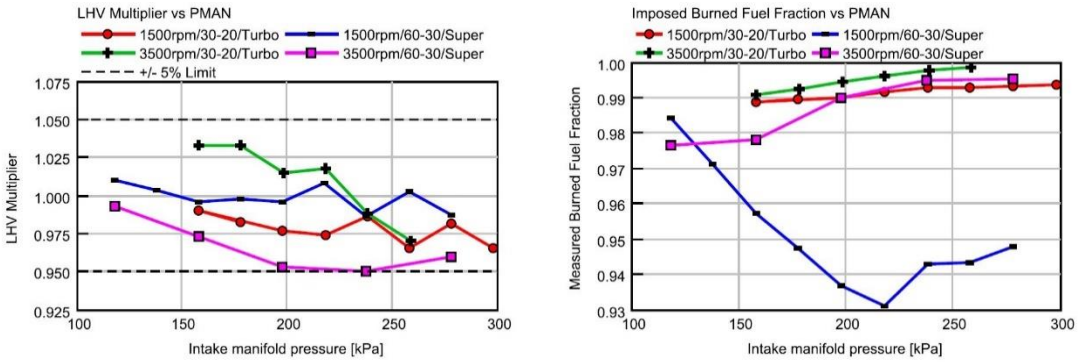

Figure 5.8 – Left: Lower Heating Value (LHV) multiplier values applied by GT to balance the energy in-flows and out-flows for the 1D model. Right: Imposed fuel mass fraction burned values (calculated from measured unburned hydrocarbon concentrations).

The left hand panel of Figure 5.8 presents the LHV multiplier values applied by GT-Power to balance the energy inflows and outflows for each simulation run. The LHV multiplier results are within the ±5% limits at all conditions, indicating acceptable energy balance errors within the model. Interestingly, in all cases the LHV multiplier decreased as load increased, suggesting that GT-Power had to remove a larger proportion of energy from the system at higher loads. This observation could indicate that the single value of 2.0 used for the Woschni convective heat transfer multiplier was not large enough at high loads. Alternatively, this downward trend could be a product of increased post-flame oxidation of crevice flows, as described below. At higher loads, combustion phasing had to be retarded in order to avoid knock. Hydrocarbon (HC) emissions are known to decrease as spark timing is retarded. Eng [115] showed that the primary reason for this decrease is that as combustion phasing is retarded, there is more time for the crevice HCs to diffuse across the quench volume and into the path of the oncoming flame front, thus allowing them to be burned normally at the tail end of the primary combustion event.

[14] Interestingly, this issue has affected collaborators to the same extent, even in full engine models where TPA has not been used.

A secondary effect of retarded combustion phasing is that burned gas temperatures remain hotter for longer during the expansion stroke. Hotter temperatures accelerate the oxidation of hydrocarbons that escape the main combustion event but that subsequently diffuse far enough out of the crevices that they become entrained within the hot burned gases and react with any available oxygen. The result of this secondary effect is an increase in oxidation rates of hydrocarbons during the latter stages of the expansion stroke and even into the exhaust stroke. Hydrocarbon oxidation reactions are reported to freeze at approximately 1300-1500K [116], which in this work corresponded to the approximate location of EVO. The net effect of this increase in post-flame oxidation chemistry is lower measured unburned hydrocarbon (uHC) concentrations in the exhaust gas. Throughout this investigation, uHC measurements that include the effects of post-flame oxidation have been used to impose burned fuel mass fraction targets on the GT-Power simulations. These burned fuel mass fraction targets are shown in the right hand panel of Figure 5.8. At no point however have the effects of post-flame oxidation been included in the 1D engine models. Removing energy from the system by reducing the LHV multiplier at conditions where post-flame oxidation is likely to have been more prevalent could therefore have been GT's way of accounting for this effect.

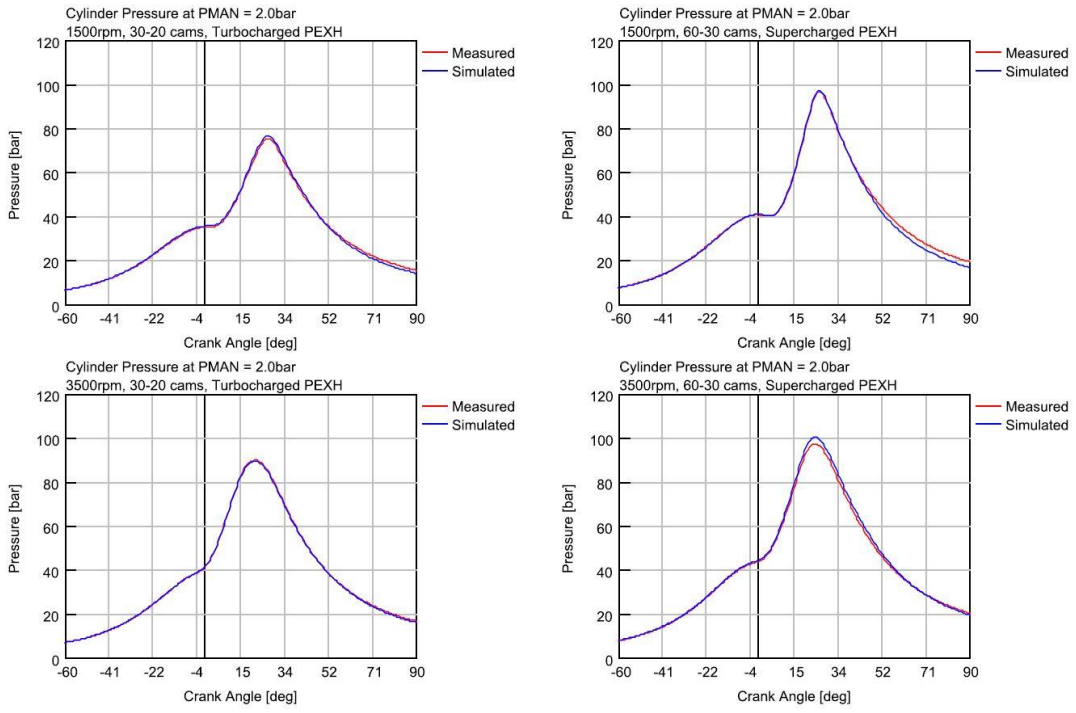

Figure 5.9 – 1D model cylinder pressure predictions at 2.0bar intake manifold pressure for all four EOCs considered during the model calibration process.

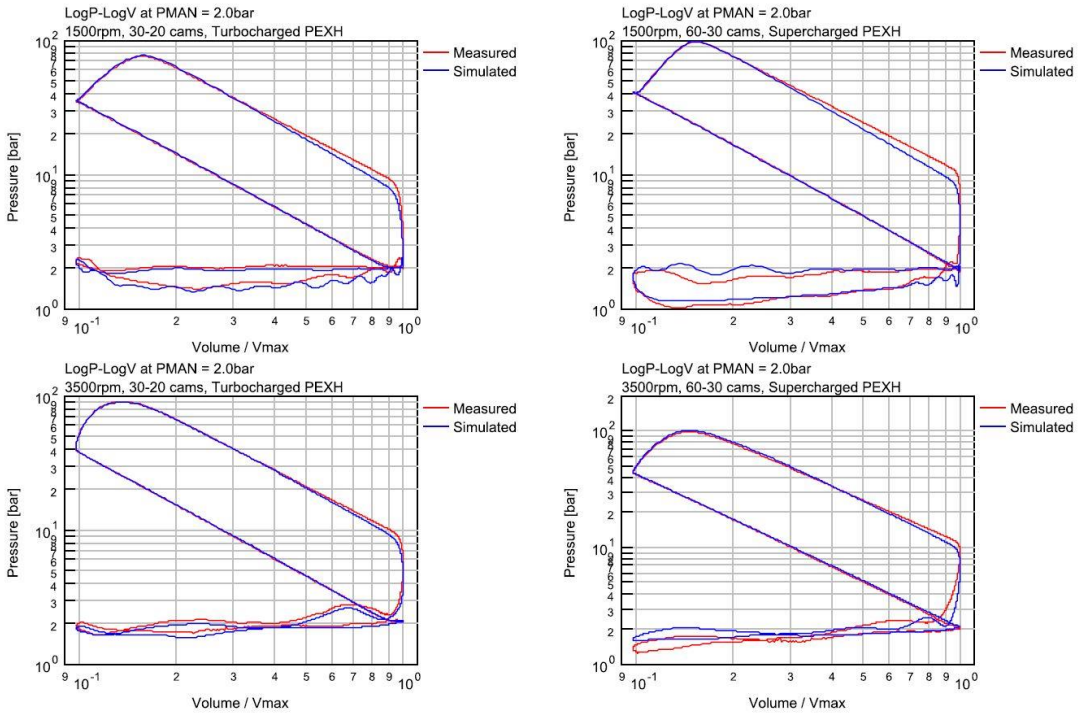

Figure 5.10 – 1D model cylinder pressure predictions plotted on a Log(Pressure)-Log(Volume) axis. Data presented for the 2.0bar intake manifold pressure condition at all four of the EOCs considered during the model calibration process.

Figure 5.9 and Figure 5.10 present the cylinder pressure predictions from the 1D model. Predicted cylinder pressure traces exhibit excellent agreement with measured cylinder pressure data during all but the expansion stage of the cycle. One explanation for this observation could be that the Woschni convective heat transfer model drew too much energy out of the combustion chamber during this period. Figure 5.11 shows that by reducing the convective heat transfer multiplier from 2.0 to 1.4, the cylinder pressure match during the expansion stroke is improved but only because the maximum predicted cylinder pressure is higher when lower values of the convective heat transfer multiplier are used. The convective heat transfer multiplier is therefore unlikely to be the source of the mismatch in cylinder pressures during the expansion stroke.

Alternatively, it is possible that GT-Power could be over-predicting the overall gamma of the combustion products. It is however highly unlikely that the main combustion products (N_2, CO_2 and H_2O) were predicted with a level of error capable of producing the difference observed here. The most likely explanation for this discrepancy is the aforementioned post-flame oxidation of HCs as they diffuse out of the crevice volumes and interact with the hot combustion products. In reality, this process would continue to release a small amount of

heat throughout the expansion stroke, thus resulting in marginally higher pressures compared to those produced by the 1D model where no post-flame oxidation or heat release occurs.

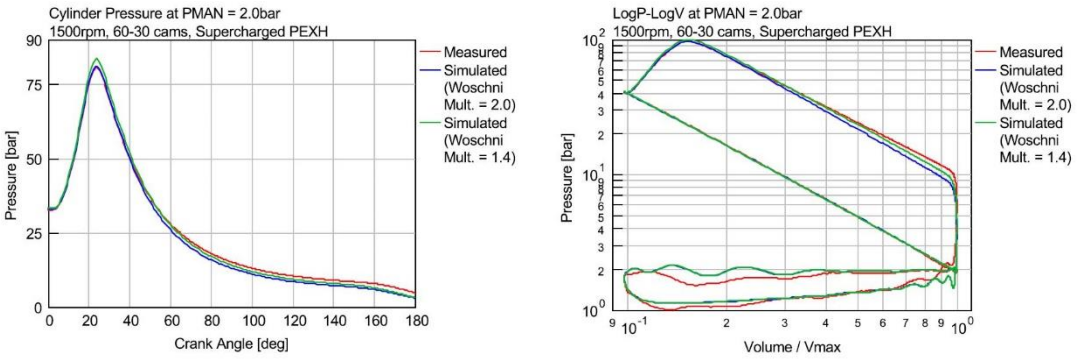

Figure 5.11 – The effect of decreasing Woschni convective heat transfer multiplier from 2.0 to 1.4 on cylinder pressure during the expansion stroke.

Finally, Figure 5.12 presents the 1D model predictions for trapped lambda and trapped residuals concentration at IVC for the four boost ramps considered in this stage of the investigation. As expected, the trapped AFR became slightly rich as boost pressure was increased for the high valve overlap and low exhaust manifold pressure conditions (i.e. 60-30 cams and supercharger-biased back-pressure targets). This observation was the result of short-circuiting of some of the fresh air charge straight into the exhaust port during the valve overlap period, facilitated by the strong positive pressure gradient between the intake and exhaust manifolds. For the same reason, scavenging of the residual burned gases was very effective at these conditions, resulting in low predicted residual gas fractions (RGFs). Predicted RGFs were slightly higher at the 3500rpm "60-30/super" condition than at the equivalent 1500rpm condition because of the shorter time available for scavenging and because of the slightly lower pressure differential across the intake and exhaust manifolds (see Table 5.4 in the following section for a comparison of supercharger and turbocharger – biased back pressures at nominally constant intake manifold pressure). At the low valve overlap/high exhaust manifold pressure conditions (i.e. 30-20 cams and turbocharger-biased exhaust manifold pressures) predicted RGFs were considerably higher due to the less favourable scavenging conditions. No scavenging of liquid/gaseous fuel was predicted for these conditions, therefore the fact that the trapped AFR predictions are lean suggests that airflow was probably over-estimated.

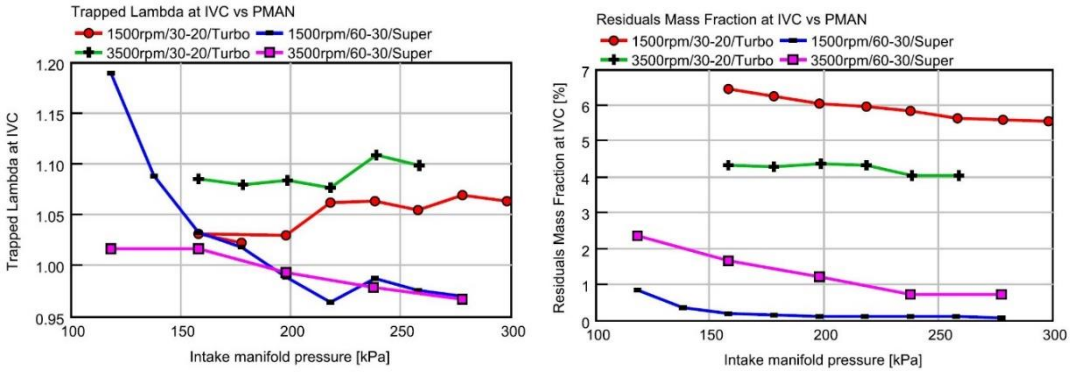

Figure 5.12 – 1D model predictions of trapped lambda and residual gas fraction (RGF) for all four EOCs considered during the model calibration process.

5.5 Knock Modelling Methodology

5.5.1 Operating Conditions Investigated

Based on the above discussion, the performance of the calibrated 1D model was deemed acceptable for use assessing the predictive capabilities of a wide range of literature IDCs. The engine operating conditions (EOCs) considered for this assessment are detailed in Table 5.4 below. These EOCs have been chosen to provide a broad range on knock-limited conditions, all of which are relevant to those experienced by modern, downsized SI engines. Ten of the twelve EOCs listed in Table 5.4 were included in the 1D model calibration and validation stage, therefore good model performance has been confirmed at these points. The two additional EOCs (#10 and #12) only differ from EOCs #9 and #11 in that they were run with 10% EGR. EGR rate is defined in GT-Power on a mass fraction basis, which differs from the mole fraction approach used to define EGR experimentally. Fortunately, the molar mass of stoichiometric combustion products is very similar to that of dry air, therefore the conversion from mole to mass fraction is virtually one to one.

At each of the 12 EOCs, three different spark settings were examined with the intention of covering three different knock intensities; heavy knock, light knock (i.e. the KLSA) and knock-free. Separate GT-Power models were built for each spark setting, resulting in 36 individual models overall. Each model was used to simulate 300 consecutive cycles using measured cylinder, intake and exhaust port pressures as the primary inputs. Additional boundary conditions were defined from measured data or estimated using the methods described previously in the model calibration section of this chapter. 10,800 individual cycles were modelled in total.

Figure 5.13 displays all 12 operating conditions graphically to highlight the operating envelope covered by this investigation. The range of intake manifold pressures considered provides a spread of BMEPs ranging from approximately 14bar up to 32bar. The range of loads investigated in this study is relevant to modern downsized engines, most of which have peak BMEP targets in excess of 30 bar. The two cam timing/exhaust manifold pressure conditions are also relevant, and provide a range of residual gas fractions and trapped AFRs. An indication of the magnitude of these ranges is provided by Figure 5.12 for the 0% EGR test points. Engine speed was limited to 3500rpm due to a lack of quality exhaust-port pressure data at higher engine speeds. This threshold is however appropriate since for most passenger

car applications, engine speeds greater than 3500rpm would be a rare occurrence during normal operation.

EOC Number	Speed (rpm)	Int. Cam Advance (°CA)	Exh. Cam Retard (°CA)	Int. Manifold Pressure (barA)	Exh. Manifold Pressure Model	Exh. Manifold Pressure (barA)	EGR Rate (%)	BMEP (bar)
1	1500	30	20	1.6	Turbo	1.45	0	14
2	1500	30	20	2.0	Turbo	1.70	0	18
3	1500	30	20	3.0	Turbo	2.45	0	25
4	1500	60	30	2.8	Super	1.70	0	31
5	3500	30	20	1.6	Turbo	1.70	0	15
6	3500	30	20	2.0	Turbo	2.20	0	19
7	3500	30	20	2.6	Turbo	2.85	0	23
8	3500	60	30	2.8	Super	2.40	0	32
9	1500	60	30	2.0	Super	1.40	0	22
10	1500	60	30	2.0	Super	1.40	10	21
11	3500	60	30	2.0	Super	1.80	0	23
12	3500	60	30	2.0	Super	1.80	10	22

Table 5.4 – Engine operating conditions considered as part of the IDC assessment

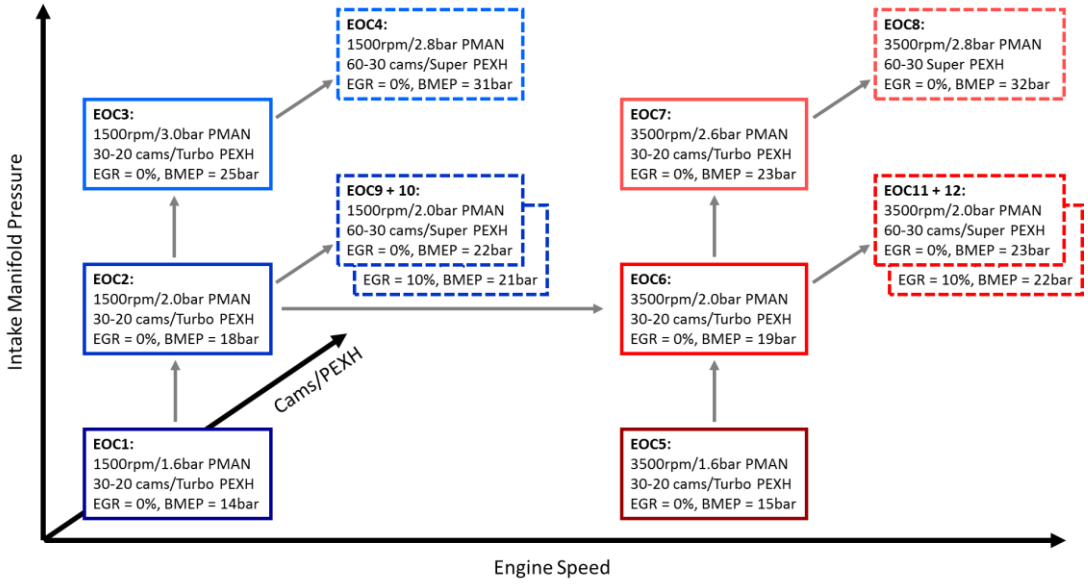

Figure 5.13 – Graphical representation of EOCs in the engine speed – Intake manifold pressure – cam timing/exhaust manifold pressure model domain.

A simplified description of the overall method applied to simulate knocking cycles is provided in Figure 5.14. After building, verifying and running the GT-Power models, model predictions were exported to Matlab for further processing. Matlab was used for the bulk of the data processing in this work due to the ease with which computations could be automated and rolled out across multiple directories with minimal user input. Matlab is also an extremely capable tool for handling large volumes of data, as was the case here.

5.5.2 Hotspot Temperature Modelling

Once the transition to Matlab was made, the next step was to estimate the temperature evolution of a hypothetical hotspot within the unburned zone. In real engines, temperatures in the end gas are not homogenous due to the effects of heat transfer and turbulent mixing. This is true of the experimental engine used in this investigation, although the high levels of turbulence that it demonstrates would surely reduce the magnitude of any thermal/ compositional stratification. Hotspots are regions of the end gas where due to the above effects, the local gas temperatures are higher than the bulk temperature. As a result, hotspots have a higher tendency to auto-ignite, leading to the prevailing theory that they are the primary cause of knock [117].

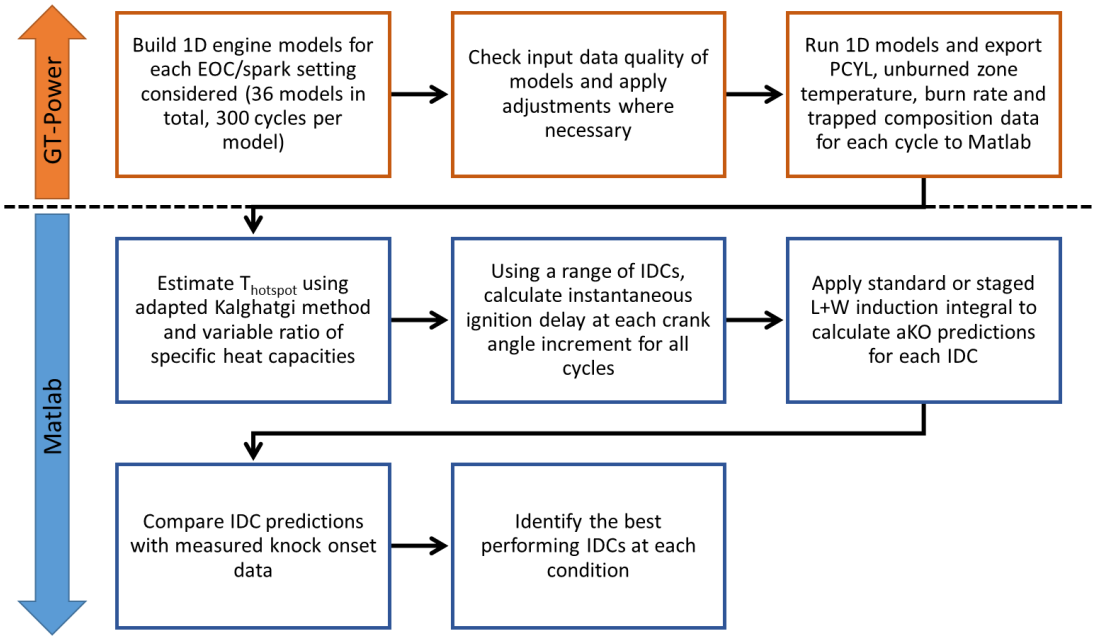

Figure 5.14 – Summary of overall method employed for assessment of IDC performance.

Unfortunately, one of the main disadvantages of the two-zone combustion modelling approach is that the unburned zone is treated as a single volume, homogenous in both temperature and composition. Two-zone models cannot therefore model the presence or temperature evolution of hotspots within the end gas[15]. A commonly employed technique

[15] GT-Power does offer a partial solution to this issue, allowing the unburned zone to be separated into a single zone for the bulk volume, plus a series of 10 or more thin sub-volumes (depending on the number of valves per cylinder). These sub-volumes are positioned between the bulk volume and the combustion chamber surfaces. The discretisation is coarse, however it allows the user to account for the increased local heat transfer to end gas regions in the vicinity of hot combustion chamber surfaces. Unfortunately, incorporating this tool within the GT/Matlab modelling framework used herein was not possible within the time constraints of the project.

to circumvent this limitation is to approximate the temperature evolution of a theoretical hotspot by assuming adiabatic compression from IVC onwards. Hotspot temperature can then be estimated according to the measured cylinder pressure (P) and the predicted bulk gas temperature at IVC (T_{IVC}) according to Equation 5.8, where γ is the ratio of specific heats.

$$T_{Hotspot} = T_{IVC}\left(\frac{P}{P_{IVC}}\right)^{\frac{\gamma-1}{\gamma}} \qquad \textit{Equation 5.8}$$

Although conditions are far from adiabatic inside the combustion chamber, the adiabatic approximation is appropriate for the fresh charge that is situated within the "core" of the combustion chamber – the central region where heat transfer from hot combustion chamber surfaces such as the piston and the exhaust valve faces can be neglected [6]. For engines capable of high tumble rates, this is especially valid since the centroid of the tumble motion is unlikely to see much influence from the combustion chamber walls until the tumble motion breaks up near TDC.

The above approach assumes that adiabatic compression would occur from the moment the intake valve closes. In highly turbulent flow fields, this assumption is probably not valid since the turbulence would probably continue to distribute the thermal energy acquired from the combustion chamber surfaces throughout a portion of the fresh charge for some time after IVC. To accommodate this behaviour, a modified version of the hotspot temperature modelling approach proposed by Kalghatgi [50] has been used. Kalghatgi's method used the ideal gas equation to estimate the bulk fresh charge temperature at 15 bar cylinder pressure (T_{15bar}) based on the cylinder volume at this point and the predicted number of moles of fuel, air and residual gases trapped inside the combustion chamber. A temperature difference ($\Delta T_{Hotspot}$) of 10 – 30°C was then applied to simulate the presence of localised hotpots that arise through mixing with hot residuals or due to heat transfer from hot combustion chamber surfaces such as the exhaust valves. For the remainder of the cycle, adiabatic compression was assumed and the hotspot temperature evolution was calculated using Equation 5.8 (but with $T_{15bar} + \Delta T_{Hotspot}$ used instead of T_{IVC}) and a fixed value of γ = 1.31. No justification is provided to support the range of $\Delta T_{Hotspot}$ values applied. It has been noted that the value of $\Delta T_{Hotspot}$ was effectively tuned at each operating condition to provide the best match between measured and predicted knock onset angles.

The significance of Kalghatgi's 15 bar cylinder pressure limit is not clear, although it could be related to the fact that at pressures below this point, gas temperatures and the resulting ignition delays are sufficiently long (>15ms) that they contribute very little to the overall L+W induction integral and can therefore be ignored. In this work, the 15bar cylinder pressure limit is used to allow the fresh charge to acquire a degree of thermal energy from the combustion chamber walls before the assumption of adiabatic compression is initiated. In retrospect, it would have made more sense to define this point in the cycle in terms of specific crank angle or unburned zone temperature rather than a pressure because the location of 15bar cylinder pressure is dependent on both intake valve timing and manifold pressure.

Figure 5.15 demonstrates the significance of opting to model the hotspot temperature in the manner described above, plotting the temperatures obtained from four different modelling approaches against crank angle. The intake manifold pressure for the two conditions plotted was 2.0 bar but the cam timings were different, hence the different locations of IVC on the two plots. Interestingly, the locations of 15bar cylinder pressure were actually quite similar. At both EOCs, the hottest temperature predictions were obtained using the Kalghatgi approach and a $\Delta T_{Hotspot}$ of 10°C. Assuming a $\Delta T_{Hotspot}$ of 0° obviously resulted in slightly cooler temperatures from the point at which cylinder pressure reached 15bar onwards. GT-Power generally produced the coldest maximum temperatures, due to the simulated effects of heat transfer from the unburned zone to the cylinder walls during combustion. The location of IVC strongly affected the relative position of the temperature profile calculated by assuming adiabatic compression from IVC onwards. At early IVC (i.e. EOC #9, where the intake cam was advanced 60°CA relative to the parked position), assuming adiabatic compression from IVC onwards resulted in comparatively cool hotspot temperature predictions. The opposite was true at late IVC (i.e. EOC #2, where the intake cam was advanced 30°CA relative to the parked position), where the assumption of adiabatic compression from IVC onwards produced the hottest hotspot temperature trace. Heat transfer to the fresh charge in the period between these two IVC settings is therefore quite considerable. The relatively hot temperature profile predicted for EOC #2 also suggests that the direction of heat transfer probably switched shortly after IVC - in this case, around 90°bTDC and at gas temperatures of approximately 400K.

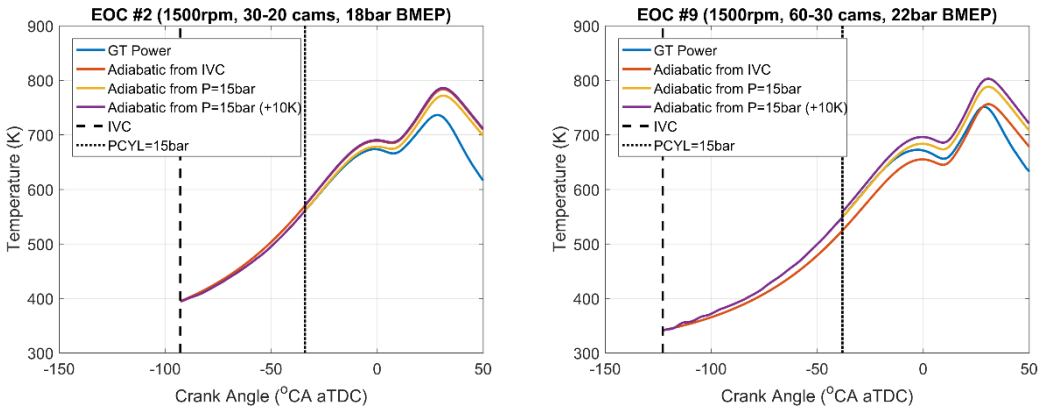

Figure 5.15 – Effect of different modelling approaches on predicted hotspot temperature profile.

Given that the intention is to model the temperature of a portion of the unburned zone that is hotter than the bulk average, it seemed nonsensical to apply the assumption of adiabatic compression from IVC onwards. Conversely, the author was reluctant to apply an arbitrary temperature gain at an arbitrary point in the cycle with little evidence to support its validity. Combining Kalghatgi's approach with a $\Delta T_{Hotspot}$ value of 0°C therefore represented the best compromise in terms of consistently predicting hotter temperatures than the bulk average predictions from GT-Power, and refraining from arbitrarily inflating the temperature values predicted.

An additional deviation from the original hotspot modelling approach detailed by Kalghatgi was applied in the form of assuming temperature-varying γ instead of fixed γ. Kalghatgi assumed a fixed γ of 1.31 for his investigations, a value obtained from analysis of measured cylinder pressure data over the 25°CA window prior to ignition. The validity of this assumption has been evaluated by investigating the effect of temperature on γ and the subsequent prediction of $T_{Hotspot}$.

As Figure 5.16 and Figure 5.17 show, temperature and composition both have a considerable effect on γ. For stoichiometric air/fuel mixtures with 0% RGF, γ decreases by approximately 8.3% over the range 300K – 1200K. Meanwhile, increased RGF serves to increase γ for a given temperature by diluting the fuel mole fraction of the mixture. Since gasoline has a very low γ relative to the other compounds present, the result is a net increase in overall γ. Similarly, decreasing the fuel mole fraction by increasing lambda also serves to increase γ at a given temperature.

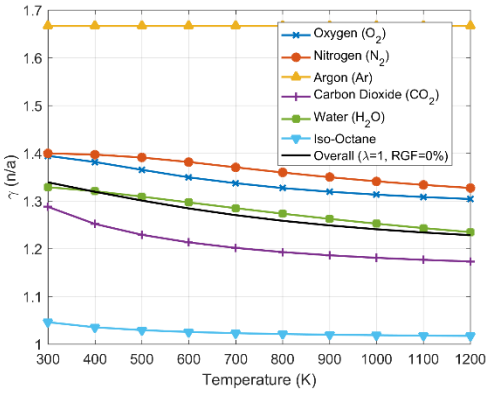

Figure 5.16 – The effect of temperature on the γ of the various species that make up air/fuel/residual gas mixtures.

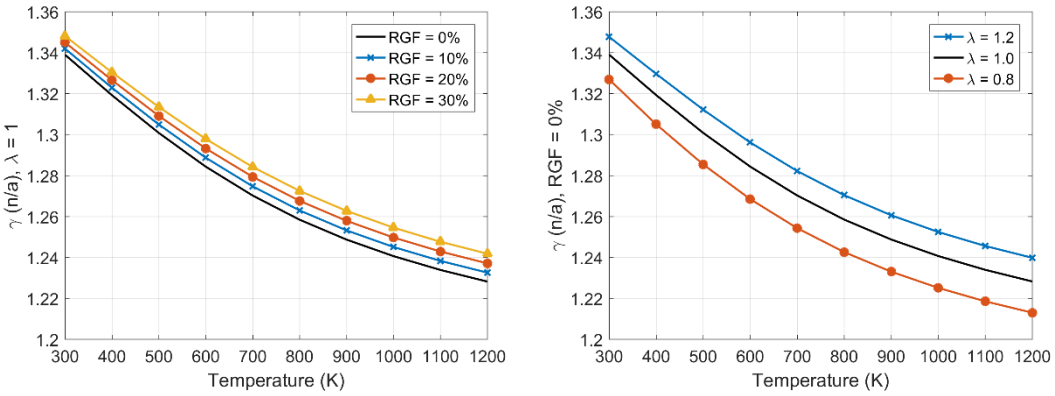

Figure 5.17 – The effect of residual gas fraction (left) and lambda (right) on the γ of air/fuel/residual gas mixtures.

The following method was used to investigate the impact of applying temperature-varying γ to the calculation of $T_{Hotspot}$. Starting at the crank angle corresponding to a cylinder pressure of 15bar, γ was estimated using GT power predictions for the composition and temperature of the trapped charge. The temperature at the next crank angle increment was then calculated using Equation 5.8 and the cylinder pressure measured at the next crank angle increment. This process was repeated until hotspot temperature predictions were obtained to a point well beyond the end of combustion (an arbitrary end-point of 60°CA aTDC was applied). The effects of blowby and oil evaporation were ignored and the fuel was assumed to be fully evaporated iso-octane. Residual gases were assumed to comprise of stoichiometric combustion products of the practical fuel blend used throughout the experimental campaign. Thermochemical data for all relevant species was obtained through the NIST WebBook [118], a free online resource.

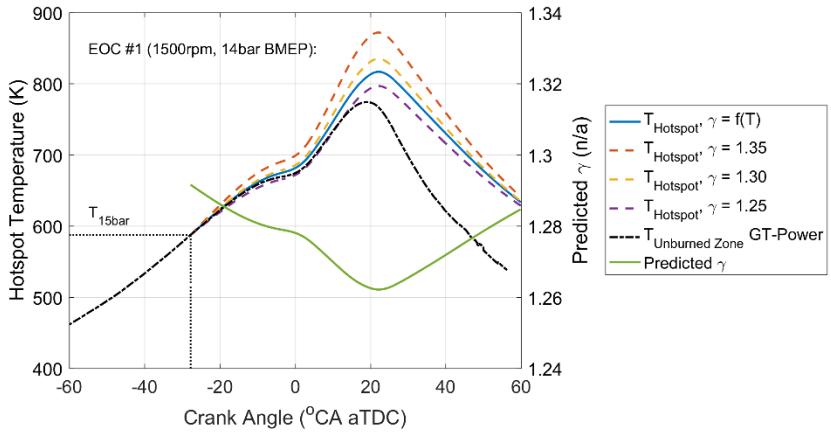

Figure 5.18 – The effect of assuming fixed vs temperature-varying γ on the predicted temperature evolution of a hypothetical hotspot. The non-adiabatic unburned-zone temperature profile predicted by GT-Power (black line) has been added for reference. Data presented for EOC #1 (1500rpm, 14bar BMEP)

Figure 5.18 shows that for EOC #1 (1500rpm, 14bar BMEP), applying a temperature-varying gamma resulted in a hotspot temperature profile between those obtained by assuming fixed γ values of 1.25 and 1.30. Between the locations of 15 bar and the maximum cylinder pressure, the overall γ was predicted to decrease from 1.29 to approximately 1.26. Although not shown, the predicted γ values agree very well with those obtained directly from the measured cylinder pressures trace over the 20°CA period before TDC/ignition (whichever came earliest). For the case presented in Figure 5.18, the mean γ calculated from the gradient of the logP-LogV diagrams of all 900 cycles was 1.269. Although the maximum temperature difference would no doubt have been quite small had this fixed value of γ been used, the decision was made to impose temperature-varying γ to estimate $T_{Hotspot}$. Since auto ignition is a cumulative process with a high sensitivity to temperature, small temperature errors can have a significant impact on predicted ignition delay times. Having validated the accuracy of the temperature-varying γ calculations by comparison with measurements from experimental cylinder pressure data, the decision was made to use them.

5.5.3 Ignition Delay Correlations

Having finalised a method for estimating the temperature evolution of a hotspot, the next step was to identify a range of ignition delay correlations from the literature and test their abilities to predict knock. A comprehensive list of IDCs was obtained, spanning the simple 4-coefficient Douaud and Eyzat correlation [55] to the relatively complex, 37-coefficient Goldsborough correlation [48]. Each IDC was written as a Matlab function that read in

measured cylinder pressure data, predicted trapped composition and the predicted hotspot temperature profile for all 900 cycles at each EOC. The output of these IDC functions was the instantaneous ignition delay at each crank angle increment for all 900 cycles. This calculation was performed over the entire hotspot temperature trace (i.e. from IVC until 60°CA aTDC).

Table 5.5 summarises the IDCs investigated in this work. For information concerning the coefficient values used by each IDC, the reader is referred to the original publications. Figure 5.19 meanwhile plots ignition delay predictions for each IDC as a function of temperature at a pressure of 60bar, λ = 1.0 and RGF = 0%. Immediately apparent is the broad range of ignition delay times predicted, with the largest differences (nearly two orders of magnitude) seen at the low and high temperature regions. Several of the correlations exhibit very strong NTC behaviour, whilst all of the single-step IDCs exhibit none at all. Within the legend of this figure, details of the fuel properties modelled by each of the correlations throughout this study are provided. Care was taken to minimise the variation in RON modelled by the different EOCs. It is worth noting however that some of the correlations investigated in this work are only valid for specific fuels (such as for a specific gasoline blend where RON > MON, or for PRFs where RON = MON). Within the time constraints of this investigation, it also was not possible to implement the mixing rule proposed by Ma for four component gasoline surrogates. Instead, the correlation provided in the original publication for pure iso-octane has been used.

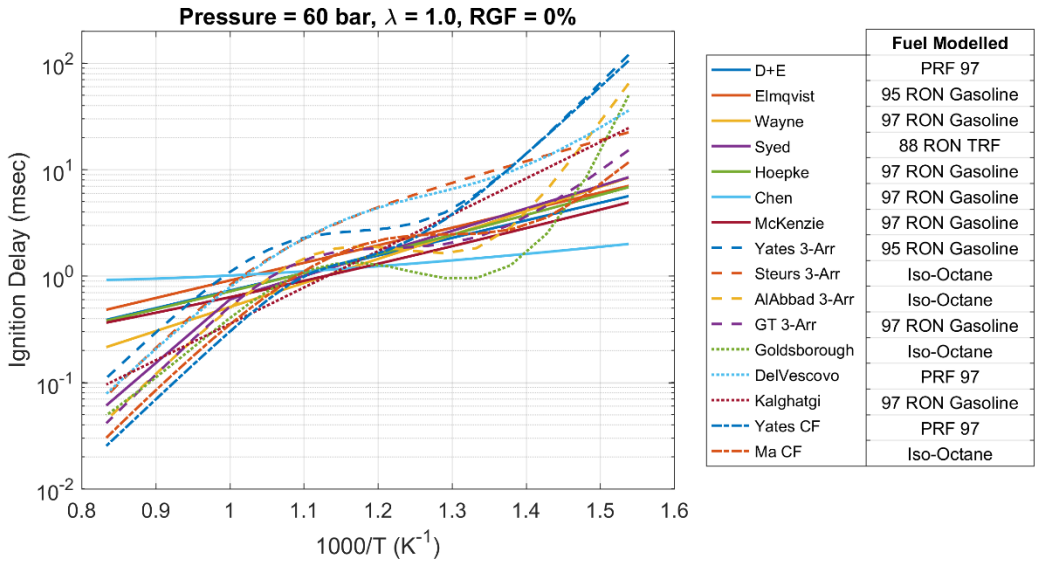

Figure 5.19 – Predicted ignition delay times for each of the IDCs investigated in this study at pressure = 60bar, λ = 1.0, RGF = 0%.

Using the IDCs listed in Table 5.5, instantaneous ignition delay was calculated for each crank angle increment over the knock-relevant portion of each cycle (IVC to 60°CA aTDC). Measured cylinder pressure and the predicted hotspot temperature were the primary inputs to this calculation, with the 1D model predictions for trapped composition and charge temperature at 15bar cylinder pressure feeding into the latter. The Livengood and Wu induction integral approaches outlined earlier in Chapter 2 were then used to determine the predicted angle of knock onset (if appropriate).

Author	Year	Correlation Type	Correlation Form	# Coeffs	Calibration/Validation Methods	Limitations/Considerations
Douaud + Eyzat [55]	1978	Single Arrhenius	$\tau = A.P^{-n}.e^{B/T}$ $A = 0.01869(ON/100)^{3.4017}$ Where n and B are constants.	4	- Minimised sum of squares of the L+W integral for experimentally observed knocking cycles. - Cylinder pressure data collected from a 1-cyl CFR engine under RON and MON test conditions for a variety of PRF fuels (80 – 100 ON). - IDC aKO predictions verified using 1D engine model and two-zone combustion model.	- Only valid for PRFs in range 80 – 100 ON. - CFR engine far removed from modern DISI engines in terms of design. - RON/MON test conditions not very representative of in-cylinder conditions inside modern DISI engines.
Wayne [64]	1998	Single Arrhenius	$\tau = A.P^{-n}.e^{B/T}$ $A = 0.389(ON/100)^{7.202}$ Where n and B are constants.	4	- Trial and error used to acquire the best overall match between predicted and measured knock onset angles (assessed subjectively). - Cylinder pressure data collected from a 1992 naturally aspirated, 1.9 litre 4-cyl engine run on four gasoline blends (RON = 87, 89, 94 and 115) - IDC aKO predictions verified using 1D engine model and two-zone combustion model.	- Valid for gasoline fuels in the range RON = 87 – 115. No information provided regarding the MON of the fuels covered. - Calibration method not particularly rigorous. - Does not consider effects of dilution or AFR. - Dated engine
Elmqvist [59]	2003	Single Arrhenius	$\tau = A.P^{-n}.e^{B/T}$ Where A, n and B are constants.	3	- "A" coefficient tuned to minimise the sum of squares between L+W integral at the measured aKO and the target value of 1.0. D+E values used for remaining model coefficients. - Cylinder pressure data collected from a 2.0 litre, turbocharged 4-cyl engine at a range of speeds and λ values with a single 95 RON gasoline. - IDC aKO predictions verified using 1D engine model and two-zone combustion model.	- Only valid for a single gasoline fuel (95 RON). No MON info provided. - Does not consider effects of dilution or AFF. - Uses same pressure and temperature parameters as D+E model.
Syed [119]	2011	Single Arrhenius	$\tau = A.P^{-n}.(1 + x_d)^m e^{B/T}$ Where A, n, m and B are constants whose values depend on ϕ and T, and x_d is the total diluent volume fraction.	4	- "Piece-wise fitting approach", using ignition delay predictions from a homogenous reactor model and a detailed CKM for gasoline/ethanol blends. Mechanism of Andrae [77] used. - CKM simulations performed over range of conditions including ϕ = 0.5/1.0/1.5, P = 20-60bar, T = 800-1200K and RGF = 0 – 0.32. - IDC aKO predictions verified using 1D engine model and two-zone combustion model.	- Only valid for a single TRF gasoline surrogate with RON = 88 and MON = 85 (not ENN228 compliant) - As with all fundamental ignition delay studies, correlation only valid for conditions at which experimental data available. Typically, this limits the valid pressure range to <60bar. - Correlation also only as good as the CKM upon which it is based.

Table 5.5 – Summary of IDCs investigated as part of this work.

Author	Year	Correlation Type	Correlation Form	# Coeffs	Calibration/Validation Methods	Limitations/Considerations
Hoepke [60]	2012	Single Arrhenius	$\tau = A.\left(\frac{P}{T}\right)^{-n}.(1 - x_{RGF})^{m}.e^{B/T}$ Where A, n, m and B are constants, and x_{RGF} is the residual gas mass fraction.	4	- Least-squares technique used to minimise error between predicted and measured aKO. - Cylinder pressure data collected from turbocharged 2.0 litre, 4-cyl DISI engine at 1500-2500rpm, 14-18bar BMEP and 0-18% EGR. - A, n and B optimised first for all EGR = 0% cases. m subsequently calibrated alone using data from EGR > 0% test conditions. - IDC aKO predictions verified using 1D engine model and two-zone combustion model.	- Only valid for gasoline fuel with RON = 97 (no info provided for MON) at λ = 1. - No information provided regarding the MON of the fuel used in this work.
Chen [61]	2014	Single Arrhenius	$\tau = A.\left(\frac{P}{T}\right)^{-n}.(1 - x_{RGF})^{m}.e^{B/T}.\lambda^{C}$ Where A, n, m, B and C are constants and x_{RGF} is the residual gas mass fraction.	5	- Multi-island genetic algorithms used to optimise coefficient set by minimising RMSE between predicted and observed aKO. - Cylinder pressure data from a turbocharged, PFI, 1.5 litre SI engine collected at 2600-3600rpm, WOT, 0-16% EGR and λ = 0.73-0.88. - IDC validated using data from a different engine - IDC aKO predictions verified using 1D engine model and two-zone combustion model.	- Only valid for a single commercial gasoline fuel blend (97 RON). No information provided regarding MON. - Model predictions very sensitive to AFR.
McKenzie [120]	2016	Single Arrhenius	$\tau = A.\left(\frac{P}{T}\right)^{-n}.(1 - w_d)^{m}.e^{B/T}$ Where A, n, m and B are constants, and w_d is an empirical function representing overall diluent fraction.	5	- Minimised sum of squares between predicted and measured aKO. - Cylinder pressure data from a 2.0 litre, turbocharged 4-cyl engine collected at 1250-2000rpm, 8-14bar gross IMEP, λ = 0.8-1.3 and EGR = 0-12.5%. - IDC aKO predictions verified using 1D engine model and two-zone combustion model.	- Only valid for a single reference fuel (Haltermann 437 – 96.6 RON, 88.5 MON)
Goldsborough [48]	2009	Single Arrhenius with advanced coefficient formulations.	$\tau = A.\phi^{\alpha}.P^{\beta}.\chi_{O2}^{\gamma}.e^{\lambda}$ Where A is a constant, χ_{O2} is the oxygen mole fraction, and α, β, γ and λ are polynomial functions in terms of T and P.	37	- Levenberg-Marquardt optimisation algorithm used to calibrate model terms such that acceptable matches between experimental and predicted functional dependencies α, β, γ and λ were achieved. - Experimental ignition delay data obtained from the literature (661 RCM/shock tube data points spanning P = 1-59 bar, T = 650-2000K, ϕ = 0.2-2.0, and χ_{O2}= 1.25-42%). - IDC predictions compared with literature ignition delay data using a homogenous constant volume reactor model.	- Only valid for iso-octane (PRF 100) - Facility-induced phenomena could lead to some discrepancies between ignition delay data obtained from different sources. - Only valid at conditions for which shock tube and RCM data available (typically much lower pressure than the maximum cylinder pressures inside highly boosted SI engines).

Table 5.5 (cont. 1) – Summary of IDCs investigated as part of this work.

Author	Year	Correlation Type	Correlation Form	# Coeffs	Calibration/Validation Methods	Limitations/Considerations
DelVescovo [75]	2016	Single Arrhenius with advanced coefficient formulations.	$\tau = A.\phi^{\alpha}.p^{\beta}.\chi_{O2}^{\gamma}.e^{\lambda}$ Where A is a constant, χ_{O2} is the oxygen mole fraction, and α, β, γ and λ are polynomial functions in terms of T and ON (for PRFs)	41	- Levenberg-Marquardt optimisation algorithm and bi-square regression used to calibrate model terms such that acceptable matches between CKM-derived and predicted functional dependencies α, β, γ and λ were achieved. - Reference ignition delay data obtained through constant volume simulations (6480 individual cases run spanning P = 10-100 bar, T = 570-1860K, ϕ = 0.3-1.5, χ_{O2} = 12.6-21% and PRF ON = 0 - 100). - Used reduced gasoline surrogate CKM produced by LLNL [52] (323 species) - IDC predictions compared with literature ignition delay data using a homogenous constant volume reactor model.	- Only valid for PRFs (0 – 100 ON) - Correlation only as good as the CKM upon which it is based. - LLNL CKM used is only valid up to 60 bar, but has been used here to predict ignition delays at pressures up to 100bar.
Kalghatgi [76]	2016	Single Arrhenius with advanced coefficient formulations.	$\tau = A.P^{-n}.e^{B/T}$ Where A, n and B are polynomial functions in terms of RON and MON.	13	- A, n and B determined through multiple linear regression applied to constant volume ignition delay predictions. Predictions obtained using the TRF CKM of Andrae [77] - Process repeated for a large number of gasolines with varying RON/MON. Polynomial relationships between A, n, B and RON/MON then devised using simple regression. - IDC aKO predictions verified using 1D engine model and two-zone combustion model.	- Correlation can be applied to model τ for any practical gasoline fuel. - Like all single-Arrhenius IDCs, formulation is incapable of modelling both high and low temperature regimes for fuels with strong NTC behaviour. - Correlation is only as good as the CKM on which it is based.
Yates [46]	2008	Cool-Flame/Staged L+W Integral	$\int_0^{t_{CF}} \frac{dt}{\tau_{CF}} = 1$ $\int_0^{t_{CF}} \frac{dt}{\tau_{h,i}} + \int_{t_{CF}}^{t_{IGN}} \frac{dt}{\tau_{h,CF}} = 1$ Where τ_{CF}, $\tau_{h,i}$ and $\tau_{h,CF}$ are of the form: $\tau = A.P^{-n}.\phi^{m}.e^{B/T}$ And where most coefficients are expressed as functions of PRF ON.	14	- Least-squares regression used to minimise the difference between constant volume ignition delay predictions obtained using the detailed PRF CKM of Curran/LLNL [121] and those obtained using the IDC. - IDC verified by comparing predicted and measured MFB at AI onset data under RON and MON test conditions for PRFs in the range 40 – 100 ON.	- Only valid for PRFs (0 – 100 ON) - Correlation only as good as the CKM on which it is based. - Only verified against ignition delay predictions from detailed CKM and cylinder pressure data from a CFR engine (not representative of modern SI engines, as previously discussed).

Table 5.5 (cont. 2) – Summary of IDCs investigated as part of this work.

Author	Year	Correlation Type	Correlation Form	# Coeffs	Calibration/Validation Methods	Limitations/Considerations
Ma [2]	2016	Cool-Flame/Staged L+W Integral	As described for Yates' Cool Flame model [46], but with modified coefficient values.	10	- Least-squares regression used to minimise the difference between shock tube ignition delay measurements and constant volume ignition delay predictions obtained using the IDC. - Separate IDCs developed for four pure fuels (iso-octane, n-heptane, toluene and ethanol). - Overall IDC verified by comparing ignition delay predictions for mixtures of the four pure fuels with experimental data from the literature.	- Proposed mixing rule allows correlation to simulate τ for 4-component gasoline surrogates where RON ≠ MON. - IDC only verified up to 50 bar (upper limit of the available experimental data).
Yates [45]	2005	Triple Arrhenius	$\tau_{Overall} = [(\tau_1 + \tau_2)^{-1} + (\tau_3)^{-1}]^{-1}$ $\tau_i = A_i . P^{-n_i} . e^{B_i/T}$ Where A_i, n_i and B_i are constants depending on fuel type.	9	- Least-squares regression used to minimise the difference between constant volume reactor model ignition delay predictions obtained using detailed CKM and those obtained using the IDC. - Process repeated for a range of six gasoline-relevant surrogate fuel compounds including iso-octane, n-heptane, toluene and ethanol, as well as for a 95 RON gasoline surrogate. - Different CKMs were used for each pure fuel.	- Valid for range of pure fuels and for a surrogate 95 RON gasoline blend. - Constant volume reactor simulations only performed up to pressures of 40bar. - Correlation only as good as the CKMs upon which it is based.
Steurs [68]	2014	Triple Arrhenius	As described for Yates 3-Arrhenius IDC [45], but with modified coefficient values for iso-octane and ethanol.	9	- Combination of sensitivity analysis and non-linear regression used to minimise differences in ignition delay times between those obtained using the detailed PRF CKM of Mehl/LLNL [122] and those from the IDC. - In both cases, simulations were performed using closed, adiabatic reactor models for P = 1-80bar and T = 600-1050K (λ = 1). - IDC verified by comparing aKO predictions with engine data collected across a broad range of speeds and air temperatures (all WOT, λ = 1). 1D engine model and 2-zone combustion model used for this purpose.	- Valid for iso-octane at λ = 1. - No consideration of dilution/EGR. - Seemingly poor representation of ignition delay times in both the low and intermediate temperature regimes compared to LLNL mechanism.

Table 5.5 (cont. 3) – Summary of IDCs investigated as part of this work.

Author	Year	Correlation Type	Correlation Form	# Coeffs	Calibration/Validation Methods	Limitations/Considerations
AlAbbad [69]	2017	Triple Arrhenius	$\tau_{Overall} = [(\tau_1 + \tau_2)^{-1} + (\tau_3)^{-1}]^{-1}$ $\tau_i = A_i . P^{-n_i} . \phi^{m_i} . e^{B_i/T}$ Where A_i, n_i, m_i and B_i are constants depending on the fuel.	12	- Regression analysis used to minimise the differences in ignition delay times between those obtained experimentally from a shock tube facility and those obtained numerically using a homogenous batch reactor model. - Shock tube tests performed over the range P = 10-40bar, T = 700-1200K and ϕ = 0.5/1.0 for four PRFs (70/80/91/95 ON). - Results extrapolated to provide estimated ignition delay times for PRF0 (n-heptane) and PRF100 (iso-octane).	- Developed for PRFs in range 0 – 100 ON. - IDCs were developed for pure iso-octane and n-heptane, but shock tube data was only collected for PRFs 70/80/91/95 ON. Ignition delay times for the pure compounds were therefore estimated from the available experimental data at each test condition, rather than measured directly. This approach would almost certainly incur errors. - No engine tests/simulations performed using IDC.
Gamma Technologies LLC. [63]	2017	Triple Arrhenius	$\tau_{Overall} = [(\tau_1 + \tau_2)^{-1} + (\tau_3)^{-1}]^{-1}$ $\tau_i = a_i . \left(\frac{ON}{100}\right)^{b_i} [Fuel]^{c_i} [O_2]^{d_i} \ldots$ $[Diluent]^{e_i} e^{f_i/T}$ Where a_i – f_i are constants and [X] denotes the concentration of X in mol/m³.	18	- IDC based on the reduced gasoline surrogate CKM developed by Ra [66]. - No information provided regarding coefficient calibration or validation.	- Valid for "gasoline". No information provided regarding the composition/ON of the gasoline for which this IDC is valid. - Again, IDC is only as good as the CKM it is based on. In this case, the CKM has been validated with shock tube data from the literature at pressures of 22 and 55 bar and equivalence ratios of 0.5/1.0/1.6.

Table 5.5 (cont. 4) – Summary of IDCs investigated as part of this work.

5.6 Knock Modelling Results

5.6.1 Assessment of IDCs using L+W Integral Error

A general assessment of IDC performance across all 12 EOCs was carried out to determine which correlations performed well at each EOC. This assessment could have been performed in a number of ways. For example, the sum of the cumulative error in knock frequency predictions across the spark sweep at each EOC could have been determined, and the IDCs ranked accordingly. However, this approach would fail to identify errors in aKO, and could be misleading for EOCs where the prevalence of knocking cycles was low. Under such conditions, it could be possible for predicted and measured knock frequencies to be closely aligned only for the individual knocking cycle classifications (i.e. whether a cycle is predicted/measured as knocking or non-knocking) to be very different. It was therefore important to adopt a method whereby the performance of each IDC was evaluated on a cycle by cycle basis at each EOC.

In a similar study, Steurs developed a method of evaluating the accuracy of IDCs based on the L+W integral [68]. For non-knocking cycles, the maximum value of the L+W integral should remain below 1.0, whilst for knocking cycles the L+W integral should reach 1.0 at the measured aKO. Using these criteria, Steurs developed a simple mathematical expression for determining the magnitude of the mean L+W integral error for a sample of cycles (see Equation 5.9, where N_{FP}, N_{FN} and N_{TP} are the number of false positive/false negative/true positive cycle classifications and LW_{max}/LW_{aKO} are the maximum and aKO values of the L+W induction integral respectively). This method is useful because it provides a single metric by which the accuracy of an IDC can be assessed for both knocking and non-knocking cycles together. Large values of this metric indicate poor IDC performance relative to measured knock onsets times.

$$LW\ Error = \frac{1}{N_{FP}} \sum_{FP} (|LW_{max} - 1|) \quad \text{Mean L+W error false +ve}$$

$$+ \frac{1}{N_{FN}} \sum_{FN} (|LW_{\alpha KO} - 1|) \quad \text{Mean L+W error false -ve}$$

$$+ \frac{1}{N_{TP}} \sum_{TP} (|LW_{\alpha KO} - 1|) \quad \text{Mean L+W error true +ve} \qquad \textit{Equation 5.9}$$

Figure 5.20 below plots L+W integral error for the sixteen IDCs listed in Table 5.5. To aid differentiation between the correlations that performed well and those that did not, the legend of this figure has been ranked according to the mean of the L+W integral error metric calculated over all 12 EOCs. Still, it is difficult to draw any conclusions from this graph due to the number of lines present. What is apparent is that a number of IDCs performed their worst at EOCs 3, 4 and 8. Intake manifold pressures at these conditions were in excess of 2.8 bar, suggesting that the accuracy of these correlations deteriorated at higher loads.

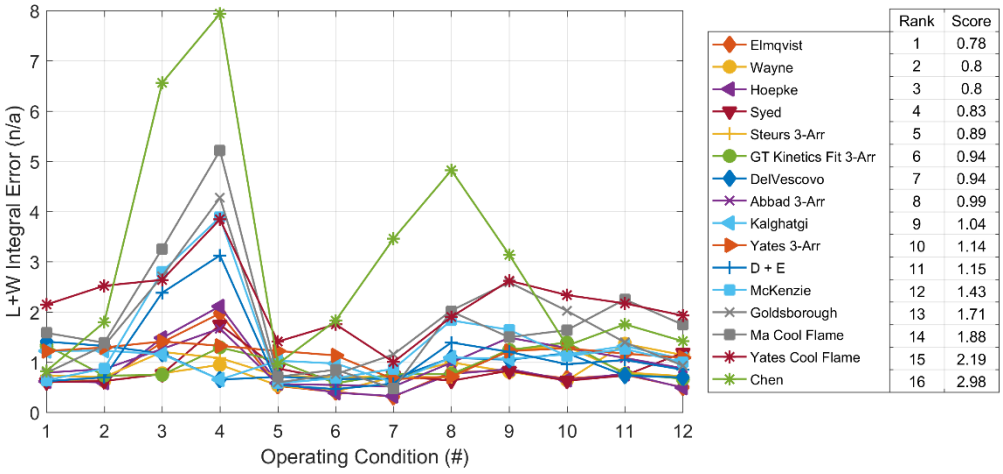

Figure 5.20 – Steurs L+W accuracy metric L+W integral error plotted for all IDCs. "Score" refers to the mean of the L+W integral error metric calculated over all 12 EOCs for each IDC.

Figure 5.21 is a reduced version of Figure 5.20, splitting the data according the two engine speeds (1500rpm and 3500rpm) and only displaying the six best-ranked IDCs at each speed for improved clarity. This figure highlights the broad spread of performance characteristics displayed by the IDCs investigated, with no single correlation demonstrating consistently strong performance across the 12 EOCs. The most consistent correlation by some margin appears to be Steurs' 3-Arrehenius formulation, with the other correlations presented in Figure 5.21 behaving somewhat more erratically.

At low speeds, the Wayne correlation performed the best overall, only being noticeably outshone at EOC #4 (1500rpm, 32 bar BMEP) by the Kalghatgi correlation. At 3500rpm however, the Wayne correlation failed to make the top six. It is surprising to note that even the best performing IDCs at each speed scored mean L+W integral errors of 0.55 to 0.74. This observation suggests that aKO was unlikely to have been predicted particularly well by any of the IDCs (more on this topic in due course).

Across the two speeds, the Elmqvist correlation performed the best overall. Like the other two correlations that featured in the top six at both speeds (Steurs' 3-Arrhenius and Hoepke's), this correlation achieved lower mean L+W integral errors at 3500rpm than at 1500rpm. This trend is presumably a result of there being less time available for the L+W integral to reach values > 1.0 at higher engine speeds. The Elmqvist correlation did however perform relatively poorly at the high BMEP condition of EOC #4. Based on this analysis using the mean L+W integral error, it would seem that no single IDC was able to deliver consistently strong performance across all 12 EOCs considered in this study.

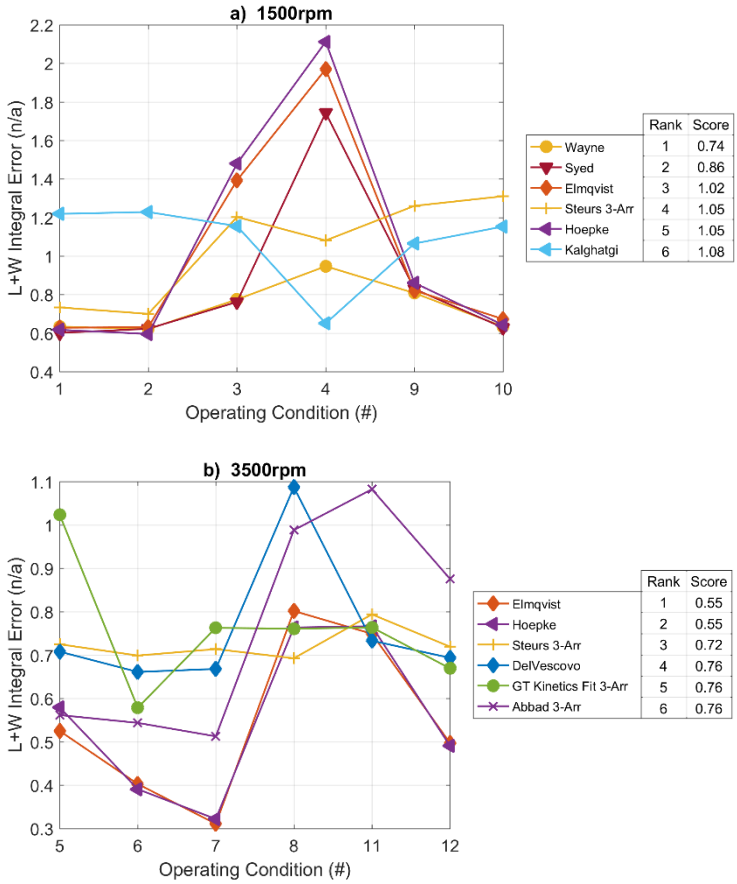

Figure 5.21 – Steurs L+W accuracy metric L+W integral error for six highest-ranking IDCs (based on their respective mean L+W integral error values calculated over the relevant speed EOCs).

Whilst the above evaluation approach is helpful, it unfairly penalises the cool flame IDCs that use the staged L+W integral approach to predict knock. This point is illustrated below in Figure 5.22 where an example of the staged L+W integral traces for the Yates cool flame correlation is provided. Due to the gradual nature in which the overall L+W integral builds prior to the onset of the cool flame, it is possible for large discrepancies to appear between it and the target L+W integral value of 1.0 at the measured aKO. In this example, the

measured aKO is before the predicted aKO, therefore the magnitude of the L+W integral error is limited to less than 1.0. However, in cases where the IDC in question is prone to predict aKO earlier than the measured aKO, L+W integral errors far greater than 1.0 are possible (as was often the case with the Ma cool flame IDC). For the cool flame IDCs, L+W integral errors arising through this set of circumstances were exaggerated by the steep nature with which the overall induction integral increased after cool flame onset.

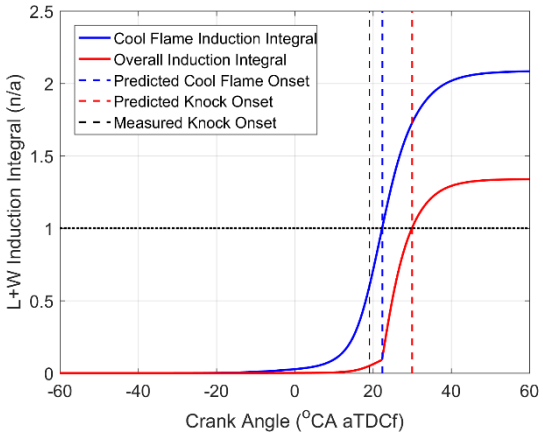

Figure 5.22 – Example of staged L+W integral traces using the Yates cool flame IDC.

5.6.2 Assessment of IDCs using aKO RMSE

To make the comparison between the different types of IDCs more fair, an assessment of overall IDC performance based on the root mean square error (RMSE) between measured and predicted aKO has been performed. The results are displayed in Figure 5.23 and Figure 5.24, where Figure 5.23 contains data for all 16 IDCs and Figure 5.24 contains data for the six best ranking IDCs at each engine speed. This time, the rankings are based on the mean aKO RMSE calculated over the relevant EOCs. Note that at some conditions, certain IDCs failed to predict knock for any of the cycles where knock was detected experimentally. It therefore wasn't possible to calculate the aKO RMSE at these conditions, hence why there are gaps in the data plotted in Figure 5.23. These gaps have been ignored when calculating the average RMSEs listed in Figure 5.23. Fortunately, all of the six best IDCs from this assessment technique generated at least one true positive classification for every EOC, therefore the comparison of aKO RMSE across all 12 EOCs is still valid for these correlations.

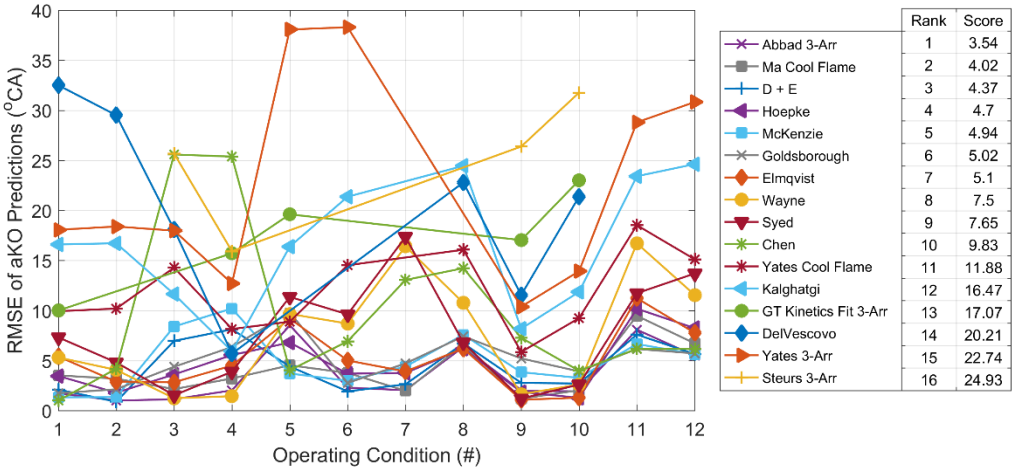

	Rank	Score
Abbad 3-Arr	1	3.54
Ma Cool Flame	2	4.02
D + E	3	4.37
Hoepke	4	4.7
McKenzie	5	4.94
Goldsborough	6	5.02
Elmqvist	7	5.1
Wayne	8	7.5
Syed	9	7.65
Chen	10	9.83
Yates Cool Flame	11	11.88
Kalghatgi	12	16.47
GT Kinetics Fit 3-Arr	13	17.07
DelVescovo	14	20.21
Yates 3-Arr	15	22.74
Steurs 3-Arr	16	24.93

Figure 5.23 – RMSE of aKO predictions for all IDCs.

Comparing Figure 5.23 with Figure 5.20, one can see that the IDCs that fared well under the L+W integral error assessment have generally fared less well compared to the other IDCs when viewed from an aKO error perspective. One of the biggest losers in this regard is the Steurs correlation, which performed consistently well in terms of its L+W integral error but was ranked worst overall in terms of its aKO error. The reason for this dramatic change in fortunes is clear from Figure 5.25. Here one can see that the average L+W integral value at the measured aKO for the Steurs 3-Arrhenius correlation is very low compared to the target value of 1.0, implying that the Steurs correlation would have predicted knock very late, if at all, at this condition (EOC #1 – 1500rpm, 14bar BMEP). A bias of knock prediction tendency in this direction limits the L+W integral error for any given cycle to values less than 1.0, thus explaining the consistently "low" L+W integral errors demonstrated by the Steurs correlation in Figure 5.21. This observation highlights another deficiency in the L+W integral error as a means of evaluating IDC performance.

From Figure 5.24, one can again see that there was a disparity in performance between high and low engine speeds, with considerably larger aKO errors obtained at 3500rpm than at 1500rpm. This result has likely arisen because of inaccuracies in the estimation of ignition delay made on a *time* basis (as every Arrhenius-based IDC is formulated to produce). These inaccuracies are effectively amplified when converted to a crank angle basis at higher engine speeds since each second represents a longer crank angle period.

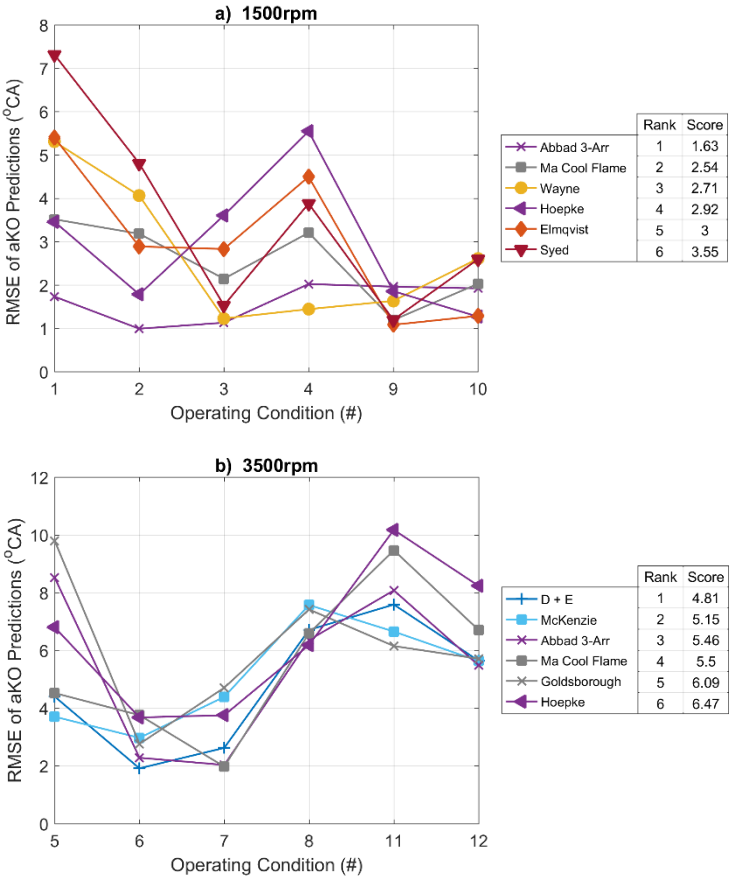

Figure 5.24 – RMSE of aKO predictions for six highest-ranking IDCs (based on their respective mean aKO RMSE values calculated over the relevant speed EOCs).

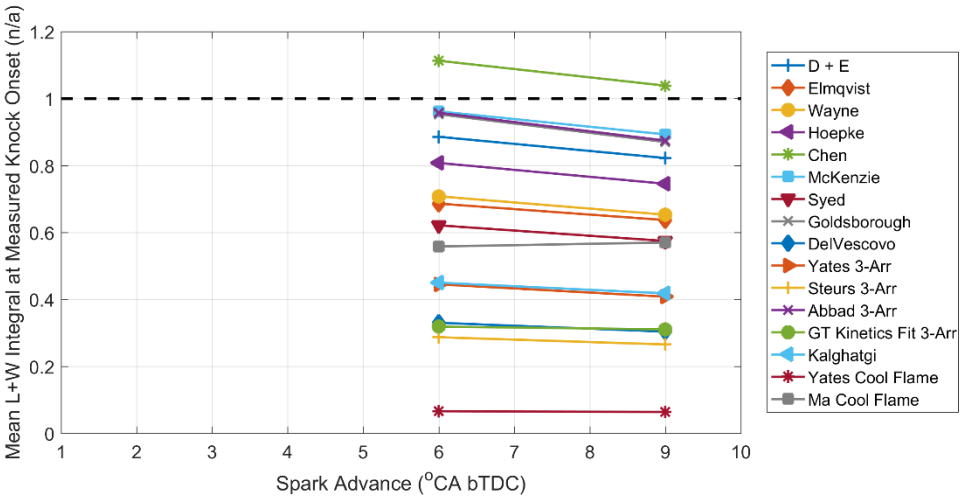

Figure 5.25 – Mean L+W integral at measured aKO for EOC #1 (1500rpm, 14bar BMEP)

The best performing correlations over the two speeds were the AlAbbad and Ma Cool Flame formulations, although the Hoepke formulation performed relatively well at both speeds also. The magnitude of the aKO errors produced by these correlations is still considerable however. In their original publications, Hoepke and Elmqvist showed that their correlations were able to predict aKO to within 0.6°CA and 2.0°CA respectively across a range of operating conditions [59, 60]. These investigations were conducted at lower BMEPs than the maximum values investigated in this work, however there is some crossover with the lower load conditions included in this work. There are no obvious trends between the magnitude of the aKO RMSE and engine load for any of the correlations.

With respect to the two conditions where external EGR rates of 10% were applied (EOCs #10 and #12), it is interesting to note the none of the correlations with specific provision for RGF demonstrated notably better performance than any of those without provision for RGF. For example, at EOC #10 the two models with the lowest aKO RMSE were the Hoepke and Elmqvist correlations. Elmqvist's IDC makes no provision for RGF, whilst Hoepke's IDC includes the multiplier $(1 - RGF)^{-0.888}$. It is possible however that had higher EGR rates been investigated at this speed and load point, the Hoepke correlation might have emerged with the lowest aKO RMSE since it was the only IDC in the top six at 1500rpm to observe a drop in aKO RMSE when the EGR rate was increased from 0% to 10% (EOC #9 and #10 respectively). At 3500rpm, all of the correlations in the top six exhibited a decrease in aKO RMSE when EGR rate was increased from 0% to 10% (EOCs #11 and #12 respectively). At the 10% EGR condition, the four highest-ranking IDCs all achieved very similar aKO RMSE scores. Out of these four correlations, only one includes specific provision for the effects of RGF on ignition delay – the McKenzie correlation. It does so in a very similar manner to the Hoepke correlation, except a "dilution factor" that includes dilution with excess air is used in place of RGF.

Since none of the "EGR-equipped" IDCs demonstrated notably better performance than the "air-only" IDCs, it has not been possible to draw any conclusions regarding which is the best method of accounting for the effects of dilution with exhaust gas on ignition delay. Further investigation at higher EGR rates may prove beneficial in this regard.

5.6.3 Assessment of IDCs using Cycle Classifications

A final IDC assessment technique based on the knock classifications rather than the L+W integral or aKO has also been investigated. In Chapter 4, the concept of using statistics derived from contingency matrices to determine the level of agreement between two dataset was introduced (see Section 4.5.2 – Knocking Cycle Detection Method Assessment). This method has been applied again here to evaluate the agreement between the experimentally observed cycle classifications and those made by each of the 16 IDCs. As with the analysis performed in Chapter 4, the agreement statistics listed in Table 4.9[16] have been calculated and averaged to produce a mean result for each IDC at each EOC. This data is presented below in Figure 5.26, with the six highest-ranking IDCs at each engine speed plotted separately in Figure 5.27.

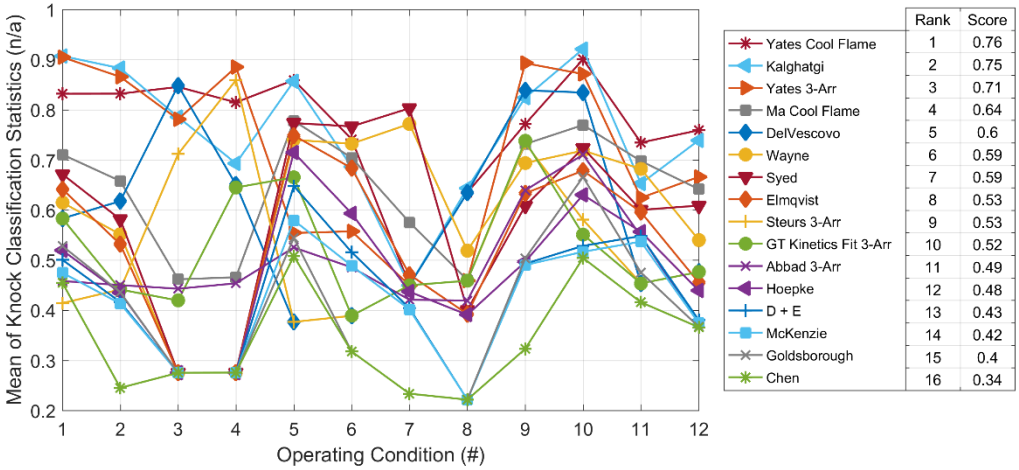

	Rank	Score
Yates Cool Flame	1	0.76
Kalghatgi	2	0.75
Yates 3-Arr	3	0.71
Ma Cool Flame	4	0.64
DelVescovo	5	0.6
Wayne	6	0.59
Syed	7	0.59
Elmqvist	8	0.53
Steurs 3-Arr	9	0.53
GT Kinetics Fit 3-Arr	10	0.52
Abbad 3-Arr	11	0.49
Hoepke	12	0.48
D + E	13	0.43
McKenzie	14	0.42
Goldsborough	15	0.4
Chen	16	0.34

Figure 5.26 – Mean of knock classification agreement statistics

In terms of the level of agreement between predicted and experimentally derived cycle classifications, the best overall match was achieved by the Yates cool flame IDC. The overall value of 0.76 achieved by this correlation suggests a strong level of agreement between the two data sets. Interestingly, this IDC ranked 15th and 11th in terms of its L+W integral error and aKO RMSE respectively (although the L+W integral error ranking is somewhat meaningless because of the aforementioned negative bias of this ranking approach towards cool-flame IDCs). The most consistent performing IDC across the two engine speeds was the Kalghatgi correlation, with the Ma cool-flame formulation also featuring in the top six at both

[16] The statistics include accuracy, sensitivity, specificity, positive predictive value, negative predictive value and Cohen's Kappa. For all statistics, values of 1.0 indicate perfect agreement, and values of zero indicate no agreement.

engine speeds. Again, no obvious trends were observed between the level of agreement and engine load for any of the correlations.

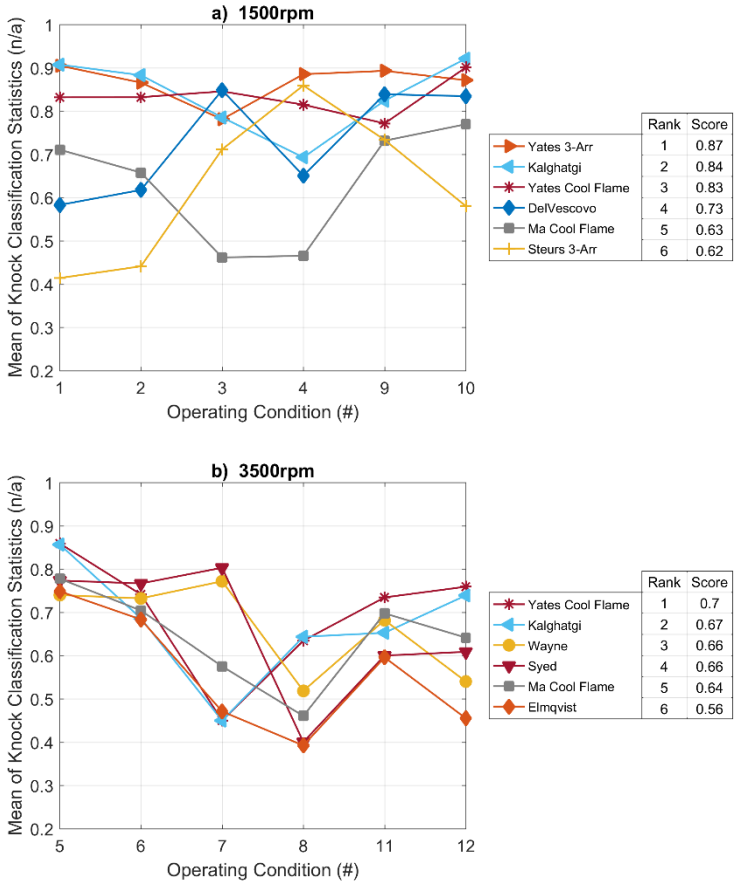

Figure 5.27 – Mean of knock classification agreement statistics for the six highest-ranking IDCs (based on their respective mean values calculated over the 12 EOCs).

Generally, better agreement between predicted and measured cycle classifications was achieved at lower engine speeds than at higher engine speeds. This observation could be because fewer knocking cycles were observed at some of the higher speeds EOCs (such as #7, #8, #11 and #12). The number and frequency of observed knock events at each EOC is displayed below in Figure 5.28. The implication of this suggestion is that under light knocking conditions, such as at the nominal KLSA for example, it is unlikely that many of the IDCs tested in this investigation would be able to classify knocking cycles with any accuracy. Figure 5.29 highlights this point, plotting knock frequency for EOC #11 against spark timing. Here one can see that at the measured KLSA, apart from the Yates cool-flame correlation, none of the tested IDCs come close in terms of their predicted knock frequencies. Admittedly, this is a crude comparison. A more complete evaluation would require each IDC to be tested at a

finer resolution of spark settings, particularly around the KLSA. This would however be a very time consuming process.

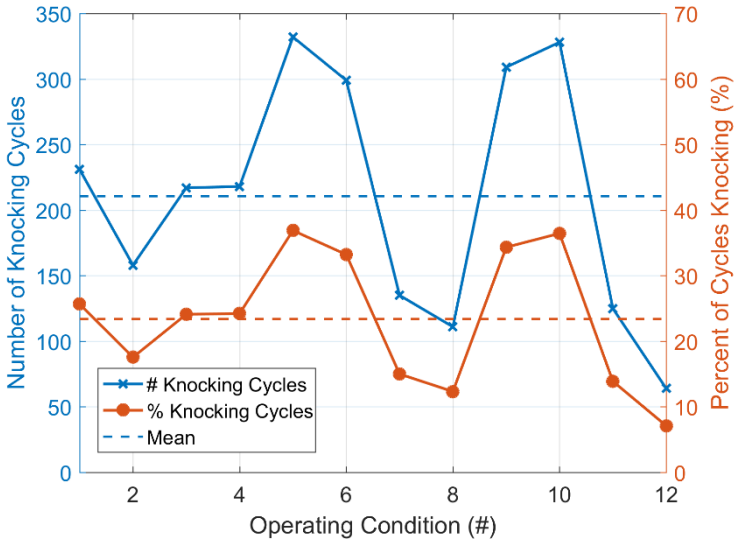

Figure 5.28 – Prevalence of knocking cycles at each EOC considered in this investigation.

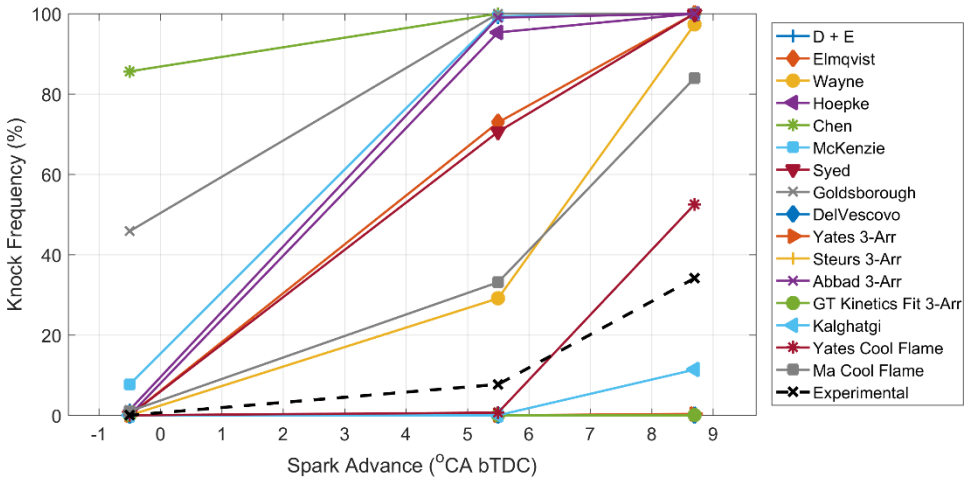

Figure 5.29 – Predicted and measured knock frequency vs. spark advance at EOC #11 (3500rpm, 23bar BMEP)

As the complexity of engines has increased enormously in recent years, so too has the task of calibration. Many OEMs have looked towards simulation as a means to reduce the costs and time associated with calibration. Unfortunately, the results of this investigation suggest that with respect to the prediction of knock, the tools that are currently available and that are practical in terms of computational cost and run times, simply are not accurate enough for virtual calibration of ignition timing.

5.6.4 Summary of IDC Assessments

The IDCs that featured in the top six overall for each of the three evaluation techniques have been listed below in Table 5.6. Unfortunately, there is very little crossover in the results produced by the three evaluation methods. To simplify selection of a single correlation going forward, the results of the L+W integral error evaluation approach have been discounted. This step was taken due to the aforementioned negative biases that this technique exhibits towards the cool-flame models and towards models that are more likely to predict knock onset earlier than in was observed experimentally.

From the ranks of the remaining two evaluation techniques, the Ma cool-flame formulation would be the obvious choice. Closer inspection of the scores listed in the ranking table of Figure 5.26 however revealed the Ma correlation demonstrated significantly worse knock classification capabilities relative to the three higher-ranking correlations of Kalghatgi and Yates. Unfortunately, none of these three correlations were able to predict angle of knock onset with an acceptable degree of accuracy, overestimating it significantly. The implication of this finding is that for the correlations tested in this investigation, predicting knock onset accurately *and* correctly distinguishing between knocking can non-knocking cycles are mutually exclusive capabilities. Selection of a single model going forward would therefore require favouring one capability over the other. Both attributes are important for a knock model to be of practical use, therefore the decision of which to favour is arbitrary.

Rank	L+W Integral Error Approach / Score	aKO RMSE Approach / Score	Mean of Knock Classification Agreement Statistics Approach / Score
1	Elmqvist / 0.78	AlAbbad / 3.54°CA	Yates Cool Flame / 0.76
2	Wayne / 0.80	Ma / 4.02°CA	Kalghatgi / 0.75
3	Hoepke / 0.80	Douaud + Eyzat / 4.37°CA	Yates 3-Arrhenius / 0.71
4	Syed / 0.83	Hoepke / 4.70°CA	Ma / 0.64
5	Steurs / 0.89	McKenzie / 4.94°CA	DelVescovo / 0.60
6	GT “Kinetics-Fit” / 0.94	Goldsborough / 5.02°CA	Wayne / 0.59

Table 5.6 – Six best ranking IDCs across all 12 EOCs according to the three evaluation techniques considered in this study

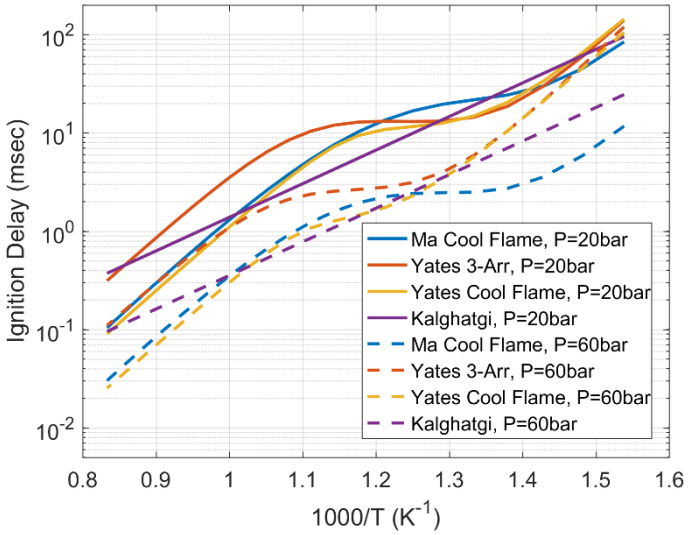

Figure 5.30 – Ignition delay times predicted by the Ma, Yates cool-flame, Yates 3-Arrhenius and Kalghatgi correlations as a function of temperature at P = 20bar and P = 60bar (λ = 1, RGF = 0%). The fuel modelled is iso-octane for the Ma and Yates cool-flame IDCs, and 95 RON gasoline for the Kalghatgi and Yates 3-Arrhenius IDCs.

Figure 5.30 explores the reasons for why the Ma, Kalghatgi and two Yates correlations behave so differently with respect to their aKO and cycle classification capabilities. At a pressure of 20bar, all four correlations predict quite similar ignition delay times in the low temperature regime (1000/T > 1.3, or T < 800K). Hotspot temperatures greater than this threshold were rarely predicted for the conditions modelled as part of this investigation. In the intermediate temperature regime, the strong NTC behaviour exhibited by the Yates 3-Arrhenius correlation causes it to predict longer delays than the other three correlations.

At a higher pressure of 60bar however, the variation in ignition delay times in the low temperature regime between the four IDCs is significant. Both Yates correlations predict very similar delay times, whilst the Ma correlation predicts delay times that are up to one order of magnitude quicker. The ignition delay time predictions from the Kalghatgi correlation appear to bisect those of the Yates and Ma correlations, however the log-scale means that the Kalghatgi predictions are actually much closer to those of the Yates correlations. In the intermediate temperature regime, the ignition delay times for all four models come together again before the strong NTC behaviour exhibited by the Yates 3-Arrhenius correlation causes it to predict longer ignition delay times relative to the other three.

At temperatures relevant to this investigation, the primary difference between these four correlations is therefore their ignition delay predictions in the low temperature regime at high pressures. Most of the conditions modelled in this study were at high boost pressures.

Coupled with the fact that the experimental engine has a relatively high compression ratio for an SI engine with a high specific power target, the fresh charge was subjected to high pressures for prolonged periods of time prior to ignition. The differences in low temperature ignition delay predictions at high pressures between these correlations would therefore have had a significant impact their respective knock onset predictions. The shorter delay times predicted by the Ma correlation under high pressure/low temperature conditions explain why it stands out from the other three, predicting knock in a much larger number of cycles and earlier in the combustion event (see Figure 5.31 below).

The values of the pressure exponents govern how pressure is accounted for by IDCs. As discussed in earlier sections, most of the correlations investigated in this work were calibrated using data recorded (or simulated) at lower pressures than those experienced inside highly boosted engines. The DelVescovo correlation is an exception, using simulated ignition delay times at pressures as high as 100 bar to calibrate their correlation. However, the constant volume simulations in their investigation were performed using a CKM that is only valid up to 60bar (the current practical limit of fundamental ignition delay measurement apparatus such as shock tubes and RCMs). The results of the current investigation show that the high cylinder pressures experienced prior to combustion inside highly boosted engines necessitate the need for ignition delay correlations that are accurate at low temperatures/ high pressures. It is not clear whether such a correlation exists at present, however the inability of any of the IDCs tested in this work to predict knock in the right cycles at the right time would suggest not. Evidently, there is also some disagreement between the correlations tested in this investigation with respect to how pressure influences ignition delay at low temperatures/high pressures.

Continuing the discussion regarding the differences in predictive performance between the Ma, Kalghatgi and two Yates correlations, Figure 5.31 compiles the data for all 10800 cycles modelled throughout the course of this investigation. In this figure, the maximum L+W integral values calculated for each cycle have been plotted against normalised MAPO. MAPO values have been normalised by the appropriate knock detection thresholds in order to fit the data from all 12 EOCs onto one axis. Normalised MAPO values greater than 1.0 represent true knocking cycles. Alongside each plot, an additional axis shows the L+W integral values at the measured aKO for true knocking cycles. This group of plots represents a useful visual tool for evaluating the difference between IDCs on a cycle-by-cycle basis. The types of

classification can also be inferred visually from this figure, with the four regions representing true positive/true negative/false positive/false negative classifications highlighted. The ideal IDC would only place cycles in the true positive and true negative quadrants.

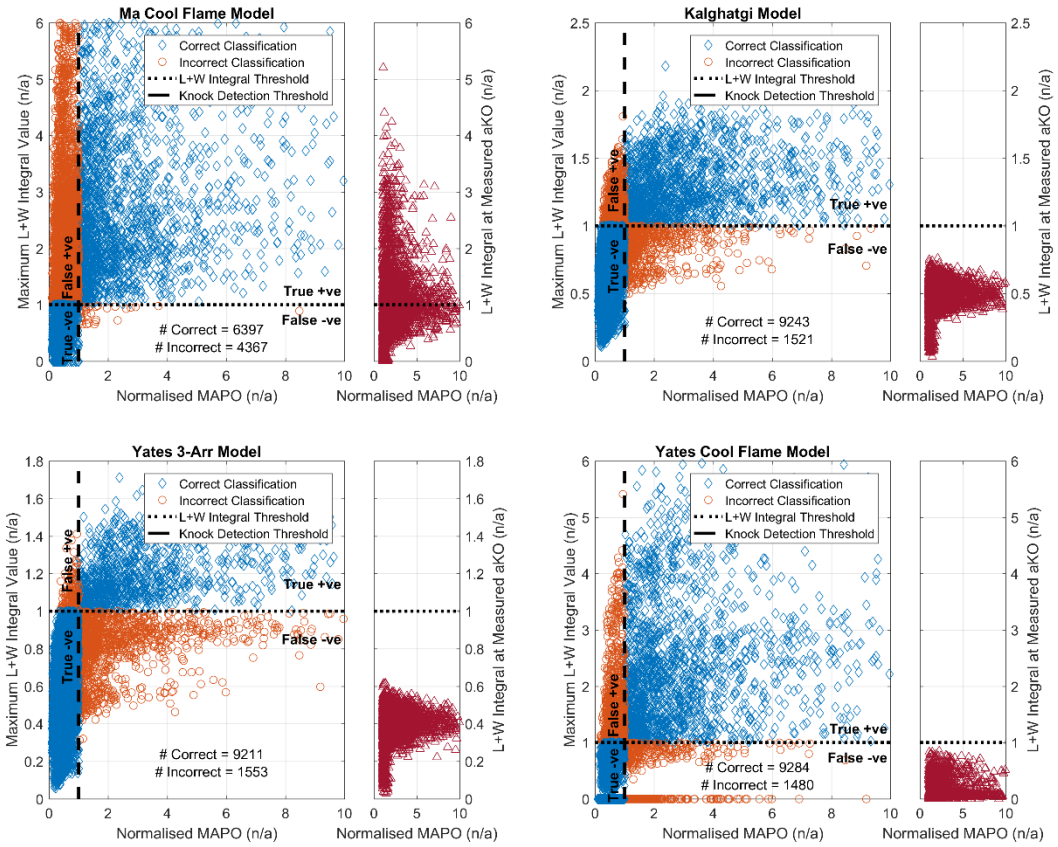

Figure 5.31 – Maximum L+W integral values and L+W integral values at measured aKO plotted against MAPO (normalised by the knock detection threshold) for the Ma, Kalghatgi and both Yates correlations.

There are multiple observations that can be drawn from Figure 5.31. The first applies to all four IDCs, where heavier knocking cycles generally produce larger values of the L+W integral. This is a useful result, and suggests that the maximum value of the L+W integral for a given cycle could be used to imply a relative knock intensity. At a fixed maximum L+W integral value, there is however considerable spread in the observed knock intensities. Much of this spread will be due to in-cylinder effects that cannot be modelled by two-zone combustion models, such as the size and thermal gradient within the auto-igniting hotspot. Bradley and co-workers have conducted extensive research in this field, correlating the intensity of pressure waves resulting from autoignition to the temperature gradient and local speed of sound within the hotspot [117, 123, 124]. In their work, they have shown that the shallower the temperature gradient, the stronger and more damaging the resulting pressure waves. To

model such behaviour inside real engines (and thus enable accurate estimation of knock intensity from the L+W integral), one would need to resort to a three-dimensional description of the unburned zone, and accept the associated increase in complexity and computational cost that this would bring.

The remaining observations to be drawn from Figure 5.31 relate to the differences in the predictions between the four correlations. The Ma correlation has the strongest tendency to predict knock events, which in this case has resulted in a large number of false positive classifications. With almost three times as many incorrect classifications, the overall accuracy of the Ma correlation was approximately 25% less than that of the other three (~60% vs ~85%). On the other hand, the Ma correlation successfully predicts knock for almost 100% of true knocking cycles. The Kalghatgi and Yates correlations all generated a significant number of false negative classifications, some of which exhibited very strong knock intensities. Failing to predict knock in heavily knocking cycles is not a good result, and again could be attributable to the aforementioned inability of the two-zone combustion modelling approach to simulate thermal and compositional gradients within the end gas. The improved aKO prediction capabilities of the Ma correlation are evident from the distribution of L+W integral values at the measured aKO being more centrally located around the target value of 1.0. Something that wasn't visible from previous analysis techniques is the spread of L+W integral values at the measured aKO, however as the most accurate IDC tested in terms of aKO, this spread has clearly not translated into a large aKO RMSE.

The remaining three correlations all make approximately the same number of incorrect classifications as one another, with a Yates 3-Arrhenius formulation displaying a higher tendency towards false positive classifications and the Kalghatgi/Yates cool flame formulations exhibiting a nominally 50:50 split between false positive and false negative classifications[17]. All three exhibit low values of the L+W integral at the measured aKO, as already discussed, and hence predict knock onsets considerably later than those measured. The higher values exhibited by the Yates cool flame IDC however give it a slight advantage over the Yates 3-Arrhenius and Kalghatgi correlations in terms of aKO accuracy, an

[17] The small fraction of cycles pertaining to the Yates cool flame IDC that have maximum L+W integral values of zero are the result of a computational error regarding the handling of cycles that were predicted to exhibit no cool-flame (and therefore would not have been predicted to knock). The actual maximum L+W integral values for these cycles should in fact be greater than zero but less than 1.0. Fortunately, this oversight has not affected either of the knock classification agreement statistics or the aKO RMSE for this correlation.

observation confirmed by the data plotted in Figure 5.23. Of these three correlations, the Yates cool flame correlation therefore performed the best overall at the conditions investigated in this study.

5.6.5 Improving the classification accuracy of the Ma correlation

A simple method to improve the knock classification accuracy of the Ma correlation without recalibrating the model coefficients and without compromising the accuracy of its aKO predictions was attempted. Initially, a simple approach based on the fuel mass fraction burned (MFB) at the measured angle of knock onset was investigated. Figure 5.32 plots aKO against fuel MFB at aKO for the predicted and measured knocking cycles across all 12 EOCs. It is apparent that across all 12 EOCs, not a single true knocking cycle was initiated at a point later than 95% fuel MFB. A modest number of the false positive classifications made by the Ma correlation were however predicted to occur later than this threshold (438 in total, out of the overall population of 10,800 cycles). Admittedly, so too were some of the true positive classifications (33 in total). The net improvement in overall cycle classification accuracy after applying a 95% fuel MFB threshold for qualifying knocking cycle predictions was only 3.8%, taking the overall accuracy to 63.2%. The impact of this change on the overall cycle-classification agreement has not been evaluated, but it would of course improve the situation slightly.

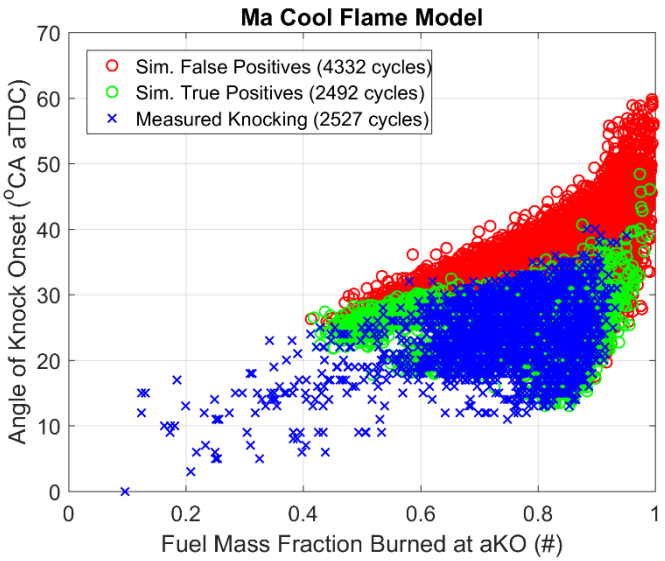

Figure 5.32 – Angle of knock onset plotted against fuel mass fraction burned at angle of knock onset. Data for knocking cycles (measured and simulated using the Ma correlation) has been pooled across all 12 EOCs.

As is evident from Figure 5.32, the bulk of the false positive classifications from the Ma correlation had predicted MFB at knock onset within the MFB limits observed experimentally. The predicted aKO for many of these cycles was however comparatively late, indicating slow overall burn rates. A more effective threshold for minimising the number of false positive classifications would therefore be one that is based on the 90% MFB crank angle (CA90) for example. The challenge in this regard would be defining an appropriate threshold that is valid across a broad range of EOCs and that requires the minimum amount of experimental data to support it. Both Franke and Worret attempted to address this challenge within their IDCs. Rather than overlooking these correlations, it therefore would have been prudent to investigate them further.

It is worth noting that applying the same 95% MFB threshold to the Yates and Kalghatgi correlations would be very detrimental to their cycle classification agreement results. As Figure 5.33 shows, a large proportion of the correct knocking cycle classifications from the Yates and Kalghatgi correlations exhibit very late MFB at aKO predictions. At the conditions modelled in this investigation, the Ma correlation, combined with the 95% MFB at aKO threshold for qualifying knocking cycle classifications, therefore represents the best overall compromise between aKO accuracy and cycle classification agreement.

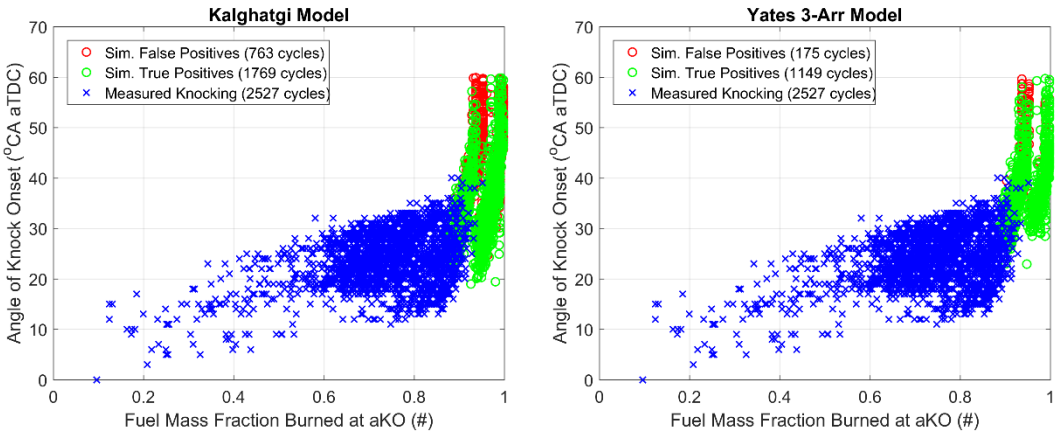

Figure 5.33 – Angle of knock onset plotted against fuel mass fraction burned at angle of knock onset. Data for knocking cycles (measured and simulated using the Kalghatgi and Yates 3-Arrhenius correlations) has been pooled across all 12 EOCs.

Further improvement to the accuracy of aKO predictions and cycle classifications for the Ma correlations might have been realised had it been possible to implement the mixing rule proposed in the original publication. This mixing rule applied to quaternary gasoline

surrogate blends consisting of iso-octane, n-heptane, toluene and ethanol. The challenge faced by the author in this regard was determining an appropriate surrogate fuel blend for the experimental fuel used in this work. A method for devising TRF surrogate blends that match both the RON and MON of any target gasoline has however been recently published by Kalghatgi [50]. Implementing this method and testing the impact of modelling a TRF with the same RON and MON as the experimental fuel (instead of modelling pure iso-octane) would be an interesting avenue for further work.

5.6.6 Detailed analysis of the Yates 3-Arrhenius IDC at low speed/high load

The operating conditions that are most susceptible to knock are low speed and high load, where there is ample time for hotspots to autoignite and where in-cylinder pressures and temperatures are high. In this work, the highest load operating condition at 1500rpm was EOC #4, achieving a BMEP of approximately 31bar at the KLSA. At this condition, the Yates 3-Arrhenius correlation achieved the highest overall knock classification agreement with the measured data, thus warranting further investigation of its characteristics.

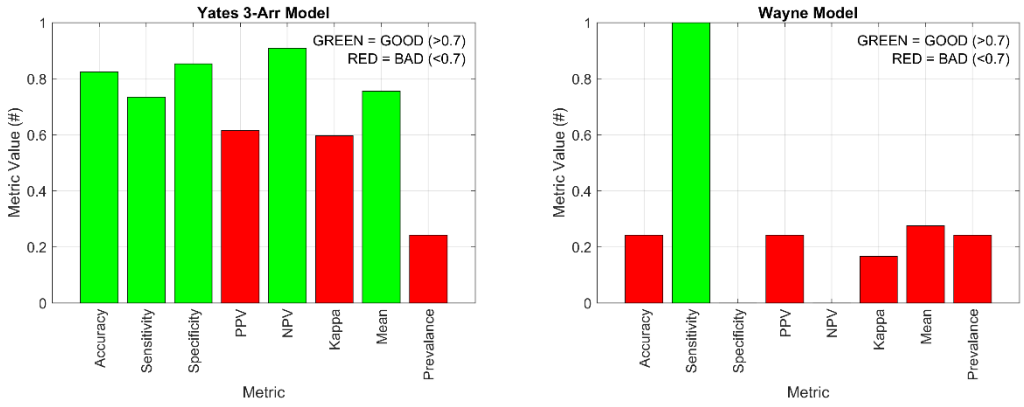

Figure 5.34 – Knock classification agreement statistics for all 900 cycles recorded at EOC #4. Yates 3-Arrhenius IDC on the left, Wayne 1-Arrhenius IDC on the right.

Figure 5.34 presents the knock categorisation agreement statistics (introduced in Chapter 4, Section 4.5.2) for the Yates 3-Arrhenius and Wayne IDCs at EOC #4. The contrast is stark, with the Yates correlation scoring a mean value of approximately 0.75 across all agreement statistics and the Wayne correlation scoring less than 0.25, the former indicating strong agreement and the latter indicating very weak agreement between the experimental and

predicted cycle classifications[18]. The only statistic in which the Wayne model scored favourably was sensitivity, which was defined as the fraction of true knocking cycles predicted to be knocking. Since the Wayne correlation classified every cycle as knocking at this EOC, it duly scored 100% for this metric. The Yates correlation achieved a sensitivity score of approximately 0.72, suggesting that nearly 30% of the true knocking cycles were misclassified.

The Yates correlation scored relatively poorly for the positive predictive value (PPV) metric and Cohen's Kappa. PPV describes the proportion of cycles predicted to be knocking that actually were knocking. A score of approximately 0.6 therefore indicates that only 60% of the cycles predicted as knocking by this correlation actually were knocking. Cohen's Kappa (κ) meanwhile describes the level of agreement between predicted and measured knock classifications relative to that which could be achieved by chance. Values of 1.0 indicate perfect agreement, whilst values of zero indicate that the agreement is no better than that which could be achieved by chance alone. According to Landis [125], κ values greater than 0.6 indicate "substantial" agreement. The Yates correlation achieved a κ score just shy of this threshold.

Having examined the knock classification statistics for the Yates correlation, the next step was to ascertain whether any systematic patterns could be spotted to help explain why misclassifications were made. To this end, four cycles were selected – one from each of the four quadrants in Figure 5.35, allowing the differences between cycles with nominally constant knock intensity and constant L+W integral values to be examined. Table 5.7 summarises some of the key properties for each of the four cycles selected, whilst Figure 5.36 plots measured cylinder pressure, band-pass filtered (BPF) cylinder pressure, predicted hotspot temperature and the resulting L+W integral as functions of crank angle.

[18] Note that the prevalence statistic has not been included in the overall mean since it doesn't have any relevance to the predictions made by each IDC. It has been included in Figure 5.34 just to highlight the fraction of cycles at this EOC that were genuinely knocking.

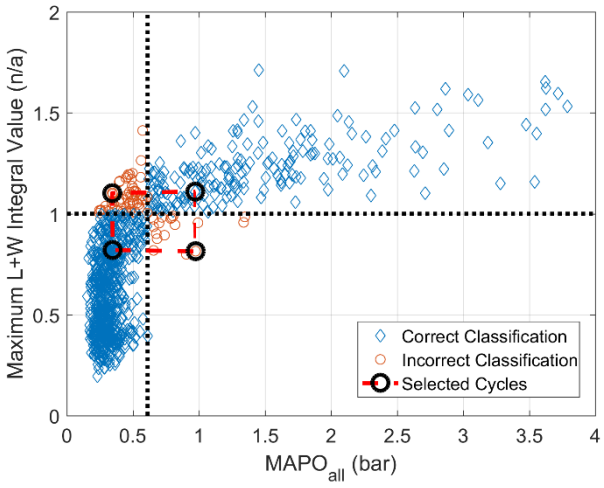

Figure 5.35 – Maximum L+W integral versus MAPO for all 900 cycles modelled at EOC #4 (1500rpm, 31 bar BMEP) using the Yates 3-Arrhenius IDC.

	Cycle #1 (True Positive)	Cycle #2 (False Positive)	Cycle #3 (True Negative)	Cycle #4 (False Negative)
MAPO (bar)	0.97	0.34	0.35	0.97
Max. L+W Integral (n/a)	1.11	1.10	0.82	0.81
Max. Cylinder Pressure (bar)	122.5	116.0	99.3	118.3
Max. Hotspot Temperature (K)	797.9	796.6	768.4	780.1
$T_{15\ bar}$ (K)	508.0	510.8	509.4	500.9
Angle of 50% MFB (°CA aTDC)	25.4	26.6	31.3	26.3
End of Combustion (°CA aTDC)	42.6	42.5	49.1	48.8
Trapped λ (#)	0.96	0.96	0.96	0.96
Trapped RGF (#)	7.5×10^{-4}	7.4×10^{-4}	7.1×10^{-4}	7.5×10^{-4}

Table 5.7 – Features of the four cycles highlighted in Figure 5.35

From Table 5.7, one can see that knock intensity (MAPO) values for the true positive and false negative cycles were virtually identical, as were those of the false positive and true negative cycles. There was very little variation in trapped λ and trapped RGF between the

four cycles, therefore the influence of these parameters on ignition delay can be discounted immediately. The influence of burn rate appears to be mixed, with cycle #2 demonstrating that faster cycles did not necessarily result in knock. Besides knock intensity, there is actually very little in Table 5.7 to separate cycles #1 and #2. Meanwhile, the burn angles of cycles #3 and #4 suggest that burn rates in the first half of the combustion event probably have a larger impact on knock tendency than those in the second half. This observation is drawn from the fact that both cycles have similar overall combustion durations, but cycle #4 displayed a much earlier CA50 than cycle #3. Faster burn rates in the early stages of combustion are more likely to generate high cylinder pressures than fast burn rates towards the end of combustion because the combustion chamber volume is that much smaller earlier in the cycle. It therefore seems logical that cycle #4 would exhibit stronger knock intensity than cycle #3.

Cycle #1 was correctly predicted to be knocking. If one had to classify just one of the cycles shown in Figure 5.36 as knocking, it would probably by cycle #1. Apart from during the compression stroke, this cycle demonstrated the highest pressure and temperature at any given crank angle prior to it reaching its maximum cylinder pressure. Cycle #3 meanwhile was correctly predicted to be non-knocking. Again, comparing the raw cylinder pressure and temperature profiles of this cycle with the other three, this result is not a surprise.

Cycle #2 on the other hand was incorrectly predicted as knocking. Comparing this cycle with cycle #4, which was incorrectly classified as non-knocking, reveals some interesting behaviours. From the cylinder pressure traces of these two cycles, the only major difference is that cycle #2 exhibits lower cylinder pressure during the central portion of the combustion event. On this basis alone, one would expect cycle #4 to be the knocking cycle of the two, not cycle #2. However, the predicted hotspot temperature evolution for cycle #2 explains why this was not the case, with cycle #2 exhibiting hotter temperatures throughout the compression and expansion strokes. Cycle #4 exhibited the lowest temperatures during the compression process of any of the four cycles. The average temperature difference between these two cycles was small (<10K at 15bar cylinder pressure and <20K from TDC onwards), however it was clearly significant enough to overcome the difference in cylinder pressure and result in a knocking cycle prediction for cycle #2. From this observation, one can conclude that the Yates 3-Arrhenius correlation is particularly sensitive to differences in temperature, with differences in pressure having less impact on the resulting L+W integral.

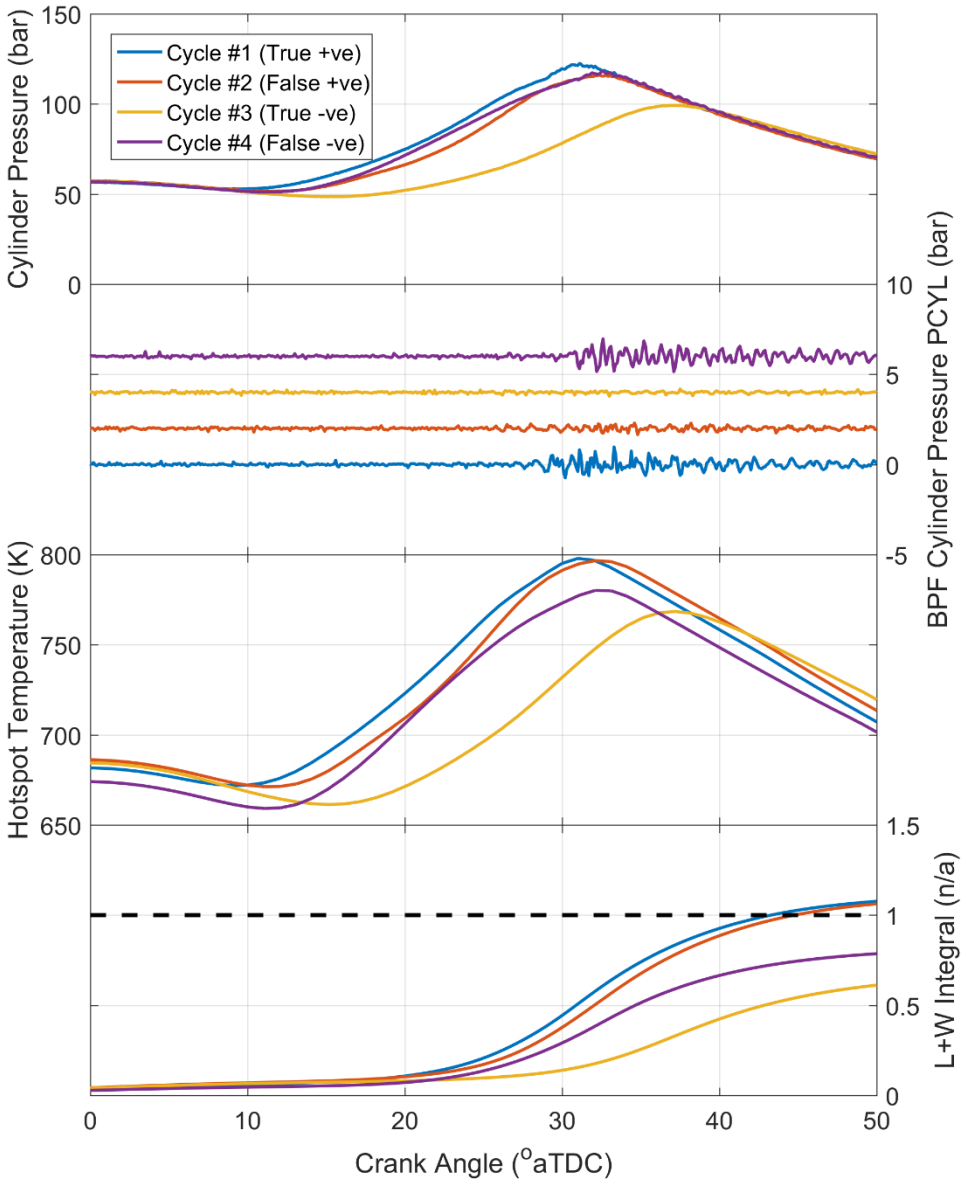

Figure 5.36 – Measured cylinder pressure data (both raw and band-pass filtered), predicted hotspot temperatures and the resulting L+W integrals plotted against crank angle for the four cycles identified in this analysis.

The above analysis highlights the importance of accurate gas temperature predictions throughout the cycle. This process starts with the fresh charge as it flows through the intake ports and into the cylinder, and should include the effects of heat transfer from the combustion chamber walls, the effects of trapped composition on the ratio of specific heats, and ideally, the effects of thermal and compositional inhomogeneity within the end gas. Unfortunately, although it may be one of the most significant attributes in terms of its effect on the development of AI in real engines, this last attribute cannot be modelled using a two-zone combustion modelling approach. Three-dimensional modelling approaches may be able to simulate this attribute more accurately, however the computational expense is several

orders of magnitude greater than that of the two-zone approach used here, and even then there is no guarantee that the IDC used to estimate knock onset will be accurate at the pressures simulated. Fortunately, the engine used in this work is not likely to have exhibited high levels of inhomogeneity (whether thermal or compositional) thanks to the high levels of turbulence it was capable of generating. Although it may be an oversimplification of the real mixing and combustion processes, the application of a two zone modelling approach in this case is therefore justified. Furthermore, several of the IDCs tested in this work were calibrated using real engine data. Thus, the effects of inhomogeneity (albeit specific to the engines used in those investigations) are implicitly included in those correlations.

5.7 Conclusions

In this chapter, the knock-prediction capabilities of sixteen ignition delay correlations (IDCs) from the literature were evaluated by way of comparison with experimental data. The IDCs tested spanned a broad range of fuels, dilution modelling approaches and calibration methods. A 1D model of the experimental engine was used to predict trapped charge composition and temperature evolution up to the point in each cycle where cylinder pressure reached 15 bar. Beyond this point, the temperature of a hypothetical hotspot within the fresh charge was assumed to evolve adiabatically and with a temperature-varying ratio of specific heat capacities. The progress of the pre-autoignition chemical reactions within this hotspot were tracked using the Livengood and Wu integral approach. The engine operating conditions (EOCs) investigated covered a broad range of speeds, loads and residual gas fractions, with particular relevance to the conditions experienced within today's generation of highly boosted, downsized SI engines.

The 1D model developed in this chapter was successfully calibrated to match measured engine data. During the model calibration process, several interesting observations were made regarding the functionality of the chosen modelling software (GT-Power).

- The blowby submodel was found to exclude the transfer of fuel from the cylinder to the crankcase. Throughout the experimental campaign, blowby mass flows accounted for approximately 1% of the combined air and fuel mass flows. Since blowby was vented to the test-cell rather than returned to the intake manifold, this flow of air and fuel represented a form of energy loss that could not be accounted for within GT-Power. As a result, its effects will have been lumped into the overall energy balance error term – a multiplier applied automatically within GT-Power to the lower heating value of the fuel.
- The default settings for fuel evaporation assume that evaporation only takes place at the flame boundary, and thus only occurs during the combustion event. To incorporate a degree of the charge cooling and volumetric efficiency effects of direct injection within the 1D model, it was necessary to define a custom fuel evaporation submodel. Parameters for this model were estimated from data found within the literature concerning the evaporation of gasoline sprays at relevant injection pressures. The difference in predicted temperatures at IVC between the default evaporation settings and those defined in the custom evaporation submodel was

approximately 15°C across a number of operating points. During compression and combustion, this temperature difference is magnified, leading to significant differences in the predicted angle of knock onset.

- A drawback of using measured exhaust species concentrations to dictate the mass fraction of fuel burned during the combustion event was highlighted. In practice, a degree of post-flame oxidation would be expected to reduce the concentration of unburned hydrocarbons after the combustion event. In this work however, no allowance was made to account for this effect, which presumably resulted in imposed burned fuel fractions that were higher than those experienced within the experimental engine (during the main combustion event at least). This could explain why the LHV multiplier applied by GT-Power was observed to decrease at higher loads, i.e. where gas temperatures are hotter and where post-flame oxidation would be expected to be more prevalent. This phenomenon is therefore unlikely to have affected the model calibration (specifically the value of the convective heat transfer multiplier used).
- The "WoschniGT" convective heat transfer model was found to underestimate heat transfer significantly. The final 1D model calibration required a convective heat transfer multiplier of 2.0 to be applied across the entire four stroke cycle.

During the knock modelling component of this chapter, considerable effort was made to ensure a high degree of realism in the hotspot temperature predictions. Autoignition is a temperature-sensitive process, therefore accurate temperature predictions are vital. Unfortunately, with no way of measuring in-cylinder gas temperatures on the experimental engine, the accuracy of these predictions couldn't be verified. The following steps were taken to minimise the potential sources of error:

- Adiabatic compression of a hypothetical hotspot was assumed to occur from a point sometime after IVC to allow enough time for the fresh charge to be heated by the hot combustion chamber surfaces in the early portion of the compression stroke. Hotspot temperature predictions were found to be very sensitive to intake valve timing and the point in the cycle when the assumption of adiabatic compression was initialised. Early intake valve closing (IVC) and the assumption of adiabatic compression from IVC onwards resulted in comparatively cool hotspot temperature predictions, even when compared with those obtained from GT power, which

included the effects of heat transfer from the unburned zone at higher pressures. Late intake valve closing on the other hand, combined with the same assumption of adiabatic compression from IVC onwards, resulted in comparatively hot hotspot temperature predictions. Heat transfer to the fresh charge during the period between the two intake valve-timing settings considered in this work was therefore considerable and should not have been ignored. The author therefore adopted an approach whereby the assumption of adiabatic compression was initialised at the point in the cycle when the cylinder pressure reached 15 bar (as is implemented in [50]). This approach resulted in much more consistent hotspot temperature predictions compared to those that would have been obtained by assuming adiabatic compression from IVC onwards.

- The ratio of specific heat capacities (γ) was modelled as a function of temperature, allowing the effects of compression and mixture composition to be accounted for. The predicted γ values agreed very well with those estimated manually from the measured cylinder pressure traces over the last 20°CA before TDC/ignition (whichever came earliest). Adopting a fixed γ from the point of 15bar cylinder pressure would have negatively affected the accuracy of hotspot temperature predictions, particularly at higher loads where 15 bar occurred earlier in the cycle. Although this impact may have been small in terms of absolute temperature difference, the cumulative nature of the L+W integral means that small differences in temperature can have a large effect on predicted autoignition onset times. Allowing γ to vary as a function of temperature minimised the risk of such errors occurring.

The sixteen literature IDCs were evaluated at twelve high-load operating conditions. Cycle classifications (“knocking” or “non-knocking”) and the angle of knock onset (aKO) were estimated from measured cylinder pressure data using the methods derived in Chapter 4. An initial assessment of IDC performance based on the error of the L+W integral suggested that the Elmqvist correlation performed the best overall. The magnitude of the L+W integral errors however implied that none of the correlations was likely to predict aKO with an acceptable degree of accuracy. Several downsides were observed with the L+W integral error approach to IDC evaluation. The first was the negative bias displayed towards the staged L+W integral correlations (Yates’ and Ma’s “cool-flame” models). The second was the positive bias displayed towards cycles that predict knock very late, or not at all. Knock

prediction bias in this direction limited the L+W integral error to values less than 1.0. It was therefore possible for IDCs to predict zero knock events across the entire population of cycles, yet still score relatively favourable L+W integral errors.

A second IDC evaluation technique based on the root mean square error (RMSE) of the predicted aKO was implemented. The results of this investigation showed that over the 12 EOCs, not one of the IDCs tested was able to predict knock within the acceptable limit of ±2°CA. This observation was partly due to the fact that aKO errors are amplified at higher engine speeds. At 1500rpm, the AlAbbad correlation was the only IDC able to predict knock onset times to within ±2°CA at every condition. At 3500rpm, the aKO RMSE of the AlAbbad correlation was 5.5°CA, which compared favourably with the best overall score of 4.81°CA achieved by the D+E correlation. Over the twelve EOCs, the AlAbadd correlation scored the lowest overall aKO RMSE (3.54°CA). No obvious correlation between aKO RMSE and BMEP or RGF could be determined. Furthermore, none of the "EGR-equipped" IDCs demonstrated notably better performance than their "air-only" counterparts. It therefore was not possible to draw any conclusions regarding the best method of accounting for the effects of dilution with exhaust gas on ignition delay. Further investigation at higher EGR rates may prove beneficial in this regard.

A third and final IDC evaluation technique based on cycle classifications was implemented. In this technique, the level of agreement between "measured" and predicted cycle classifications was assessed at each EOC using the mean of the following statistics – accuracy, sensitivity, specificity, precision, positive predictive value, negative predictive value and Cohen's Kappa. Scores close to 1.0 for this metric indicate almost perfect agreement between the measured and predicted cycle classifications, whilst scores close to zero indicate almost no agreement. A distinction is made between accuracy and agreement, since it would be possible to an IDC to achieve an overall accuracy of approximately 76% just by predicting every cycle to be non-knocking. The best overall correlation in this regard was the Yates cool-flame formulation, achieving a mean score of 0.76 over the 12 EOCs. This was closely followed by the Kalghatgi and Yates 3-Arrhenius correlations, achieving mean cycle-classification agreement scores of 0.75 and 0.71 respectively. Again, no obvious trends between overall agreement and BMEP or RGF were observed, and better performance was achieved at lower engine speeds. This last outcome could be because fewer knocking cycles were observed at the higher speeds EOCs, suggesting that under light knocking conditions,

very few of the IDCs tested in this investigation would be able to identify knocking cycles with an acceptable level of accuracy at conditions relevant to downsized engines. The implication of this observation is that for the time being at least, complete design and calibration of an engine in the virtual domain (i.e. without any physical testing) would not be possible because the tools available are simply not accurate enough.

Comparison of the IDCs that scored favourably in both the aKO RMSE and the cycle-classification agreement evaluations revealed that only the Ma correlation was able to perform reasonably well in both respects. For the most part, IDCs that performed well in terms of aKO RMSE performed badly in terms of cycle classification agreement, and vice-versa. This behaviour occurred because the sensitivity required for accurate aKO predictions also resulted in a large number of false positive classifications. The majority of these false positive classifications occurred in slow burning cycles, but at mass fractions burned (MFB) that were within the limits observed experimentally for genuinely knocking cycles. It is not sufficient therefore to clip the maximum MFB before aKO for a cycle to qualify as knocking.

Much of the difference between IDCs that were accurate in terms of aKO and those that demonstrated high agreement with measured cycle classifications appeared to stem from their low temperature/high pressure characteristics. IDCs that demonstrated high aKO accuracy predicted much shorter ignition delay times in this regime compared to those that achieved good cycle-classification agreement. Maximum hotspot temperature predictions across all twelve EOCs rarely exceeded 850K, putting the ignition delay behaviour investigated in this study squarely inside the low-temperature regime. Further study regarding the ignition delay characteristics of practical gasoline surrogates in this regime is therefore required.

The L+W integral was found to be a relatively good indicator of knock intensity. However, the limitations of the two-zone combustion modelling approach used in this work meant that factors such as thermal and compositional inhomogeneity within a hotspot, which have been shown to have a strong impact on the intensity of autoignition events, could not be modelled. To do so would require a detailed three-dimensional representation of the unburned zone, which would be prohibitively expensive computationally for the majority of applications. Even then, there is also no guarantee that ignition delay would be modelled accurately.

In summary, none of the IDCs tested in this investigation performed particularly well, with most actually performing particularly badly. Indeed, many of the IDCs performed very badly. The model that achieved the best overall balance between aKO accuracy and cycle-classification agreement however was Ma's cool-flame correlation for iso-octane. A modest improvement to the classification accuracy of this correlation could have been obtained by limiting the latest MFB for which knocking cycles would be permitted to 95%. Still, the overall aKO RMSE for this correlation was approximately 3.5°CA (unacceptably high compared to the ±2°CA limit observed by the literature) and the overall cycle-classification accuracy was only 59.4%. The main reason for this relatively modest accuracy was a large number of false-positive cycle classifications, i.e. instances of cycles predicted to be knocking when in fact they were not. The majority of these false-positive classifications were for slow or late burning cycles. Further work should focus on methods to reduce the number of false positive classifications obtained using this correlation, possibly using the method proposed by Worret [90] whereby the critical MFB threshold for knocking cycles is expressed in terms of the angle of 75% MFB. Although the Ma correlation makes no provision for the effects of EGR on ignition delay, at the conditions run at 10% EGR it outperformed most of the "EGR-equipped" correlations.

As powertrains and IC engines continue to grow in complexity, many OEMs are turning to simulation in an effort to reduce design validation and calibration costs. Ultimately, their aim is to complete this process entirely within the virtual domain, without the need for any physical testing. This work highlights however, that for the purposes of spark timing calibration and the avoidance of knock, the current crop of practical simulation tools are not accurate enough at the conditions relevant to modern SI engines for this aim to be a reality.

Chapter 6 – Conclusions and Further Work

Chapter Summary

The work in this thesis has focussed on evaluating the applicability of existing IDCs for the simulation of knock in high BMEP engines. In Chapter 2, knocking combustion and knock mitigation strategies were discussed, followed by a review of the various practical knock modelling approaches found in the literature. Chapter 3 described the experimental facilities and methods used to acquire the necessary high load experimental data. In Chapter 4, a detailed assessment of current and novel knock detection and angle of knock-onset estimation techniques was carried out. The best performing techniques were then carried forward to Chapter 5 where the knock onset predictions from sixteen gasoline-relevant ignition delay correlations were compared with measured data.

6.1 Conclusions

The conclusions from this investigation are presented below against the objectives laid out in Chapter 1.

1) *To conduct a detailed literature review on the factors that affect autoignition and knock in SI engines, and to achieve a thorough understanding of the limitations posed by the various empirical autoignition modelling approaches available.*

As outlined in the literature review in Chapter 2, Knock is the acoustic by-product of autoignition within some or all of the end gas. Autoignition was understood to be a chemical process that is highly sensitive to temperature, pressure, mixture composition and fuel reactivity. Knock mitigation has traditionally relied on strategies that penalise high load emissions and fuel economy. However, as emissions legislation have become stricter in recent years, the need for less polluting knock mitigation strategies has increased. Of the strategies described that are yet to become mainstream, EGR has emerged as one of the more viable approaches, offering advantages of better combustion stability and simpler

after-treatment requirements compared to dilution with excess air. The reactivity of fuel is a major factor in the knock tendency of an engine. The low temperature, high pressure conditions inside modern, highly boosted SI engines was identified as an operating regime that could enhance low temperature heat release, causing earlier knock onset. Unfortunately, this hypothesis could not be verified due to the pressure limitations of conventional ignition delay measurement equipment. This nevertheless presents an interesting opportunity for single-step IDCs calibrated using high load engine data – an area where again, there is a gap in the literature. Assuming the conditions within high BMEP engines were confined to the low temperature regime of practical gasolines, then there would be a strong argument for pursuing this route.

2) *To design and execute an experimental campaign capable of delivering combustion data across a broad range of knock-limited operating conditions relevant to downsized engines. The product of this objective is a rich data set that can be used to support further research in this field.*

An experimental approach was designed to maximise the advantages offered by the availability of a forced induction simulator (FIS) and bespoke EGR pump. The experimental strategy primarily consisted of intake manifold pressure sweeps at four different engine configurations, providing combustion data at BMEPs of up to 34 bar and in conditions relevant to two different boosting hardware configurations. EGR sweeps up to 15% dilution were also carried out at BMEPs between 17.5 and 25 bar. Engine load was found to have a significant impact on the knock-limited spark advance, resulting in less-optimal combustion phasing and hotter exhaust gas temperatures at higher loads. EGR was observed to mitigate this effect, supporting the observations made previously by other researchers in the field. At constant IMEP, it is possible that higher rates of internal EGR were detrimental to knock, resulting in less-optimal combustion phasing and longer burn durations.

3) To develop data processing techniques that can accurately extract knock-relevant metrics from cylinder pressure data collected at high loads.

A wide range of knock intensity (KI) metrics was gathered from the literature, critically evaluated and compared for uniqueness. Of the twelve metrics initially identified, only four

were found to be worthy of further consideration for knock detection. Lee's [86] metric normalisation technique offered some advantage with respect to knock threshold calibration by levelling the background noise level of the cylinder pressure data at retarded spark settings. However it also had the undesirable effect of reducing the KI observed under heavy knocking conditions, resulting in unrealistic KI vs spark timing characteristics. The four KI metrics were combined with three different knocking cycle detection methods. The KI metric/knock detection method combination that best matched cycle classifications made manually by the author was based on the maximum amplitude pressure oscillation (MAPO) KI metric and the "Maximum Non-knocking Value" KI threshold calibration approach. A similar screening approach was applied to angle of knock onset (aKO) estimation techniques. Among them, the Signal Energy Ratio approach proposed by Shahlari [1] best matched manually estimated aKO.

4) *To build a one-dimensional model of the experimental engine, and to calibrate it to the necessary degree of accuracy using measured data.*

Chapter 5 detailed the techniques used to build and calibrate a 1D model of the engine. The model was successfully calibrated to an acceptable degree of accuracy compared with measured data. Over the course of this investigation, some important observations were made regarding the functionality of the 1D modelling software used (GT-Suite). With respect to temperature predictions for the unburned zone, an important observation was made regarding the manner in which GT-Power simulates the evaporation of liquid fuel. To enhance the realism of the overall model, it was necessary to implement a custom fuel evaporation sub-model. This model was calibrated using data obtained from the literature regarding the evaporation rate of gasoline sprays at high injection pressures.

5) *To critically evaluate the performance of a variety of ignition delay correlations under conditions relevant to highly boosted, downsized engines by comparing knock onset predictions with experimentally measured knock onset times, to identify which correlations perform the best overall and to propose areas in which they could be improved.*

Sixteen gasoline-relevant IDCs were evaluated at twelve high-BMEP operating conditions. Cycle classifications ("knocking" or "non-knocking") and the angle of knock onset were estimated from measured cylinder pressure data using the methods derived in Chapter 4. A technique that assumed adiabatic compression from a point after IVC and temperature-varying ratio of specific heats was developed to simulate the temperature evolution of a hypothetical hotspot in the end gas. This revealed that none of the IDCs tested performed well at conditions relevant to modern, downsized engines. It is likely that the primary reason for this observation is that none on the IDCs tested were calibrated for use at the types of pressures observed within the experimental engine.

The IDC that achieved the best overall balance between aKO accuracy and cycle-classification agreement was the "cool-flame" correlation for iso-octane proposed by Ma [2]. However, this had an unacceptably high average aKO error of ±3.5° compared to the ±2°CA limit observed within the literature, and its average cycle-classification accuracy was below 60%. The main reason for this relatively modest accuracy was a large number of false-positive cycle classifications, which mainly occurred in slow or late burning cycles. Further work should therefore focus on methods to reduce the number of false positive classifications obtained with this correlation, and could be achieved using empirical correlations to describe the latest point in the cycle for which knock would be permitted to occur in terms other measureable combustion parameters.

Overall, this work has demonstrated that for the purposes of virtual spark timing calibration and the avoidance of knock, the current crop of practical simulation tools are not accurate enough at the conditions relevant to modern SI engines.

6.2 Further Work

This research has generated a unique insight into knocking combustion at very high loads, as well as an extensive dataset that can be used for future research to improve the accuracy of empirical knock modelling techniques.

The hotspot temperature predictions generated throughout the course of this work suggest that the experimental engine operated almost exclusively in the low temperature regime. At the highest intake manifold pressure conditions considered, the maximum predicted temperatures were in the region of 800K. This observation suggests that it could be possible to achieve relatively accurate recreation of the ignition delay characteristics of the fuel using a single-step IDC. The simplicity of such correlations makes them ideal candidates for calibration with real engine data, of which there is now ample supply. Generation of such a correlation would fill the void in the literature concerning IDCs that are applicable to combustion in high BMEP engines.

As mentioned above, Ma's cool-flame correlation for iso-octane achieved the best overall match with measured knock onset times and cycle classifications. In the original publication however, Ma proposed an approach for modelling the ignition delays of gasoline surrogates comprising of up to four constituents, two of which exhibit no NTC behaviour and thus have high sensitivities. Recent work by Remmert [126] has shown that at conditions relevant to modern SI engines, fuels with a high RON high sensitivity (i.e. *low* MON) offer a distinct performance advantage over fuels with equivalent RON but lower sensitivity. It would therefore be worth investigating this potential factor numerically to see if the behaviours reported in Remmert's experimental investigation can be recreated using a gasoline surrogate with sensitivity > 0.

In Chapter 3, it was noted that the experimental assessment on the impact of EGR on knock could have been improved had the experiments been conducted at fixed load. This experiment would be relatively inexpensive to perform, and the results would enhance the observations drawn regarding the effect of EGR on knock limited combustion phasing and the potential for BSFC improvement. In addition, it would be prudent to confirm the distribution of EGR between the four cylinders of the test engine. This task could be performed with relative ease by measuring CO_2 concentration within each intake port (currently, CO_2 concentration is only measured at one location along the top of the intake

manifold). A simple system of air lines running from the four intake ports to an emissions analyser via a manual control valve (to select which intake port to sample from) would suffice. The data obtained from such a setup would confirm whether poor delivery of EGR was responsible for cylinder-to-cylinder variations in IMEP and knock tendency.

Finally, in Chapter 4, a method of minimising the opportunity for bias to influence the manual knocking-cycle classification process was introduced. Regrettably, due to the time consuming nature of this process, its repeatability was not evaluated. A short exercise whereby one person manually classifies he same sample of cycles 3-4 times, with several days between each repeat attempt, would however allow the repeatability and robustness of this method to be examined. In addition, it would be worth investigating whether the guidelines outlined in the manual cycle classification decision tree (Figure 4.24) are effective at minimising the differences in manual classification results between operators. Comparing results from different operators would indicate how effective the proposed guidelines are at minimising the opportunity for personal bias to influence cycle classification decisions.

Bibliography

1. Shahlari, A.J. and J.B. Ghandhi, *A Comparison of Engine Knock Metrics*. 2012, SAE International.
2. Ma, J., et al., *An empirical modeling approach for the ignition delay of fuel blends based on the molar fractions of fuel components.* Fuel, 2016. 164(Supplement C): p. 305-313.
3. Turner, J.W.G., et al., *Ultra Boost for Economy: Extending the Limits of Extreme Engine Downsizing.* SAE Int. J. Engines, 2014. 7(1): p. 387-417.
4. Lumsden, G., et al., *Development of a Turbocharged Direct Injection Downsizing Demonstrator Engine.* SAE Int. J. Engines, 2009. 2(1): p. 1420-1432.
5. Neubauer, M., *AVL HyPer 200kW/Litre: TGDI High Performance Demonstrator*. 2016.
6. Heywood, J.B., *Internal combustion engine fundamentals*. 1988: McGraw-Hill.
7. Towers, J.M. and R.L. Hoekstra, *Engine Knock, A Renewed Concern In Motorsports - A Literature Review.* 1998, SAE International.
8. Lumley, J.L., *Engines : an introduction*. 1999, Cambridge: Cambridge University Press.
9. Stone, R., *Introduction to internal combustion engines*. 4th ed. ed. 2012, Basingstoke: Macmillan.
10. Attard, W.P., et al., *Abnormal Combustion including Mega Knock in a 60% Downsized Highly Turbocharged PFI Engine.* 2010, SAE International.
11. Sloboda, R., *Procedure to Calibrate Pre-Ignition in Highly Boosted Turbo Engines*, in *IMechE "Can Engines be Better by Design?" seminar*. 2012, The Institute of Mechanical Engineers: Peterborough, UK.
12. Dahnz, C., et al., *Investigations on Pre-Ignition in Highly Supercharged SI Engines.* SAE Int. J. Engines, 2010. 3(1): p. 214-224.
13. Inoue, T., Y. Inoue, and M. Ishikawa, *Abnormal Combustion in a Highly Boosted SI Engine - The Occurrence of Super Knock*. 2012, SAE International.
14. Kalghatgi, G.T. and D. Bradley, *Pre-ignition and 'super-knock' in turbo-charged spark-ignition engines.* International Journal of Engine Research, 2012. 13(4): p. 399-414.
15. Amann, M., D. Mehta, and T. Alger, *Engine Operating Condition and Gasoline Fuel Composition Effects on Low-Speed Pre-Ignition in High-Performance Spark Ignited Gasoline Engines.* SAE Int. J. Engines, 2011. 4(1): p. 274-285.
16. Amann, M., T. Alger, and D. Mehta, *The Effect of EGR on Low-Speed Pre-Ignition in Boosted SI Engines.* SAE Int. J. Engines, 2011. 4(1): p. 235-245.
17. Amann, M., et al., *The Effects of Piston Crevices and Injection Strategy on Low-Speed Pre-Ignition in Boosted SI Engines.* SAE Int. J. Engines, 2012. 5(3): p. 1216-1228.
18. Westin, F., B. Grandin, and H.-E. Ångström, *The Influence of Residual Gases on Knock in Turbocharged SI-Engines.* 2000, SAE International.
19. Alger, T., et al., *Cooled exhaust-gas recirculation for fuel economy and emissions improvement in gasoline engines.* International Journal of Engine Research, 2011. 12(3): p. 252-264.
20. Turner, J.W.G., R.J. Pearson, and S.A. Kenchington, *Concepts for improved fuel economy from gasoline engines.* International Journal of Engine Research, 2005. 6(2): p. 137-157.
21. Wirth, M., et al., *Turbocharging the DI Gasoline Engine.* 2000, SAE International.
22. Rask, R.B., *Laser Doppler Anemometer Measurements in an Internal Combustion Engine*. 1979, SAE International.

23. Wilson, N.D., A.J. Watkins, and C. Dopson, *Asymmetric Valve Strategies and Their Effect on Combustion*. 1993, SAE International.
24. Bohacz, R. *Eliminating Knock Retard*. How to Eliminate Knock Retard - Feedforward 2009 April, 2009; Available from: http://www.gmhightechperformance.com/tech/0904gmhtp_how_to_eliminate_knock_retard/viewall.html#ixzz2OGoRyFko
25. Grandin, B. and H.-E. Ångström, *Replacing Fuel Enrichment in a Turbo Charged SI Engine: Lean Burn or Cooled EGR.* 1999, SAE International.
26. Cairns, A., H. Blaxill, and G. Irlam, *Exhaust Gas Recirculation for Improved Part and Full Load Fuel Economy in a Turbocharged Gasoline Engine.* 2006, SAE International.
27. Turner, J.W.G., et al., *Improving Fuel Economy in a Turbocharged DISI Engine Already Employing Integrated Exhaust Manifold Technology and Variable Valve Timing.* 2008, SAE International.
28. Potteau, S., et al., *Cooled EGR for a Turbo SI Engine to Reduce Knocking and Fuel Consumption.* 2007, SAE International.
29. Kaiser, M., et al., *"Doing More with Less" - The Fuel Economy Benefits of Cooled EGR on a Direct Injected Spark Ignited Boosted Engine.* 2010, SAE International.
30. Alger, T., T. Chauvet, and Z. Dimitrova, *Synergies between High EGR Operation and GDI Systems.* SAE Int. J. Engines, 2008. 1(1): p. 101-114.
31. Cruff, L., et al., *EBDI® - Application of a Fully Flexible High BMEP Downsized Spark Ignited Engine.* 2010, SAE International.
32. Stein, R.A., C.J. House, and T.G. Leone, *Optimal Use of E85 in a Turbocharged Direct Injection Engine.* SAE Int. J. Fuels Lubr., 2009. 2(1): p. 670-682.
33. Grabner, P., H. Eichlseder, and G. Eckhard, *Potential of E85 Direct Injection for Passenger Car Application.* 2010, SAE International.
34. Kasseris, E. and J. Heywood, *Charge Cooling Effects on Knock Limits in SI DI Engines Using Gasoline/Ethanol Blends: Part 2-Effective Octane Numbers.* SAE Int. J. Fuels Lubr., 2012. 5(2): p. 844-854.
35. Pearson, R.J., et al., *Energy Storage via Carbon-Neutral Fuels Made From CO_2, Water, and Renewable Energy.* Proceedings of the IEEE, 2012. 100(No. 2): p. 440 - 460.
36. Turner, J.W.G., et al., *The Turboexpansion Concept - Initial Dynamometer Results*. 2005, SAE International.
37. Whelan, C.D., et al. *Design and development of a turbo-expander for charge air cooling*. in *9th International Conference on Turbochargers and Turbocharging, May 19, 2010 - May 20, 2010*. 2010. Westminster, London, United kingdom: Woodhead Publishing Ltd.
38. Romagnoli, A., et al., *Characterization of a supercharger as boosting & turbo-expansion device in sequential multi-stage systems.* Energy Conversion and Management, 2017. 136: p. 127-141.
39. Hancock, D., et al., *A New 3 Cylinder 1.2l Advanced Downsizing Technology Demonstrator Engine.* 2008, SAE International.
40. Taylor, J., N. Fraser, and P. Wieske, *Water Cooled Exhaust Manifold and Full Load EGR Technology Applied to a Downsized Direct Injection Spark Ignition Engine.* SAE Int. J. Engines, 2010. 3(1): p. 225-240.
41. Nishino, T., H. Senba, and N. Murakami, *Study of Engine Cooling Technologies for Knock Suppression in Spark Ignited Engines.* Mitsubishi Motors Technical Review Series, No. 16, 2004(16).
42. Takahashi, D., K. Nakata, and Y. Yoshihara, *Engine Thermal Control for Improving the Engine Thermal Efficiency and Anti-Knocking Quality*. 2012, SAE International.

43. Thiel, N., et al., *Advanced Piston Cooling Efficiency: A Comparison of Different New Gallery Cooling Concepts*. 2007, SAE International.
44. Leppard, W.R., *The Chemical Origin of Fuel Octane Sensitivity*. 1990, SAE International.
45. Yates, A.D.B., A. Swarts, and C.L. Viljoen, *Correlating Auto-Ignition Delays And Knock-Limited Spark-Advance Data For Different Types Of Fuel*. 2005, SAE International.
46. Yates, A.D.B. and C.L. Viljoen, *An Improved Empirical Model for Describing Auto-ignition*. 2008, SAE International.
47. Kalghatgi, G.T., *Auto-Ignition Quality of Practical Fuels and Implications for Fuel Requirements of Future SI and HCCI Engines*. 2005, SAE International.
48. Goldsborough, S.S., *A chemical kinetically based ignition delay correlation for iso-octane covering a wide range of conditions including the NTC region.* Combustion and Flame, 2009. 156(6): p. 1248-1262.
49. Tao, M., D. Han, and P. Zhao, *An alternative approach to accommodate detailed ignition chemistry in combustion simulation.* Combustion and Flame, 2017. 176(Supplement C): p. 400-408.
50. Kalghatgi, G., H. Babiker, and J. Badra, *A Simple Method to Predict Knock Using Toluene, N-Heptane and Iso-Octane Blends (TPRF) as Gasoline Surrogates.* SAE Int. J. Engines, 2015. 8(2): p. 505-519.
51. Mehl, M., et al., *An Approach for Formulating Surrogates for Gasoline with Application toward a Reduced Surrogate Mechanism for CFD Engine Modeling.* Energy & Fuels, 2011. 25(11): p. 5215-5223.
52. Mehl, M., et al., *Kinetic modeling of gasoline surrogate components and mixtures under engine conditions.* Proceedings of the Combustion Institute, 2011. 33(1): p. 193-200.
53. Blomberg, C.K., et al., *Extension of the Phenomenological 3-Arrhenius Auto-Ignition Model for Six Surrogate Automotive Fuels.* SAE International Journal of Engines, 2016. 9(3): p. 1544-1558.
54. Livengood, J.C. and P.C. Wu, *Correlation of autoignition phenomena in internal combustion engines and rapid compression machines.* Symposium (International) on Combustion, 1955. 5(1): p. 347-356.
55. Douaud, A.M. and P. Eyzat, *Four-Octane-Number Method for Predicting the Anti-Knock Behavior of Fuels and Engines.* 1978, SAE International.
56. Mittal, V. and J.B. Heywood, *The Relevance of Fuel RON and MON to Knock Onset in Modern SI Engines*. 2008, SAE International.
57. Amer, A., et al., *Fuel Effects on Knock in a Highly Boosted Direct Injection Spark Ignition Engine.* SAE Int. J. Fuels Lubr., 2012. 5(3): p. 1048-1065.
58. Wang, C., et al., *Significance of RON and MON to a modern DISI engine.* Fuel, 2017. 209(Supplement C): p. 172-183.
59. Elmqvist, C., et al., *Optimizing Engine Concepts by Using a Simple Model for Knock Prediction.* 2003, SAE International.
60. Hoepke, B., et al., *EGR Effects on Boosted SI Engine Operation and Knock Integral Correlation.* SAE Int. J. Engines, 2012. 5(2): p. 547-559.
61. Chen, L., et al., *A predictive model for knock onset in spark-ignition engines with cooled EGR.* Energy Conversion and Management, 2014. 87(0): p. 946-955.
62. Burluka, A.A., et al., *The Influence of Simulated Residual and NO Concentrations on Knock Onset for PRFs and Gasolines*. 2004, SAE International.
63. Gamma Technologies Inc., *GT-Suite User Manual (EngCylKnock - SI Knock Models)*. 2017.

64. Wayne, W.S., N.N. Clark, and C.M. Atkinson, *Numerical Prediction of Knock in a Bi-Fuel Engine*. 1998, SAE International.
65. Weisser, G.A., *Modelling of Combustion and NO Formation for Medium Speed DI Diesel Engines*. 2001, Technische Wissenschaften ETH Zürich.
66. Ra, Y. and R.D. Reitz, *A combustion model for IC engine combustion simulations with multi-component fuels.* Combustion and Flame, 2011. 158(1): p. 69-90.
67. Vandersickel, A., *Two Approaches to Autoignition modelling for HCCI Engines*. 2011, ETH Zurich.
68. Steurs, K., C. Blomberg, and K. Boulouchos, *Formulation of a Knock Model for Ethanol and Iso-Octane under Specific Consideration of the Thermal Boundary Layer within the End-Gas.* SAE Int. J. Engines, 2014. 7(4): p. 1752-1772.
69. AlAbbad, M., et al., *Ignition delay time measurements of primary reference fuel blends.* Combustion and Flame, 2017. 178(Supplement C): p. 205-216.
70. Yates, A., A. Bell, and A. Swarts, *Insights relating to the autoignition characteristics of alcohol fuels.* Fuel, 2010. 89(1): p. 83-93.
71. Iqbal, A., et al., *Ignition Delay Correlation for Predicting Autoignition of a Toluene Reference Fuel Blend in Spark Ignition Engines.* SAE Int. J. Engines, 2011. 4(1): p. 219-234.
72. Andrae, J.C.G., et al., *Autoignition of toluene reference fuels at high pressures modeled with detailed chemical kinetics.* Combustion and Flame, 2007. 149(1): p. 2-24.
73. Hernández, J.J., et al., *Ignition delay time correlations for a diesel fuel with application to engine combustion modelling.* International Journal of Engine Research, 2010. 11(3): p. 199-206.
74. Pan, J., et al., *A predictive Livengood–Wu correlation for two-stage ignition.* International Journal of Engine Research, 2016. 17(8): p. 825-835.
75. DelVescovo, D., S. Kokjohn, and R. Reitz, *The Development of an Ignition Delay Correlation for PRF Fuel Blends from PRF0 (n-Heptane) to PRF100 (iso-Octane).* SAE Int. J. Engines, 2016. 9(1): p. 520-535.
76. Kalghatgi, G., et al., *Knock Prediction Using a Simple Model for Ignition Delay*. 2016, SAE International.
77. Andrae, J.C.G., T. Brinck, and G.T. Kalghatgi, *HCCI experiments with toluene reference fuels modeled by a semidetailed chemical kinetic model.* Combustion and Flame, 2008. 155(4): p. 696-712.
78. Kalghatgi, G.T., K. Nakata, and K. Mogi, *Octane Appetite Studies in Direct Injection Spark Ignition (DISI) Engines*. 2005, SAE International.
79. Vancoillie, J., L. Sileghem, and S. Verhelst, *Development and Validation of a Knock Prediction Model for Methanol-Fuelled SI Engines*. 2013, SAE International.
80. Francqueville, L. and J.-B. Michel, *On the Effects of EGR on Spark-Ignited Gasoline Combustion at High Load.* SAE Int. J. Engines, 2014. 7(4): p. 1808-1823.
81. Roberts, P.J. and C.G.W. Sheppard, *The Influence of Residual Gas NO Content on Knock Onset of Iso-Octane, PRF, TRF and ULG Mixtures in SI Engines.* SAE Int. J. Engines, 2013. 6(4): p. 2028-2043.
82. Andreae, M.M., et al., *On HCCI Engine Knock*. 2007, SAE International.
83. Spelina, J.M., J.C. Peyton Jones, and J. Frey, *Recent Advances in Knock Analysis, Simulation, and Control.* SAE Int. J. Engines, 2014. 7(2): p. 947-955.
84. Millo, F. and C.V. Ferraro, *Knock in S.I. Engines: A Comparison between Different Techniques for Detection and Control.* 1998, SAE International.

85. Naber, J.D., et al., *Analysis of Combustion Knock Metrics in Spark-Ignition Engines*. 2006, SAE International.
86. Lee, J.-H., et al., *A New Knock-Detection Method using Cylinder Pressure, Block Vibration and Sound Pressure Signals from a SI Engine*. 1998, SAE International.
87. Rosseel, E., R. Sierens, and R.S.G. Baert, *Evaluating Piezo-electric Transducer Response to Thermal Shock from In-cylinder Pressure Data.* 1999, SAE International.
88. Kistler Group. *Watercooled PiezoStar Pressure Sensor (Type 6041B)*. [Datasheet] 2015; Available from: https://www.kistler.com/?type=669&fid=66335&model=document&callee=frontend
89. Scholl, D., et al., *The Volume Acoustic Modes of Spark-Ignited Internal Combustion Chambers*. 1998, SAE International.
90. Worret, R., et al., *Application of Different Cylinder Pressure Based Knock Detection Methods in Spark Ignition Engines.* 2002, SAE International.
91. Brunt, M.F.J., C.R. Pond, and J. Biundo, *Gasoline Engine Knock Analysis using Cylinder Pressure Data.* 1998, SAE International.
92. Davis, R.S. and G.J. Patterson, *Cylinder Pressure Data Quality Checks and Procedures to Maximize Data Accuracy*. 2006, SAE International.
93. Cavina, N., et al., *Individual Cylinder Combustion Control Based on Real-Time Processing of Ion Current Signals*. 2007, SAE International.
94. Philipp, H., et al., *Localization of Knock Events in Direct Injection Gasoline Engines*. 2001, SAE International.
95. Geiser, F., F. Wytrykus, and U. Spicher, *Combustion Control with the Optical Fibre Fitted Production Spark Plug*. 1998, SAE International.
96. AVL List GmbH. *Product Description - VisioKnock*. 2009 01/03/2009; Available from: https://www.avl.com/documents/10138/885965/ProductDescription_Gasoline_Engines_MPFI_and_DI_Knock.pdf
97. Abu-Qudais, M., *Exhaust gas temperature for knock detection and control in spark ignition engine.* Energy Conversion and Management, 1996. 37(9): p. 1383-1392.
98. Grandin, B. and I. Denbratt, *The Effect of Knock on Heat Transfer in SI Engines.* 2002, SAE International.
99. Checkel, M.D. and J.D. Dale, *Computerized Knock Detection from Engine Pressure Records.* 1986, SAE International.
100. Checkel, M.D. and J.D. Dale, *Pressure Trace Knock Measurement in a Current S.I. Production Engine*. 1989, SAE International.
101. Ferraro, C.V., M. Marzano, and P. Nuccio, *Knock-Limit Measurement in High-Speed S. I. Engines*. 1985, SAE International.
102. Eng, J.A., *Characterization of Pressure Waves in HCCI Combustion*. 2002, SAE International.
103. Vavra, J., et al., *Knock In Various Combustion Modes in a Gasoline-Fueled Automotive Engine.* Journal of Engineering for Gas Turbines and Power, 2012. 134(8): p. 082807-082807.
104. Siano, D., M.A. Panza, and D. D'Agostino, *Knock Detection Based on MAPO Analysis, AR Model and Discrete Wavelet Transform Applied to the In-Cylinder Pressure Data: Results and Comparison.* SAE Int. J. Engines, 2014. 8(1).
105. Brecq, G., J. Bellettre, and M. Tazerout, *Experimental Determination of Knock in Gas SI Engine*. 2001, The Automotive Research Association of India.
106. Chun, K.M. and J.B. Heywood, *Characterization of Knock in a Spark-Ignition Engine*. 1989, SAE International.

107. Xiaofeng, G., et al., *The Detection and Quantification of Knock in Spark Ignition Engines.* 1993, SAE International.
108. Siokos, K., Z. He, and R. Prucka, *Assessment of Model-Based Knock Prediction Methods for Spark-Ignition Engines*. 2017, SAE International.
109. Shahlari, A.J. and J. Ghandhi, *Pressure-Based Knock Measurement Issues*. 2017, SAE International.
110. Watson, P.F. and A. Petrie, *Method agreement analysis: A review of correct methodology.* Theriogenology, 2010. 73(9): p. 1167-1179.
111. Gamma Technologies Inc., *GT-Suite User Manual (Modelling Theory - Flow)*. 2017.
112. Gamma Technologies Inc., *GT-Suite User Manual (Modelling Applications - Engine Performance)*. 2017.
113. Franzke, D.E., *Beitrag zur Ermittlung eines Klopfkriteriums der ottomotorischen Verbrennung und zur Vorausberechnung der Klopfgrenze*. 1981, Technische Universität München.
114. Huang, Y., et al., *Spray and evaporation characteristics of ethanol and gasoline direct injection in non-evaporating, transition and flash-boiling conditions.* Energy Conversion and Management, 2016. 108(Supplement C): p. 68-77.
115. Eng, J.A., *The Effect of Spark Retard on Engine-out Hydrocarbon Emissions*. 2005, SAE International.
116. Vera, J. and J. Ghandhi, *Investigation of Post-Flame Oxidation of Unburned Hydrocarbons in Small Engines.* 2011.
117. Bradley, D., *'Hot spots' and gasoline engine knock.* Journal of the Chemical Society - Faraday Transactions, 1996. 92(16): p. 2959-2964.
118. National Institute of Standards and Technology. *NIST Chemistry WebBook, SRD 69*. 2018 18th January, 2018]; Available from: http://webbook.nist.gov/chemistry/
119. Syed, I.Z., A. Mukherjee, and J.D. Naber. *Numerical simulation of autoignition of gasoline-ethanol/air mixtures under different conditions of pressure, temperature, dilution, and equivalence ratio*. in *SAE 2011 World Congress and Exhibition, April 12, 2011 - April 14, 2011*. 2011. Detroit, MI, United states: SAE International.
120. McKenzie, J. and W.K. Cheng, *Ignition Delay Correlation for Engine Operating with Lean and with Rich Fuel-Air Mixtures*. 2016, SAE International.
121. Curran, H.J., et al., *A comprehensive modeling study of iso-octane oxidation.* Combustion and Flame, 2002. 129(3): p. 253-280.
122. Mehl, M., et al., *Detailed Kinetic Modeling of Low-Temperature Heat Release for PRF Fuels in an HCCI Engine*. 2009, SAE International.
123. Gu, X.J., D.R. Emerson, and D. Bradley, *Modes of reaction front propagation from hot spots.* Combustion and Flame, 2003. 133(1–2): p. 63-74.
124. Bradley, D., *Autoignitions and detonations in engines and ducts.* Philosophical Transactions of the Royal Society A: Mathematical, Physical and Engineering Sciences, 2012. 370(1960): p. 689-714.
125. Landis, J.R. and G.G. Koch, *The measurement of observer agreement for categorical data.* Biometrics, 1977. 33(1): p. 159-74.
126. Remmert, S., et al., *Octane Appetite: The Relevance of a Lower Limit to the MON Specification in a Downsized, Highly Boosted DISI Engine.* SAE International Journal of Fuels and Lubricants, 2014. 7(3): p. 743-755.